Unsteady Aerodynamics of

Static and Oscillating Airfoils at Large Angles of Attack

Guanqun Xu

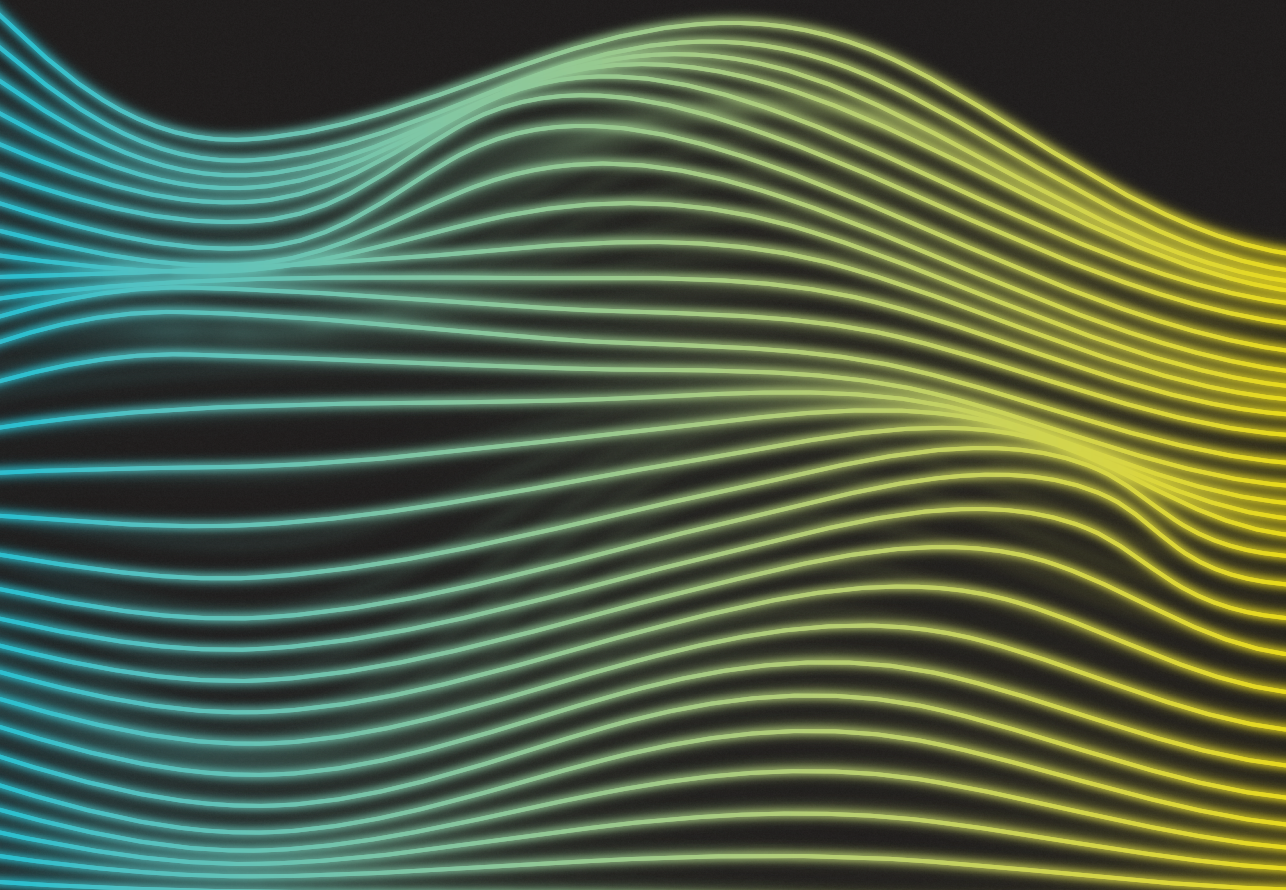

Unsteady Aerodynamics of Static and Oscillating Airfoils at Large Angles of Attack

Unsteady Aerodynamics of Static and Oscillating Airfoils at Large Angles of Attack

Dissertation

for the purpose of obtaining the degree of doctor
at Delft University of Technology
by the authority of the Rector Magnificus,
Prof.dr.ir. H. Bijl,
chair of the Board for Doctorates
to be defended publicly on
Monday, 20 April 2026, 10:00

by

Guanqun XU

This dissertation has been approved by the (co)promotors.

Composition of the doctoral committee:

Rector Magnificus,	chairperson
Prof. dr. ir. C.J. Simao Ferreira,	Delft University of Technology, promotor
Dr. A. Sciacchitano,	Delft University of Technology, promotor
Dr. W. Yu,	Delft University of Technology, copromotor
Independent members:	
Prof. dr. ir. J. Westerweel,	Delft University of Technology
Dr. C. Grinderslev,	Technical University of Denmark, Denmark
Prof. dr. M. Raffel,	The German Aerospace Center, Germany
Prof. dr. V.A. Riziotis,	National Technical University of Athens, Greece
Prof. dr. F. Scarano,	Delft University of Technology, *reserve member*

TU Delft Delft University of Technology

Keywords: Airfoil aerodynamics, reverse flow, deep dynamic stall, vortex shedding, large angles of attack, vortex-induced vibrations, Particle Image Velocimetry

Printed by: Proefschriftspecialist

Cover by: Adhyanth Giri Ajay

ISBN 978-94-6518-292-6

An electronic version of this dissertation is available at http://repository.tudelft.nl/.

致我的奶奶和外公

To my grandma and grandpa

Contents

Summary

In a world with an urgent demand for sustainable energy, the wind energy industry plays a key role in accelerating this transition. Over the past decades, wind turbines have evolved from expensive, relatively inefficient machines into increasingly cost-effective and highly efficient technologies, supported and promoted by many countries worldwide. However, this rapid progress has come at a cost: larger and more efficient turbines require substantial investments in raw materials, research and development, component standardization, and supply chain optimization.

In recent years, the curtailment of wind power in Europe has increased, largely due to insufficient grid capacity and limited energy storage. As a result, wind turbines are more frequently operated in parked conditions, with their rotors brought to a standstill. Under these circumstances, one of the key challenges in scaling up turbine size is the risk of vortex-induced vibrations (VIV) in the blades. In parked conditions, the blades are often pitched to very high angles of attack (close to 90°) to cut out of the wind. If the vortex shedding frequency approaches the blade's natural frequency, a lock-in phenomenon may occur, leading to strong vibrations. This vibration in the long term can contribute to the overall fatigue load of the wind turbine and reduce the structural life.

Although increasing attention has been given to VIV in wind turbine blades, significant gaps remain in understanding the fundamental flow physics that govern these vibrations, specifically, the unsteady aerodynamics of airfoils at high angles of attack. This dissertation therefore investigates the unsteady aerodynamics of both static and oscillating airfoils under such conditions, with the aim of building a detailed physical understanding of VIV from an aerodynamic perspective.

The research was carried out through a series of wind tunnel measurements. First, a campaign on a static airfoil examined unsteady aerodynamics across a wide range of angles of attack (up to 310°). Aerodynamic forces, vortex shedding patterns, and shedding frequencies were compared between forward flow (leading edge upwind) and reverse flow (trailing edge upwind) conditions. Although reverse flow is uncommon in normal operation, it can occur during parked or installation phases; the insights gained in this research therefore form a critical foundation for subsequent studies on oscillating airfoils.

The main focus of the dissertation is the unsteady aerodynamics of oscillating airfoils, studied using the forced motion method to mimic VIV. Three motion types, namely surging, plunging, and pitching, were investigated. Particle Image Velocimetry (PIV) was employed to capture the flow fields, while surface pressure measurements provided aerodynamic forces. By correlating vortex dynamics with force responses, the study reveals how the mean angle of attack and motion parameters (such as frequency and amplitude) influence the overall unsteady aerodynamics of the airfoil and how lock-in is triggered under different motion kinematics. Comparisons between forward and reverse flow conditions further enrich the findings, where the reverse flow dynamic stall was thoroughly discussed

from vortex dynamics and aerodynamic forces, to a newly proposed dynamic stall vortex and trailing edge vortex onset determination method.

Overall, the comprehensive experimental dataset and resulting conclusions advance the fundamental understanding of unsteady airfoil aerodynamics at large angles of attack. These findings not only clarify the underlying mechanisms causing VIV from the vortex dynamics and aerodynamic force point of view, but also provide a valuable basis for future aeroelastic VIV studies and the development of engineering models.

Samenvatting

In een wereld met een dringende vraag naar duurzame energie speelt de windenergie-industrie een sleutelrol in het versnellen van deze transitie. In de afgelopen decennia zijn windturbines geëvolueerd van dure, relatief inefficiënte machines naar steeds kosteneffectievere en zeer efficiënte technologieën, ondersteund en gepromoot door vele landen wereldwijd. Deze snelle vooruitgang heeft echter een prijs: grotere en efficiëntere turbines vereisen aanzienlijke investeringen in grondstoffen, onderzoek en ontwikkeling, standaardisatie van componenten en optimalisatie van de toeleveringsketen.

In de afgelopen jaren is de *curtailment* (het afschakelen) van windenergie in Europa toegenomen, grotendeels door onvoldoende netcapaciteit en beperkte energieopslag. Als gevolg hiervan staan windturbines vaker stil in geparkeerde toestand, waarbij de rotoren tot stilstand zijn gebracht. Onder deze omstandigheden is een van de belangrijkste uitdagingen bij het opschalen van de turbinegrootte het risico op *vortex-induced vibrations* (VIV), oftewel door wervelingen opgewekte trillingen, in de bladen. In geparkeerde toestand worden de bladen vaak naar zeer grote invalshoeken gedraaid (dicht bij 90°) om ze uit de wind te houden. Als de frequentie van het loslaten van wervels (*vortex shedding*) de eigenfrequentie van het blad nadert, kan er een *lock-in* fenomeen optreden, wat leidt tot sterke trillingen. Op de lange termijn kunnen deze trillingen bijdragen aan de totale vermoeiingsbelasting van de windturbine en de structurele levensduur verkorten.

Hoewel er steeds meer aandacht is voor VIV in windturbinebladen, blijven er aanzienlijke hiaten in het begrip van de fundamentele stromingsfysica die deze trillingen beheerst, specifiek de instationaire aerodynamica van vleugelprofielen bij grote invalshoeken. Dit proefschrift onderzoekt daarom de instationaire aerodynamica van zowel statische als oscillerende vleugelprofielen onder dergelijke omstandigheden, met als doel een gedetailleerd fysisch begrip van VIV op te bouwen vanuit een aerodynamisch perspectief.

Het onderzoek is uitgevoerd door middel van een reeks windtunnelmetingen. Allereerst is in een meetcampagne met een statisch vleugelprofiel de instationaire aerodynamica onderzocht over een breed bereik van invalshoeken (tot 310°). Aerodynamische krachten, patronen van wervelafschudding en afschudfrequenties werden vergeleken tussen *forward flow* (voorwaartse stroming, neus in de wind) en *reverse flow* (achterwaartse stroming, achterlijst in de wind). Hoewel *reverse flow* ongebruikelijk is tijdens normaal bedrijf, kan het voorkomen tijdens geparkeerde of installatiefasen; de inzichten uit dit onderzoek vormen daarom een cruciaal fundament voor vervolgstudies naar oscillerende vleugelprofielen.

De focus van het proefschrift ligt op de instationaire aerodynamica van oscillerende vleugelprofielen, bestudeerd met behulp van de *forced motion* methode om VIV na te bootsen. Drie bewegingstypes, namelijk *surging* (langsbeweging), *plunging* (dwarsbeweging) en *pitching* (hoekverdraaiing), werden onderzocht. *Particle Image Velocimetry* (PIV) werd gebruikt om de stromingsvelden vast te leggen, terwijl oppervlakte-drukmetingen de aerodynamische krachten leverden. Door de werveldynamica te correleren met de krachtres-

ponsen, laat de studie zien hoe de gemiddelde invalshoek en bewegingsparameters (zoals frequentie en amplitude) de algehele instationaire aerodynamica van het profiel beïnvloeden en hoe *lock-in* wordt geactiveerd onder verschillende bewegingskinematiek. Vergelijkingen tussen *forward* en *reverse flow* condities verrijken de bevindingen verder, waarbij de dynamische overtrek (*dynamic stall*) in *reverse flow* grondig is besproken vanuit het oogpunt van werveldynamica en aerodynamische krachten, tot aan een nieuw voorgestelde methode voor het bepalen van het ontstaan van de *dynamic stall vortex* en *trailing edge vortex*.

Over het geheel genomen bevorderen de uitgebreide experimentele dataset en de daaruit voortvloeiende conclusies het fundamentele begrip van instationaire profiel aerodynamica bij grote invalshoeken. Deze bevindingen verhelderen niet alleen de onderliggende mechanismen die VIV veroorzaken vanuit het oogpunt van werveldynamica en aerodynamische krachten, maar bieden ook een waardevolle basis voor toekomstige aero-elastische VIV-studies en de ontwikkeling van ingenieursmodellen.

I

Introduction

1

Introduction

1.1 Wind energy development

Back in the 1980s, wind energy was considered as an unconventional, weather-driven, variable power source [1]. The technology at that time lacked efficiency and reliability, with smaller turbines producing inconsistent output. Meanwhile, it also faced integration challenges with electrical grids, which were designed for stable, controllable energy sources like fossil fuels or nuclear. As a result, utilities were hesitant to adopt wind energy at scale, viewing it as unreliable compared to conventional power sources.

Figure 1.1: Wind turbines in Askov, Denmark, constructed following a government grant awarded to Poul la Cour in 1897. Photo courtesy of the Poul la Cour Museum, used with permission.

In the early 2000s, the wind energy industry started to grow. By 2001, the cumulative installed wind power capacity worldwide was approximately 24 gigawatts (GW). By 2009,

1

this number has increased more than 6 folds, to 159 GW [2]. This dramatic growth was not accidental but driven by a confluence of technological, economic, and policy factors.

First, the high installation is related to the high demand for energy, with the awareness of reducing carbon emissions. During the early 2000s, several policies aimed at reducing carbon emissions were implemented, including the Kyoto Protocol [3] and the European Union Emission Trading System [4], which led to government policies that encouraged the development of renewable energy. Without such regulatory pressure, the transition to renewables might have lagged behind fossil fuel dependence.

Second, policy fastens the process of renewable energy development. In the early 2000s, several countries in Europe such as Germany and Spain introduced feed-in tariffs [5], where guaranteed fixed prices for electricity generated from wind, making investments more attractive. Meanwhile, the US and India introduced tax incentives for renewable energy production [5]. All of these policy mechanisms were critical in creating stable markets, attracting investment, and accelerating project approvals, which are key enablers of the industry' s exponential growth.

Third, with the advancement in turbine technology, wind turbines are designed to have larger blades, taller towers (see Figure 1.3), and better materials, all of which increase the capacity factors and reduce costs per MW. At the same time, offshore wind energy starts to grow (especially after 2010s), which brings even more potential for the wind industry.

Nowadays, wind energy is considered to be one of the most powerful renewable sources. In 2023, renewable energy sources (including solar, hydropower, biomass, and geothermal) contributed around 30.2% of global electricity generation, among which, wind energy takes 7.8% [6]. By 2024, the global cumulative installed wind power capacity has reached 1173 GW (Figure 1.2), and China (561.5 GW), the United States (154.6 GW), and Germany (72.6 GW) are the leading three countries [7]. Based on the prediction in [6], the global renewable energy industry is on course to add more renewable capacity in the next five years. In 2028, it is predicted that renewable energy sources will contribute approximately 41.6% of global electricity generation, and wind energy will share 12.1% [6], which is more than 50% of the current share.

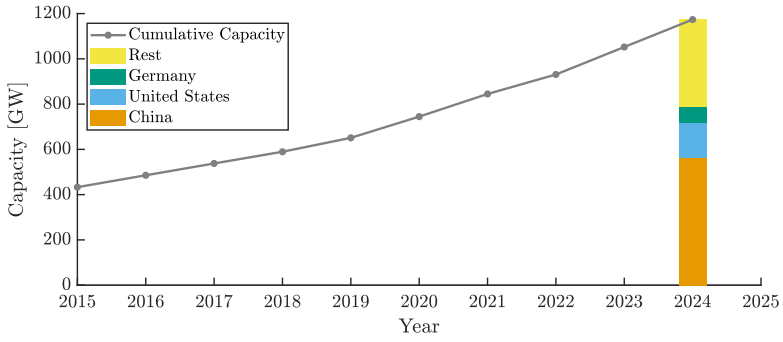

Figure 1.2: Cumulative wind power capacity worldwide. Data source: [7]

1.2 Growth and challenges of modern wind turbines

The rapid advancements in wind energy technology have led to the development of more efficient and reliable wind turbines, which are essential for meeting growing energy demands and reducing carbon emissions. Figure 1.3 presents the growth of wind turbine size for onshore and offshore wind turbines. Overall, the growth trend is more pronounced for offshore wind turbines in terms of tip height, rotor diameter, and rated power, while both onshore and offshore turbines continue to develop at relatively high speeds. For example, the rotor diameter of both types grew from below 50m in the 1980s and 1990s to 220m to 280m in 2023. Although upscaling wind turbines appears promising, it does not necessarily lead to more cost-effective energy in a straightforward manner. As wind turbines become larger, a significant amount of cost is required for research and development due to the complexity of aerodynamics, structural loads, and fatigue concerns [8], not to mention the increased pressure on raw materials. In addition, more factors are important to make the wind industry cost-effective, such as adapting to specific site conditions, standardising components, and streamlining supply chains [2].

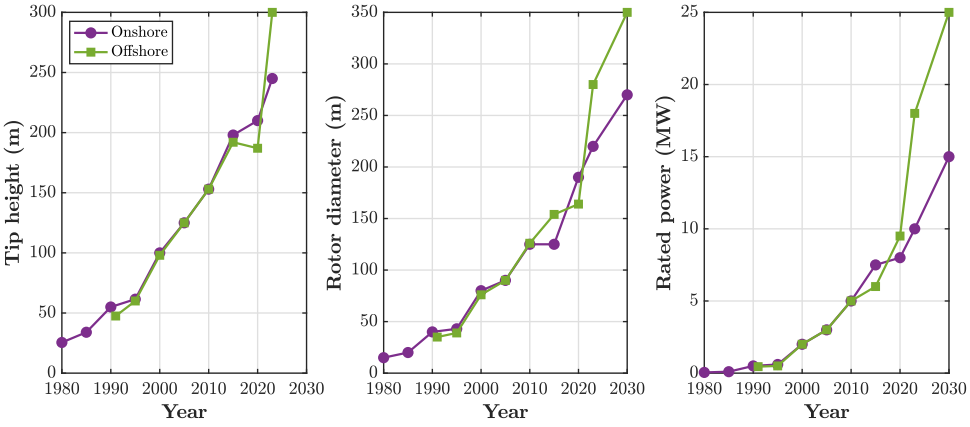

Figure 1.3: Trend of onshore and offshore wind turbine size with the (estimated) rotor diameter and (estimated) rated power till the year 2030. Data source: [2].

1.3 Vortex-induced vibrations on wind turbine blades

A critical technical challenge in wind turbine upscaling is vortex-induced vibration (VIV) on wind turbine blades, which significantly impacts blade fatigue, structural integrity, and operational efficiency. VIV occurs when vortex shedding frequencies synchronize with the blade's natural frequency, leading to excessive displacements and dynamic loads [9]. While VIV has been extensively studied in other engineering fields, such as bridges, offshore structures, and transmission lines, as reviewed by [10], [11], and [12], its implications for wind turbine blades have only recently gained attention.

The growing size of modern turbine blades, designed to capture more aerodynamic power, exacerbates VIV risks, particularly during parked conditions or installation. In these scenarios, blades operate at unusually high pitch angles (e.g., up to 88.3°, as observed

in the Belwind wind farm [13]), making them more susceptible to VIV-induced fatigue and structural damage. This phenomenon implies the need for a deeper understanding of unsteady aerodynamic loads on stationary and parked blades, which is a key motivation for this dissertation on unsteady airfoil aerodynamics.

1.4 State of the art

In this section, the state of the art related to the background of this dissertation is presented. Specifically, two research areas are reviewed: (i) vortex-induced vibration problems and (ii) unsteady airfoil aerodynamics. Relevant studies in each field are discussed below.

1.4.1 Vortex-induced vibrations

Over the past few decades, several studies have emerged that investigate VIV on wind turbine blades, primarily through numerical simulations. This section provides a brief review of past research on VIV on wind turbine blades. Based on the research model scale, the study can be divided into full wind turbine level, blade level, and airfoil level.

Studying VIV at the wind turbine level either involves a field test or building an accurate aeroelastic model. Bouwmeesters [14] analysed the field measurement data from a 3.8 MW and demonstrated that parked wind turbines can experience stall and vortex-induced vibration under specific yaw and pitch conditions, with certain angles (particularly near 100° and 200°). Manolas et al. [15] apply the empirical VIV model from EUROCODE [16] to the aeroelastic tool to predict wind turbine loads and deformation from both the tower and the blades. Pirrung et al. [17] conducted full rotor simulations with a forced-motion method of IEA 10 MW reference turbine [18] in a parked configuration (80° degrees pitch and 90° yaw). The first [15] presents the empirical model that can be used for the efficient scan of a wide list of criticals for VIV cases, while the second [17] provides more detailed insights in a single VIV case regarding the oscillation amplitude, mode shapes, etc. Apart from these, studies [19, 20] also focused on the overall stability of the parked or idling wind turbines. Leng et al. [19] investigated the aeroelastic characteristics of a parked 5 MW offshore wind turbine and showed that extreme wind conditions and yaw misalignment can induce significantly high frequency edgewise vibrations and load fluctuations during idling. Meng et al. [20] studied the stall-induced aeroelastic instability of a standstill NREL OC3-Hywind 5MW floating offshore wind turbine, which shows that the rotor edgewise and tower side-side modes are related to stall-induced instability due to negative aerodynamic damping at specific yaw and azimuth angles. In the meantime, we should acknowledge the high computational expense associated with the full wind turbine simulation. As mentioned by Pirrung et al. [17], the computational cost for a forced-motion simulation can be nine times higher than a single-blade simulation, considering three blades and three different modes need to be evaluated. Therefore, conducting full-scale turbine simulation on VIV still remains a significant challenge, partially relying on the development of computer science.

Comparably, more VIV studies have been conducted on a blade level, which indicates that VIV is strongly influenced by blade geometry and inflow conditions. Multiple studies highlight that variations in tip shape and inflow angle significantly affect vibration amplitude, mode shapes, and the spatial distribution of shed vorticity along the blade span.

For instance, Horcas et al. [21, 22] demonstrated that different tip configurations produce distinct vibrational behaviors, emphasizing the need to reassess sensitivity for each new blade design. Similarly, Heinz et al. [23] found that inclined flow improves the correlation of shed vorticity, which can in turn excite edgewise vibrations, while Skrzypiński et al. [24] showed that inflow angle directly affects the accuracy of three-dimensional DES predictions of vortex-induced integral loading. Meanwhile, efforts to mitigate VIV have explored aerodynamic control surfaces, such as flaps, which can reduce vibration amplitudes under specific configurations [25]. However, these strategies require a deeper understanding of the underlying fluid-structure interaction mechanisms to ensure robust performance across operating conditions. In addition to geometric and control factors, blade response is sensitive to physical and numerical parameters. Hoskoti et al. [26] demonstrated that larger mass ratios increase the possibility of VIV, while Grinderslev et al. [27] highlighted the critical role of grid strategies and turbulence modeling, particularly under low-inclination flow. Overall, these studies collectively highlight the importance of geometric design, inflow characteristics, and modeling choices in shaping VIV behavior, which provides a foundation for future optimization strategies.

On the contrary, research on VIV at the airfoil level is more widely conducted, as simplified geometries and controlled conditions allow for detailed investigations of fundamental fluid-structure interaction mechanisms, reduced-order modeling, validation of computational methods, etc. This area of study can be broadly classified into two categories, based on how airfoil motion is treated. The first category focuses on elastically mounted airfoils, where structural flexibility allows natural coupling between aerodynamic forces and structural dynamics. These studies examine how vortex shedding interacts with airfoil modes to induce VIV. For instance, Skrzypiński et al. [28] numerically studied an elastically mounted DU96-W-180 airfoil, revealing that the vortex shedding frequency locks onto the first chordwise blade mode, leading to oscillatory aerodynamic loading and VIV. Similarly, Ehrmann et al. [29] performed experiments comparing different airfoil shapes at a 90° angle of attack, demonstrating that sharp leading or trailing edges significantly affect the amplitude and frequency response of VIV. These studies highlight how both airfoil geometry and structural properties influence the characteristics of VIV.

The second category focuses on stiff airfoils with forced motion, where the motion of the airfoil is prescribed to maintain constant frequency and amplitude. This approach addresses the challenge that, in free vibration, the natural oscillation frequency and vortex shedding frequency cannot remain constant over time due to added mass variations [12]. By imposing a controlled oscillation, researchers can systematically explore the lock-in phenomenon, where vortex shedding synchronizes with the airfoil motion. Studies can be found in Besem et al. [30], Benner et al. [31], Hu et al. [32], Meskell and Pellegrino [33], and Zou et al. [34], where the lock-in is present based on whether the shedding frequency locks into the motion frequency (i.e., the ratio between the vortex shedding frequency and the motion frequency is close to one) by varying different mean angles of attack, frequency of airfoil oscillation, amplitudes, and Reynolds numbers. Among them, [30, 32, 33] characterize the lock-in region, typically exhibiting a V-shaped pattern (see Figure 1.4), where the x-axis is the frequency ratio (r) between the airfoil oscillation frequency (f_{pitch} or f_{plunge}) and the static vortex shedding frequency (f_{vs}), and the y-axis denotes the pitching amplitude for the pitch motion (Figure 1.7a) or amplitude ratio be-

1

tween the motion amplitude and the airfoil chord for the plunge motion (Figure 1.7b). Inside the boundary of the V-shape (the shaded area), the frequencies are locked in. This shape indicates that, for r closer to 1, a small amplitude ratio can cause frequency lock-in, while when the oscillation frequency is away from the vortex shedding frequency, a larger oscillation amplitude is required to trigger lock-in.

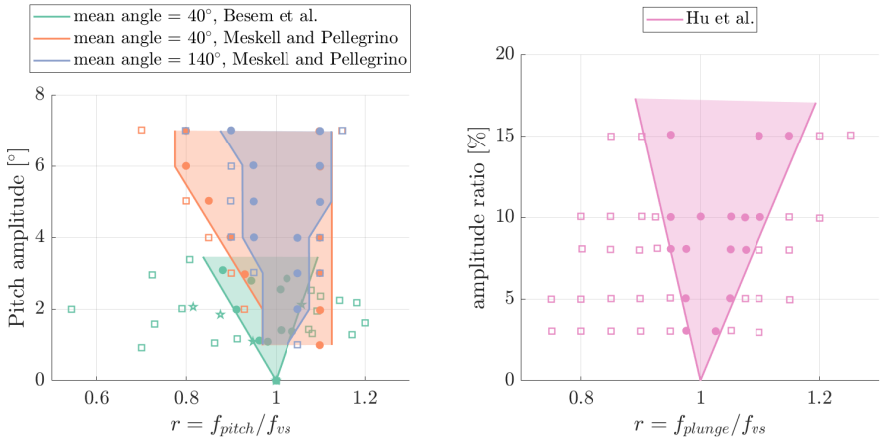

(a) Pitch motion (experimental data)

(b) Plunge motion (simulation data)

Figure 1.4: The V-shaped lock-in region adopted from Besem et al [30], Maskell and Pellegrino [33] for the pitch motion, and Hu et al. [32] for the plunge motion. The locked-in cases are marked by solid circles with corresponding colors, while the unlocked-in cases and the edge cases are marked by empty rectangles and pentagrams, respectively.

In all, recent research of VIV on wind turbine blade has gained significant attention due to the growing relevance for large-scale wind turbines, where increased blade flexibility exacerbates VIV risks. Existing studies have broadly investigated the lock-in phenomena with the focus on motion frequency, force variations, and overall aerodynamic response, which provides valuable guidelines for VIV thresholds and mitigation strategies. However, a fundamental understanding of the underlying aerodynamics during VIV remains incomplete, as prior work has not thoroughly examined the transient flow physics governing lock-in mechanisms. This knowledge gap leaves critical questions unanswered about VIV. To provide a more fundamental knowledge based on previous work, the following section delves into the state-of-the-art research on unsteady airfoil aerodynamics, especially those relevant to VIV conditions.

1.4.2 Unsteady airfoil aerodynamics

Static airfoil

To study the unsteady aerodynamics of a static airfoil, surface pressure measurements in wind tunnels are often employed to characterize the instantaneous pressure distributions over airfoils. For example, experimental pressure measurements were carried out on a static airfoil to study the stall behaviour [35], the effect of the LSB with different turbulence levels [36], the influence of pressure tap layouts [37], the effect of Reynolds number

and separated shear layer behavior on airfoil wake development [38], and comparison between two different flow regimes in terms of separation bubble, laminar-to-turbulence transition [39]. These research findings contribute essential knowledge to unsteady airfoil aerodynamics; however, most of them study at angles of attack lower than 20°, which is far below the range when VIV would happen.

In contrast, studies of unsteady aerodynamics on static airfoils at high angles of attack remain limited in scope and availability. Swalwell et al. [40] studied the static airfoil NACA0021 up to 90° angles of attack, with a focus on establishing the universal Strouhal number based on the vortex shedding frequency. Timmer [41] compared several wind tunnel pressure measurements across various airfoil profiles, highlighting a general trend in maximum drag coefficient and lift-drag ratio. However, these studies primarily focus on global aerodynamic coefficients rather than fundamental flow physics. Critical aspects of flow separation, vortex formation mechanisms, their unsteady behavior at extreme angles, etc, remain uncharacterized.

During parked wind turbine conditions (e.g., under extreme winds), the incoming flow direction becomes arbitrary. At the airfoil level (as demonstrated in Figure 1.5), when the angle of attack (AoA, defined as the angle between the incoming wind U_∞ and the chord-line) falls within the 90° to 270° range, the geometric trailing edge effectively becomes the windward side. This orientation triggers reverse flow conditions, leading to fundamentally distinct aerodynamic behavior compared to conventional operation. Lind and Jones

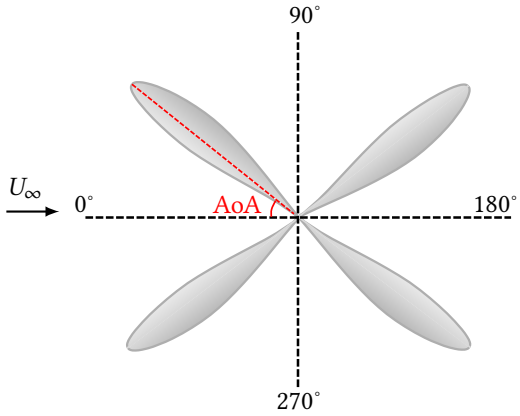

Figure 1.5: Illustration of reverse flow. Four airfoils are plotted to demonstrate the angle of attack (AoA) within 0° to 90° and within 270° to 0° (360°) are forward flow conditions, and within 90° to 270° are reverse flow conditions. U_∞ is the incoming wind from the left.

[42] experimentally investigated vortex shedding from static airfoils over a full range of angles of attack, with particular emphasis on the reverse flow region (α between 150° and 180°). They identified three distinct reverse flow regions by comparing sharp and blunt trailing edge airfoils: slender body vortex shedding, turbulent, and deep stall vortex shedding. In a follow-up study, Lind and Jones further analyzed pressure distributions on the airfoil surface at large angles of attack between 0° and 180° [43]. They found out that the airloads during stall (both positive and negative) are fundamentally linked to stall type: for a leading edge stall, there is a rapid increase in unsteady airloads at the onset of stall;

1

for a trailing edge stall, the unsteady airloads increase gradually. The study further identified maximum unsteady airloads near blunt trailing edges, highlighting the critical role of airfoil geometry in load determination. Given the prevalence of asymmetric airfoils in wind turbine design, these findings neglect the need to characterize how vortex shedding dynamics differ between symmetric and asymmetric profiles, particularly since different geometries may alter stall behaviors and load distributions under reverse flow conditions during VIV.

Oscillating airfoils

Since the pioneering research into establishing inviscid models for unsteady airfoils from Theodorsen [44], Sears [45], and Greenberg [46], a few works that relate to oscillating airfoils have been performed over the past decades. The following discussion categorizes the most relevant works according to the type of airfoil motion: surging, plunging, and pitching, and highlights key topics in vortex dynamics, lock-in effects, and aerodynamic loads.

1. Surging motion

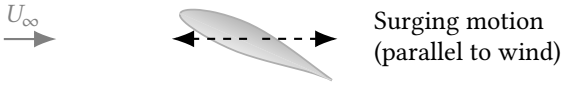

Figure 1.6: Schematic representation of the airfoil surging motion.

The surging motion, defined as the movement of an airfoil parallel to the incoming flow (see Figure 1.6), has been the subject of several studies investigating its aerodynamic consequences. Choi et al. [47] examined a plunging and surging airfoil and identified two distinct ranges of reduced frequencies (k) where the cycle-averaged lift is maximized and minimized, respectively, with the reduced frequency defined as [48]:

$$k = \frac{2\pi f \frac{c}{2}}{U_\infty}, \tag{1.1}$$

where f is the motion frequency, c the chord length, and U_∞ the incoming wind speed. However, their analysis was limited to cycle-averaged forces and did not explore the instantaneous evolution of aerodynamic loads or associated vortex structures. Zhu et al. [49] approached surging differently, imposing a harmonic surging inflow rather than oscillating the airfoil. They demonstrated that even when parameters such as reduced frequency, velocity amplitude ratio, angle of attack, and Reynolds number satisfy the thin airfoil theory, the classical Kutta condition fails due to significant transverse motion of the trailing edge stagnation streaklines (Figure 1.7). Strangfeld et al. [50] further showed that for an airfoil undergoing synchronized surging and pitching, the lift cannot be accurately predicted by linear superposition of the individual effects, as the effective reduced frequency varies dynamically during the pitching motion. Together, these studies highlight the complex aerodynamics during a surging motion, as well as deviations from classical theory at moderate angles of attack. Kirk and Jones [51] extended the angle of attack under reverse

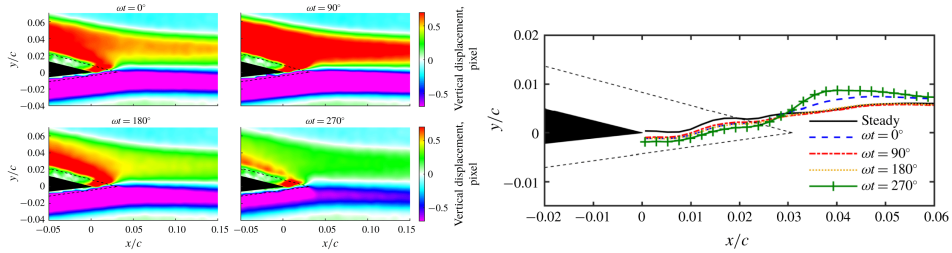

(a) (b)

Figure 1.7: Illustration of (a) the trailing edge displacement from a background-oriented schlieren field and (b) the oscillation of the trailing edge stagnation streakline. Adapted from Zhu et al. [49].

flow conditions, with a focus on the leading edge vortex (LEV) dynamics, showing that the LEV convects faster under reverse flow conditions than in high-advance-ratio rotor flows. However, their work focused primarily on LEV behavior at specific conditions (especially limiting mean angle of attack variations), leaving the broader unsteady aerodynamics, including other vortex structures and force fluctuations, less explored. Overall, while these studies provide valuable knowledge of surging aerodynamics at moderate angles of attack, they suggest that classical theories and simplified models are insufficient for large angles of attack conditions. A detailed, time-resolved investigation of aerodynamic forces and vortex dynamics under such conditions is therefore essential to fully understand and predict the unsteady behavior of surging airfoils.

2. Plunging motion

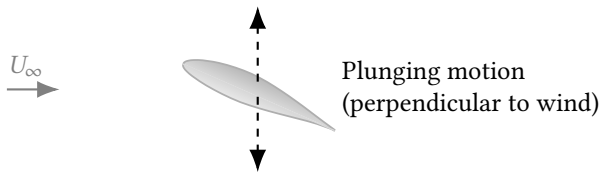

Figure 1.8: Schematic representation of the airfoil plunging motion.

Research on plunging airfoils has consistently demonstrated that their aerodynamic response is governed predominantly by vortex dynamics rather than quasi-steady or linear aerodynamic behavior. When an airfoil undergoes vertical plunging motion (see Figure 1.8), the rapid change in effective angle of attack generates strong leading edge shear layers that roll up into coherent LEVs. These vortices grow, convect, and eventually detach, producing large peaks in aerodynamic force that cannot be captured by steady assumptions. A wide range of studies have confirmed this behavior. Young and Lai [52, 53], Fenercioglu and Cetiner [54], and Kang et al. [55] observed that transitions in wake topology are strongly correlated with plunging frequency and amplitude. Once separation is present, the flow is dominated by discrete vortex events rather than attached boundary layer development. More recently, Kissing et al. [56] used Lagrangian flow analysis to

show that secondary vortical structures play a key role in initiating LEV detachment, specifically when the shear-layer angle at the leading edge stops increasing. This finding provides a fundamental explanation of vortex evolution and force variation, which demonstrates that vortex dynamics are central to understanding the aerodynamics of an oscillating body.

There is a broad consensus that predictive modeling remains challenging in the vortex-dominated regime. Linear theory (e.g., Theodorsen's unsteady linear airfoil theory [44]) aligns with measurements only when separation is weak, and high-fidelity simulations diverge from experiments during later shedding stages [57, 58] (Figure 1.9). Meanwhile,

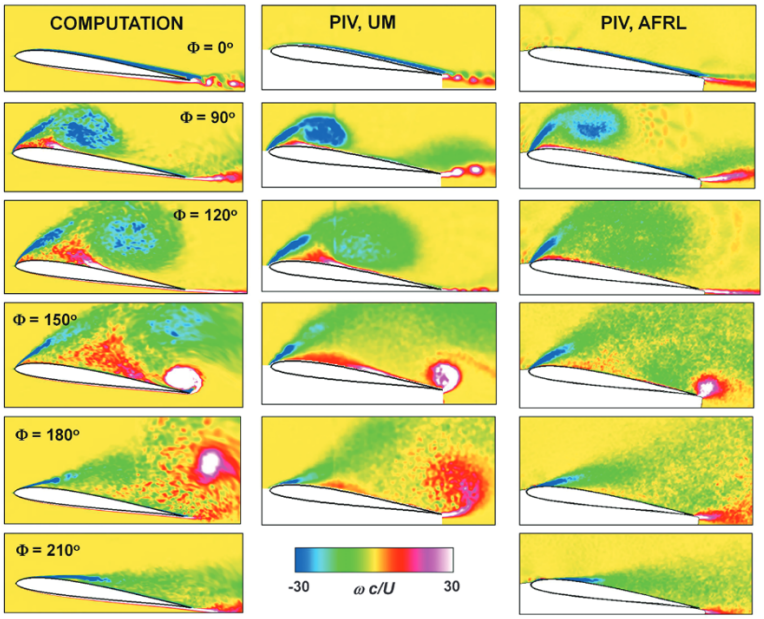

Figure 1.9: Comparison between numerical simulation (the left column), and two PIV measurements (the middle and right columns) of a plunging airfoil from the water channel facilities from the University of Michigan (UM), and the Air Force Research Laboratory (AFRL), respectively. Adapted from Visbal [57].

reduced-order models, such as those developed by Troshin and Seifert [59], show promise in capturing the dominant flow structures and force trends, but rely on empirical input and calibration, which lack generality. In all, these challenges emphasize the need for carefully designed experimental studies on oscillating airfoils to support and validate aerodynamic models in strongly separated flow conditions.

A common conclusion across the literature is that motion kinematics, particularly oscillation frequency and amplitude, play a more dominant role in vortex behavior than Reynolds number within typical experimental ranges. Changes in Strouhal number or reduced frequency can alter the timing of LEV formation and shedding, shift wake mode boundaries, or cause lock-in between structural and vortex shedding frequencies [53, 54]. Experiments indicate that even modest variations in kinematics can transit the system from weakly separated periodic shedding to strong vortex-dominated flow with large force

fluctuations. This raises an important open question for the present dissertation: how will the motion kinematics influence the overall vortex dynamics and the resulting aerodynamic load under VIV conditions where large oscillations occur at high angles of attack?

Another recurring research focus concerns the influence of geometry on the behavior of separated flow. Comparative studies on plunging flat plates and airfoils [55, 60, 61] highlight that even small geometric changes can meaningfully alter the flow topology. Sharp leading edges tend to facilitate rapid shear layer roll-up and produce strong LEVs, whereas more rounded profiles delay separation but may generate weaker vortices. The trailing edge shape has also been shown to control the symmetry and timing of vortex release. Young and Lai [53] linked asymmetric shedding to the presence of a sharp trailing edge, which promotes vortex formation predominantly on one surface during the cycle. These findings are particularly relevant for large amplitude oscillations under VIV conditions. As the body oscillates under large angles of attack (e.g., between 90° and 180°), the original trailing edge may become the effective leading edge during part of the motion. This alters the LEV formation and potentially leads to reverse flow separation mechanisms, which are rarely explored in existing plunging literature.

3. Pitching motion

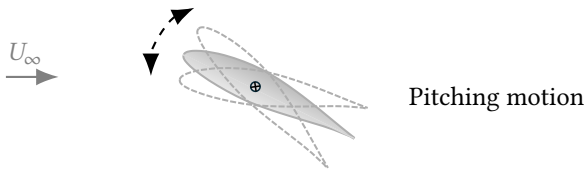

Figure 1.10: Schematic representation of the airfoil pitching motion.

One crucial phenomenon in the unsteady aerodynamics of an oscillating airfoil is dynamic stall. Dynamic stall appears in a wide range of aerodynamic applications such as helicopters, rapidly maneuvering aircraft, wind turbines, and insect wings [62]. The process of a typical dynamic stall event is shown in Figure 1.11. It occurs when a lifting surface undergoes rapid changes in angle of attack (such as pitching, as shown in Figure 1.10), with features including higher aerodynamic forces, delayed stall, vortex convention, and boundary layer reattachment. These processes significantly impact aerodynamic performance, often resulting in large unsteady loads, vibrations, fatigue, and potential structural damage. Understanding dynamic stall is therefore essential for optimizing the design and operation of aerodynamic systems, particularly under unsteady conditions.

Highly influential pioneering work from the 1970s to the 1990s provides not only a wide range of experimental studies on the forces and vortex dynamics during dynamic stall (see McCroskey and Fisher [63], Carr [62], McCroskey [64], and Mcalister et al. [65]), but also widely used numerical models for dynamic stall (see Leishman and Beddoes [66], Truong [67], and Tran and Petot [68]). In recent years, research on dynamic stall has continued to advance, with a strong focus on conventional flow conditions. Akbari and Price [69] applied a vortex method to simulate the pitching NACA 0012 airfoil under dynamic stall conditions, where the effects of pitching parameters of reduced frequency, mean an-

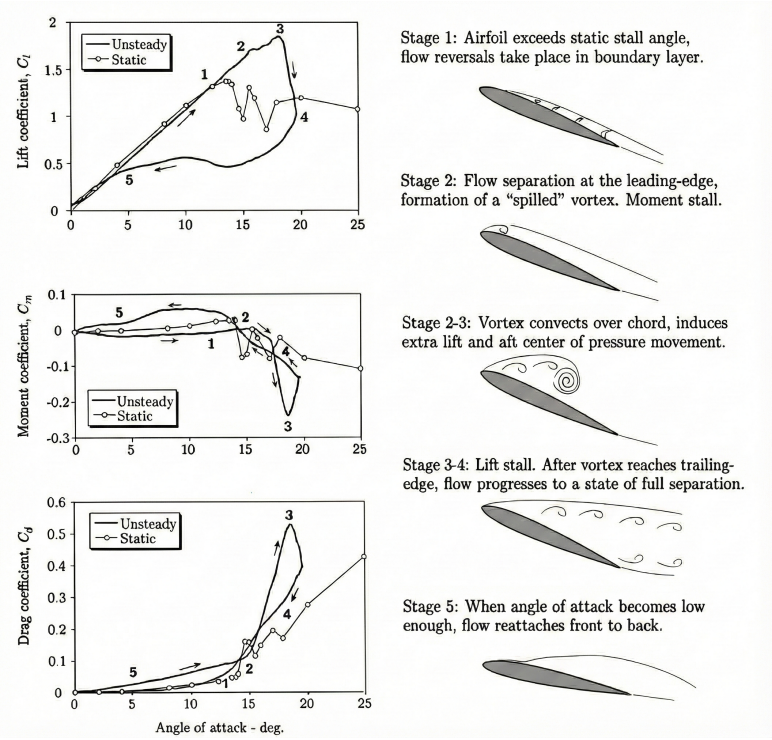

Figure 1.11: Illustration of a dynamic stall process. Adapted from Leishman [48].

gle of attack, location of pitch axis, and Reynolds numbers were investigated. Mulleners and Raffel [70] conducted an experimental investigation of a pitching airfoil under dynamic stall, employing various numerical methods to identify coherent flow structures. Their work classified dynamic stall into distinct stages based on the life cycle of dynamic stall vortices, providing significant insights into vortex development. Building on this, Mulleners and Raffel [71] further explored the vortex dynamics and flow mechanisms during dynamic stall, identifying primary and secondary instabilities. Similarly, Gupta and Ansell [72] studied experimentally the unsteady flow physics, with a particular focus on the airfoil boundary layer, leading edge laminar separation bubble, and dynamic stall vortex. Kiefer et al. [73] expanded on these findings by conducting experimental measurements on a ramp-type pitching airfoil, revealing universal pressure patterns independent of parameter variations of mean angle, angle amplitude, Reynolds number and reduced frequency. Their study also emphasized the impact of Reynolds number and reduced frequency on dynamic stall behavior, demonstrating that the angle of attack during pitching relative to the static stall angle, which depends on Reynolds number, plays a key role in the temporal progression of the stall process. Additionally, they found that once a critical reduced frequency is reached, both the load magnitude and vortex evolution become independent of further increases in the reduced frequency. Collectively, these works provide a detailed evaluation of vortex formation, force variation, and parameter sensitivity

in conventional forward flow dynamic stall.

In contrast, dynamic stall under reverse flow conditions, where the geometric trailing edge faces the incoming flow, remains far less understood. Meanwhile, reverse flow dynamic stall has been documented in helicopter applications [74, 75]. For wind turbines, this phenomenon is critical during parked conditions or during installation, as omnidirectional wind exposure can trigger VIV and significantly accelerate fatigue damage. However, the fundamental flow mechanisms governing reverse flow dynamic stall remain unsolved, leaving a critical gap in our ability to address these operational challenges.

One of the most defining features of dynamic stall, whether under conventional or reverse flow conditions, is the development of the dynamic stall vortex (DSV). The DSV typically forms near the aerodynamic leading edge, grows in size as it convects downstream, and eventually detaches from the airfoil surface, causing significant variations in aerodynamic forces and moments. In conventional cases, this process is well-documented and characterized by strong hysteresis effects in lift, drag, and pitching moment. Guillaud et al. [76] numerically investigated a pitching airfoil under forward flow conditions and observed that as k increases, the LEV exhibits a shorter life span, although its formation and shedding occur over a larger range of angles of attack. This behavior results in a more abrupt drop in force at higher reduced frequencies. Wei et al. [77] studied a conventional dynamic stall case, where the near-wall development characteristics and near-wall evolution velocity are studied in detail. From their pressure measurement, it is found that two LEVs are formed at different locations on the airfoil surface, which then develop together into a DSV. Khalifa et al. [78] performed high-fidelity numerical simulations of dynamic stall on a pitching NACA 0012 airfoil, revealing the inherently three-dimensional nature of the phenomenon. Their results captured the formation and evolution of LEVs and their interaction with the turbulent separated vortices (TSV), as shown in Figure 1.12. This result highlights the complicated interaction and breakdown of vortical systems during the dynamic stall. By contrast, for reverse flow dynamic stall, much less is known. Lind and Jones [79] observed the formation of two DSVs in a single cycle (Figure 1.13), with fewer vortices at higher reduced frequency, attributing the secondary force peak to weaker vortex shedding. Yet, without detailed flow field validation, such interpretations remain tentative. Thus, while DSV dynamics in conventional stall are now well established, their manifestation in reverse flow conditions is still an open question, which also directly motivates this dissertation.

1.4.3 Summary

The study of VIV on wind turbine blades has gained increasing attention due to the upscaling of modern wind turbines. While most research has been conducted at the blade or airfoil level, owing to the high computational costs and experimental challenges of full turbine simulations, significant gaps remain in understanding the fundamental flow physics of VIV. Existing studies primarily focus on the lock-in effect and overall aerodynamic response, often overlooking the underlying vortex dynamics and unsteady aerodynamic mechanisms. Furthermore, while unsteady aerodynamics has been extensively investigated for static or oscillating airfoils, these studies are typically limited to small angles of attack under normal operating conditions. In contrast, VIV often involves large angles of attack, including reverse flow regimes, which can trigger severe vibrations; however, this

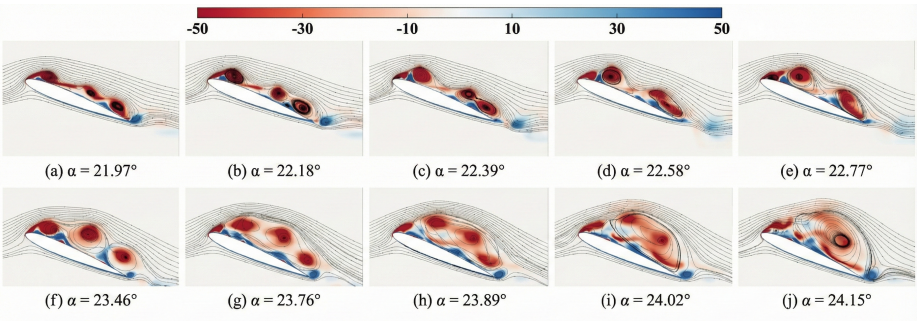

Figure 1.12: Illustration of the interaction between the leading edge vortices (LEV) and the turbulent separated vortices (TSV) during a dynamic stall process. Adapted from Khalifa et al. [78].

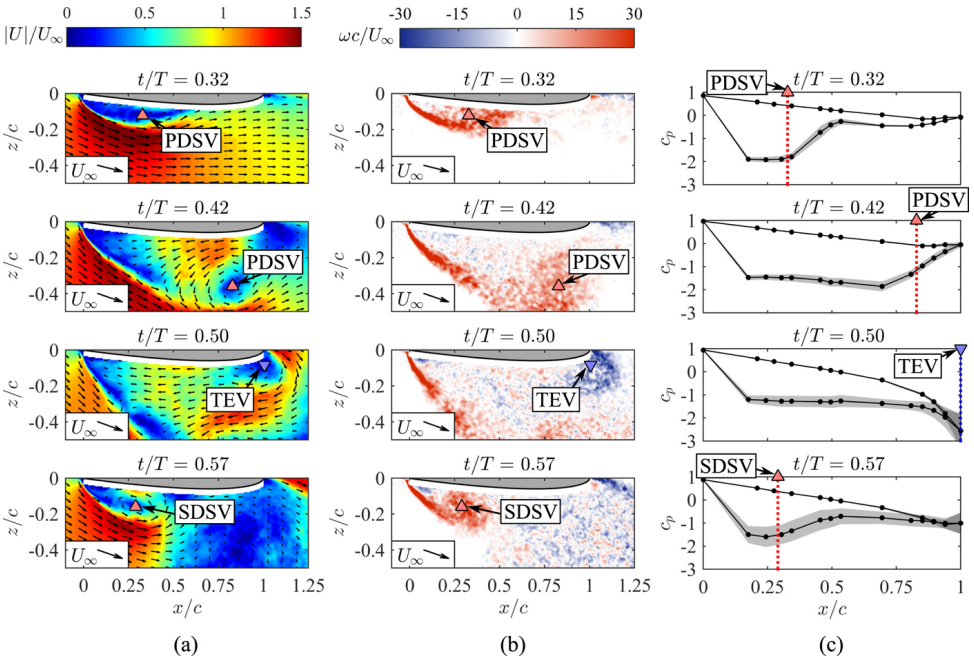

Figure 1.13: Evolution of a reverse flow dynamic stall case. (a) Total velocity fields. (b) Vorticity fields. (c) Chordwise pressure coefficient. PDSV: primary dynamic stall vortex, TEV: trailing edge vortex, SDSV: secondary dynamic stall vortex. Adapted from Lind and Jones [79].

part is not clearly understood.

1.5 Research questions

The present work is motivated by the lack of a comprehensive understanding of VIV in airfoils, particularly the role of unsteady aerodynamic effects driven by structural oscillations. Specifically, the main research objective is to **investigate the unsteady aerodynamics of static and oscillating airfoils at large angles of attack exceeding** 20°, primarily through **experimental methods** to capture complex flow phenomena associated with VIVs.

Overall research question: How do unsteady aerodynamic phenomena influence the forces and flow dynamics of static and oscillating airfoils at high angles of attack?

Serving as a baseline study of a static airfoil, the following sub-questions are addressed in Part II related to **static airfoil behavior at high angles of attack**:

1. How do forward and reverse flow conditions affect the unsteady aerodynamic loading and vortex shedding characteristics of a static airfoil at large angles of attack?

After investigating the fundamental unsteady aerodynamics of a static airfoil, the rest of the research focuses on the three dynamic motions of airfoils: plunging, surging, and pitching. The major research gap in the airfoil forced motion study is the need for detailed flow physics analysis based on experimental data, especially for the large angles of attack region. Therefore, the goal of Part III is to answer the following sub-questions related to **dynamic airfoil behavior under forced motion**:

2. How do the evolution and interaction of vortices in various forced motions affect aerodynamic performance?
3. How does motion frequency alter the formation, interaction, and synchronization of vortices, and what is its role in driving frequency lock-in?
4. How do reverse flow conditions influence the aerodynamic response of a pitching airfoil compared to the conventional cases?
5. What approach can be developed to accurately identify the onset of DSV and TEV formation during dynamic stall under reverse flow?

1.6 Thesis outline

This thesis is structured into four parts, where Part I provides the background introduction in wind energy, the technical issues in the industry, and the methodologies used in the research.

- **Chapter 1** has introduced the development of wind energy and the state-of-the-art studies related to airfoil dynamics motions, especially at high angles of attack. In the end, the research questions are proposed and the thesis structure is presented.
- **Chapter 2** provides an overview of the experimental setup and methodologies employed throughout this research. It introduces the wind tunnels used for testing,

including their specifications and operational parameters. The chapter also outlines the experimental procedures, instrumentation, and data acquisition systems. Additionally, it describes the data correction and processing methods applied to refine the raw experimental results.

Part II presents the analysis for the experimental campaign where the airfoil is static. This analysis serves as the baseline discussion to be applied and compared with the following forced motion cases.

- **Chapter 3** presents the analysis from a static airfoil DU91-W1-150. In this chapter, the airfoil static polar and unsteady aerodynamic forces and vortex shedding are compared for forward flow and reverse flow conditions.

Part III contains the analysis of airfoil experiments with forced motions. Three forced motions were investigated: surging, plunging, and pitching.

- **Chapter 4** presents the experimental campaign on an NACA0021 airfoil with a surging motion. The airfoil is set at 90° angles of attack. The vortex dynamics and the intra-cycle aerodynamic forces are examined and compared with semi-empirical models.
- **Chapter 5** builds upon the experiments presented in the previous chapter. Instead of a surging motion, a plunging motion was imposed to the same airfoil model. The vortex dynamics and intra-cycle aerodynamic forces are investigated and the differences compared to the surging case are discussed.
- **Chapter 6** evaluates the airfoil under periodic pitching conditions. The airfoil NACA 643418 was set to large angles of attack (AoA $\geq 155^{\circ}$), which leads to reverse flow conditions. The dynamics of the dynamic stall vortex and trailing edge vortex are analysed and compared with conventional dynamic stall cases. In addition, the dynamic stall vortex and the trailing edge vortex initiation time are determined using a newly proposed method.

Part IV concludes this dissertation.

- **Chapter 7** summarizes the findings from this dissertation. In the end, the future recommendations on the VIV problem are provided.

Part V provides the appendix for each study.

The outline of this dissertation (excluding Part V) is illustrated in Figure 1.14.

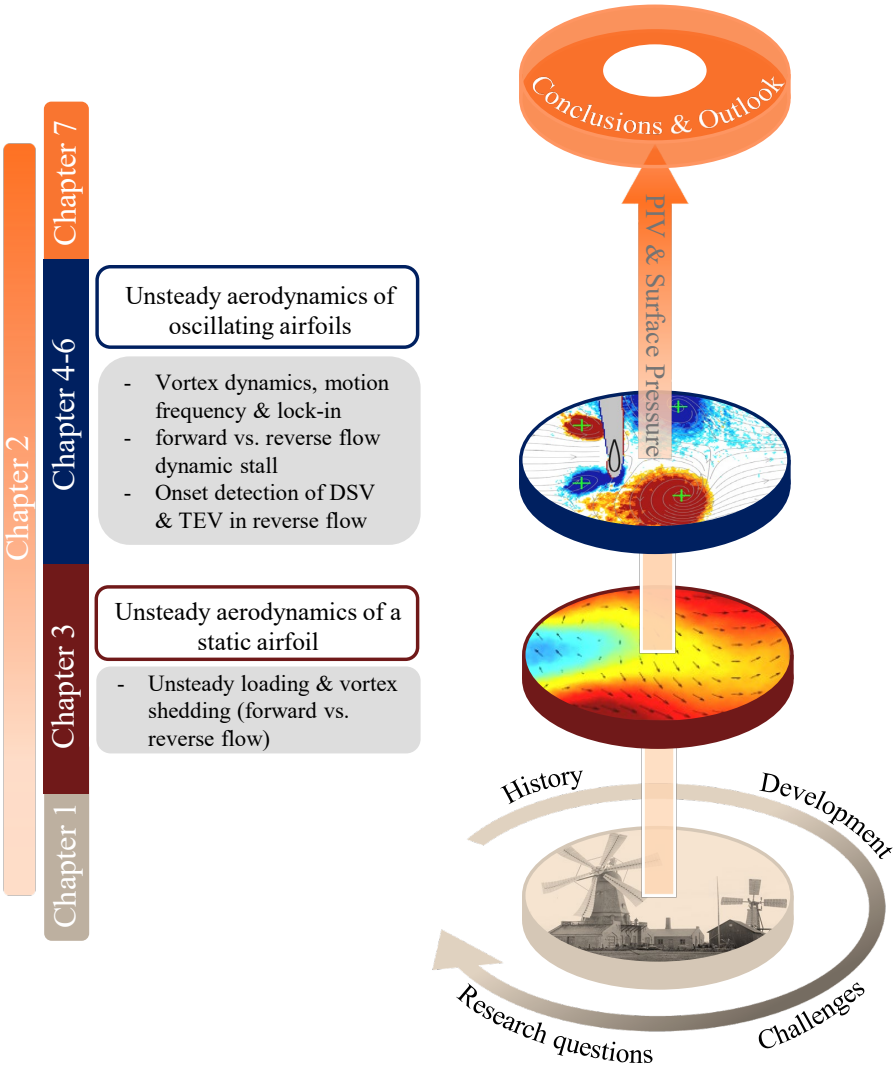

Figure 1.14: Thesis Outline.

2

Methodology

Chapter 2 introduces the overall methodology adopted in this dissertation. It begins with a brief overview of the wind tunnel facility and the experimental equipment, followed by a description of the data correction procedures applied to account for discrepancies between wind tunnel conditions and real-life scenarios. Finally, the methods employed for data analysis are presented.

2.1 Wind tunnels

The experiments involved in this thesis were conducted at two different wind tunnels at Delft University of Technology, the Netherlands, namely the Low Turbulence Tunnel (LTT) and the Open Jet Facility (OJF). Here is a brief overview of the wind tunnels.

2

2.1.1 Low Turbulence Tunnel (LTT)

The Low Turbulence Tunnel (LTT) is a closed-circuit single-return atmospheric wind tunnel. The 2D side view is shown in Figure 2.1. The fan and engine ((1) and (2)) are on the ground level while the settling chamber ((4)) and the test section ((9)) are on the second floor. Powered by a 525 kW DC motor, the maximum test section velocity is about 120 m/s. The nominal turbulence intensity varies from 0.015% at 20 m/s to 0.07% at 75 m/s. The octagonal test section is 1.80 m wide, 1.25 m high, and 2.60 m long. Motorized turntables, mounted flush with the upper and lower walls of the test section, enable accurate positioning and secure attachment of both two-dimensional and three-dimensional models.

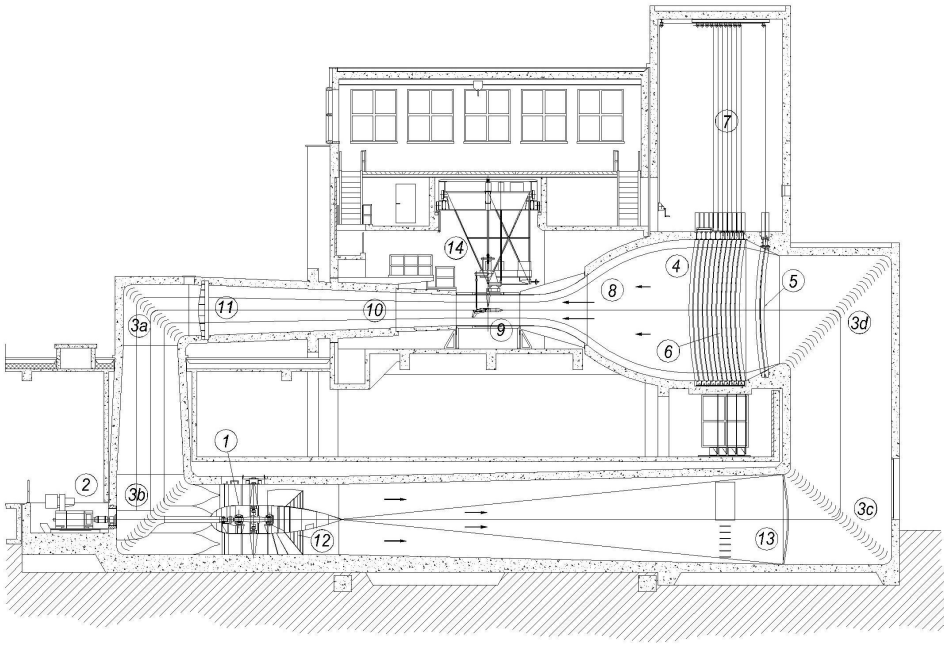

Figure 2.1: Schematic drawing of LTT. Source: https://www.tudelft.nl/lr/organisatie/afdelingen/flow-physics-and-technology/facilities/low-speed-wind-tunnels/low-turbulence-tunnel. Different parts of this wind tunnels are: (1): fan and straighteners (2): motor (3): corner vanes (4): settling chamber (5): expansion screen (6): 7 anti-turbulence screens (7): screen store room (8): contraction (9): exchangeable test section (10): diffuser (11): security screen (12): spider web (13): screen (14): six-component balance.

2.1.2 Open Jet Facility (OJF)

The Open Jet Facility (OJF) is a closed-circuit wind tunnel with an open, 2.85m ×2.85m octagonal test section. The schematic plot is shown in Figure 2.2. Powered by a 500 kW electric engine, the maximum test section velocity is about 35 m/s. The outlet diameter is almost 3 m, which can handle very large models with minimum blockage effect. This big test section also allows for uniform flow, where the nominal freestream turbulence intensity is 0.5%.

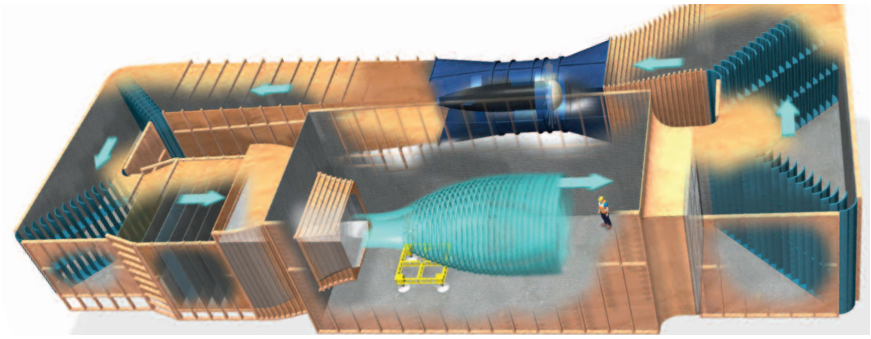

Figure 2.2: Schematic drawing of OJF. Source: https://www.tudelft.nl/lr/organisatie/afdelingen/flow-physics-and-technology/facilities/low-speed-wind-tunnels/open-jet-facility.

2.2 Experimental techniques

Two main experimental techniques are used in these campaigns: airfoil surface pressure measurement, which measures the aerodynamic force, and Particle Image Velocimetry (PIV), which measures the flow field of interest. The brief introduction of these two measurement techniques is described below.

2.2.1 Airfoil surface static pressure measurement

Airfoil surface static pressure measurement serves as a direct measurement system for obtaining the airfoil aerodynamic forces. The pressure taps are connected to the small orifices located near the mid-span of the wing model. An example of the pressure measurement location in the chordwise direction of airfoil NACA 643418 is shown in Figure 2.3. The other end of the taps (as shown in Figure 2.4) is connected to the pressure scanning system to obtain the instantaneous pressure during measurement. In LTT, the Digital Temperature Compensation (DTC) Initium electronic pressure scanning system is used, a figure of which can be seen in Figure 2.5. It supports up to 8 DTC scanners to facilitate as many as 512 channels of pressure measurements. The accuracy is ±0.05% for a full-scale (> 34.5 kPa) range measurement. The system can measure with a maximum of 1200 Hz when scanning 16 channels per scanner.

2.2.2 Particle Image Velocimetry (PIV)

Particle Image Velocimetry (PIV) is a widely used non-intrusive optical measurement technique in experimental fluid mechanics. It can determine flow velocities within the cap-

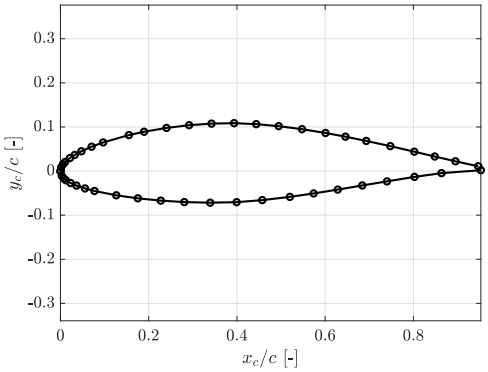

Figure 2.3: The cross section of airfoil NACA 643418, where the locations of the pressure taps are marked as circles.

Figure 2.4: Pressure tubes connected to a connector that attaches to the DTC Initium.

Figure 2.5: Pressure scanning system DTC Initium in LTT. Source: https://www.te.com/en/product-CAT-SCS0010.html.

tured instantaneous flow field by tracking the movement of tracer particles between two consecutive images. This technique was employed in all experiments conducted in this dissertation, which are essential for analyzing flow physics and vortex dynamics near an airfoil. A standard PIV system comprises imaging equipment, illumination sources, tracer particles, and data acquisition software. An example of a typical experimental setup is illustrated in Figure 2.6 [80].

The components of a two-dimensional planar PIV system are introduced and described in the following sections.

- Imager sCMOS camera: The sCMOS camera is shown in Figure 2.8 with a Nikon lens mounted. It has a resolution of 2560 ×2160 pixel with 6.5 μm pixel pitch. The frame rate is 50 Hz at full resolution. The minimum interframing time is 120 ns, which makes it suitable for all kinds of PIV applications.

- Quantel EverGreen 200 laser: This machine generates a dual-pulsed Nd:YAG laser with a wavelength of 532 nm from the laser head, as shown in Figure 2.8. The maximum pulse repetition rate is 15 Hz, and the energy for each pulse is 200 mJ. It features precisely overlapped beams, which are designed to minimize correlation noise.

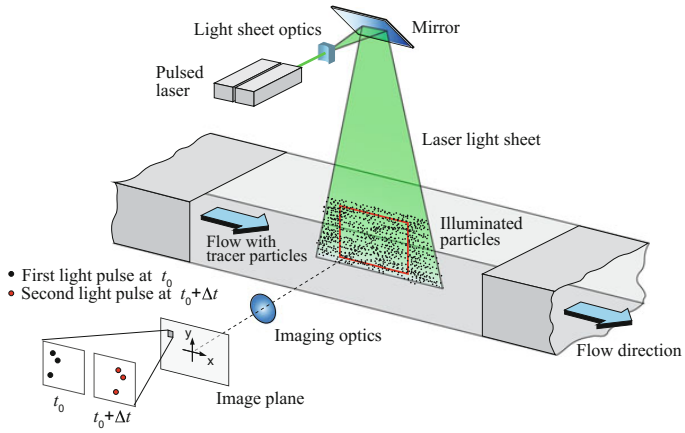

Figure 2.6: A typical PIV experimental setup [80].

Figure 2.7: LaVision CMOS camera. Source: https://www.lavision.de/en/products/cameras/cameras-for-piv/.

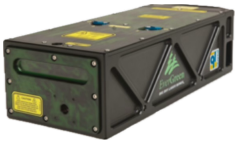

Figure 2.8: Quantel EverGreen 200 laser head. Source: https://www.quantel-laser.com/en/products/item/evergreen-70-200-mj-.html.

- SAFEX fog generator: This machine produces non-toxic water-glycol based fog with a median diameter of 1 μm.
- acquisition software: LaVision DaVis 8
- Programmable Time Unit (PTU): Figure 2.9 shows the front view of a PTU. This is a device that generates precise triggers for the camera(s), laser, and other external devices under the control of DaVis software. It offers highly accurate timing (0.05 ns jitter) on multiple outputs.

Figure 2.9: Programmable Time Unit (PTU).

2.3 Wind tunnel data correction

2.3.1 Wind tunnel corrections

When an airfoil is tested inside a closed wind tunnel test section, the flow field can be altered due to the existence of the test section wall, depending on the airfoil's angle of attack ad chord length. The model and its wake partially obstruct the flow passage, causing a local increase in velocity. Additionally, the expanding wake creates a pressure gradient in the flow direction, a phenomenon known as wake buoyancy [81]. Furthermore, the curvature of the streamlines, which results from the lift generated by the model, is also influenced by the straight walls of the tunnel. There are mainly two correction methods which correct either the streamline flow or the separated flow. The corrections for each of them is shown below.

Corrections for streamlined flow

Combining the effect of solid and wall blockage, wake buoyancy, and lift interference, the pressure coefficient corrections for the upper surface (C_{p_u}) and lower surface (C_{p_l}) are [81]:

$$C_{p_u} = 1 - \frac{\left[\left(\frac{\sqrt{q_u^*}+\sqrt{q_l^*}}{2}\right)^2 + \left(\frac{q_u^*-q_l^*}{4} - \left(\frac{\sigma}{\pi\beta^2} - 5.25\frac{\sigma^2}{\pi\beta^4}\right)C_l'\sqrt{1-\left(1-\frac{2x}{c}\right)^2}\right)\right]^2}{\left(\frac{\sqrt{q_u^*}+\sqrt{q_l^*}}{2}\right)^2} \tag{2.1}$$

$$C_{p_l} = 1 - \frac{\left[\left(\frac{\sqrt{q_u^*}+\sqrt{q_l^*}}{2}\right)^2 - \left(\frac{q_u^*-q_l^*}{4} - \left(\frac{\sigma}{\pi\beta^2} - 5.25\frac{\sigma^2}{\pi\beta^4}\right)C_l'\sqrt{1-\left(1-\frac{2x}{c}\right)^2}\right)\right]^2}{\left(\frac{\sqrt{q_u^*}+\sqrt{q_l^*}}{2}\right)^2} \tag{2.2}$$

Note that parameters with a prime refer to the uncorrected values. q_u^* and q_l^* are calculated as:

$$q_u^* = (1 - C_{p_u}')\frac{q'}{q} \tag{2.3}$$

$$q_l^* = (1 - C_{p_l}')\frac{q'}{q} \tag{2.4}$$

and the dynamic pressure ratio $\frac{q'}{q}$ can be obtained from:

$$q = q'\left[1 + \frac{2-M'^2}{\beta^3}\Lambda\sigma\left(1+\frac{1.1\beta}{(t/c)}\alpha^2\right) + \frac{(2-M'^2)(1+0.4M'^2)}{4\beta^4}\left(\frac{c}{h}\right)C_d'\right] \tag{2.5}$$

where M' is the uncorrected Mach number, $\frac{t}{c}$ is the relative thickness of the airfoil, and $\frac{c}{h}$ is the ratio of the chord length and the width of the test section. C_d' is the uncorrected drag

coefficient. The body-shape factor Λ, tunnel blockage factor σ and the Prandtl-Glauert compressibility factor β are defined in Equation (2.6), Equation (2.7), and Equation (2.8) separately:

$$\Lambda = \int_0^1 \frac{y}{c} \sqrt{(1 - C_p)\left(1 + \left(\frac{dy}{dx}\right)^2\right)} d\frac{x}{c} \tag{2.6}$$

$$\sigma = \frac{\pi^2}{48}\left(\frac{c}{h}\right)^2 \tag{2.7}$$

$$\beta = \sqrt{1 - M'^2} \tag{2.8}$$

In addition, the corrected angle of attack AoA is calculated as:

$$\text{AoA} = \text{AoA}' + \frac{\sigma}{2\pi\beta}(C_l' + 4C_m') \tag{2.9}$$

An example of correction is given in Figure 2.10, which will be discussed later.

Corrections for separated flow

When an airfoil in the test section is pitched to a certain angle of attack, especially when it is at the deep stall region, the classical small-perturbation approach to blockage effects becomes invalid [81]. The airfoil works more like a bluff body. In this thesis, the Maskell method [82] was applied for bluff body correction. In this method, the dynamic pressure ratio $\frac{q}{q'}$ is calculated as:

$$\frac{q}{q'} = 1 + \theta\frac{S}{C}C_d \tag{2.10}$$

where C is the cross-sectional area of the tunnel and S the frontal area of the airfoil. θ is the blockage factor for bluff body flow:

$$\theta = \frac{1}{k^2 - 1} \tag{2.11}$$

and the parameter can be obtained through iterations using the measured mean base pressure C_{pb}' as a starting value, with $(k_\theta^2)_0 = 1 - C_{pb}'$:

$$(k_\theta^2)_n = k_\theta'^2[1 + \frac{1}{(k_\theta^2)_{n-1} - 1}C_d'\frac{S}{C}]^{-1} \tag{2.12}$$

θ is recommended as 0.96 for two-dimensional flow [82]. The corrected drag coefficient C_d is obtained through the following equation:

$$C_d = \frac{C_d'}{1 + \theta\frac{S}{C}C_d} \tag{2.13}$$

Then, the pressure coefficient C_p can be corrected as:

$$C_p = 1 - \frac{1 - C_p'}{q/q'} \tag{2.14}$$

The correction methods are illustrated in Figure 2.10. Airfoil NACA 643418 was tested in the LTT under Reynolds number 2.5 $\times 10^5$. The top figure shows the corrected and uncorrected lift coefficient C_l while the bottom figure shows the corrected and uncorrected pressure drag coefficient C_{d_p}, with an angle test range AoA of 0° to 180°. The corrections for streamlined flows are applied for AoA smaller than 20° or larger than 160°. For the rest of the angles of attack, the corrections for separated flows were applied. The result shows that when AoA is below 30° and above about 155°, the corrected results are very close to the raw data (with the standard deviation of 0.02 for C_l and 0.01 for C_d), due to the small blockage effect. However, when the airfoil is outside this range, the largest C_l corrections can be found near 50° and 130°; the largest C_{d_p} can be found near 90°, with a difference of more than 1. This result further demonstrates the need for correction, especially at large AoA values, which is also the main focus angle range of this thesis.

2.3.2 Pressure tube corrections for unsteady airfoil measurement

If we consider the averaged aerodynamic performance of an airfoil, the correction accounting for the wall is enough. However, if we need to look into the unsteady time series of the aerodynamic performance, we need to take into account the phase delay and amplitude attenuation caused by different geometries (diameter, length, etc.) of the measuring pressure tube. The following theory is based on Bergh and Tijdeman [83], where the dynamic response of the pressure measurement system to a sinusoidal input pressure was derived. The theory assumes that: (1) the sinusoidal disturbances are very small, (2) the internal radius of the tube is small compared to its length, and (3) the flow is laminar throughout the system.

For N connected tubes with N volumes as shown in Fig. 2.11, a recursive formula for the pressure P in volume j can be derived:

$$\frac{P_j}{P_{j-1}} = \begin{cases} \left[\cosh(\phi_j L_j) + \dfrac{V_{v_j}}{V_{t_j}} \left(\sigma_j + \dfrac{1}{k_{0,j}} \right) n_j \phi_j L_j \sinh(\phi_j L_j) \right. \\ \quad + \dfrac{V_{t_{j+1}} \phi_{j+1} L_j J_0(\alpha_j) J_2(\alpha_{j+1})}{V_{t_j} \phi_j L_{j+1} J_0(\alpha_{j+1}) J_2(\alpha_j)} \cdot \dfrac{\sinh(\phi_j L_j)}{\sinh(\phi_{j+1} L_{j+1})} & \text{if } j < N \\ \left. \quad \cdot \left(\cosh(\phi_{j+1} L_{j+1}) - \dfrac{P_{j+1}}{P_j} \right) \right]^{-1} \\ \cosh(\phi_j L_j) + \dfrac{V_{v_j}}{V_{t_j}} \left(\sigma_j + \dfrac{1}{k_{0,j}} \right) n_j \phi_j L_j \sinh(\phi_j L_j) & \text{if } j = N \end{cases} \tag{2.15}$$

where L is the tube length, V_v is the pressure transducer volume, V_t is the tube volume, σ is the dimensionless increase in transducer volume due to diaphragm deflection, k_0 is the polytropic constant for the pressure expansion in the transducer volume, equaling to

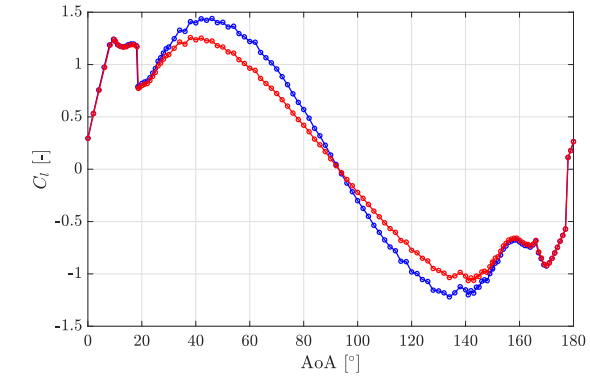

(a)

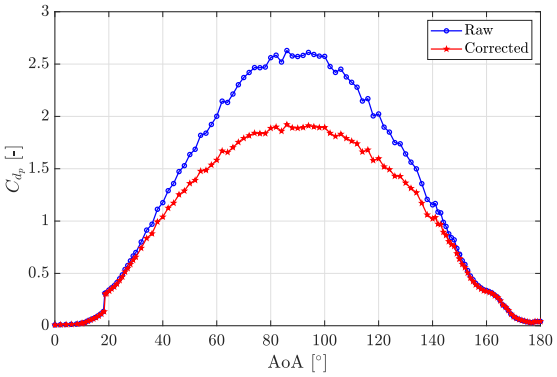

(b)

Figure 2.10: Corrected and uncorrected lift and pressure drag coefficient C_l and C_{d_p} for the wind tunnel test of airfoil NACA 643418 at Reynolds number 2.5 $\times 10^5$.

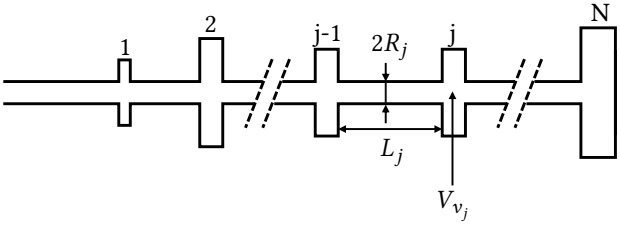

Figure 2.11: A series of N connected tubes with N different volumes at the end of each tube. R_j represents the tube radius.

1.4 for isentropic pressure expansion, J_0 and J_2 are Bessel function of first kind of orders 0 and 2.

In addition, ϕ_j, α_j (shear wave number), n_j (kind of polytropic constant) are calculated

as:

$$\phi_j = \frac{\omega}{a_0}\sqrt{\frac{J_0(\alpha_j)\,k}{J_2(\alpha_j)\,n_j}} \tag{2.16}$$

$$\alpha_j = i\sqrt{i}\sqrt{\frac{\omega \mathrm{P}_m}{R_0 T \mu}}R_j \tag{2.17}$$

$$n_j = [1 + \frac{\gamma - 1}{\gamma}\cdot\frac{J_2\left(\alpha_j\sqrt{\mathrm{Pr}}\right)}{J_0\left(\alpha_j\sqrt{\mathrm{Pr}}\right)}]^{-1} \tag{2.18}$$

where ω is the angular frequency, P_m is the atmospheric pressure, R is the tube radius, R_0 is the specific air constant, which is 287 J/kg·K, T is ambient air temperature, μ is dynamic viscosity of air, γ is specific heat ratio, which is equal to the ratio between the specific heat at constant pressure and the specific heat at constant volume, Pr is the Prandtl number.

After Equation (2.15) is obtained, the phase delay and the amplitude ratio between the corrected and uncorrected pressure can be calculated by taking the absolute value and the angle value of the response.

An example of a correction for pressure dynamic response with the measuring tubes is demonstrated here. The airfoil NACA 643418 was tested in LTT with sinusoidal pitching motion; the specifications of the tubes are:

- Number of tubes: 7
- The length of the tubes from airfoil skin (in mm): 3, 450, 220, 2000, 6.9, 500, 15
- The radius of the tubes (in mm): 0.2, 0.35, 0.4, 0.5, 0.475, 0.5, 0.325
- The volume at the end of each tube (in mm^3): 0, 0, 0, 0, 0, 0, 0
- The increase in transducer volume due to diaphragm deflection: (in mm^3): 0, 0, 0, 0, 0, 0, 0

The pressure was measured at 300 Hz. After applying to Equation (2.15) until Equation (2.18), the phase delay and amplitude ratio are obtained as shown in Figure 2.12. The amplitude ratio between the correct and raw pressure decreases significantly when the frequency increases from 0 to 50 Hz, where the amplitude of correct pressure decreases from the same as the measured data to nearly 10% of the measured data. As the frequency increases to even larger values, the amplitude ratio slowly drops while showing almost an asymptotic trend. Meanwhile, the phase delay decreases linearly with the increase in frequency.

Note that the amplitude ratio and phase delay are a function of frequency, which needs to be applied to the Fourier-transformed pressure. Afterwards, the pressure should be transformed back to the time domain for further analysis. The corrected pressure P at x_c/c = 0 (leading edge) on the suction side of the airfoil is shown in Figure 2.13. The airfoil was pitched at 1 Hz. According to Figure 2.12a, the amplitude difference is minimal. However, the phase shift is clearly seen with the corrected pressure in advance by approximately 0.07 s, which is 21 time steps (300 Hz acquisition frequency).

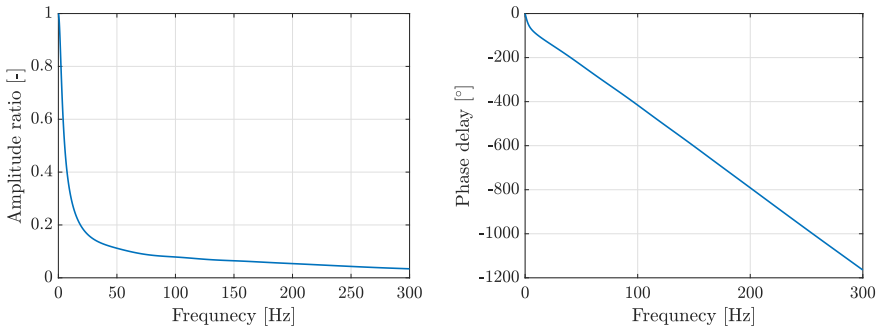

Figure 2.12: Amplitude ratio (left) and frequency delay (right). Obtained using the tube information for NACA643418 measurement.

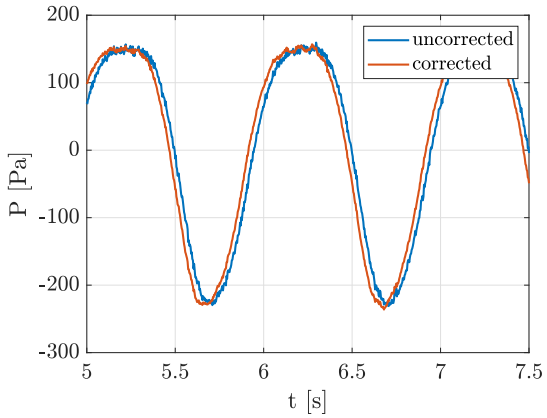

Figure 2.13: Pressure time series at the leading edge ($x/c = 0$) for the corrected (from the tube dynamic response) and uncorrected (raw measurement) data.

2.4 Data analysis method

2.4.1 Proper Orthogonal Decomposition

The Proper Orthogonal Decomposition (POD) is a well-established mathematical method aimed at obtaining low-dimensional approximate descriptions of high-dimensional processes [84]. In flow dynamics, POD is extremely helpful because it extracts the most energetic coherent structures from complex, high-dimensional flow fields. In this dissertation, POD analysis is performed on both the two-dimensional flow field $\mathbf{u} = (u_x, u_y)$ from the PIV measurement and the airfoil suction side surface pressure coefficient $C_p(x_c/c, t)$. In POD, $\mathbf{u}$ and $C_p(x_c/c, t)$ are decomposed into a linear combination of spatial modes ($\boldsymbol{\phi}_k^{(u)}(x, y)$ and $\phi_k^{(C_p)}(x_c/c)$) and time coefficients ($a_k^{(u)}(t)$ and $a_k^{(C_p)}(t)$), using Equation (2.19) and Equation (2.20) separately:

$$\mathbf{u}(x,y,t) \cong \sum_{k=1}^{M_u} a_k^{(u)}(t)\boldsymbol{\phi}_k^{(u)}(x,y) \tag{2.19}$$

$$C_p(x_c/c,t) \cong \sum_{k=1}^{M_{C_p}} a_k^{(C_p)}(t),\phi_k^{(C_p)}(x_c/c) \tag{2.20}$$

where the approximation becomes the exact limit as M_u and M_{C_p} (the number of retained POD mode for each case) reaches infinity. The decomposition is derived from solving the eigenvalue problem of the spatial correlation matrix, ensuring that the modes optimally capture the pressure fluctuations.

2.4.2 Evaluating time-dependent force on the airfoil using velocity fields from PIV measurements

Due to the highly unsteady character of the flow near or in the wake of an airfoil under large angles of attack, unsteady load measurements are sometimes difficult to obtain. However, with the help of the velocity fields obtained from PIV measurements, obtaining unsteady forces becomes feasible. In this dissertation, the aerodynamic forces are determined through a control volume momentum analysis. The method is explained below.

First, the pressure gradient can be obtained through the Reynolds Averaged Navier-Stokes Equation:

$$-\frac{1}{\rho}\frac{\partial(\overline{p})}{\partial x_i} = \frac{\partial(\overline{u}_i)}{\partial t} + \overline{u}_j\frac{\partial(\overline{u}_i)}{\partial x_j} - \nu\frac{\partial^2(\overline{u}_i)}{\partial x_j \partial x_j} + \frac{\partial(\overline{u_i' u_j'})}{\partial x_j} \tag{2.21}$$

where $\overline{u}_i$ represents the time-average velocity component for the static case (and phase-average for the oscillating cases) in the i direction, $\overline{p}$ is the time-average pressure for the static case (and phase-average for the oscillating cases), ν is the kinematic viscosity, ρ is the air density and $\overline{u_i' u_j'}$ represents the Reynolds stress tensor. The pressure $\overline{p}$ can then be calculated by reformulating the problem as the Poisson equation for pressure, as described by van Oudheusden [85], with appropriate boundary conditions: for the inlet of undisturbed flow, the Dirichlet boundary condition is applied; for the remaining boundaries, Neumann boundary conditions are applied.

Second, for two-dimensional evaluation, the aerodynamic forces can be evaluated via the conservation of momentum in a control contour around the airfoil body (Rival and van Oudheusden [86]). In this dissertation, an arbitrary rectangle contour C is applied to the airfoil, as shown in Figure 2.14.

In this dissertation, the approach employed by Ragni et al. [87], van De Meerendonk et al. [88], and Rival and van Oudheusden [86] for load evaluations from phase-locked PIV measurements is followed:

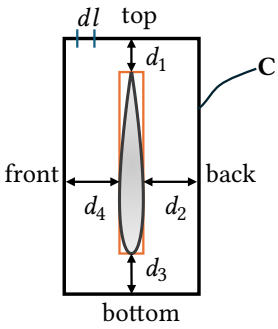

Figure 2.14: Illustration of the control boundary **C** used for the load integration. d_1 to d_4 represent the distance between the boundary and the airfoil surface from the top, back, bottom, and front, respectively.

$$\bar{F}_i = -\rho\frac{\partial}{\partial t}\oint_C \bar{u}_i n_j x_j \, dl - \rho\oint_C \bar{u}_i\bar{u}_j n_j \, dl - \rho\oint_C \overline{u_i' u_j'} n_j \, dl$$
$$-\oint_C \bar{p} n_i \, dl + \rho\nu\oint_C \left(\frac{\partial \bar{u}_i}{\partial x_j} + \frac{\partial \bar{u}_j}{\partial x_i}\right) n_j \, dl \tag{2.22}$$

with n_i, n_j the normal unit vector (pointing outward) in the i and j directions, respectively. From left to right of the right-hand side of the equation, the integrals represent the contributions to the aerodynamic loads from the flow unsteadiness (TD) , mean convection (MC), turbulence momentum transfer (TMT), pressure (press), and mean viscous stress (MV). These terms are defined as:

$$\text{MC} = -\rho\oint_C \bar{u}_i\bar{u}_j n_j \, dl \tag{2.23}$$

$$\text{press} = -\oint_C \bar{p} n_i \, dl \tag{2.24}$$

$$\text{TD} = -\rho\frac{\partial}{\partial t}\oint_C \bar{u}_i n_j x_j \, dl \tag{2.25}$$

$$\text{TMT} = -\rho\oint_C \overline{u_i' u_j'} n_j \, dl \tag{2.26}$$

$$\text{MV} = \rho\nu\oint_C \left(\frac{\partial \bar{u}_i}{\partial x_j} + \frac{\partial \bar{u}_j}{\partial x_i}\right) n_j \, dl \tag{2.27}$$

Note that in the approach of phased-locked PIV measurements, the field of view (FoV) is fixed for different phases. Thus, the flow unsteadiness term (the first term on the right-hand side) in Equation (2.22) can be written as:

$$-\rho\frac{\partial}{\partial t}\oint_C (x_i \bar{u}_i n_i) \, dl = -\rho\oint_C \left(x_i \frac{\partial \bar{u}_i}{\partial t} n_i\right) dl \tag{2.28}$$

Specifically, $\frac{\partial \bar{u}_i}{\partial t}$ (equals to zero for a static case) is obtained from the consecutive phases measured, as shown in Equation (2.29):

$$\frac{\partial \bar{u}_i}{\partial t} = \frac{\partial \bar{u}_i}{\partial \phi_k}\frac{\partial \phi_k}{\partial t} = \frac{\partial \bar{u}_i}{\partial \phi_k} 2\pi f \approx \frac{\bar{u}_{i,k+1} - \bar{u}_{i,k-1}}{\phi_{k+1} - \phi_{k-1}} 2\pi f \tag{2.29}$$

Here, ϕ_k denotes the phase at the k-th point in the cycle and $\phi_k = 2\pi f t_k$. $\bar{u}_{i,k+1}$ and $\bar{u}_{i,k-1}$ are the phase-averaged velocities at the adjacent phases.

Equation (2.22) is valid when the flow is incompressible, and the body is thin (Rival and van Oudheusden [86]). In this work, when the airfoil model acts as a bluff body (e.g., at angles of attack larger than 20°), thus yields an additional body force term on the right side of Equation (2.22):

$$F(t)_B = -\rho B \frac{\partial \dot{h}}{\partial t} \tag{2.30}$$

where B is the surface area of the airfoil's cross-section and $\frac{\partial \dot{h}}{\partial t}$ is the airfoil's acceleration.

2.4.3 Vortex identification method and calculation of circulation

Following the approach from Graftieaux et al. [89] and Morgan et al. [90], the so-called Γ_1 method is introduced here, which is employed to identify the vortex center(s) in the flow fields in this dissertation.

The illustration of the method is shown in Figure 2.15. Given a two-dimensional flow field as those measured by PIV, a user-defined rectangular region S is selected, composed of N data points. Let P be a fixed center point in this region. At each point M within the region S, θ_M is the angle between the location vector $\mathbf{PM}$ and the velocity vector $\mathbf{u_M}$. The sine of the angle θ_M can then be calculated, which gives the dimensionless scalar function Γ_1 at P:

$$\Gamma_1(P) = \frac{1}{N}\sum_S \frac{\mathbf{PM} \times \mathbf{u}_\mathrm{M}}{\|\mathbf{PM}\| \cdot \|\mathbf{u}_\mathrm{M}\|} = \frac{1}{N}\sum_S \sin(\theta_M) \tag{2.31}$$

The value of Γ_1 is calculated for all the data points in the measurement domain. Notice that $|\Gamma_1|$ is bounded by 1; such bound is reached at the center of the vortex if the vortex is axisymmetric. Typically, $|\Gamma_1|$ near the vortex center is between 0.9 and 1.

Once the center of the vortex has been identified using the Γ_1 criterion, the circulation Γ of the vortex can be computed by integration of the vorticity ω within a certain area A:

$$\Gamma = \iint_A \omega \, dA \tag{2.32}$$

The area A can be selected based on the vortex boundary, identified using the Γ_2 method (Graftieaux et al. [89], Morgan et al. [90]). However, in the present dissertation, because the vortices are shed from the leading and trailing edges and separated, a user-defined area is selected as follows. For each phase of measurement, a rectangular boundary is set around each vortex in the flow field; the region is large enough to cover more than the area of the vortex. Then, the integration for the circulation using Equation (2.32) is performed, excluding the contribution from the vortices in the opposite direction (opposite sign of vorticity). The schematic plot is shown in Figure 2.16.

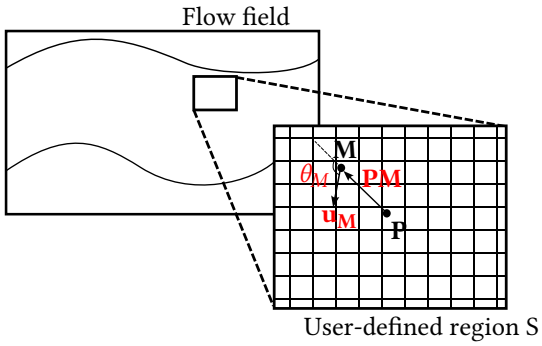

Figure 2.15: Illustration of Γ_1 method.

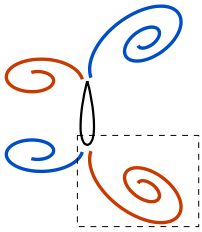

Figure 2.16: Demonstration of the user-defined area for circulation calculation. The dashed rectangle represents the user-defined area. The red and blue curls represents the vortices with opposite signs.

II

Unsteady aerodynamics of static airfoil at large angles of attack

3

Baseline study: static airfoil aerodynamics

This chapter presents a fundamental study on a static airfoil, with a focus on the larger angle of attack region. The experimental campaign addresses a gap in the existing data by providing valuable insights into airfoil behavior at high angles of attack, especially the unsteadiness in the force variations. The results highlight the wake variation across different angles of attack under forward and reverse flow conditions, and a generalized Strouhal number trend is validated against previous research.

This chapter is based on
G. Xu, W. Yu, A. Sciacchitano, C. Simão Ferreira, *An experimental study of the unsteady aerodynamics of a static DU91-W2-150 airfoil at large angles of attack*, Wind Energy **28** (3), 19, 2025 [91].

3.1 Introduction

The field of wind turbine aerodynamics, which addresses the complex interactions between wind and the blades and tower of a wind turbine, continues to draw significant research attention. A critical component of this field is the aerodynamic behavior of airfoils on turbine blades, as it directly influences force generation and, ultimately, the turbine's power output. However, accurately capturing the unsteady aerodynamic phenomena associated with airfoils remains a considerable challenge, attributed to the flow characteristics and airfoil geometry [92].

At moderate to high angles of attack (α), flow separation may occur on the suction side of the airfoil. This phenomenon arises from an increase in the adverse pressure gradient; as this gradient intensifies, flow separation tends to initiate earlier. Flow separation can be categorized as either closed or open. Closed separation often manifests as laminar separation bubbles (LSBs) [93], where the flow detaches from the surface and reattaches downstream. These are typically identified by a plateau in the surface pressure distribution from the point of separation to the onset of transition to turbulence [36]. In contrast, open separation occurs when the boundary layer does not reattach, instead interacting with the free shear layer in the wake, producing regions of recirculating "dead air" with pressure close to the freestream value [93].

In various vortex-induced vibration (VIV) scenarios, wind turbine blades are subjected to extreme α values. Such conditions can arise during sudden changes in wind direction, yaw misalignment, or when turbines are parked. Under these circumstances, blade sections behave more like bluff bodies than streamlined airfoils [94]. Moreover, reverse flow conditions can develop due to omnidirectional wind exposure, further complicating the aerodynamic response.

This chapter aims to explore the fundamental aerodynamic behavior of an airfoil under large angles of attack. The DU91-W2-150 airfoil is analyzed in static wind conditions over a wide range of AoA values, from 0° to 310°. The focus of this study is wake flow dynamics, vortex shedding characteristics, and aerodynamic loading, with a specific focus on the reverse flow regime and its differences compared to conventional forward flow conditions.

3.2 Methodology

The experiment was conducted in the Low Speed Low Turbulence Tunnel (LTT) at the Delft University of Technology. The wing with profile DU91-W2-150 was flush-mounted between the top and bottom walls of the test section, as shown in Figure 3.1. The wing spans the entire vertical dimension of the test section (1.8 m) and has a chord of 150 mm. A total of 42 pressure orifices (21 on either side of the wing, as shown on the right in Figure 3.1) were used to measure the static pressure over the airfoil surface. The orifices were connected to pressure transducers (DTC Initium) with a sampling frequency of 331.6 Hz. Time series of pressure were acquired for approximately 10 s for each test case. The geometry of the DU91-W2-150 airfoil is shown on the right in Figure 3.1, where the pressure tap locations are marked by cycles.

PIV measurements were conducted with the schematic plot shown in Figure 3.2. The flow inside the tunnel was seeded with water-glycol droplets of 1 μm median diameter produced by a SAFEX smoke generator. The flow was illuminated by a Quantel Evergreen

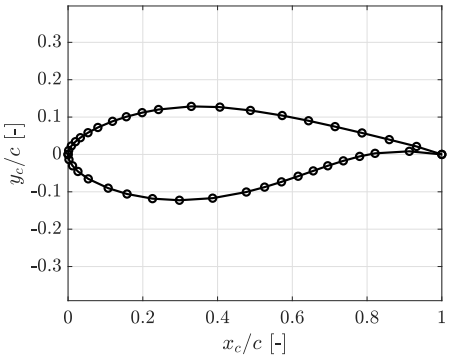

Figure 3.1: Side view of the test section with the mounted airfoil (left) and the non-dimensionalized geometry of airfoil DU91-W2-150 with locations of pressure taps marked with circles (right).

Nd:YAG laser (200 mJ pulse energy, 15 Hz repetition rate, 532 nm wavelength). It created a 2 mm thin laser sheet. The measurement plane was located close to the mid-span of the airfoil, avoiding the location of the pressure orifices used for pressure measurement. Flow field imaging in the wake of the airfoil was conducted using two LaVision's Imager sCMOS cameras (2560 × 2160 pixel, 16 bit, 6.5 × 6.5 μm pixel size). A 50 mm Nikon lens was mounted on each camera, and the lens numerical aperture was set to $f_{\#}$ of 4. This camera can capture two images with 120 ns interframe time. These two cameras were mounted side by side so that a large field of view could be achieved, capturing the airfoil wake and the evolution of the vortex shedding. The averaged imaging magnification was $M = 0.05$ with a digital resolution of 8 pixels/mm. The cameras were controlled by a LaVision programmable timing unit PTU X, where precise pulses are triggered and synchronized for cameras and lasers. This PTU X is controlled through the software DaVis 8.4 from LaVision GmbH. In the experiment, the acquisition frequency was set at 15 Hz. For most test cases, 200 images were acquired for each camera; For the cases of $\alpha = 0^{\circ}$, 100 images were acquired. The convergence study can be found in Appendix A.1 and the PIV uncertainty analysis can be found in Appendix A.2.

Pressure measurements were carried out for a wide range of α values: from 0° to 130° and from 175° to 310°. Note that the missing range from 130° to 175° and from 310° to 360° was due to the pitch limitation of the turning table of the setup. However, since our primary focus is on the high angles of attack, we chose to concentrate on the remaining angles that could be measured more readily. The test cases are shown in Table 3.1. It is important to note that we were unable to reach higher Reynolds numbers (Re) due to the relatively short (15 cm) chord length of the model employed in this study. At large angles of attack and Re above 8×10^5, we observed significant tunnel and model vibrations accompanied by intense aeroacoustic noise. The maximum wind speed tested in this campaign is aligned with the maximum wind speed tested for high AoA values in this wind tunnel

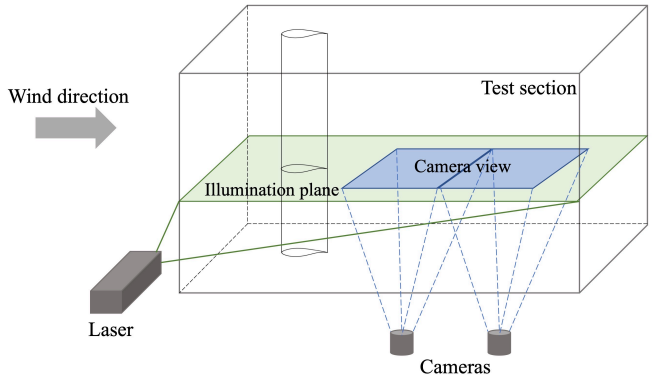

Figure 3.2: Schematic of the PIV measurement setup for the wing with the DU91-W2-150 profile.

Table 3.1: Test cases for the pressure measurement. U_∞ is the corresponding freestream wind speed at each Re.

Re	U_∞ [m/s]	AoA [˚]
2×10^5	21.8	For all Re:
5×10^5	53.5	$\alpha \in \{[0,130] \cup \{175\} \cup [178,210] \cup [215,310]\}$
8×10^5	92.5	with step size: 2˚ for $[0,130]$, $[178,210]$; 5˚ for $[215,310]$

previously [95].

PIV measurements were carried out along with the pressure measurement. However, due to optical blockage in the cameras' fields of view, PIV measurements could be conducted only at AoA = 90˚, 130˚, 270˚ and 310˚.

3.3 Results and discussion

3.3.1 Time-averaged behaviour

Airfoil aerodynamic performance

The lift and drag polar of the DU91-W2-150 airfoil is shown in Figure 3.3 by taking the average of the unsteady data from the experiment. The performance for $Re = 5 \times 10^5$ and 8×10^5 is similar while that for 2×10^5 deviates: It has higher drag at 90˚ but lower drag and lift after 210˚. This can mean that at $Re = 2 \times 10^5$ and at those AoA values, viscosity plays a larger role which has a greater influence on the airfoil than at other higher Re values.

As the airfoil passes through a wide range of AoA values, reverse flow can happen at specific locations as the geometric trailing edge is in the front, which creates immediate separation. The illustration of the AoA values with respect to the wind is shown in Figure 3.4. Figure 3.5 shows the C_l and C_d comparison between forward flow and reverse flow at three Re values. For the forward flow region of AoA between 0˚ and 90˚ (the left plots), the comparison is made with the reverse flow region of AoA from 180˚ to 270˚. And the AoA at the reverse flow region is subtracted by 180˚ to match the comparison. Similarly, for the forward flow region of 270˚ to 310˚ (airfoil nose down), a fair comparison is made

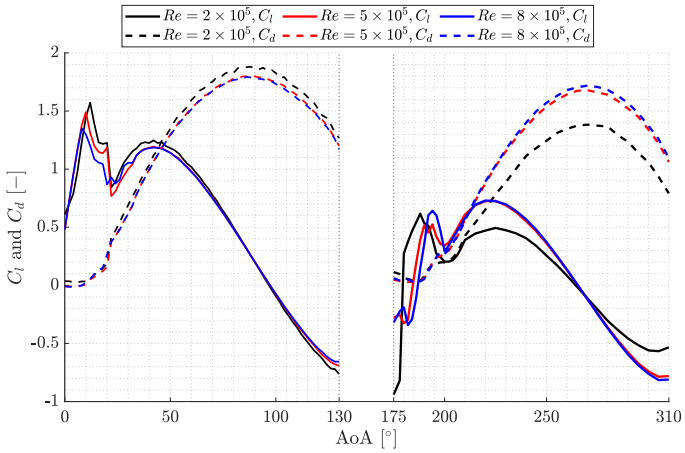

Figure 3.3: Aerodynamic performance of DU91-W2-150 at three *Re* values.

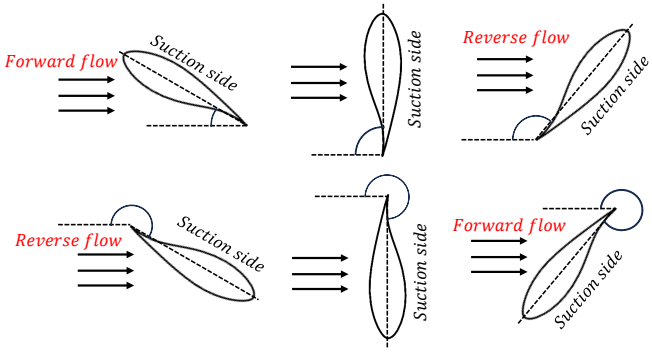

Figure 3.4: Schematic plot of different AoA values tested in the campaign. The wind comes from left to right. The corresponding AoA is 30°, 90° and 130° for the first row and 210°, 270° and 310° for the second row. When the geometric trailing edge is facing the front wind, reverse flow occurs.

with AoA from 90° to 130° (the right plot). And this reverse flow AoA region is added by 180° in the plot.

For AoA and AoA−180° between 0° and 90°, the airfoil has higher C_l in forward flow conditions. In this condition, C_d is slightly higher despite slightly lower reverse flow conditions when AoA and AoA−180° is lower than 20°. However, when AoA and AoA+180° are between 270° and 310°, in general, the airfoil in the reverse flow condition has higher C_l and C_d.

As C_l and C_d are calculated from the pressure difference from the upper and lower surface, the C_p comparison between forward flow and the corresponding reverse flow condition is shown in Figure 3.6. For AoA = 40°, the local stagnation near the leading edge on the pressure side makes the pressure difference smaller than that for the corresponding reverse flow case where AoA−180° = 40° case, which proves the higher lift in the forward flow case. When AoA = 270°, the pressure difference in the trailing edge region is smaller

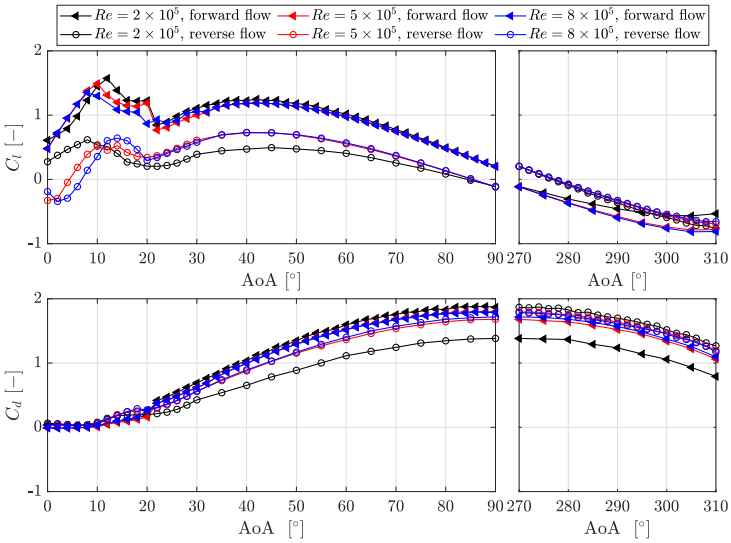

Figure 3.5: Aerodynamic performance in forward flow and reverse flow conditions at three *Re* values. For the reverse flow condition, the AoA is subtracted by 180° to fit in the left plot and added by 180° to fit in the right plot.

than that of the corresponding value at AoA+180° = 270° due to a different influence of separation on the pressure side, which gives a higher lift for the reverse flow condition. The above results show that no matter whether the flow is forward or reverse, as long as the concave surface is facing upwind as the pressure side, aerodynamic loads are in general higher. When AoA is between 0° and 90° and when AoA+180° is between 270° and 310° (AoA between 90° and 270°), the concave pressure side brings higher aerodynamic force as there might be local separation near the trailing edge concave area.

Figure 3.7 depicts C_l slope for the forward flow and reversed flow cases. When C_l slope is smaller than 0, the region is unfavorable for wind turbine blade structures as it indicates a higher possibility of negative aerodynamic damping, which can lead to structural instability [96]. This figure shows that the influence of *Re* is minimal, especially at large incidence angles (AoA (or AoA−180) larger than 25° and AoA (or AoA+180) between 270° and 310°). At these angle regions, $\partial C_l/\partial$AoA maintains slightly below zero, contributing marginally to negative aerodynamic damping. Before the static stall angle (approximately 10°), $\partial C_l/\partial$AoA presents an overall positive value for both forward flow and reverse flow cases. In contrast, after the static stall angle, $\partial C_l/\partial$AoA sharply drops to negative values with a minimum of approximately −0.18 from all the test cases. This sharp decline highlights a strong destabilizing effect, indicating a risk of structural instability near stall.

Reynolds effect on the separation point

The time-averaged surface pressures are plotted for all the measured *Re* values near the positive stall region in Figure 3.8. At AoA = 8°, the transition point to the turbulence region, indicated by the sudden drop of C_p, gets closer and closer to the leading edge

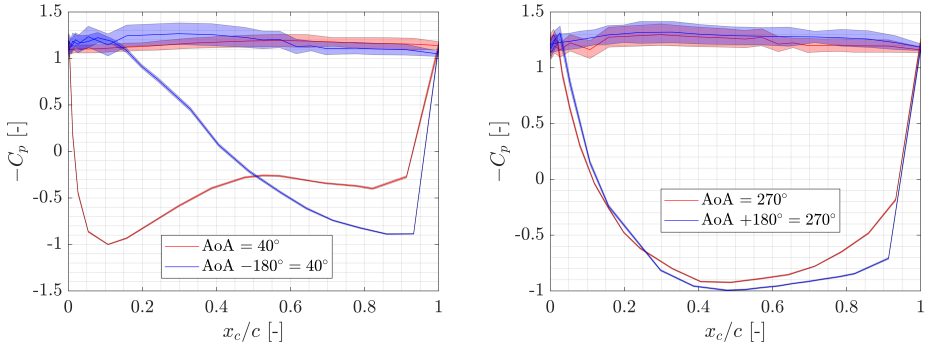

(a) (b)

Figure 3.6: Surface pressure comparison between forward flow and the corresponding reverse flow angle at $Re = 5 \times 10^5$. Shaded area represents the standard deviation.

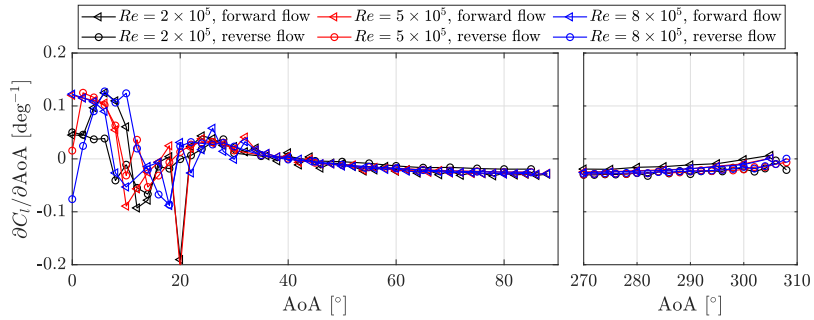

Figure 3.7: C_l slope in forward flow and reverse flow conditions at three Re values. For the reverse flow condition, the AoA is subtracted by 180° to fit in the left plot and added by 180° to fit in the right plot.

as Re increases. At AoA = 10°, the flow is separated for $Re = 8 \times 10^5$, with a plateau after $x/c = 0.6$. For lower Re values, the flow remains attached despite of transition to a turbulent boundary layer. At AoA = 14°, flow is separated for all Re values, while the highest Re has the separation point more towards the leading edge. The experiment results align with the previous findings [35], indicating that a higher Re leads to an earlier stall. This is attributed to the increased dominance of viscous forces at lower Re values, promoting flow attachment to the surface.

Similarly, the surface pressures near the negative stall region from 188° to 198° are plotted for all the measured Re values in Figure 3.9. The x axis is flipped in order to show the aerodynamic leading edge (the geometric trailing edge) first. The suction side is the concave surface, which is the pressure side for the positive stall case. Different from the positive stall region, a local separation near the leading edge is happening, which can be seen for AoA up until 196° at $Re = 8 \times 10^5$, up until 194° at $Re = 5 \times 10^5$, up until 192° at $Re = 2 \times 10^5$. This is attributed to the sharp geometry of the leading edge, while it still follows the same separation order as the positive stall onset, where lower Re induces earlier separation.

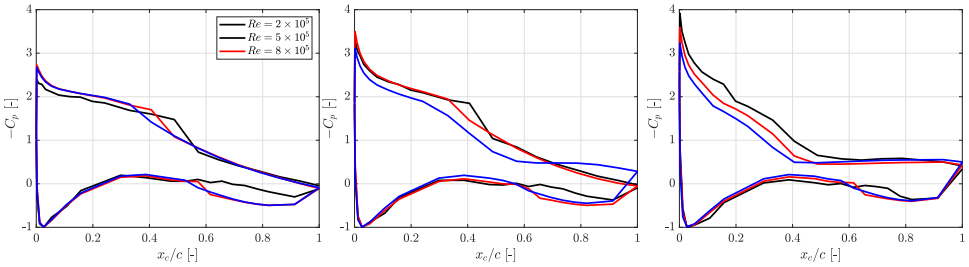

(a) AoA = 8° (b) AoA = 10° (c) AoA = 14°

Figure 3.8: Pressure coefficient C_p near the possible stall region for all the measured Re values.

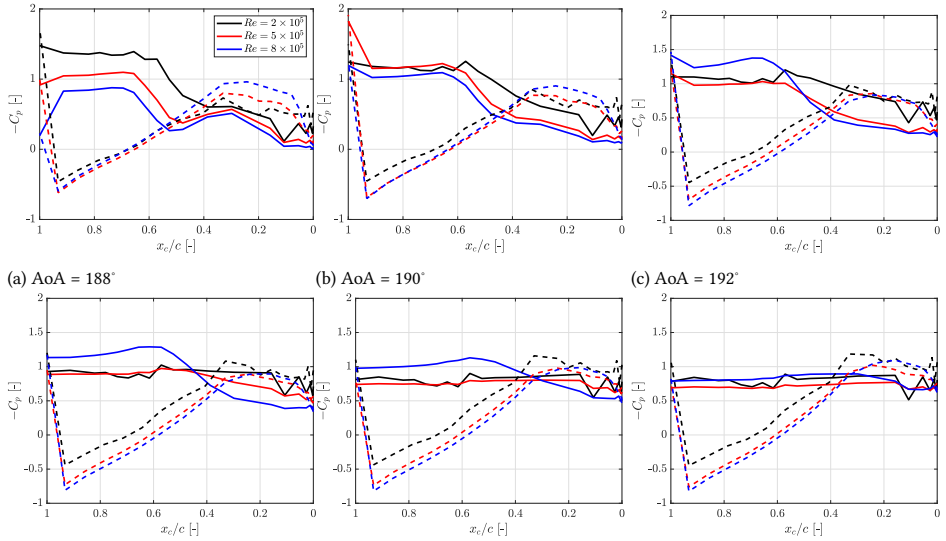

(a) AoA = 188° (b) AoA = 190° (c) AoA = 192°

(d) AoA = 194° (e) AoA = 196° (f) AoA = 198°

Figure 3.9: Pressure coefficient C_p near the negative stall region for all the measured Re values. The x direction was flipped in the plot, which shows the geometric leading edge first, as it serves as the aerodynamic leading edge.The pressure side are shown as dashed in order for clarification.

The separation locations for all Re values on the suction side of the airfoil are depicted in Figure 3.10. It is important to note that the plotted points correspond to locations that are fully separated up to the trailing edge, excluding those that have been reattached to the surface. Across all Re values, there is a distinct trend of the separation location moving towards the leading edge as the AoA increases. As AoA increases, at $Re = 2 \times 10^5$, the separation is the latest. For $Re = 8 \times 10^5$, separation happened the earliest as AoA increases to 20°. Then the separation remains in the same position at $x/c = 0.08$ for 6° more and slowly reaches the leading edge at AoA = 38°. As can be seen in Figure 3.3, the force at AoA region between 20° and 38° after the stall angle is highly nonlinear. Under high Re conditions, this situation worsens. The presence of small leading-edge vortices can quickly shed with rapid reattachment, causing the separation point not to remain fixed at

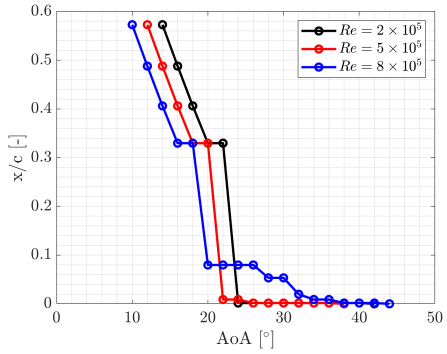

Figure 3.10: Separation locations on the airfoil surface on the suction side for different Re values.

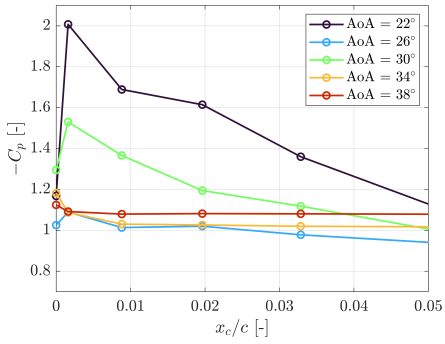

Figure 3.11: Leading edge surface pressure for AoA from 20° to 38° at $Re = 8 \times 10^5$.

the leading edge for this Re. This is illustrated by the suction peaks near the leading edge area in Figure 3.11.

Surface pressure

The time-averaged surface pressure at $Re = 5 \times 10^5$ is further compared for different AoA values and is shown in Figure 3.12. The two plots in the first row show the C_p surface for the AoA values measured on the suction side, while the two plots in the second row show the pressure side. Suction peaks are shown in the forward flow (AoA between 0° and 30°) and reverse flow (AoA between 180° and 270°) cases near the leading edge and trailing edge region, respectively. Due to the early separation at the aerodynamic leading edge, the suction peak region is smaller in reverse flow than in forward flow. The stagnation point on the pressure side ($-C_p = -1$) moves towards the trailing edge as AoA increases from 0° to 130° and moves back towards the leading edge as AoA goes from 180° to 310°. On the suction side, beyond AoA of 40° and 215°, the C_p surface smoothens and maintains a uniform distribution. The obtained results align with previous measurements [43] for the available results of AoA lower than 180°. As shown in Figure 3.3, the flow well exceeds the positive stall and negative stall onset region after these two AoA values (36° and 215°), which indicates that the flow does not undergo a sudden change in pressure, as, in most instances, the flow is fully separated.

PIV mean flow field

Figure 3.13 shows the mean flow field and vorticity field at AoA = 90°, 270°, 130° and 310° at $Re = 5 \times 10^5$. As shown in Figure 3.13a, a region with stalled flow is shown near the middle of the chord at AoA = 90°. As a comparison, the result of AoA = 270° at $Re = 5 \times 10^5$ is presented here in Figure 3.13c and Figure 3.13d. When AoA = 270°, the pressure side of AoA = 90° becomes the suction side. Due to the concave curvature of the aerodynamic suction side, the center of the wake (blue area in Figure 3.13c) shifts slightly towards the trailing edge.

This is also revealed in Figure 3.14a where the wake contour lines of $\bar{u}/U_\infty = -0.2$, 0, 0.4 and 0.75 are plotted together with 90° cases. The 270° case has a faster wake recovery since it reaches the same speed with a shorter downwind distance compared with 90°. This

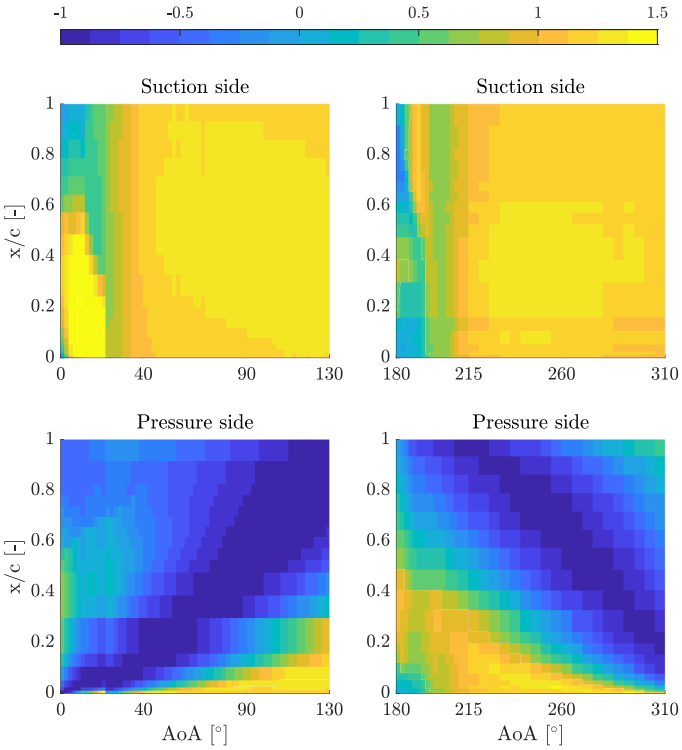

Figure 3.12: Average of pressure coefficient $-C_p$ for all AoA values tested at $Re = 5 \times 10^5$. Note that the suction side is the different side for AoA larger than 180°.

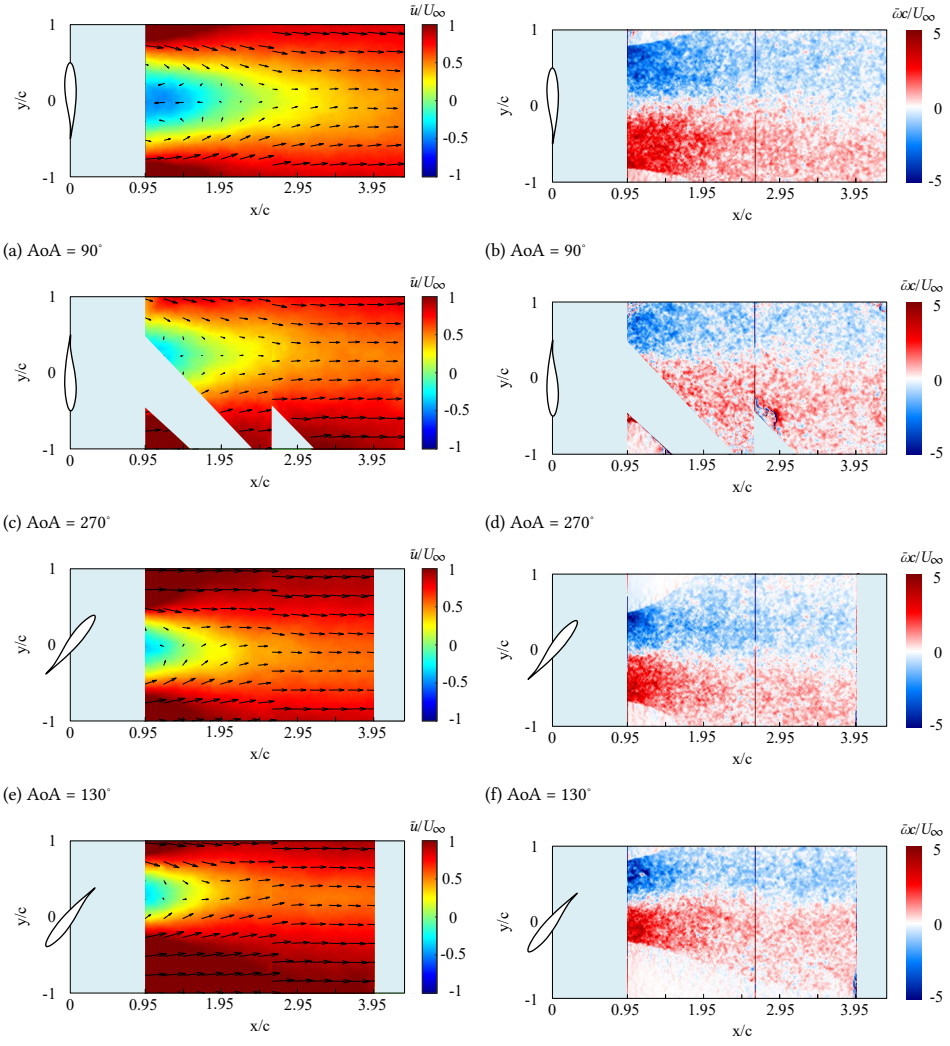

(a) AoA = 90°

(b) AoA = 90°

(c) AoA = 270°

(d) AoA = 270°

(e) AoA = 130°

(f) AoA = 130°

(g) AoA = 310°

(h) AoA = 310°

Figure 3.13: Mean flow field (left column) and vorticity field (right column) at AoA = 90°, 270°, 130° and 310°, $Re = 5 \times 10^5$

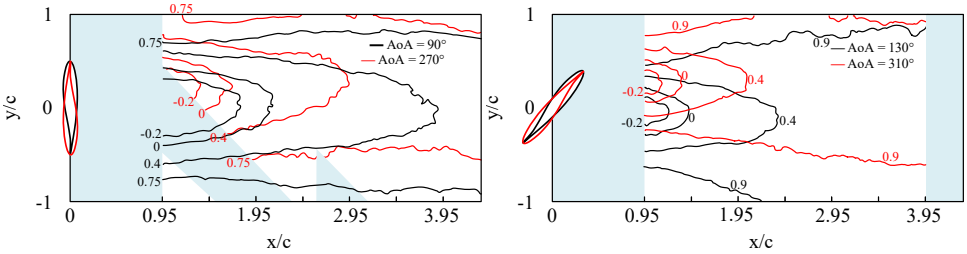

(a) AoA = 90° and 270°

(b) AoA = 130° and 310°

Figure 3.14: Wake contour lines of $\bar{u}/U_\infty$ = −0.2, 0, 0.4 and 0.75(0.9) for several AoA values at $Re = 5 \times 10^5$. Note that the contour line $\bar{u}/U_\infty$ = 0.75 was plotted for 90° and 270° while $\bar{u}/U_\infty$ = 0.9 was plotted for 130° and 310°.

Table 3.2: Wake width at four AoA values.

AoA [°]	Wake width D/c [-]	Location x/c [-]	Wake velocity $\bar{u}/U_\infty$ [-]
90	1.52	2	0.75
270	1.49	2	0.75
130	1.09	1	0.9
310	1.01	1	0.9

reveals that the convex and concave surfaces of the asymmetric airfoil create different aerodynamic effects on the airfoil. When AoA is below 180°, the concave surface is facing the wind. This surface will cause a drastic change to the flow field, which has the potential to expand the wake. On the other hand, when AoA is above 180°, the convex surface is facing upwind. This more streamlined surface has less influence on the flow field than the concave surface, which results in a faster recovery. This is also confirmed with the wake width comparison shown in Table 3.2 where the wake width of 90° at velocity $\bar{u}/U_\infty$ = 0.75 is wider than that of 270°.

Figure 3.13e to Figure 3.13h present the wake results for AoA = 130° and 310° at $Re = 5 \times 10^5$. Note that 310° is the angle where the leading edge and trailing edge swap their positions compared with 130°. For these two AoA values, the average flow fields (Figure 3.13e and Figure 3.13g) and vorticity fields (Figure 3.13f and Figure 3.13h) are similar, except for the locations of the maximum reverse velocity. This difference is also shown in Figure 3.14b, where the wake contour lines of $\bar{u}/U_\infty$ = −0.2, 0, 0.4 and 0.9 are plotted for 130° and 310°. This contour plot also shows a faster recovery and a smaller wake for 310° due to the upwind concave curvature where the reverse flow occurs. Compared with 90° and 270°, the wakes at 130° and 310° are narrower. At 130° and 310°, the projected length at the wind tunnel cross section is smaller, which leads to a smaller interference on the flow. When the airfoil is at 90° or 270°, the flow separates abruptly from the airfoil, giving a longer recovery time. While for 130° and 310°, the shorter projected length in the wind tunnel direction gives less blockage to the flow.

3.3.2 Unsteady behaviours

Variation of C_l and C_d

Variations of the time series of forces are examined to study the unsteadiness. Specifically, the influence of forward flow and reverse flow is compared and shown in Figure 3.15. Here, two times the standard deviation (2σ) is used to represent the overall fluctuation. When AoA or AoA−180° is between 0° and 30°, the fluctuation of Cl remains relatively low (below 0.1), despite some spikes in the stall onset between 10° and 20° and between the corresponding negative stall region of AoA−180 between 10° and 20°. When AoA is between 20° and 30°, a higher 2σ is expected as the flow fluctuates near the leading edge region with an unfixed separation point, which is shown in Figure 3.10.

As the angle exceeds 30°, 2σ starts to increase for both C_l and C_d and $2\sigma(C_l)$ reaches the local maximum near 40° (220°). Afterwards, the flow remains fully separated and $2\sigma(C_d)$ stays at almost the same level while $2\sigma(C_l)$ slowly drops to below 0.05 to 90° (and 270°) as C_l slowly diminishes to near 0 as shown in Figure 3.3. In the nose-down region of 270° to 310° and its corresponding reverse flow region, an axis-symmetric variation pattern is shown compared to the range from 50° to 90°. In this region, $2\sigma(C_l)$ is the lowest for 270° (and 90° for the reverse flow condition) and gradually increases as AoA increases. Meanwhile, in general, the forward flow (indicated as triangle markers) has less fluctuation compared to reverse flow regions (indicated as the circle marker) in each Re. The higher fluctuation for the reverse flow cases is attributed to the earlier separation in the aerodynamic leading edge, which induced instability.

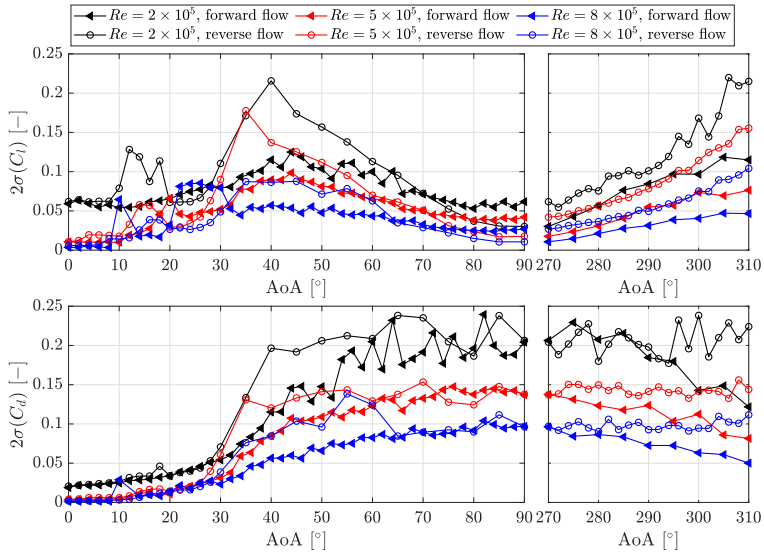

Figure 3.15: Fluctuations (two times the standard deviation 2σ) of unsteady C_l and C_d for different Re values in the forward flow and reverse flow conditions. For the reverse flow condition, the AoA is subtracted by 180° to fit in the left plot and added by 180° to fit in the right plot.

POD analysis

POD analysis results are presented in Figure 3.16 for AoA = 90°. The first two dominant modes in the streamwise direction from POD analysis are shown in Figure 3.16a and Figure 3.16c for AoA = 90°. From the energy plot in Figure 3.17, the first mode accounts for 29.9% of the energy and the second accounts for 23.8%. Therefore, the first two modes take up more than half of the total energy, which makes the first two modes dominant in the flow movement. It can be seen from the structure that the first two modes are in the same shape and are paired. The dashed lines in the center of the peaks reveal the shift of one-quarter wavelength, which corresponds to a phase shift of 90°, which is in agreement with the previous finding [97]. These two modes lead to the vortices shedding from the leading and trailing edges in turn and together formulate the sinusoidal shape wake, as shown from the wake reconstruction in Figure 3.16b. The temporal coefficients of the first two modes are plotted against each other in Figure 3.16d, and the red circle represents the theoretical values. The scatter of the points in the vicinity is also an indication of the cyclic vortex-shedding process where the first two modes are paired.

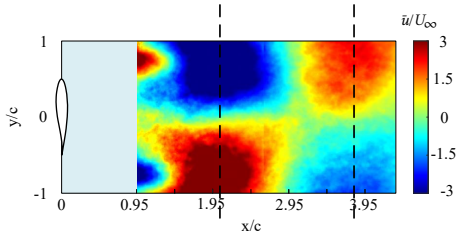

(a) Mode 1

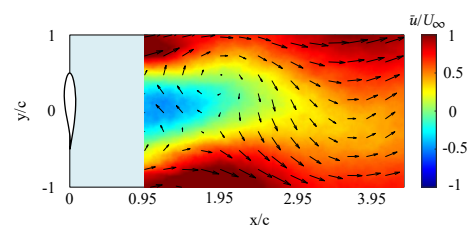

(b) Stream flow reconstruction(+)

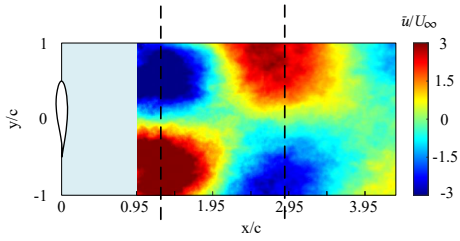

(c) Mode 2

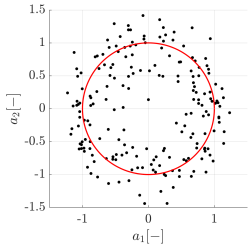

(d) Correlation of the temporal coefficient of the first two modes

Figure 3.16: POD mode analysis at AoA = 90°, $Re = 5 \times 10^5$. (a) and (c): First two modes. (b) Corresponding wake reconstruction basedbases on the first two modes. (d) Correlation of the temporal coefficient of the first two modes.

Variation of vortex shedding frequency and corresponding St number

The time series of corrected pressure was transformed into the frequency domain using the Welch method, where a flattop window was applied. By taking the Fast Fourier transform (FFT), the Power Spectrum density (PSD) of C_p at the suction surface under different AoA values at chordwise locations near the leading edge ($x/c = 0.05$), in the middle of the chord ($x/c = 0.49$) and in the trailing edge ($x/c = 1$) were plotted and shown in Figure 3.18 for $Re = 5 \times 10^5$. Owing to the periodicity of vortex shedding, the dominant peak shown in

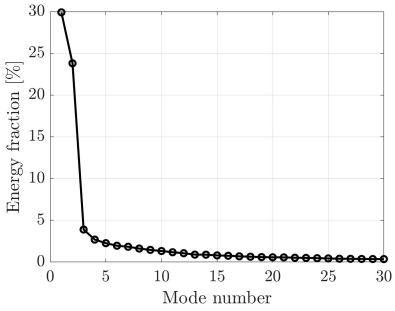

Figure 3.17: Energy fraction for the first 30 modes at 90° in Re 5×10^5.

the FFT plot indicates the dominant vortex shedding frequency. For Figure 3.18a (10°) and Figure 3.18b (190°), the FFT for each chordwise location is mixed together and they do not show a dominant peak. As these two AoA values are in the vicinity of stall, the aerodynamic force experiences large variations and non-periodic vortex shedding which makes the process unstable. Thus, multiple shedding frequencies can occur and the dominant shedding frequency is not obvious in the FFT plot.

The vortex shedding frequencies are different if one considers forward flow and reverse flow. Differences can be found in the last three rows of subfigures in Figure 3.18. For AoA at 30°, 50°, and 90°, the shedding frequency is always slightly smaller than the corresponding cases in AoA at 210°, 230°, and 270°. This also coincides with the result of the wake contours in Figure 3.14, which shows a thinner wake when the convex surface is facing upwind and undergoing reverse flow. A thinner wake results in a higher shedding frequency due to a smaller projected length in the flow. It is also noted that all the subfigures show a wide range of high-power spectral density at low frequencies. This may be due to the vibration of the model.

The dominant peak for each AoA is plotted with regard to AoA in Figure 3.19a. It is noted that when AoA = 90° (Figure 3.18g), the dominant peak occurs near 56 Hz, and a second peak near 112 Hz is observed, which is likely the first harmonic (twice the frequency) of the fundamental 56 Hz peak. The vortex shedding frequency is non-dimensionalized into St as shown in Figure 3.19b where St is calculated as $St = fc\sin(\text{AoA})/U$. Here, the characteristic length used for calculating St is the projection length of the chord (c) in the cross-section plane of the wind tunnel. It is noted that in order to obtain the dominant frequency more precisely, the FFT of C_l was used for finding the peaks. This is because C_l takes the integral of the surface pressure; therefore, the small peaks shown in the FFT of C_p will be minimized, and the dominant peak will be more noticeable.

Figure 3.19a shows that for AoA between 0° and 180° and between 180° and 360°, the vortex shedding frequency follows the same trend: it drops until 90° (or 270°) and then increases after that. A similar trend can be seen for frequencies of different Re values, with higher shedding frequency at the higher Reynolds number. Although the vortex shedding frequency is sensitive to Re, the corresponding St is not influenced by the tested three Re values or AoA. In Figure 3.19b, St at different Re values collapse onto one single curve, remaining almost constant for different AoA values, although with minor fluctuations. This

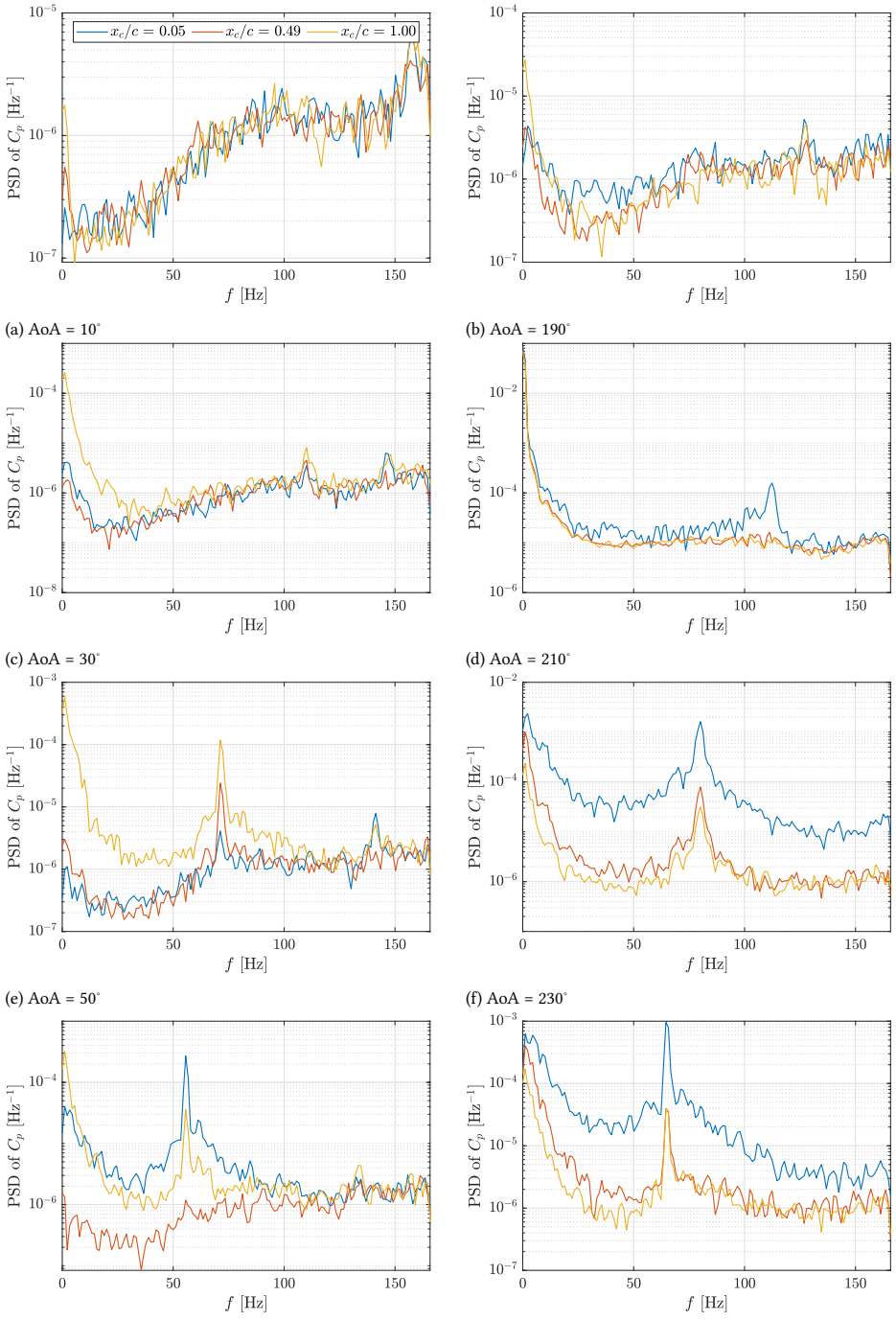

(a) AoA = 10°

(b) AoA = 190°

(c) AoA = 30°

(d) AoA = 210°

(e) AoA = 50°

(f) AoA = 230°

(g) AoA = 90°

(h) AoA = 270°

Figure 3.18: FFT of C_p at airfoil suction surface at $Re = 5 \times 10^5$.

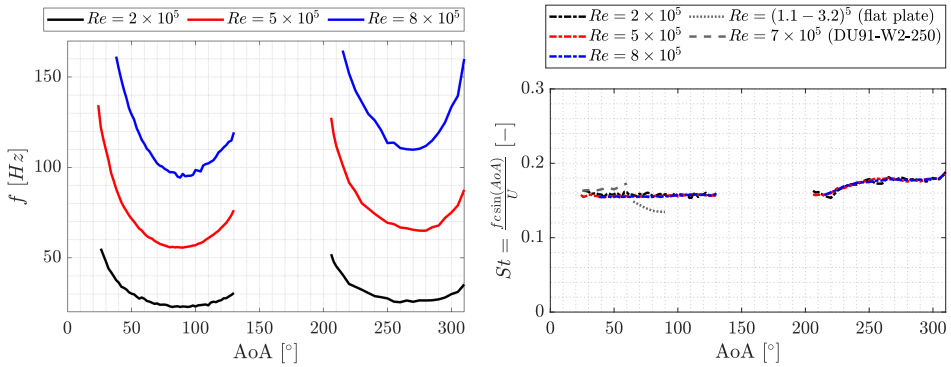

(a) Vortex shedding frequency

(b) Strouhal number calculated with projected height

Figure 3.19: Vortex shedding frequency and Strouhal number calculated with projected height. The result of St at $Re = (1.1 - 3.2) \times 10^4$ for a flat plate [98] and the result for DU91-W2-150 at 7×10^5 [99].

uniformity is due to the full stall characteristics of the airfoil, where the flow is dominated by flow separation. In this condition, the vortices are mainly shed from the edges of the airfoil, and the shedding process is not influenced by either Re or AoA. Previous research [98] showed a similar result. In their research, the universal St of the shedding frequency has been found at large AoA values from 65° to 90° for a flat plate with beveled sharp edges. The result is also replotted in Figure 3.19b. The St of the flat plate has a slightly lower value than that of the airfoil, which may be due to a difference in the Re (in the order of 10^3 and 10^4 in their campaign) and model geometry. In addition, an experiment was conducted in the same laboratory with the same airfoil but with different thicknesses [99]. A possible explanation for the higher St from that campaign can be a larger influence of the blockage effect, which slightly influences the vortex shedding frequency, flow speed, etc.

It is noted that St at AoA lower than 130° matches the flat plate St of 0.16 [100]. When AoA is larger than 180°, St increases to between 0.16 and 0.18. This is mainly due to the convex upwind curvature of the airfoil, which leads to higher vortex shedding frequencies and St. This finding significantly proves the consistency of St while also providing a more detailed comparison when there is a reverse flow for an asymmetric airfoil.

Apart from obtaining vortex shedding frequency from the pressure measurement, the shedding frequency can also be extracted from the modes shown in POD. In Figure 3.16c for AoA 90°, half of the wavelength (the length from the two neighbouring peaks in the streamwise direction) is approximately $1.76c$. With the wake velocity obtained from PIV, the shedding frequency is 63 Hz, which matches that obtained from the pressure data in Figure 3.19a. The vortex shedding frequency and corresponding wavelengths for the cases at $Re = 0.5 \times 10^5$ are concluded in Figure 3.20a for AoA = 90°, 270°, 130°, and 310°. The difference between POD analysis and the pressure measurement mainly comes from the limited spatial resolution to determine the distance (λ) and the averaged wake velocity in PIV data (approximately 60% free stream velocity) when calculating the estimated frequency.

The wake of the flow is strongly influenced by the force experienced by the airfoil. As

depicted in Figure 3.20, the impact of drag on vortex shedding in the wake conforms to a linear relationship. This can be attributed to two factors. Firstly, this is related to the blockage of the airfoil to the flow. When an airfoil has a relatively large angle, it projects a longer length in the wind, which leads to a larger C_d. This explains the trend from the group of AoA = 90˚ and 270˚, and the group of 130˚ and 310˚. On the other hand, in the case of 90˚ and 270˚ (or the case of 130˚ and 310˚), although the relative angle is the same in each case, due to the upwind convex characteristic of the airfoil surface for AoA 270˚ and 310˚, these two AoA values have slightly lower drag. And since the upwind convex surface has a smaller impact on expanding the wake, these two AoA values also have shorter vortex wavelengths. Hence, these two reasons account for the linear relationship as shown.

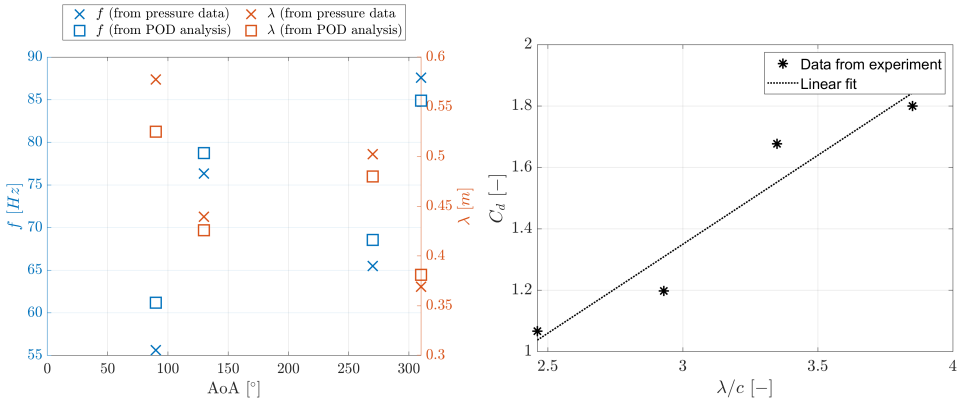

(a) Comparison of frequency and wave length (λ)

(b) The relation of drag coefficient with wavelength (λ)

Figure 3.20: Comparison of frequency and wavelength (λ) from experiment measurement and from POD analysis (left) and the relation of drag coefficient with wavelength (λ). On the right figure, the data from experiments from left to right are the case of AoA 310˚, 130˚, 270˚ and 90˚.

3.4 Conclusion

In this paper, an experimental research is presented to study the unsteady aerodynamic performance of a DU91-W2-150 airfoil under a wide range of AoA values up until 310˚ at three *Re* values at the magnitude of 10^5 using pressure measurement and PIV technique. The experimental data for large AoA values are valuable either for future fundamental airfoil study or wind turbine study at stand still condition. A wide variety of effects were studied. Four conclusions can be drawn from the analysis here.

- *Effect of airfoil geometry on the mean airfoil load*: The plot of C_l and C_d for the forward flow and reverse flow shows that no matter the direction of the flow, as long as the concave surface is facing upwind, the aerodynamic loads are higher. The wake contour lines of AoA = 90˚, 270˚, 130˚ and 310˚ further validate this result.
- *Effect of Re on the separation on the airfoil*: The separation point on the airfoil was found based on the previous theory and for all three *Re* values tested in the campaign, the separation points tend to move towards the leading edge as AoA increases.

For this DU91-W2-150 airfoil, as Re increases from 2×10^5 to 8×10^5, separation tends to happen earlier for both the positive stall and the negative stall. This is mainly due to that the viscous force is less dominant in the flow as Re increases. For the highest Re tested, local separation very close to the leading edge happened just before the positive stall onset as the high Re flow induces instabilities in the flow.

- *Effect of forward flow and reverse flow*: The 2σ plot of C_l and C_d indicates that reverse flow induces more fluctuations compared to forward flow. This is attributed to the occurrence of separation at the aerodynamic leading edge in a reverse flow scenario, as shown in the surface pressure plot as well.

- *Vortex shedding frequency and Strouhal number*: The vortex shedding frequency matches with the frequency estimated from POD, where the vortex shedding wavelengths show a strong relation with airfoil drag. The result from normalized St reveals that St remains approximately constant at large AoA values despite different Re and AoA values, due to full stall characteristics. Meanwhile, St is slightly higher when AoA is larger than 180° as an airfoil with a convex curvature in the upwind direction has a smaller effect to expand the wake, thus higher shedding frequency.

III

Unsteady aerodynamics of oscillating airfoil at large angles of attack

4

Surge motions: lock-in and load variations at 90° angles of attack

The previous chapter examined the fundamental aerodynamic performance and vortex shedding characteristics of a static airfoil at large angles of attack under both forward and reverse flow conditions. Establishing this understanding of a static airfoil is essential before progressing to oscillating cases. In this chapter, an experimental campaign is conducted on a surging airfoil at a constant angle of attack of 90°*, oriented perpendicular to the incoming flow. Using PIV measurements, the study investigates the vortex dynamics, lock-in characteristics of vortex shedding at large angles of attack, and the associated aerodynamic force variations, an area that has received limited attention in previous research. Two reduced frequencies are tested, and the results reveal distinct flow patterns and vortex dynamics that give rise to different load variations.*

This chapter is based on
G. Xu, A. Sciacchitano, C. Simão Ferreira, W. Yu, *On the unsteady aerodynamics of a surging airfoil at* 90° *incidence,* Experiments in Fluids **66** (5), 85, 2025 [101].

4.1 Introduction

A relevant phenomenon occurring in vortex-induced vibrations is the so-called lock-in effect. In Bearman's review [10], the lock-in region, also called the "range of capture," refers to a narrow range of reduced velocities—defined as the ratio of the free-stream velocity to the product of the bluff body's characteristic dimension and its oscillation frequency—where the flow conditions around the bluff body, as well as the force coefficient, change rapidly. Williamson and Roshko [102] define the lock-in as the condition where the structural oscillation frequency and the vortex formation frequency are close to the structure's natural frequency. The authors also point out that large amplitude motion can be triggered at frequencies that are hundreds of times larger than the structural natural frequency. This is confirmed in the work of Sarpkaya, who showed that lock-in can happen at the super-harmonics of the natural frequency (Sarpkaya [12]).

In this research, the forced motion method is used as the frequency and amplitude of the object's motion can be maintained constant. It is important to note that under the forced vibration condition, the classical definition of lock-in needs to be modified. For the forced oscillation of a circular cylinder, Bishop and Hassan [103] define lock-in or synchronization when the forcing frequency (f) approaches the vortex shedding frequency (f_{st}). This is the definition used in this research, which is also used in Besem et al. [30] and Tang and Dowell [104].

The present work is motivated by the need for fundamental understanding of the VIV of airfoils at high AoA from an aerodynamic perspective, as previous studies focus on a limited range of low angles of attack (typically below 15°). Following the same approach as Young and Lai [52] and Choi et al. [47] which investigate forced vibrations on airfoils, the case of an airfoil undergoing forced surging motion is considered. The main goal is to investigate the vortex structures from formation, evolution, to shedding and their role in the aerodynamic forces. In the following sections, the experimental approach and analysis methodology are introduced. Then, an overview of vortex kinematics and flow development is provided for the two motion cases at each phase of the measurement. The main results detailing the aerodynamic forces are discussed in two sections: (i) the overall force and the contribution of each force component and (ii) the comparison of the experimental data with the flat plate reduced-order model.

4.2 Methodology

4.2.1 Experimental setup

Wind tunnel setup

The experiments were conducted in the Open Jet Facility (OJF) of Delft University of Technology. The setup is depicted in Figure 4.1.

Wing model

A 40 cm span wing with NACA0021 airfoil of 7.5 cm chord was used in the experimental campaign. The model was 3D printed, and carbon fiber strips were attached at the location of the one-quarter chord to enhance its stiffness. Although not commonly used in modern horizontal-axis wind turbines, it remains an appropriate choice for this investigation for two primary reasons. First, under the high angle of attack conditions considered,

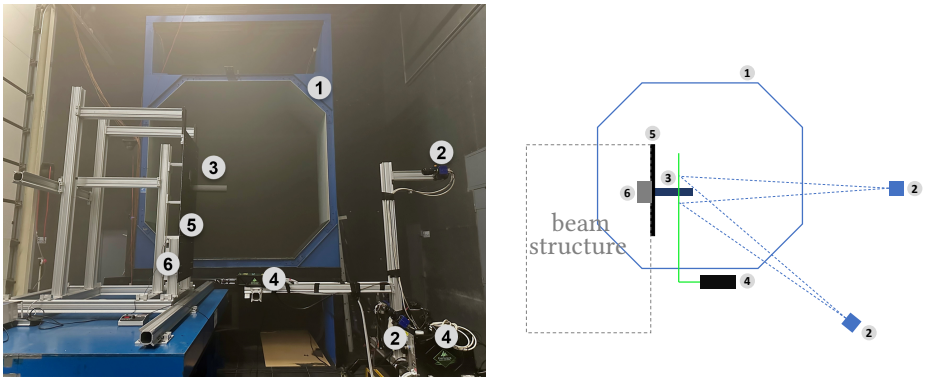

Figure 4.1: Experimental setup of the experiments in the OJF, looking in the upstream direction. The relevant components are: 1. Flow outlet 2. LaVision Imager sCMOS camera 3.Airfoil model 4. Quantel Evergreen Nd:YAG laser 5. The base plate 6. Surging mechanism. Note that the schematic plot of the experimental setup (on the right) is not to scale.

the flow physics are dominated by vortex shedding from the leading and trailing edges. Consequently, the specific aerodynamic curvature becomes minor to the global flow dynamics. Second, the NACA 0021 is a commonly used shape in aerodynamic and aeroelastic literature, which provides a robust baseline for characterizing fundamental behavior. The results obtained in this study are compared to static experimental data, for example, from Holst et al. [105].

The AoA of the wing was fixed at 90°. Note that in the experiment, the airfoil was oriented at 270° due to experimental constraints, while the result remains the same due to its symmetry. A motor with a slider crank mechanism was used for the surging motion of the wing. The wing is subjected to the sinusoidal surging motion (i.e., parallel to the free-stream direction, as shown in Figure 1.6), with a nominal amplitude of $1.1c$, similar to the simulation from Heinz et al. [23]. The motion frequency was set to 5 Hz and 2.5 Hz, yielding the reduced frequencies ($k = \pi f c/U_\infty$) of 0.38 and 0.19, respectively. In order to trigger the lock-in phenomenon, an appropriate combination of motion frequency and amplitude needs to be considered. As was discussed by Koopmann [106], Anagnostopoulos [107], and Meneghini and Bearman [108], the boundary of the lock-in region presents a V-shape: the larger the departure of the frequency ratio f/f_{st} from unity, being f_{st} the static vortex shedding frequency, the larger the amplitude required to trigger lock-in. Considering that the static vortex shedding frequency was $f_{st} = 6.4$ Hz (the procedure to obtain the static shedding frequency is discussed in the results section), and the limitations of the motor, at the highest motion frequency of 5 Hz, the frequency ratio was $f/f_{st} = 0.78$, corresponding to a reduced frequency $k = 0.38$. The motion frequency 2.5 Hz was also investigated in the experiments, yielding $f/f_{st} = 0.39$ and $k = 0.19$. The experimental parameters are summarized in Table 4.1. The wing's kinematic motion is driven by a slider-crank linkage, which transfers a circular motion to a linear motion. The wing's actual motion amplitude h is obtained by physically tracking the airfoil leading edge position from the phase-averaged Particle Image Velocimetry (PIV) images. The velocity $\dot{h}$ and acceleration $\ddot{h}$ of the motion were calculated by temporal derivatives of the wing's positions. The results of the wings

Table 4.1: Experimental parameters for the surging airfoil NACA 0021.

Parameter	Symbol	Value
Freestream velocity	U_∞	3.1 m/s
Model chord	c	0.075 m
Reynolds number	Re	1.5×10^4
Static vortex shedding frequency	f_{st}	6.4 Hz
Model angle of attack	AoA	90°
Model span	s	0.4 m
Model aspect ratio	AR	5.33
Motion frequency	f	2.5 Hz, 5 Hz
Reduced frequency	k	0.19, 0.38
Frequency ratio	f/f_{st}	0.39, 0.78
Motion amplitude	h_{max}	0.083 m (1.1c)

kinematics are shown in Figure 4.2a and the relative locations are shown in Figure 4.2b for four phases of the motion: 0° and 180°, corresponding to the wing's position close to the center of its trajectory, 90° and 270°, corresponding to the most upwind and downwind positions, respectively.

PIV measurements

Stereoscopic PIV measurements were performed to evaluate the flow fields surrounding the wing. A SAFEX smoke generator created water-glycol droplets with a median diameter of 1 μm to seed the flow within the tunnel. The illumination was provided by a Quantel Evergreen Nd:YAG laser (200 mJ pulse energy, maximum 15 Hz repetition rate, 532 nm wavelength). To acquire the three velocity components within the measurement domain, two LaViSion Imager sCMOS cameras (2560 × 2160 pixel, 16 bit, 6.5 × 6.5 μm pixel size) were installed at the tunnel's side at a relative angle of 40°, as shown in Figure 4.1. The size of a single field of view (FoV) is 269.4 × 331.8 mm, which corresponds to approximately 3.6c in the streamwise direction and 4.4c in the cross-flow direction. The image magnification factor is 0.05 with a digital resolution of 7.92 pixels/mm. The experimental procedure involved two stages: initially, a measurement with the static wing was performed to determine the static vortex shedding frequency f_{st}, which was then used to select the frequencies for unsteady measurements. Two single FoVs were stitched together, giving the total FoV of 5.2c in the streamwise direction and 4.2c in the cross-flow direction. Secondly, the unsteady measurements were performed for the surging airfoil. The measurement plane was placed at a distance of 3c from the tip of the wing where the flow is less affected by the three-dimensional effects occurring at the wing tipto minimize the three-dimensional flow occurring at the wing's tip. To achieve a broader FoV, the entire PIV system was traversed twice in the streamwise direction, which gives the total FoV of 8c in the streamwise direction and 4.2c in the cross-flow direction. Phase-averaged acquisitions were obtained at 12 phases: 0°, 45°, 80°, 90°, 100°, 135°, 180°, 225°, 260°, 270°, 280°, and 315°. For each phase at each local FoV, 200 image pairs were captured, and the time interval between the images of a pair is 417 μs.

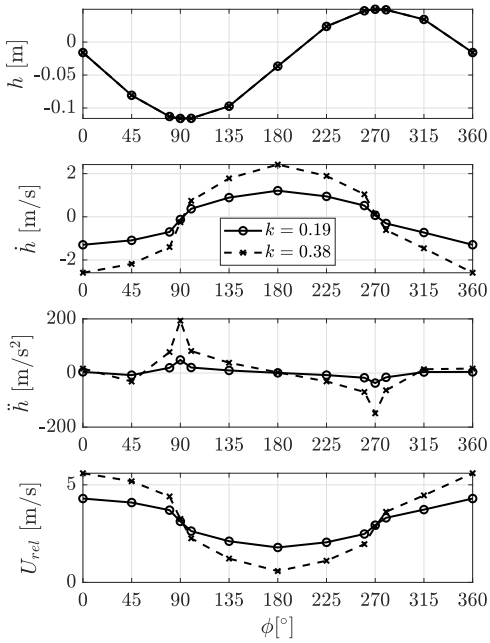

(a)

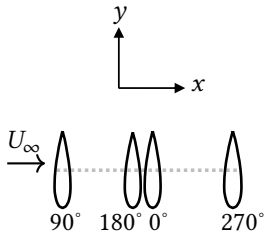

(b)

Figure 4.2: (a) The actual motion amplitude (h) based on the leading edge of the airfoil, velocity ($\dot{h}$) and acceleration ($\ddot{h}$) of the surging motion for two motion frequencies. Note that the lines for h overlap each other since two cases have the same travel distance. The bottom panel represents the relative wind speed ($U_{rel} = U_\infty - \dot{h}$) experienced by the airfoil. (b) The relative locations of the airfoil at four different phases: 0° and 180° where the wing is near the center of its trajectory, 90° and 270°, where it is in the most upwind and downwind positions, respectively.

Definition of lock-in in the context of phase-locked PIV

The definition for the lock-in under forced motion is the frequency match between the vortex shedding and the forced motion [30, 103]. In this study, this frequency match is identified through the vorticity fields from the phase-locked PIV measurements.

If, during one plunging cycle (containing 12 measured phases), the pair of vortices experiences one cycle of growth and shedding, then the vortex shedding cycle matches the motion cycle, which is considered locked in. However, if during one plunging cycle, multiple vortex shedding events occur, there is no lock-in between motion frequency and vortex shedding frequency.

Uncertainty analysis of the PIV measurements

The uncertainty of the PIV measurements can be estimated from the ensemble data size and the flow velocity fluctuation (Ye et al. [109]). For each phase measured, 200 uncorrelated snapshots were taken; hence, the standard uncertainty of the phase-average flow velocity is equal to:

$$\varepsilon_u = \frac{\sigma_u}{U_\infty \sqrt{N}} \tag{4.1}$$

σ_u is the representative standard deviation value of the streamwise velocity component (σ_u/U_∞ is approximately 0.1 in the wake of the wing) and N represents the number of uncorrelated samples. This equation yields $\varepsilon_u \approx 0.7\%$ for the present experiment.

The uncertainty of the Root Mean Square (RMS) of the velocity fluctuations is estimated as (Sciacchitano and Wieneke [110]):

$$\varepsilon_{u'} = \frac{\sigma_u}{U_\infty \sqrt{2(N-1)}} \tag{4.2}$$

The expression yields $\varepsilon_{u'} \approx 0.5\%$.

4.2.2 Analytical solution for the surging airfoil

Accelerating motion in one direction

Since the surging airfoil has a fixed AoA of 90°, its shape and the resulting flow dynamics resemble those of a flat plate normal to the free-stream direction, whereby the leading and trailing edge vortices are dominant. This research compares a low-order model of a flat plate at 90° incidence presented by Corkery et al. [111] with the loads estimated from PIV. In the low-order model, the vortices are assumed to be concentrated into two parts: a leading edge vortex (LEV) and a trailing edge vortex (TEV). The analytical solution for the accelerating flat plate is presented below.

This method decomposes the force into the added mass force (non-circulatory force) and the circulatory force. The former is due to the acceleration induced by the plate to the flow and is equal to the product between added mass and acceleration:

$$F_{non-circ} = \frac{\rho \pi c^2}{4} \ddot{h} \tag{4.3}$$

This force can be non-dimensionalized with respect to the dynamic pressure force ($1/2\rho c U_\infty^2$) to obtain the force coefficient:

$$C_{non-circ} = \frac{\pi c}{2U_\infty^2} \ddot{h} \tag{4.4}$$

The circulatory force, instead, is ascribed to the vortex pair generated by the impulsive motion of the plate. If the strengths of the two vortices are ±Γ, with the distance d between the cores of the two, the impulse (momentum) (Lamb [112]) of the vortex pair is:

$$J = \rho \Gamma d \tag{4.5}$$

The time derivative of Equation (4.5) gives the force in the streamwise direction:

$$F_{circ} = \rho(\dot{\Gamma} d + \Gamma \dot{d}) \tag{4.6}$$

where $\dot{\Gamma}$ and $\dot{d}$ are the time derivative of circulation and vortex distance, respectively. The schematic plot of the model is shown in Figure 4.3.

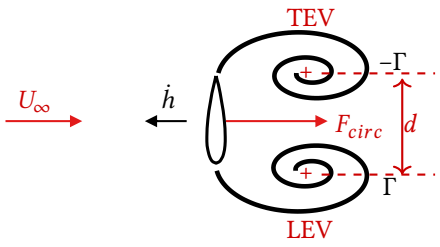

Figure 4.3: Illustration of the airfoil's vorticity field and circulatory force moving in the upstream direction. Γ represents the absolute value of the circulation from LEV and TEV. "+" represent the vortex cores. F_{circ} represents the circulatory drag force.

The circulatory force can then be non-dimensionalized with respect to dynamic pressure force $(1/2\rho c U_\infty^2)$ as:

$$C_{circ} = \frac{2}{U_\infty^2 c}(\dot{\Gamma} d + \Gamma \dot{d}) \tag{4.7}$$

The total drag force coefficient C_d is the sum of the non-circulatory and circulatory terms:

$$C_d = C_{non-circ} + C_{circ} = \frac{\pi c}{2U_\infty^2}\ddot{h} + \frac{2}{U_\infty^2 c}(\dot{\Gamma} d + \Gamma \dot{d}) \tag{4.8}$$

Equation (4.8) presents the low-order force solution with the contribution from virtual mass and circulatory force, where the circulatory force component is influenced by both the growth of the vortices and the relative motion between LEV and TEV.

Modified model for surging motion

One limitation of the reduced order model Equation (4.8) is that it only considers the accelerating motion of a flat plate, assuming that the motion is only in one direction. In the case of the surging wing, accelerations and decelerations occur, with the wing moving both upwind and downwind. In particular, a vortex pair is generated downstream of the wing during the upwind motion, as for the flat plate. Instead, during the downwind motion, depending on the reduced frequency k, vortices can also be generated upwind of the wing, resulting in a situation where both upwind and downwind vortices are present. In this case,

Equation (4.8) cannot be applied anymore. Let us consider, for instance, the case when the wing is moving downstream in a surging case, as illustrated in Figure 4.4. The downstream motion of the wing causes the formation of two upwind vortices of circulation (Γ_{us} and -Γ_{us}), whose contribution to the drag is $F_{circ,us}$. However, the wing is moving in a region of flow directed upstream at a velocity U_{ds}. In this flow region, two vortices are present, generated from the previous upwind motion of the wing, whose circulation is Γ_{ds} and -Γ_{ds}, which contribute to the drag force via $F_{circ,ds}$. Considering this situation in the flat plate model Equation (4.8), the circulatory force in the updated model is computed as the sum of the circulatory forces from each vortex pair. Thus, during the downstream motion in certain cases, the drag coefficient is calculated as:

$$C_d = (F_{non-circ} + F_{circ,us} - F_{circ,ds})/(\frac{1}{2}\rho U_\infty^2 c) \tag{4.9}$$

Using Equation (4.3) to calculate $F_{non-circ}$ and Equation (4.8) to calculate $F_{circ,us}$ and $F_{circ,ds}$, Equation (4.9) becomes:

$$C_d = \frac{\pi c}{2U_\infty^2}\ddot{h} + \frac{2}{U_\infty^2 c}(\dot{\Gamma}_{us} d_{us} + \Gamma_{us}\dot{d_{us}} - \dot{\Gamma}_{ds} d_{ds} - \Gamma_{ds}\dot{d_{ds}}) \tag{4.10}$$

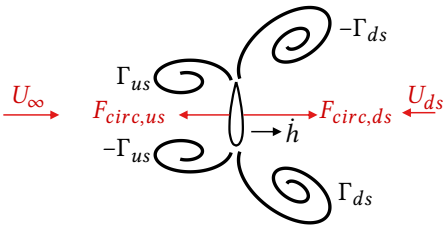

Figure 4.4: Illustration of the airfoil's vorticity field and circulatory force moving in the downstream direction during a surging motion. The circulatory force and circulation are split into two groups. The ones with the underscore "us" represent the circulatory force and circulation generated by the wake velocity U_{ds} during the downwind motion of the wing. The ones with the underscore "ds" represent the circulatory force and circulation generated during the upwind motion of the wing.

4.3 Results and discussion

4.3.1 Velocity and vortex dynamics

Static case

The static wing case is discussed first regarding velocity and vorticity fields. Figure 4.5 shows the time-averaged (from 200 samples) streamwise velocity $\bar{u}/U_\infty$ and vorticity $\bar{\omega}c/U_\infty$ field at $3c$ distance from the wing's tip, with the airfoil at AoA = 90°. The grey area in the plots represents the shadow region where the airfoil blocked the laser light from the bottom, as shown in Figure 4.1; hence, no velocity measurement is possible in that region. At such large AoA, the airfoil generates a large wake, whose width scales with the airfoil's chord, where a significant flow reversal occurs (velocity up to about 0.3 of U_∞). Vortices are shed alternatively from the leading and trailing edges but are not visible in the mean

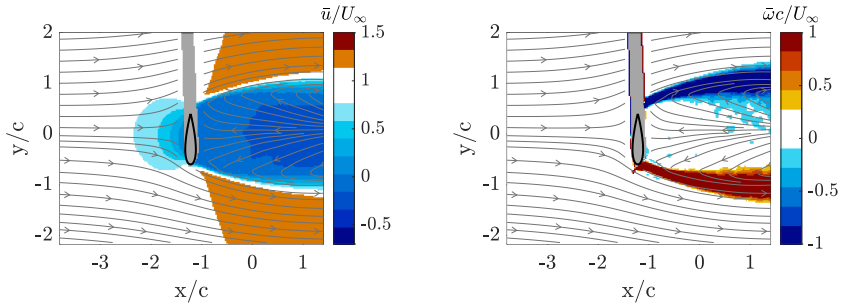

(a) $\bar{u}/U_\infty$ (b) $\bar{\omega}c/U_\infty$

Figure 4.5: Streamwise velocity field $\bar{u}/U_\infty$ and vorticity field $\bar{\omega}c/U_\infty$ of the static wing at $3c$ location from the tip.

4

flow field. Instead, high vorticity is present in the shear layers emanating from the leading and trailing edges.

Flow fields are captured $2.5c$ downstream of the wing to determine the vortex shedding frequency of the static wing. The distance is defined between the airfoil chord line to the left boundary of the FoV. Two instantaneous flow fields at t = 10.27s and = 15.65s are shown in Figure 4.6a and Figure 4.6b. In the figure, the vortex shedding from the leading edge and trailing edge is visible, resulting in a sinusoidal shape of the wake. Proper Orthogonal Decomposition (POD) analysis is performed on the flow fields to identify the most energetic modes associated with the wake dynamics (Smith et al. [113]). The first two modes feature a comparable energy content of 9.5% and 8.1% (as shown in Figure 4.7) and are in quadrature of phase; the first two modes of the cross-flow velocity component v, shown in Figure 4.6c and Figure 4.6d, represent the convection of the streamwise vortices shed from the leading and trailing edges of the wing. The distance between the two neighboring peaks in the streamwise direction ($1.88c$) in Figure 4.6c represents half of the wavelength of the vortex. Based on the convective velocity in the shear layer, which is estimated as 60% of the free stream, the vortex shedding frequency f_{st} for the static wing (defined as velocity divided by wavelength) is calculated as 6.4 Hz, resulting in a Strouhal number $St = f_{st}c/U_\infty = 0.159$.

Surging cases

The surging motion was conducted at 5 Hz and 2.5 Hz. Based on the f_{st} obtained from the static measurements, the corresponding frequency ratio of the motion frequency f with respect to f_{st} is 0.78 and 0.39. The phase-averaged streamwise velocity fields superimposed with streamlines are shown in Figure 4.8 during a cycle of motion for the reduced frequency $k = 0.38$. In total, 12 phases were captured, and the result is shown in a vortex formation order in the wake instead of the phase-increasing order. When the airfoil moves in the upstream direction (for instance, phases $\phi = 0^\circ$ and 45°), the flow shares similarity with that of the static wing, even though with a stronger velocity deficit inside the wake and a larger flow acceleration outside of the wake. When the airfoil moves in the downstream direction, instead, a region of velocity higher than U_∞ is formed upwind of the wing, whereas the wake downwind of the wing elongates on the top and bottom

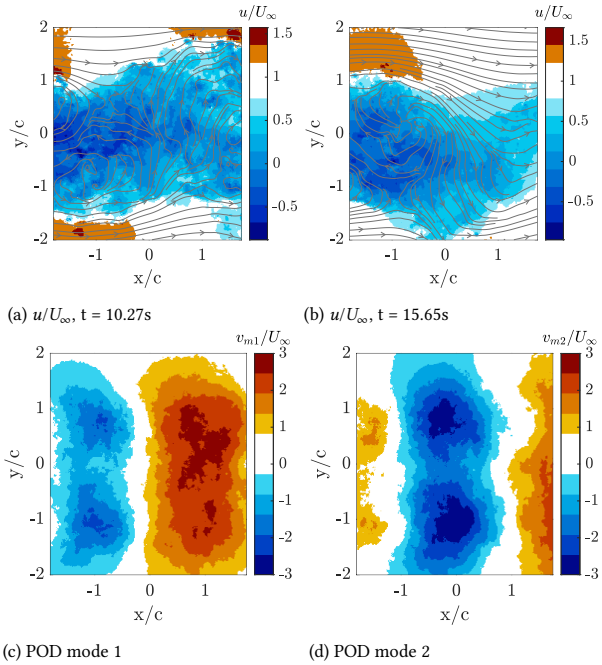

Figure 4.6: Instantaneous streamwise velocity field u/U_∞ 2.5c downstream from the airfoil at (a) t = 10.27s, (b) t = 15.65s and the first two modes of the cross-flow velocity component v (c) and (d) from the POD analysis. Note that distance of the FoV with respect to the airfoil is defined as the distance between the airfoil chord line and the left boundary of the FoV.

of the wing in the upwind direction (see, for instance, phases ϕ = 180° and 225°). The phase-averaged vorticity fields superimposed with streamlines for the same k are shown in Figure 4.9. The green crosses in Figure 4.9 represent the vortex cores identified using the Γ1 method explained in the methodology section. For the k = 0.38 surging case, the vortex formation in the wake starts from ϕ = 270°, where the airfoil is at the most downstream position. At this phase, the wing starts moving upwind from zero velocity; thus, a vortex pair starts to form at the leading and trailing edges. As the wing moves upwind, the vortices grow in size and strength, fed by the vorticity of the shear layers. The end of the vortex formation period can be determined through the circulation of each phase, which for the leading edge vortices is shown in Figure 4.10. The circulation is calculated using Equation (2.32), excluding the points where the vorticity has the opposite sign with respect to that of the vortex. For the k = 0.38 case, Γ reaches the maximum at ϕ = 80° (close to the most upwind location) and remains approximately constant afterwards. From ϕ = 80°(Figure 4.9g) to ϕ = 100°(Figure 4.9i), the wake vortices increase their distance in the cross-flow direction, while shrinking their size in the streamwise direction. Before ϕ = 80°, the vortex pair builds up and the vortex formation length (the distance between the airfoil and the vortex core) elongates. When the airfoil decelerates towards ϕ = 90°, the trailing vortices decelerate, because their motion is obstructed by the airfoil itself. When the airfoil starts to move in the downwind direction (ϕ > 90°), it induces an increase of

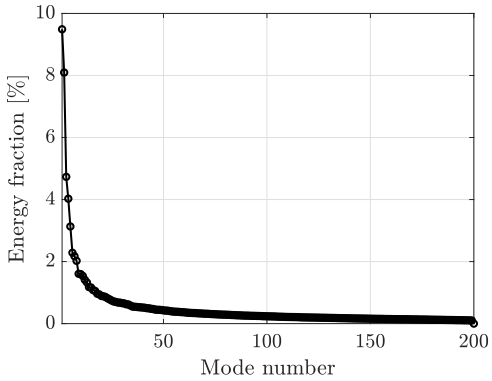

Figure 4.7: Energy content at different mode number.

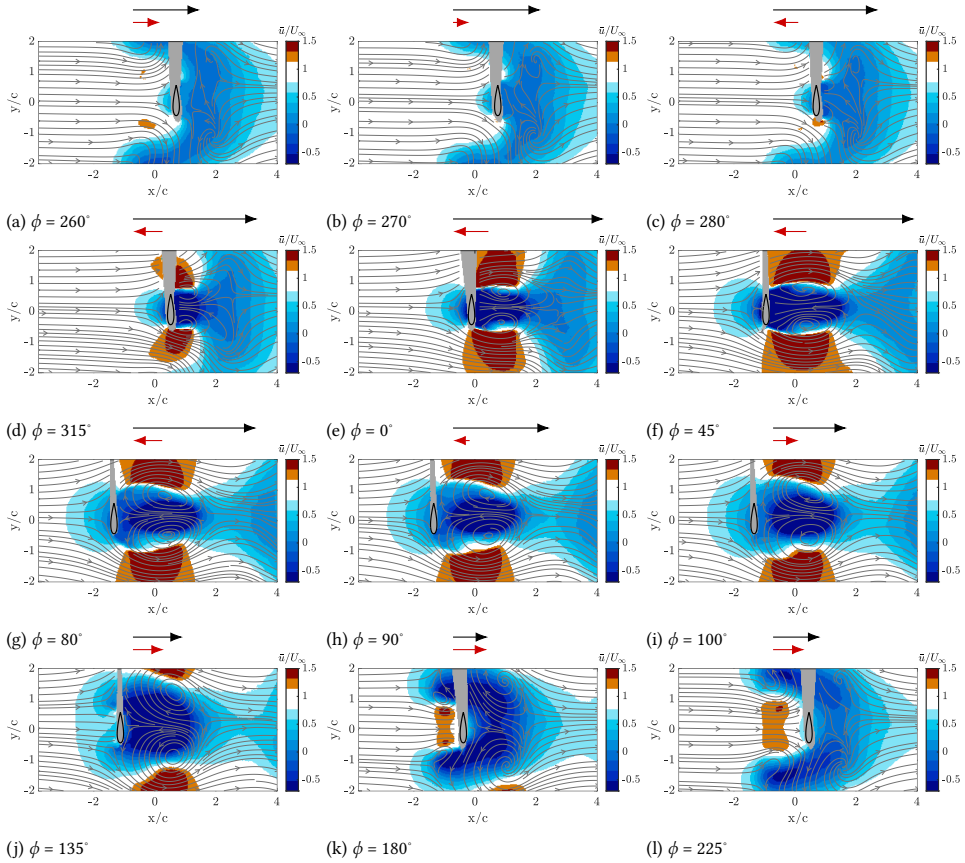

Figure 4.8: Streamwise velocity field $\bar{u}/U_\infty$ for k = 0.38 surging case for all the measured phases. Instead of showing the increasing phase order, the same order as Figure 4.9 is shown here. The black arrow represents the scaled relative velocity U_{rel} and the red arrow represents the scaled motion velocity $\dot{h}$.

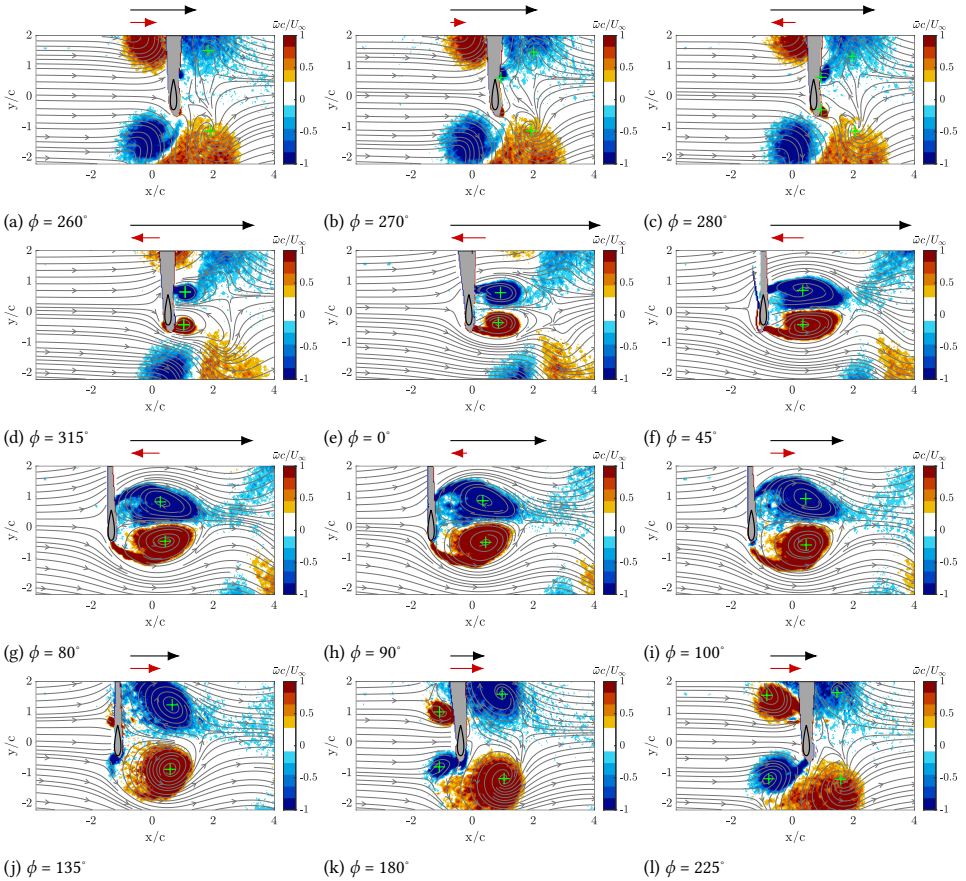

Figure 4.9: Contours of the phase-averaged spanwise vorticity component superimposed with streamlines. Vortex identified using Γ_1 method for k = 0.38 surging case. The vortex center is marked as crosses in green. The black arrow represents the scaled relative velocity U_{rel} and the red arrow represents the scaled motion velocity $\dot{h}$.

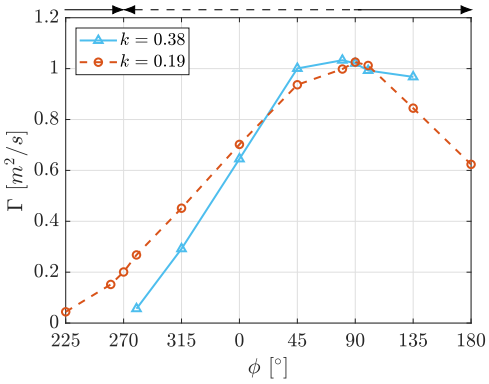

Figure 4.10: Circulation Γ of the wake vortex in the downstream side from the leading edge at different phases in a cycle.The solid horizontal arrow pointing right on top of the plot represents the downstream motion, and the dashed arrow pointing left represents the upstream motion of the airfoil.

pressure between the vortices: as a consequence, the vortices detach and move apart in the crossflow direction. From $\phi = 90^\circ$ (the most upstream position) onwards, as the airfoil moves downwind, the vortices are pushed away from the airfoil, causing the vortex pair to detach from the airfoil's leading edge and trailing edge. This is identified by the fact that at 135°(Figure 4.8j), the two vortices are cut off from the supply of fluid circulation from the shear layer connected to the airfoil leading and trailing edges.

Starting from $\phi = 135^\circ$, another pair of starting vortices, in the upwind direction, starts generating and growing until $\phi = 225^\circ$. At $\phi = 180^\circ$, while the upwind vortices grow in size and strength, the downwind vortices gradually move away in the cross-flow direction from the wing. Similar to the downwind vortices, from $\phi = 225^\circ$ the upwind vortices start to separate from the wing due to the deceleration of the latter. At $\phi = 280^\circ$, they move away from the wing at a comparable speed as the downwind vortices. As the airfoil moves downstream, it moves within its own wake, characterized by low streamwise velocity generated during its upwind motion. With the relatively low incoming velocity and the relatively high wing motion velocity, the vortices shed upwind remain roughly at the same streamwise location during the downwind motion of the wing. It is noticed that one pair of downwind vortices (generated during the upwind motion) and one pair of upwind vortices (generated during the downwind motion) are shed simultaneously during one cycle of motion. Hence, it is concluded that, for the current case (frequency ratio $f/f_{st} = 0.78$), lock-in occurs between the vortex shedding and wing's motion.

Figure 4.11 displays the superimposed streamlines with streamwise velocity fields for all the measured phases for the $k = 0.19$ case. Compared with the $k = 0.38$ case, the wing's velocity is lower, meaning that the perceived wind of the airfoil is closer to the free-stream velocity; as a consequence, the resulting flow fields exhibit higher similarity to that of the static wing case shown in Figure 4.5a. In particular, during the downwind motion of the wing (phases between $\phi = 90^\circ$ and $\phi = 270^\circ$), the wing's velocity is not high enough to move the downwind vortices laterally. Furthermore, the flow stagnation always occurs on the upwind side of the wing, whereas the wake is always on the downwind side. From the vorticity fields, illustrated in Figure 4.12 , two main observations can be made: (i)

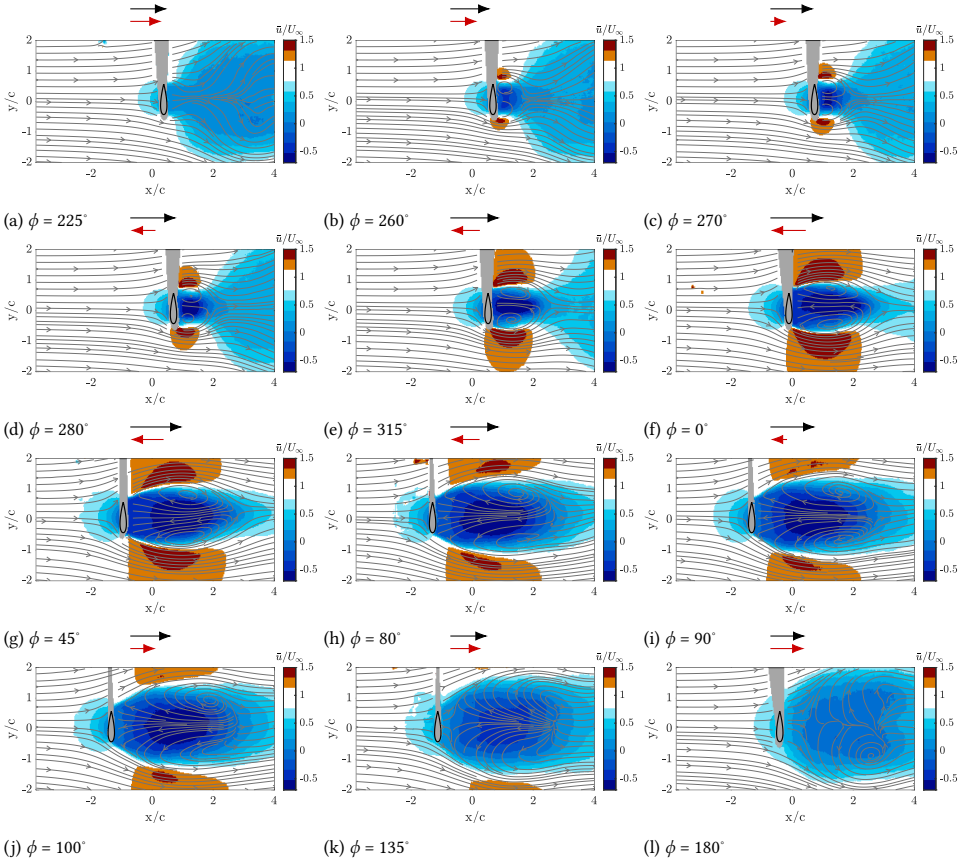

Figure 4.11: Streamwise velocity field $\bar{u}/U_\infty$ for k = 0.19 surging case for all the measured phases. Instead of showing the increasing phase order, the same order as Figure 4.12 is shown here.The black arrow represents the scaled relative velocity U_{rel} and the red arrow represents the scaled motion velocity $\dot{h}$.

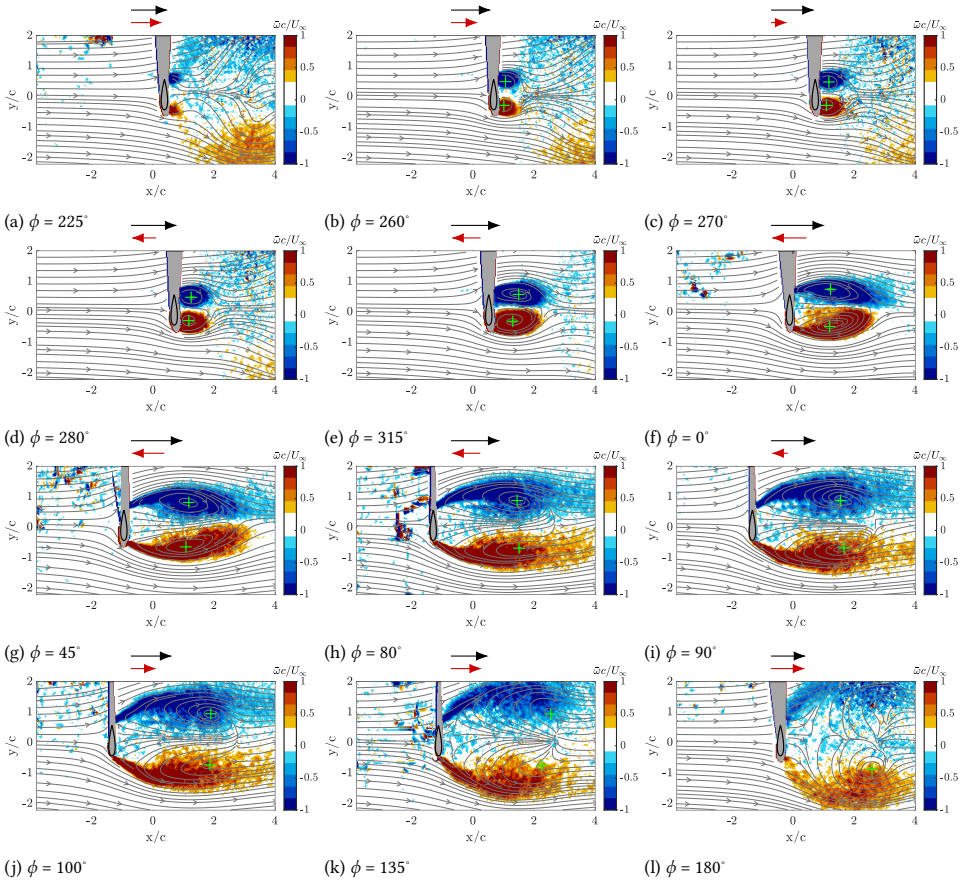

Figure 4.12: Contours of the phase-averaged spanwise vorticity component superimposed with streamlines. Vortex identified using Γ_1 method for the k = 0.19 surging case. The vortex center is marked as crosses in green. The black arrow represents the scaled relative velocity U_{rel} and the red arrow represents the scaled motion velocity $\dot{h}$. Note that for ϕ = 225°, this method cannot recognize the vortices near the leading edge and trailing edge of the airfoil, as the small vortices are near the shadow region.

contrary to the k = 0.38 case, vortices are shed only on the downwind side of the wing and not on the upwind side: this result is because the wing motion velocity is low compared with the free-stream velocity, hence no starting vortex is formed when the wing moves downwind; (ii) Although different from the k = 0.38 case where two pairs of vortices (one pair upwind and one pair downwind) shed, at k = 0.19, during one period of motion, only one pair of counter-rotating vortices is shed, which indicates a different form of lock-in between the wing motion and the vortex shedding. The first observation implies that the motion kinematics of the wing dominates the upwind vortex shedding, thus highlighting the importance of motion-reduced frequency on the flow dynamics. From the measured data, the start of the vortex generation is at ϕ = 225°, where a pair of small vortex blobs starts to form downstream of the airfoil. From Figure 4.10, it is noticed that, for the k = 0.19 case, Γ increases until ϕ = 90° and decreases afterward. At ϕ = 135°, it is observed that the

vorticity exhibits a "noisy" pattern between $x/c = 1$ and 2. Although this is ascribed to the limited ensemble size (it is reminded that the phase-average flow fields were obtained from 200 instantaneous fields), it indicates that the wake vortices are not stable and dissipate to the surrounding flow. At $\phi = 180^\circ$, the vorticity is spread in a larger area, and only the leading edge vortex core can be found in the measurement domain. Compared with $k = 0.38$ case, when the wing is moving upwind, the wake generated in the $k = 0.19$ case is downwind of the wing, similarly to the $k = 0.38$ case. However, in the latter case, a higher reverse velocity is encountered. In this condition, when the airfoil moves back in the downwind motion, the energy that the wing feeds into the flow combines with the energy of the wake flow: because of the lower wing velocity in the $k = 0.19$ case, the wake remains downwind of the wing, contrary to the $k = 0.38$ case, where the wake elongates to the sides and upwind of the wing. It is noticed that, in the $k = 0.19$ case, the vorticity field is significantly different from that of the $k = 0.38$ case, indicating that k influences the vortex dynamics to a large extent. On the other hand, the second observation (namely the fact that only one pair of counter-rotating vortices is shed during one motion cycle under this frequency, which is different from the $k = 0.38$ case where two pairs of vortices are generated and shed simultaneously during one cycle, only one pair of counter-rotating vortices is shed) indicates that even though the two motion cases have different vortex dynamics, they all eventually feature the lock-in effect. While the lock-in from the high reduced frequency is expected due to f/f_{st} close to unity, the lock-in in the low reduced frequency case is ascribed to the large motion amplitude. The simulation results from Choi et al. [114] of an oscillating airfoil indicate that lock-in occurs for small motion amplitudes for f/f_{st} closes to unity. In contrast, for large motion amplitudes, it can also occur for sub-harmonics, e.g., $f/f_{st} = 0.5$. In the present test case, for the low reduced frequency ($k = 0.19$) case, the frequency ratio is $f/f_{st} = 0.39$, which, given the motion amplitude of $1.1c$ yields a lock-in between frequency of motion and vortex shedding.

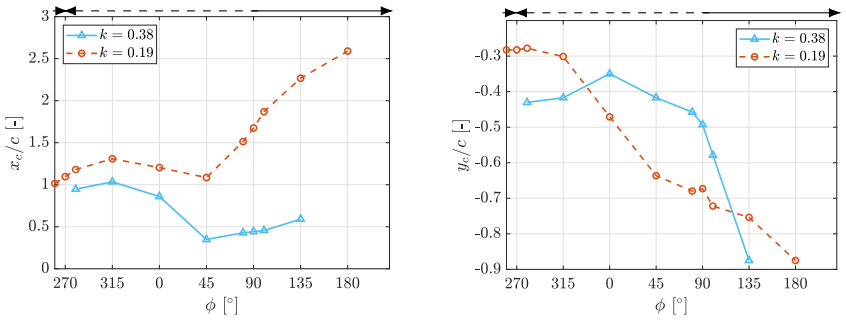

(a) Streamwise trajectory

(b) Lateral trajectory

Figure 4.13: streamwise and lateral trajectory of the leading edge vortex core (in the order of vortex formation) for $k = 0.38$ and $k = 0.19$ surging motions. Only the core of the downwind vortex is considered. The solid horizontal arrow pointing right on top of the plot represents the downstream motion, and the dashed arrow pointing left represents the upstream motion of the airfoil.

Figure 4.13 presents the trajectory of the downwind leading edge vortex along a cycle. The vortex core is identified using the Γ_1 method explained in the previous section. Starting from the beginning of the vortex formation ($\phi = 280^\circ$ for $k = 0.19$ case and $\phi = 260^\circ$

for $k = 0.38$ case) to $\phi = 45^\circ$, the motion in the streamwise direction follows the sinusoidal shape. For both the reduced frequencies, up to $\phi = 315^\circ$, the vortex moves slightly downstream because of the free-stream velocity in the downwind directions; for successive phases up to $\phi = 45^\circ$, the vortex moves upstream instead, subject to the flow velocity induced by the upwind motion of the wing. Clearly, such displacement is significantly larger for the $k = 0.38$ case due to the higher speed of the wing. From $\phi = 45^\circ$, the vortex moves downstream because of the decreasing wing velocity (up to $\phi = 90^\circ$) and its successive motion in the downwind direction (from $\phi = 90^\circ$ onward). When looking at the transverse displacement of the vortex (along the y direction, illustrated in Figure 4.13b), it can be seen that, for the lower reduced frequency $k = 0.19$, the vortex gradually moves away from the airfoil starting from phase $\phi = 315^\circ$. Instead, at the higher reduced frequency $k = 0.38$, the vortex transverse position remains approximately constant up to $\phi = 45^\circ$; afterward, the vortex quickly moves away from the wing due to the high wing velocity that has the effect of displacing the vortex in the vertical direction.

4.3.2 Load estimation

Static case

The load estimation method from Equation (2.21) to Equation (2.30) is applied to the static wing first; in this case, because the wing is static and the time-average flow field is considered, the time derivative term in Equation (2.22) is null. The pressure field is shown in Figure 4.14a. The pressure field is non-dimensionalized as $C_P = (P - P_\infty)/(1/2\rho U_\infty^2)$, where P is the static pressure in the flow field and P_∞ is the free stream pressure. The shadow region at the top of the airfoil, present in the velocity fields, was interpolated to allow for the pressure calculation using the Poisson equation. It is important to note that, although the shaded area is present, it primarily remains outside the wake region. For the sake of computation of the aerodynamic loads via Equation (2.22), linear interpolation of the velocity at the boundaries of the shaded region is performed. Because in the shaded region, the flow is mainly a potential flow, and because the aerodynamic loads are evaluated from the line integral along the control boundaries, the uncertainty associated with this interpolation is deemed negligible. Upwind of the wing, the flow field clearly follows potential flow theory: As the wind approaches the airfoil, the speed decreases and the pressure increases, based on Bernoulli's principle. Instead, downstream of the airfoil, a wake is present, where C_P is lower than 0 due to the presence of wake vortices and reverse flow. The corresponding force contributions from mean convection (MC), pressure (press), and turbulence momentum transfer (TMT) are shown in Figure 4.14b, with the definitions provided from Equation (2.23) to Equation (2.26). The mean viscous stress term is not included in the bar plot because it is several orders of magnitude lower than the others. Also, for the static case, the body force term is zero. For the calculation of the force contributions via Equation (2.22), a control contour around the airfoil shall be defined. The control contour surrounding the airfoil, shown in Figure 4.14a, extends from 10 dx to 30 dx from the airfoil surface, where d$x = 0.027c$ represents the streamwise grid spacing. Error bars of forces determined using the different control contours are added to the bar plot of Figure 4.14b, whose sizes represent the uncertainty at 95% confidence level. From the load result of 21 different control contours, the drag coefficient C_d is obtained with a mean value of 0.95 and a 95% confidence interval of 0.01. The pressure term pro-

vides the only positive contribution to the total force, while MC and TMT give a negative contribution, which is ascribed to the fact that all control contours are relatively close to the airfoil. As the airfoil stands as the bluff body in the flow at AoA 90°, the pressure force from the flow acts mainly horizontally, that is, normal to the chord line, thus giving rise to a relatively high-pressure drag. The contribution of MC to the control contour boundary is shown in Figure 4.15. The control contour showcased has a fixed 20 dx distance from each boundary of the airfoil surface. The curve starts from the bottom-left of the control contour; The dashed lines represent the boundary of the turning point in the control contour. Note that for the rest of the discussion, the control contour follows the same as here. The figure shows that even though the front boundary has a positive contribution from MC due to the deceleration of flow in front of the airfoil, the top, bottom, and back boundaries provide a negative contribution due to the accelerated flow at the top, bottom, and downwind of the airfoil outside the shear layer (Figure 4.5a).

In order to examine the validity of the load estimation method, C_d obtained from each control boundary is plotted against the control boundary width w/c in Figure 4.14c. The black horizontal line represents the mean value. It is shown that as w/c increases, C_d first decreases, reaching a local minimum, and then increases again. Therefore, the result does not show a convergence related to the control boundary. Firstly, when the control boundary is too small, the relatively high velocity gradients near the airfoil cause larger uncertainty in the local pressure value and, in turn, in the estimated load. Secondly, as we neglect the spanwise flow in the load estimation method, the mass and momentum are not preserved in the two-dimensional control boundary. As a result, the larger the control volume, the less two-dimensional mass and momentum conservation are expected to hold. This poses a limitation to the method used here. However, it is further noted that the error for the total drag coefficient is smaller than the error from MC and pressure, indicating that the momentum and pressure terms are more influenced by the control volume boundary, while the total drag coefficient is minimally affected due to the cumulative contribution of all forces. The variation of C_d in the range of considered contours is approximately 5% to 10%, which is much smaller than the variation of C_d at the different phases of the surging motion cases (discussed later). Thus, the average C_d is used to represent the mean value of the tests.

To validate the result, measurements reported in the literature have been reviewed. Even though this airfoil profile has been widely studied, the large angle of attack case is rarely considered. Experimental load measurements can be found in Holst et al. ([105]). In their study, load measurements were conducted at AoA 90° and $Re = 1.4 \times 10^5$, from which a drag coefficient of 0.87 was computed. However, the C_d obtained from this campaign is 0.95 for a lower Re of 1.5×10^4. In the wind tunnel measurement in Chapter 3, a DU91 airfoil was tested with three different Re numbers.The results showed a slightly higher C_d at the lowest Re value of 2×10^5, compared to the other two values ($Re = 5 \times 10^5$ and $Re = 8 \times 10^5$) at AoA 90°. Thus, the effect of Re is one of the contributing factors to the difference in Cd compared with the result of Holst et al. [105]. Apart from this, both campaigns use an open jet, while two end plates were applied to the airfoil for the campaign by Holst et al. [105], whereas only one end plate was applied for this campaign. This may induce some three-dimensional effects in our campaign, where the spanwise velocity is not zero. Regarding uncertainty, the difference between the experimental measurements

by Holst et al. [105] and the integration method presented here mainly stems from (1) the uncertainty of the PIV measurements compared to the pressure measurements and (2) the uncertainty in the interpolated shadow region in the PIV data. Since uncertainties and three-dimensional effects are inevitable in this campaign, the results from the integration method are considered valid for the dynamic case measurements.

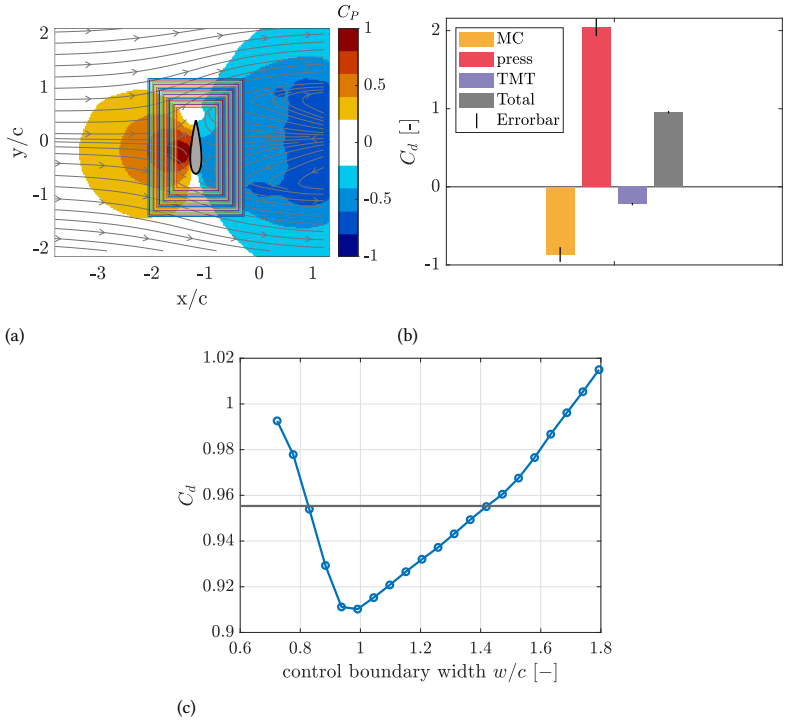

Figure 4.14: (a) Pressure field of the static blade at 3c location from the tip. The control contour outside of the airfoil in Figure 4.14a ranges from 10 dx to 30 dx from the airfoil surface, with dx = 0.027c. (b) Force contribution from mean convection (MC), pressure (press), and turbulence momentum transfer (TMT) for the static case. The errorbar height represents the uncertainty at 95% confidence level. (c) C_d as a function of control boundary length, where the black horizontal line is the mean value.

Surging cases

The load estimation method was then applied to the surging motion case. Figure 4.16a presents the C_d as a function of the motion phase, whereas Figure 4.16b presents the C_d as a function of the wing's position. For both plots, the shaded area represents the 95% confidence interval based on all the control contours tested. The control boundaries were set the same as the static case, varying such that $d_1 = d_2 = d_3 = d_4$ (illustrated in Figure 2.14), ranging from 10 dx to 30 dx with an interval of dx. The solid lines in Figure 4.16b represent the airfoil moving in the upwind direction, while the dashed curves represent the airfoil moving in the downwind direction. The grey line in both plots represents the static C_d value. As the 95% confidence interval is rather small for the static case, it cannot be seen in the plot.

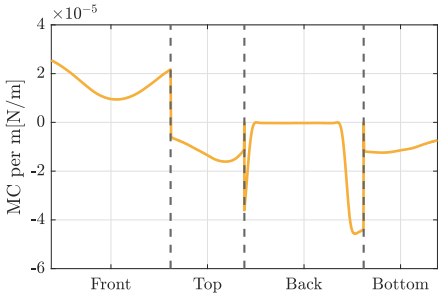

Figure 4.15: Force component from mean convention (MC) on the control contour for the static measurement. The control contour presented here has a fixed 20 dx distance from each boundary of the airfoil surface. The curves start from the bottom-left of the control contour. The dashed lines represent the boundary of the turning point in the control contour.

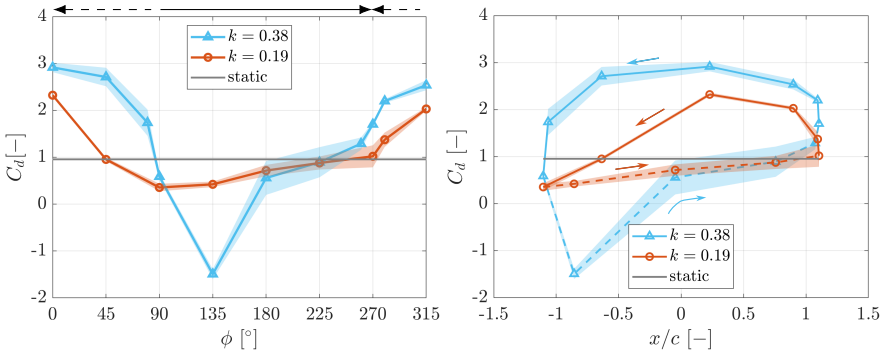

(a) (b)

Figure 4.16: Drag coefficient C_d (a) at each phase and (b) at each location. The shaded area represents 95% confidence intervals of the mean value. The horizontal line in the plot represents the static C_d. The solid horizontal arrow pointing right on top of the plot represents the downstream motion, and the dashed arrow pointing left represents the upstream motion of the airfoil. Note that the shaded area for the static case is barely visible as the value is small. Solid lines in (b) represent the airfoil moving in the upstream direction, and the dashed lines in (b) represent the airfoil moving in the downstream direction. The arrows represent the direction of the motion.

Figure 4.16a shows that the highest C_d occurs at $\phi = 0^\circ$ for both reduced frequencies. At this phase, the airfoil is at the center of the travel and is moving upstream, bringing high momentum in the direction opposite to the free-stream, thus resulting in the highest relative velocity perceived by the airfoil. In this case, the surging motion at $k = 0.38$ has 3 times the C_d compared with the static case, whereas for the $k = 0.19$ motion, the C_d is 2.4. This result emphasizes the importance of studying the wing dynamics because the wing's motion can yield force coefficients that are several times larger than the corresponding static ones.

For most of the tested phases, the drag force is positive, meaning that it is directed downstream (same direction as the free-stream velocity). However, around $\phi = 135^\circ$, C_d has a negative value, which means that the drag force is directed upwind. The force contribution in the streamwise direction from MC, press, TMT, and TD on the control contour is shown in Figure 4.17. Note that the viscous force and the body force term are not included and will not be included in the discussion, as they are relatively small compared to the rest of the force terms. At this phase, the flow field (Figure 4.8j) shows that, as the airfoil moves downwind, the downwind side still preserves the reversed flow from the previous upstream motion. As a result, the flow at the back of the airfoil potentially pushes the airfoil in the upwind direction, thus creating a considerable force towards the upwind. This leads to the substantial negative contribution from MC at the back boundary. Conversely, Figure 4.17 shows that the pressure term has a positive contribution to the total C_d. In addition, the TD term has a negative contribution to the total C_d; in fact, it can be seen from the figure that the major part of the TD curve is below zero, including the front boundary, and the parts of the top and bottom boundary which are in the upwind of the airfoil. This is because at this phase, when the airfoil is moving downstream, the flow in the upwind part of the airfoil is accelerated, as can be seen from Figure 4.8i to Figure 4.8k. At the back of the airfoil, due to the vortex shedding process (see Figure 4.9i to Figure 4.9k), the vortices are moving away from the airfoil in the crossflow direction, creating a larger area of deep reverse flow. This leads to the positive TD term at the back part of the boundary. The TMT term is almost zero in the upwind direction of the airfoil, due to the almost parallel incoming wind. It has a negative value at the top, bottom, and especially back due to the airfoil encountering reverse flow, which increases the Reynolds stresses. Therefore, by adding up all the contributions from the force, the total drag coefficient is negative despite the positive contribution from the pressure.

From a different perspective, Figure 4.16b shows the C_d hysteresis in the wing's motion loop. The kinematics highly influences the variation of C_d in a loop. The hysteresis loop has a larger amplitude difference for $k = 0.38$ compared to $k = 0.19$. This result also follows the trend from the result of Choi et al. [114], where the slender loop represents the sub-harmonic lock-in and the more round loop represents the lock-in when f/f_{st} gets close to unity. During one motion cycle, the sub-harmonic lock-in presents a flow field closer to the steady case than the higher k case. The wake vortices grow only at the downwind side of the airfoil. In contrast, for the higher frequency case ($k = 0.38$), wake vortices form on both sides of the airfoil, resulting in greater flow variability. This increased variation amplifies the hysteresis loop compared to the lower frequency case ($k = 0.19$). Specifically, when the airfoil moves in the downstream direction, it moves into its own wake. Thus, the relative wind speed is much lower than the free-stream velocity. As a result, the vortices

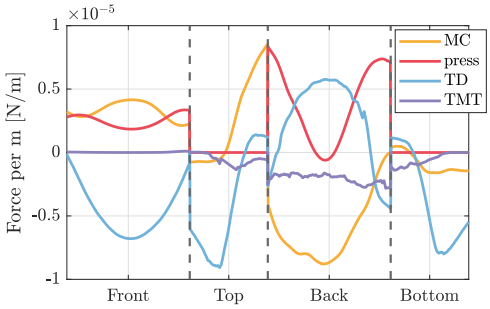

Figure 4.17: Force component from mean convention (MC), time derivative (TD), and turbulence momentum transfer (TMT) on the control contour for $\phi = 135^\circ$, $k = 0.38$ case. The control contour presented here has a fixed 20 dx distance from each boundary of the airfoil surface. The curves start from the bottom-left of the control contour as shown in Figure 2.14. The dashed lines represent the boundary of the turning point in the control contour.

4

are shed towards the upstream direction for phases from $\phi = 135^\circ$ to $\phi = 280^\circ$, leading to a high difference with the upstream motion case.

The results of the force components from time derivative (TD), mean convection (MC), turbulence momentum transfer (TMT), and pressure (press) are shown in Figure 4.18 for the two reduced frequencies. The mean viscous stress term and the body force term are not included in the bar plot as they have relatively small contributions. The error bar height represents the 95% confidence intervals from all the control contours tested. Comparing the two frequencies, the case with $k = 0.38$ exhibits a significantly higher C_d for each force component. For instance, at $\phi = 0^\circ$, both the MC and pressure terms are approximately twice as large for $k = 0.38$ compared to the $k = 0.19$ case, further confirming that the flow dynamics greatly affect the aerodynamic loads. Despite this, the periodic motion causes the force contributions to follow a distinct trend over each cycle for both motion frequencies, particularly for the MC and pressure terms. The MC term increases from $\phi = 0^\circ$ to $\phi = 180^\circ$, then decreases until the cycle's end (see Figure 4.18). In contrast, the pressure term peaks at $\phi = 0^\circ$, decreases to $\phi = 180^\circ$, and then rises again by the cycle's completion. Since both frequencies exhibit the same trend for the main force component, the force components at $\phi = 0^\circ$ and $\phi = 180^\circ$ are compared as representative cases for $k = 0.38$ only.

The MC term, pressure term, and TD term are shown in Figure 4.19. The MC term on the boundary (Figure 4.19a) reveals that at $\phi = 0^\circ$, when the airfoil is moving against the wind, a velocity deficit forms at the rear of the airfoil. In contrast, at $\phi = 180^\circ$, when the airfoil moves downwind, the accelerated velocity at the front of the airfoil (as shown in Figure 4.8k) leads to an MC deficit along the front boundary, albeit with smaller amplitude. Additionally, as the flow accelerates at $\phi = 0^\circ$ and decelerates at $\phi = 180^\circ$ along the top and bottom boundaries (see Figure 4.8e and Figure 4.8k), the MC force contributes negatively at these boundaries for $\phi = 0^\circ$ and positively for $\phi = 180^\circ$.

The pressure term in the streamwise direction (Figure 4.19b) is derived from the pressure field of the two cases shown in Figure 4.20. At the front of the airfoil, $\phi = 0^\circ$ exhibits high positive pressure on the pressure side, while at $\phi = 180^\circ$, the front serves as the suction side, resulting in a negative pressure contribution. Conversely, at the back of the airfoil,

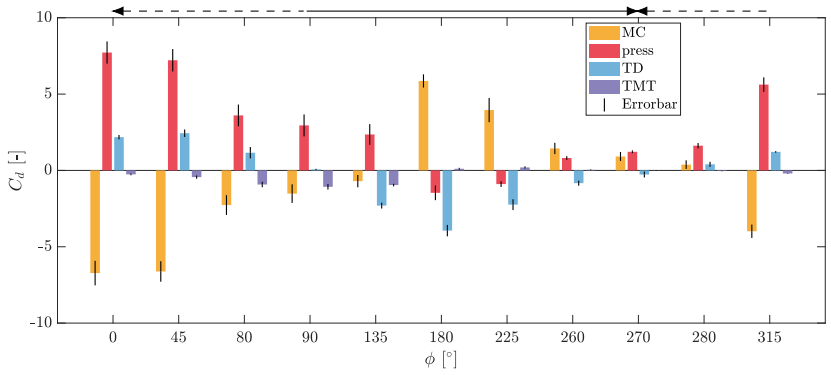

(a) k = 0.38

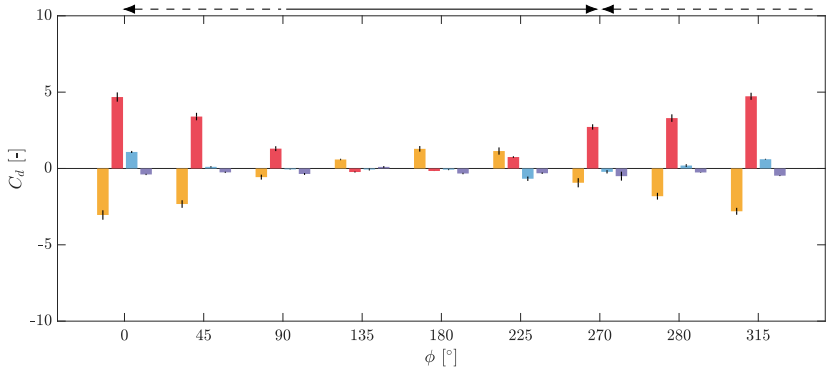

(b) k = 0.19

Figure 4.18: Aerodynamic force contribution at k = 0.19 and k = 0.38 from mean convection (MC), pressure (press), turbulent momentum transfer (TMT), and time derivative (TD). The definitions of each term are shown from Equation (2.23) to Equation (2.26). The errorbar height represents the 95% confidence intervals. The solid horizontal arrow pointing right on top of the plot represents the downstream motion, and the dashed arrow pointing left represents the upstream motion of the airfoil.

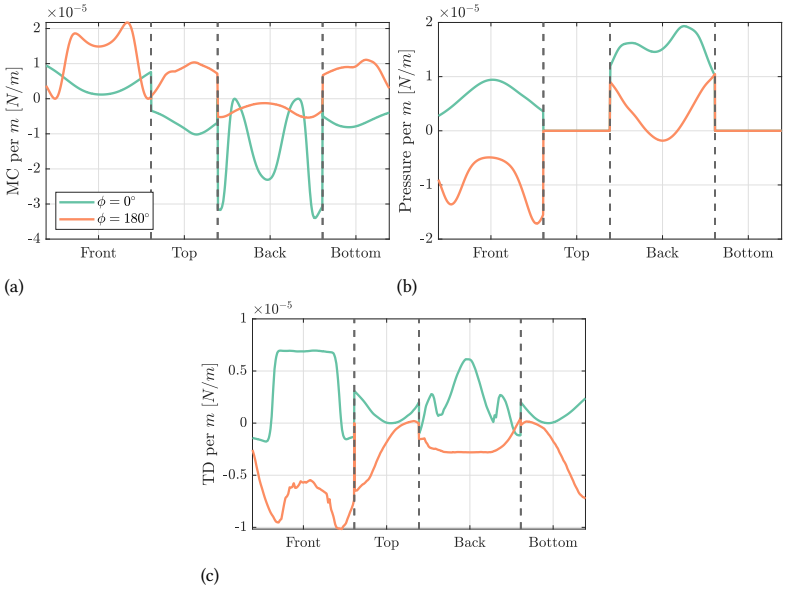

Figure 4.19: MC (a), pressure term (b), and TD term (c) in the streamwise direction in Equation (2.22) for $\phi = 0^\circ$ and $\phi = 180^\circ$ at $k = 0.38$.

$\phi = 0^\circ$ has a reverse flow region that induces negative pressure. However, this negative pressure adds to the positive pressure term due to its sign in Equation (2.22), as illustrated in Figure 4.19b. For $\phi = 180^\circ$, positive pressure is present on the airfoil surface, leading to a negative contribution in the central part of the back boundary. Although shed vortices create negative pressure, resulting in a positive contribution at the sides of the back, the overall pressure force term remains negative.

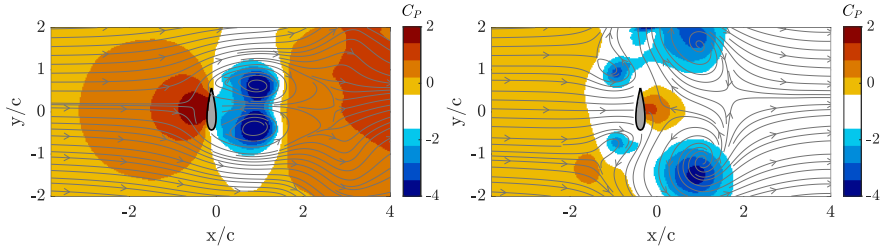

Figure 4.20: Pressure field for (a) $\phi = 0^\circ$ and (b) $\phi = 180^\circ$ at $k = 0.38$.

The TD term on the boundary, shown in Figure 4.19c, is calculated using the first term in Equation (2.22) and is obtained from its two adjacent phases. Due to the negative sign in the front, the decelerating flow from $\phi = 315^\circ$ (Figure 4.8k) to $\phi = 45^\circ$ (Figure 4.8f) in the front and wake region of the airfoil results in a positive contribution to the TD at $\phi = 0^\circ$. In contrast, the accelerating flow from $\phi = 135^\circ$ (Figure 4.8j) to $\phi = 225^\circ$ (Figure 4.8l) in the

same region leads to a negative contribution to the TD at $\phi = 180^{\circ}$. By analyzing the three most dominant force components – MC, pressure, and TD– from the two extreme motion phases, it emerges that due to the difference in the flow dynamics, the force components have opposite effects on these two phases, which results in different total C_d as shown in Figure 4.16b.

The non-dimensionalized aerodynamic power P* is shown in Figure 4.21. It is calculated as $P^* = C_d\dot{h}/(h_{max}f)$, where C_d is the drag coefficient, h_{max} is the motion amplitude, and f is the motion frequency. If P* is positive, it means the force is in the same direction as the motion, indicating that the flow does positive work on the airfoil. Conversely, if P* is negative, the aerodynamic force is acting in the opposite direction to the motion. In this case, the airfoil does positive work on the flow. This means that the flow does negative work on the airfoil in this period instead. This definition of dimensionless power is the same as that introduced in Skrzypiński et al. [28]. Before $\phi = 90^{\circ}$ and after $\phi = 280^{\circ}$, P* is below zero for both the motion cases, meaning the airfoil does work on the flow. As a consequence, this phase range is characterized by the vortex growing period, where continuous energy is fed to the vortices, which increases their strength. Between $\phi = 90^{\circ}$ and $\phi = 180^{\circ}$, instead, P* has positive values for the $k = 0.19$ motion cases, which means the airfoil extracts energy from the wind. As a result, this phase range is characterized by vortex shedding, where the flow loses energy to sustain the vortices. From $\phi = 180^{\circ}$ to $\phi = 270^{\circ}$, P* still remains positive for $k = 0.19$ motion case. In this phase range, the vortex motion is the combination of vortex shedding in a larger area in the downwind side and vortex growing in a smaller area in the closer downwind side. This means that the energy the airfoil extracts from the flow (that causes vortex shedding) is higher than the work the airfoil does on the flow (that causes vortex growing). For the $k = 0.38$ case, $\phi = 135^{\circ}$ has negative P*. The flow at this phase is composed of vortex shedding in the downwind side and vortex growing in the upwind side. On the energy level, it means that the airfoil feeds more energy to the wind for the vortex growing than extracting the energy from the wind for the vortex shedding. Afterward, at $\phi = 180^{\circ}$, P* returns to positive values again. Although the basic flow features are similar to those at $\phi = 135^{\circ}$, the key difference is that the upwind vortices at $\phi = 135^{\circ}$ are part of the start-up period. This suggests that, while the generated upwind vortices continue to grow during this phase (extracting energy from the airfoil and causing P* to decrease), the positive P* at $\phi = 180^{\circ}$ indicates that less energy is required for the vortices to grow compared to the start-up phase at $\phi = 135^{\circ}$.

Comparison with flat plat reduced order model

Because the flat plat reduced order model introduced previously (Equation (4.8)) only applies to an accelerating plate, it is applied to the surging airfoil between $\phi = 0^{\circ}$ to 90° and between $\phi = 270^{\circ}$ to 315°, where the airfoil is moving in the upstream direction. During the airfoil's motion in the downwind direction, Equation (4.10) is applied for both of the motion cases, except that for $k = 0.19$ case where there are no upstream vortices, which gives zero value for $\dot{\Gamma}_{us}d_{us}$ and $\Gamma_{us}\dot{d}_{us}$. Note that the C_d values in the $\phi = 180^{\circ}$ and $\phi = 225^{\circ}$ cases are not calculated due to the missing information of vortex distance ($\phi = 180^{\circ}$) and circulation ($\phi = 225^{\circ}$), as at least one of the vortices exits the measurement domain. Also, because of the missing information of vortex distance at $\phi = 180^{\circ}$, the vortex separation velocity $\dot{d}$ at $\phi = 135^{\circ}$ is obtained based on the backward differentiation only, contrary to the other cases where central differentiation was applied. The final result is shown

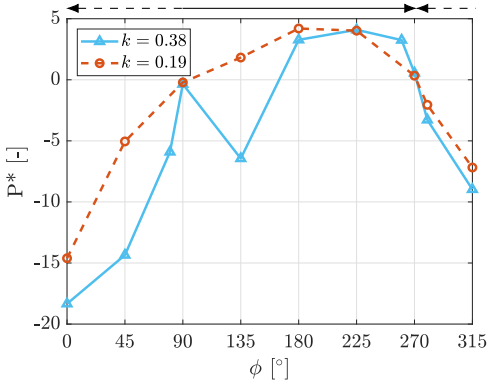

Figure 4.21: Non-dimensional aerodynamic power P* in a cycle. P* is calculated as: P* = $C_d\dot{h}/(h_{max}f)$, where C_d is the drag coefficient, h_{max} is the motion amplitude and f is the motion frequency. The solid horizontal arrow pointing right on top of the plot represents the downstream motion, and the dashed arrow pointing left represents the upstream motion of the airfoil.

in Figure 4.22, where the results from the flat plate model (FP) are marked as green and yellow crosses for k = 0.38 and k = 0.19, respectively. Due to the limitation of the field of view, Equation (4.10) is only applied for ϕ = 135° and 180°. For ϕ = 180°, the $\dot{\Gamma}$ term in Equation (4.10) is modified from the experimental result as the vortices at ϕ = 225° are not fully inside the FoV. Therefore, based on the portion of vortices outside the FoV as shown in Figure 4.9l, a 33% (0.2 m^2/s in absolute value) increase of Γ is applied to the circulation of ϕ = 225°. Note that the endpoint of ϕ = 90° is removed from the discussion for the two motion cases, as it may cause large errors in the time derivative term. The result shows a good match for the two phases of ϕ = 135° and 180° when the airfoil is moving downstream at k = 0.38. For ϕ = 135°, k = 0.19 case, the flat plate model result is higher than the experiment. On the one hand, this difference is caused by the accuracy of the two differential methods, where the backward differential method used for the ϕ = 135°, k = 0.19 case has lower accuracy. On the other hand, by assuming zero value for $\dot{\Gamma}_{us}d_{us}$ and $\Gamma_{us}\dot{d}_{us}$, it is assumed that the downwind wake flow has no impact on the airfoil. However, even though no upwind vortices are generated, the downwind flow pushes the downwind vortices to separate. Therefore, this effect is not reflected in the model for this specific case. When the airfoil moves upstream, the FP model result matches better for k = 0.19 than for the k = 0.38 case. For the k = 0.38 case, the most significant error appears at ϕ = 45° and 90°. As shown in Figure 4.2a, the airfoil decelerates at ϕ = 45°, different from the overall accelerating trend during surging between ϕ = 0° and 90°. Due to this disturbance, it is speculated that the sum of the force from circulatory (Equation (4.7)) and non-circulatory terms (Equation (4.4)) cannot correctly represent the drag force. Overall, the modified model (Equation (4.10)) correctly reproduces the trend of the experimental results for most of the phases.

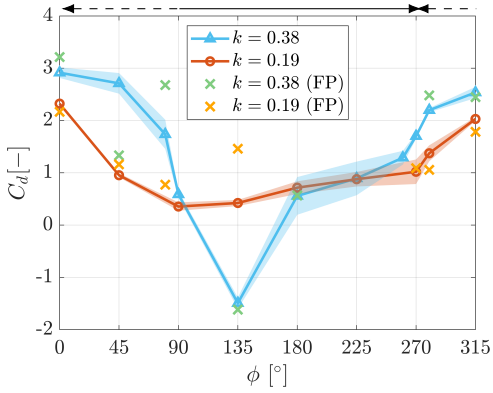

Figure 4.22: Drag coefficient from control contour approach (Equation (2.22)) and from the modified flat plate (FP) model (Equation (4.10)). The solid horizontal arrow pointing right on top of the plot represents the downstream motion, and the dashed arrow pointing left represents the upstream motion of the airfoil.

4.4 Conclusion

The development of vortex structures in the wake of a periodically surging NACA 0021 airfoil at 90° angles of attack has been studied experimentally at Reynolds number 1.5×10^4. The motion amplitude is fixed at 1.1 times the chord length (with peak-to-peak amplitude 2.2 times the chord length). Two motion frequencies were investigated: one with reduced frequency $k = 0.19$ and frequency ratio with respect to the static vortex shedding frequency $f/f_{st} = 0.39$; the other one with reduced frequency $k = 0.38$ and $f/f_{st} = 0.78$. Through the comparison of the two motion cases, the results focus on the vortex dynamics in a motion cycle, the total drag force, and the contributions from each component of the force.

The comparison of the two motion cases ($k = 0.19$ and $k = 0.38$) reveals significant differences in the vortex structures. For the $k = 0.38$ motion case, the vortices generate in the wake during the surging motion in the upwind direction. Conversely, at the beginning of the motion in the downwind direction, a pair of vortices starts to accumulate at the upwind side. During this period, as the airfoil is moving in its own wake generated during the upwind motion, the wing's velocity is higher than the incoming flow velocity. At the end of the downwind motion, the two pairs of vortices shed simultaneously away from the airfoil. This contrasts with the $k = 0.19$ case, where the vortices are confined to the downstream side of the airfoil throughout the motion cycle. The vortices tend to be more elongated and dissipate because of turbulence.

Furthermore, this study provides clear experimental evidence of the lock-in phenomenon in both motion cases. For the $k = 0.38$ case, one pair of wake vortices and one pair of upwind vortices grow at different phases within a cycle, but shed simultaneously. For the $k = 0.19$ case, one pair of wake vortices grows and sheds within a cycle. The $k = 0.38$ case aligns with the result of previous work from Koopmann [106], Anagnostopoulos [107], and Meneghini and Bearman [108]: as the motion frequency is very close to the static shedding frequency, lock-in happens. For the latter case, the motion frequency is far from the static shedding frequency, but lock-in still happens due to the large motion amplitude. This finding aligns with and extends previous work, such as that by Choi et al.

[114], demonstrating that lock-in can happen at the sub-harmonics of the static shedding frequency, but with large amplitude.

The load estimation method was tested out on the static measurement of the airfoil, which shows fair comparison with the experimental measurement from Holst et al. [115]. Then, this method is applied to the surging airfoil to obtain the force on each phase of the motion. Both of the motion cases show that the total drag force is predominantly influenced by the mean convection force and the pressure force, and it is mainly the balance between the two that influences the trend of the total drag force. For the $k = 0.19$ case, drag is always in the same direction as the wind speed, as the wake is always occurring at the downstream side of the airfoil. For the $k = 0.38$ case, the highest drag coefficient within a cycle is around three times higher than the static case. A notable finding at this k is the occurrence of negative drag at $\phi = 135^{\circ}$ where the airfoil is moving downstream. This is because at this phase, as the pressure force gives a positive contribution to the airfoil and points downstream, the mean convection force provides a larger negative deficit on the airfoil due to the preserved reversed flow in the front of the motion direction. In addition, in agreement with the result from Choi et al. [114], the drag coefficient plot with respect to location suggests a larger force difference for the $k = 0.38$ case.

Finally, the load estimated from the experiment was compared with the reduced-order flat plate load model (Corkery et al. [111]). The original model correctly predicts the trend and fits well with the experimental data when the airfoil is moving in the upstream direction and the wake is generated in the downstream direction. The model was further refined by summing up the circulatory force from all the vortex pairs to account for the two-pair vortices condition during the downstream motion of the $k = 0.38$ case, leading to improved agreement with the experimental data.

5

Plunge motions: lock-in effect and load variations

Chapter 4 investigates the flow physics, vortex dynamics, and lock-in effect of a plunging airfoil at a 90° *angle of attack. This orientation was chosen to represent the flapwise vibrations of a wind turbine blade during VIV. In this chapter, the airfoil is forced to plunge periodically in the crossflow direction, mimicking the edgewise vibrations of a wind turbine blade under VIV. The analysis similarly focuses on the flow physics, vortex dynamics, and lock-in behavior. Compared with the surging case, the results show that, due to the varying effective angle of attack, frequency lock-in in a plunging airfoil is more sensitive to the motion frequency. This chapter contributes to the understanding of the lock-in phenomenon by demonstrating that, while motion frequency strongly influences the occurrence of lock-in, the kinematics of the motion, specifically whether it promotes coherent vortex structures, are equally critical.*

This chapter is based on
G. Xu, A. Sciacchitano, C. Simão Ferreira, W. Yu, *Unsteady aerodynamics of a plunging airfoil at large angles of attack*, Experiments in Fluids, *accepted.*

5.1 Introduction

The VIV simulation results from Pirrung et al. [17] indicate that when a rotor is subjected to 80° pitch and 90° yaw, VIV can trigger flapwise or edgewise vibrations on different blades on a rotor. Similar to the surging motion discussed in Chapter 4, few studies have examined a plunging airfoil under large-angle-of-attack conditions. The fundamental understanding in this area remains incomplete, despite its significance for predicting and mitigating unsteady loading, deep dynamic stall (due to changes in the angle of attack), and associated fatigue damage in VIV conditions.

Building on the insights gained from the previously discussed surging airfoil experiments, wind tunnel measurements were conducted on a plunging airfoil operating at large angles of attack. In this configuration, the airfoil is oriented perpendicular to the incoming wind and oscillates in the crosswind direction. This chapter presents the results of this experimental campaign, focusing on the unsteady vortex dynamics and corresponding aerodynamic forces generated during the plunging motion. By directly comparing these findings with the surging cases, the study seeks to reveal how different motion directions influence vortex formation, shedding mechanisms, force variations, and the lock-in effect under extreme conditions. Such comparisons provide not only a deeper understanding of unsteady aerodynamic behavior at large angles of attack but also valuable guidance for future refining of numerical models of rotor performance under VIV conditions and structural loading in real-world environments.

5.2 Methodology

5.2.1 Experimental setup

This experiment shares the same wind tunnel setup, wing model, reduced frequency, motion amplitude, and PIV measurement equipment as the experiment discussed in Chapter 4. The PIV setup is shown in Figure 5.1. The primary difference lies in the orientation of the slider–crank mechanism (marked by the dashed rectangle in the left panel of Figure 5.1). For the plunging motion considered here, the mechanism is mounted vertically to generate the desired cross-flow motion (Figure 1.8), whereas in the surging configuration, it was oriented horizontally. The key parameters for the PIV setup are listed in Table 5.1.

The key experimental parameters are summarized in Table 5.2. It is worth mentioning that in this experiment, the angle of attack AoA_g is defined as the angle between the incoming wind and the airfoil chord line, which is always 90° for both the plunging motion (the present study) and the surging motion Chapter 4. However, the effective angle of attack AoA, which is the angle between the chord line and the relative wind speed (composed of the incoming wind and the perceived wind speed in the crossflow direction) is different for the plunging case, which will be discussed in Section 5.2.2.

5.2.2 Motion kinematics

The wing's motion kinematics are shown in Figure 5.2a, where the wing's actual motion amplitude h is obtained by physically tracking the airfoil leading edge position from the phase-averaged PIV images. The velocity $\dot{h}$ and acceleration $\ddot{h}$ of the motion were obtained by taking temporal derivatives of the fitted wing position data ($h = 0.0616 \sin(\phi - 5.7) + 0.015$, the dashed line with the cross markers in the top figure in Figure 5.2a). The airfoil relative

Table 5.1: Summary of stereoscopic phase-locked PIV setup and parameters.

Category	Parameter	Specification / Description
Seeding	Tracer particle	Water–glycol droplets generated by SAFEX smoke generator
	Particle size	Median diameter ≈ 1 μm
Illumination	Laser type	Quantel Evergreen Nd:YAG, double-pulse system
	Pulse energy	200 mJ per pulse
	Wavelength	532 nm (green)
	Field of View (FoV)	269.4 × 331.8 mm (≈ $3.6c \times 4.4c$), extended to $8c \times 4.2c$ by traversing
Imaging	Camera model	LaVision Imager sCMOS (2 units)
	Sensor size	2560 × 2160 pixels
	Pixel pitch	6.5 × 6.5 μm
	Time separation (Δt)	417 μs between image of a pair
	Sampling frequency	2.5 Hz and 5 Hz (equal to motion frequency)
	Method	Phase-locked (realized by optical encoder)
	No. image pairs	200 per phase
	No. phases	12 per plunging cycle
Optics	Lens focal length	105 mm (Nikon)
	Numerical aperture (f/#)	f/8
	Measurement plane	Located at $3c$ from the wing tip
Data Processing	Interrogation window	32 × 32 pixels (3.37 mm ×4.92 mm)
	Overlap factor	75%
	Vector pitch	≈ 1.0 mm

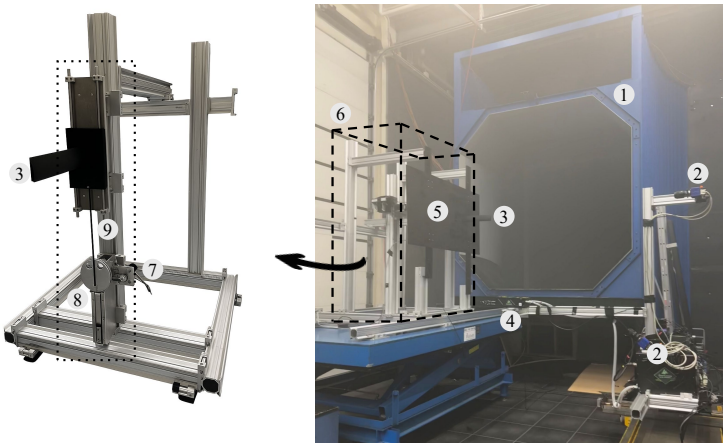

5

Figure 5.1: Experimental setup in the OJF. The relevant components are: 1. Flow outlet 2. LaVision Imager sCMOS camera 3. Wing model 4. Quantel Evergreen Nd:YAG laser 5. Base plate 6. Beam structure (including the slider-crank mechanism) 7. Motor 8. Turning wheel 9. Rod for straight motion.

Table 5.2: Experimental parameters.

Parameter	Symbol	Value
Freestream velocity	U_∞	3.1 m/s
Model chord	c	0.075 m
Reynolds number	Re	1.5×10^4
Static vortex shedding frequency at AoA = 90°	$f_{st,90}$	6.4 Hz
Geometric angle of attack	AoA_g	90°
Model span	s	0.4 m
Model aspect ratio	AR	5.33
Motion frequency	f	2.5 Hz, 5 Hz
Reduced frequency	k	0.19, 0.38
Frequency ratio	$f/f_{st,90}$	0.39, 0.78
Motion amplitude	h_{max}	0.083 m (1.1c)

location at three intermediate phases of 0°, 90°, and 270° is shown in Figure 5.2b. The origin is located at the plunging axis; at $\phi = 0°$, the leading edge is located at $y = -0.78c$, and the trailing edge is located at $y = 0.22c$.

Compared to a surging motion, where the wing moves in the same direction as the wind, which does not change the effective angle of attack at 90°, a plunging wing experiences a varying effective angle of attack, even though its physical orientation remains at 90° ($\text{AoA}_g = 90°$). As shown in Figure 5.3, the effective angle of attack (AoA) is determined by the combination of the freestream velocity (U_∞) and the velocity component induced by the airfoil' s vertical motion ($\dot{h}$), which acts in the opposite direction to the motion in

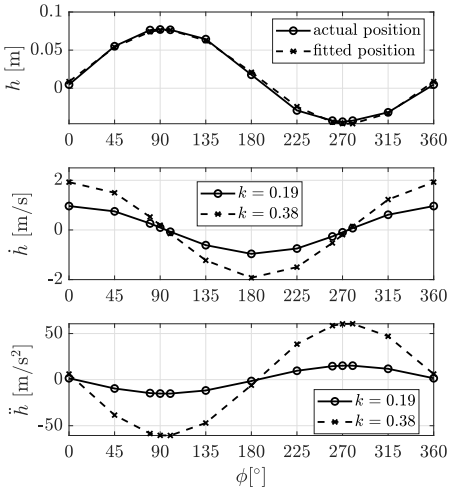

(a) The actual motion amplitude (h) based on the leading edge of the airfoil, velocity ($\dot{h}$), and acceleration ($\ddot{h}$) of the plunging motion for two motion frequencies. Note that the lines for h overlap each other since two cases have the same travel distance.

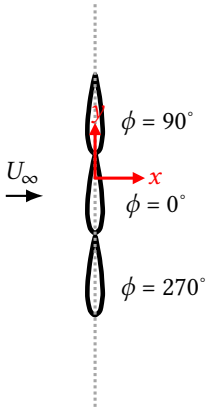

(b) The relative locations of the airfoil at three different phases: $\phi = 0^\circ$, where the wing is near the center of its trajectory, $\phi = 90^\circ$, and $\phi = 270^\circ$, where it is in the most top and bottom positions, respectively.

Figure 5.2: Motion kinematics of the plunging airfoil.

the crossflow:

$$\text{AoA} = \begin{cases} \arctan\left(\dfrac{U_\infty}{|\dot{h}|}\right), & \text{if } \dot{h} \le 0, \\ \arctan\left(\dfrac{\dot{h}}{U_\infty}\right) + 90^\circ, & \text{if } \dot{h} > 0. \end{cases} \tag{5.1}$$

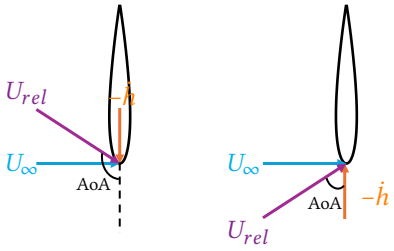

Figure 5.3: Illustration of the effective angle of attack AoA during upstroke (left) and downstroke (right). U_{rel} represents the relative velocity experienced by the airfoil.

The effective angle of attack within a plunging cycle is plotted in Figure 5.4 for both motion cases. For $k = 0.38$ case, the variation of AoA is larger, ranging from approximately 58° to 122°, while that for $k = 0.19$ is between 73° and 108°. Note that due to the varying angle of attack, the frequency ratio listed in Table 5.2 is the ratio between the motion

frequency and static vortex shedding frequency at 90° angles of attack, where the latter was obtained through the POD analysis as discussed in Chapter 4.

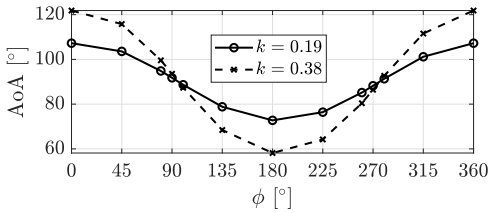

Figure 5.4: The effective angle of attack at different phases for two motion cases.

5.2.3 Airfoil wake topology

Due to the varying effective angle of attack, the wake exhibits a periodic skewness during the plunging cycle. To quantify this behavior, the wake skew angle is defined in two steps.

First, the center of the wake at each streamwise location, $y_w(x)$, is determined using the center-of-mass method, which has also been applied in wind turbine wake studies [116, 117]. For discrete experimental measurements, $y_w(x)$ is expressed as

$$y_w(x) = \frac{\int_{\Omega(x)} y\left[U_\infty - \bar{u}(x,y)\right] dy}{\int_{\Omega(x)} \left[U_\infty - \bar{u}(x,y)\right] dy}, \tag{5.2}$$

where $\Delta U(x,y) = U_\infty - \bar{u}(x,y)$ with $\bar{u}(x,y) \leq U_\infty$. Thus, $y_w(x)$ is obtained through discrete integration in the cross-flow direction y, considering only regions where $\bar{u}(x,y) \leq U_\infty$.

where $\Omega(x) = \{\, y : \bar{u}(x,y) \leq U_\infty \,\}$ and $\bar{u}(x,y)$ is the time-averaged flow velocity, meaning the y region is limited to the wake of the airfoil. For the discrete experimental measurement, the integrals in Equation (5.2) are computed by summing the velocity difference $(U_\infty - \bar{u}(x,y))$ (or the product of the y-location and the velocity difference) over the PIV grid points within $\Omega(x)$.

Next, the local wake skew angle (in degrees) is calculated as

$$\gamma(x_i) = \arctan\left(\frac{\Delta y_w}{\Delta x}\right) = \arctan\left(\frac{y_w(x_{i+1}) - y_w(x_i)}{x_{i+1} - x_i}\right) \tag{5.3}$$

In this study, $\gamma = 0°$ corresponds to a wake aligned with the free-stream velocity U_∞. A positive skew angle ($\gamma > 0$) indicates an upward deflection of the wake, while a negative skew angle ($\gamma < 0$) corresponds to a downward deflection.

5.2.4 Load estimation from PIV results

The aerodynamic load during the plunging motion is estimated from the PIV flow field using the method described in Section 2.4.2. An arbitrarily selected rectangular control boundary, similar to that illustrated in Figure 2.14, is employed for the control-volume

analysis. For each frequency case, a total of 14 different control boundaries are considered to compute ensemble-averaged quantities and their associated uncertainties. The boundary dimensions are varied such that $d_1 = d_2 = d_3 = d_4$, with values ranging from $10, dx$ to $23, dx$ in increments of dx, where $dx = 0.027c$ denotes the vector spacing within the measured FoV.

In order to make a fair comparison of the aerodynamic load between the plunging motion (the present study) and the surging motion (Chapter 4), the control boundaries for the force integration should have the same range. Note that for the surging cases discussed in Chapter 4, $d_1 = d_2 = d_3 = d_4$, ranging from 10 dx to 30 dx. However, due to the limitation of the FoV in the crossflow direction, the control boundary for the plunging case cannot reach more than 23 dx. Therefore, for the result of the surging cases, the same control boundaries as the plunging cases are set ($d_1 = d_2 = d_3 = d_4$, ranging from $10\,dx$ to $23\,dx$ with an interval of dx).

5.3 Results and discussion

5.3.1 Vortex dynamics and vorticity

The low frequency case: $k = 0.19$

The streamwise velocity fields at different measured phases are shown in Figure 5.5 for the $k = 0.19$ ($f/f_{st,90} = 0.39$) case. The phases are shown in the order of trailing edge vortex (TEV) formation and shedding. The wake centers are calculated using Eq. 5.2 and Eq. 5.3 and are plotted with a black circled line, with the calculation starting at $x/c = 0.1$ and extending up to $x/c = 3$. Compared to the static measurement as shown in Figure 4.5, the velocity fields at each measurement phase show high similarities: a suction region is generated downstream of the airfoil (highest suction centered between $x/c = 1$ to 3 for this plunging case) while accelerated flow is formed downwind of the airfoil outside of the wake region (shown as deeper red color in Figure 5.5). The plunging case at $k = 0.19$ shows higher flow velocity in this region than the static case because the airfoil's vertical motion increases the local relative flow speed near the airfoil. The wake skew angle distribution is shown in Figure 5.6a for the $k = 0.19$ case. For each phase, γ remains nearly constant up to $x/c \approx 2$. Beyond this point, noticeable variations occur, especially at $\phi = 80 - 135^\circ$ and 225°, where the standard deviation reaches up to $\pm 15.9^\circ$ (at $\phi = 100^\circ$) within the $3c$ downstream position. This high variation is closely associated with the high crossflow aerodynamic force (not shown here) during these phases, which is caused by asymmetric vortex shedding and wake deformation. The vortex dynamics are discussed in the following paragraphs.

The spanwise vorticity contour at $k = 0.19$, as shown in Figure 5.7, exhibits the evolution of the vortices in the plunging cycle. The phases also follow the order of the TEV formation and shedding. The cycle starts from $\phi = 180^\circ$, where the airfoil is near the center of the travel and moving down. The starting vortex at the trailing edge is established, and its non-dimensionalized circulation $\frac{\Gamma}{U_\infty c}$ is -1.94, as shown in Figure 5.8. As the airfoil plunged down to $\phi = 225^\circ$ (Figure 5.7b), 260° (Figure 5.7c), and 270° (the lowest location, Figure 5.7d), the vortex grows and the magnitude of Γ increases steadily, where $\frac{\Gamma}{U_\infty c}$ reaches -3.0 at $\phi = 270^\circ$. Subsequently, as the airfoil begins its upward motion, the wake gradually

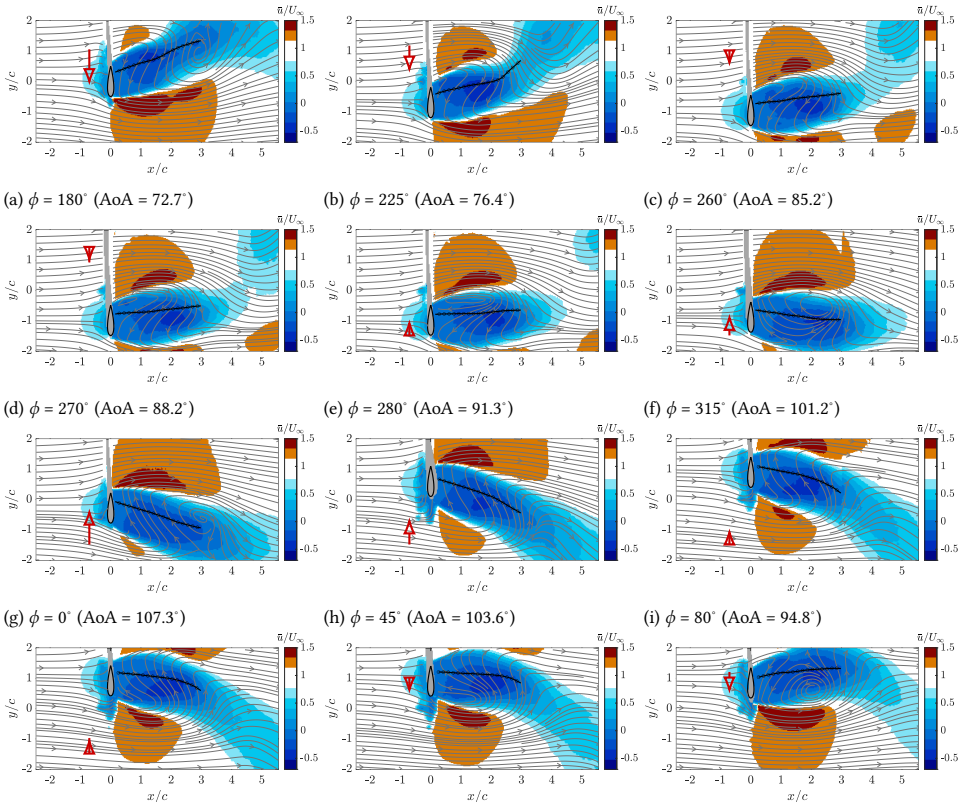

(a) ϕ = 180° (AoA = 72.7°) (b) ϕ = 225° (AoA = 76.4°) (c) ϕ = 260° (AoA = 85.2°)

(d) ϕ = 270° (AoA = 88.2°) (e) ϕ = 280° (AoA = 91.3°) (f) ϕ = 315° (AoA = 101.2°)

(g) ϕ = 0° (AoA = 107.3°) (h) ϕ = 45° (AoA = 103.6°) (i) ϕ = 80° (AoA = 94.8°)

(j) ϕ = 90° (AoA = 91.8°) (k) ϕ = 100° (AoA = 88.7°) (l) ϕ = 135° (AoA = 78.8°)

Figure 5.5: Streamwise velocity field $\bar{u}/U_\infty$ for k = 0.19 plunging case at all measured phases. The red arrow represents the scaled motion velocity $\dot{h}$. The wake center line is marked by the black circled line.

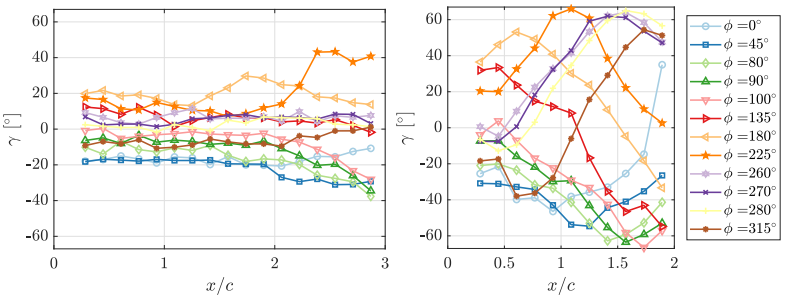

(a) k = 0.19 (b) k = 0.38

Figure 5.6: Wake skew angle distribution γ at different phases.

reorients from being directed upward (e.g., averaged $\gamma \approx 21^\circ$ at $\phi = 180^\circ$) to nearly parallel to the inflow at $\phi = 280^\circ$ (Figure 5.7e, $\gamma \approx 2.8^\circ$) and $\phi = 315^\circ$ (Figure 5.7f, $\gamma \approx -6.3^\circ$), to being directed downward at $\phi = 0^\circ$ (Figure 5.7g, $\gamma \approx -17.0^\circ$) and $\phi = 45^\circ$ (Figure 5.7h, $\gamma \approx -22^\circ$). During this period from $\phi = 270^\circ$ to $\phi = 315^\circ$, the TEV circulation magnitude continues to increase, fed by the boundary layer, while the TEV adopts a more diffused structure. However, when the airfoil reaches $\phi = 80^\circ$ (Figure 5.7i), the elongated TEV exhibits a discontinuity. The portion of the TEV located upstream of $x/c \approx 2$ follows the airfoil motion closely and is oriented with a small γ of approximately $\approx -10.0^\circ$. In contrast, in the region of $x/c > 2$, a smaller γ of lower than -20° is shown in Figure 5.6a, meaning the rear part of the wake is skewed more downward. The rear portion of the TEV, located downstream of $x/c \approx 2$, remains almost stationary and lies below $y/c \approx 1$. At this phase, the airfoil' s vertical velocity is relatively small ($\dot{h} = 0.5$ m/s), while its acceleration is significant ($\ddot{h} = -58.5$ m/s^2). Consequently, the rear portion of the TEV, located downstream of $x/c \approx 2$, does not immediately follow the airfoil motion. The fluid responds slowly to the changing flow due to the inertia, causing it to lag behind the upstream portion; this lag manifests as a larger negative skew angle ($\gamma < -20^\circ$) and keeps the rear TEV nearly stationary below $y/c \approx 1$. When the airfoil moves up to $\phi = 90^\circ$ (the highest point, Figure 5.7j) and then down to $\phi = 100^\circ$ (Figure 5.7k) and $\phi = 135^\circ$ (Figure 5.7l), the airfoil changes its motion direction with high acceleration (as shown in Figure 5.2a), the part of the TEV with $x/c > 2$ could not maintain its motion with the airfoil and starts to separate from the trailing edge, and convects into the wake at $\phi = 135^\circ$ (marked in Figure 5.7l). At $\phi = 180^\circ$, traces of the separated vortex (the medium blue colors) of the TEV between $x/c = 3$ and 5 are shown, where in the front ($x/c < 2$) the new cycle begins.

On the contrary, the leading edge vortex (LEV) exhibits a different timing in its formation and shedding during the plunging motion at $k = 0.19$. Interestingly, the LEV separation occurs twice during one plunging cycle. The first one happens from $\phi = 225^\circ$ (Figure 5.7b, with the separated LEV marked by the red dashed circle) to 260° (Figure 5.7c), where $\frac{\Gamma}{U_\infty c}$ decreases from 4.6 to 2.7, as shown in Figure 5.8. This LEV separation is followed by the TEV separation from the previous phases from $\phi = 135^\circ$ (Figure 5.7l) to 180° (Figure 5.7a), which results in the formation of a separated vortex pair. Meanwhile, it is also observed that between $\phi = 315^\circ$ (Figure 5.7f), $\phi = 0^\circ$ (Figure 5.7g), and $\phi = 45^\circ$ (Figure 5.7h), the LEV evolves from extending to approximately $x/c = 4.5$ at $\phi = 315^\circ$, to exhibiting a discontinuity near $x/c = 3$ at $\phi = 0^\circ$, and finally to forming a shorter structure terminating before $x/c = 3$ at $\phi = 45^\circ$. Although the FoV is insufficient to directly capture the complete shedding process, these observations provide strong evidence that the LEV undergoes separation during this interval: it is shown that among the three phases ($\phi = 260^\circ$ to 280°), the LEV continues to accumulate circulation, and the LEV elongates in the streamwise direction. Due to the change in airfoil motion direction from $\phi = 270^\circ$ to $\phi = 280^\circ$ and $\phi = 315^\circ$, the wake changes its averaged skew angle (before $x/c = 2$) from 4.8° to 2.3°, and -8.2° (tilting down). This change causes the LEV to stretch from an upward-pointing orientation to a downward-pointing one (marked by the dashed arrows in the plots). At the same time, when the airfoil advances to $\phi = 0^\circ$ (near the center of travel, moving upward), the TEV grows in size and dissipates to a larger area into the wake region, with the lowest point of y/c near $x/c = 3$. The induced velocity from the expanding TEV modifies the local pressure distribution around the LEV, eventually contributing to

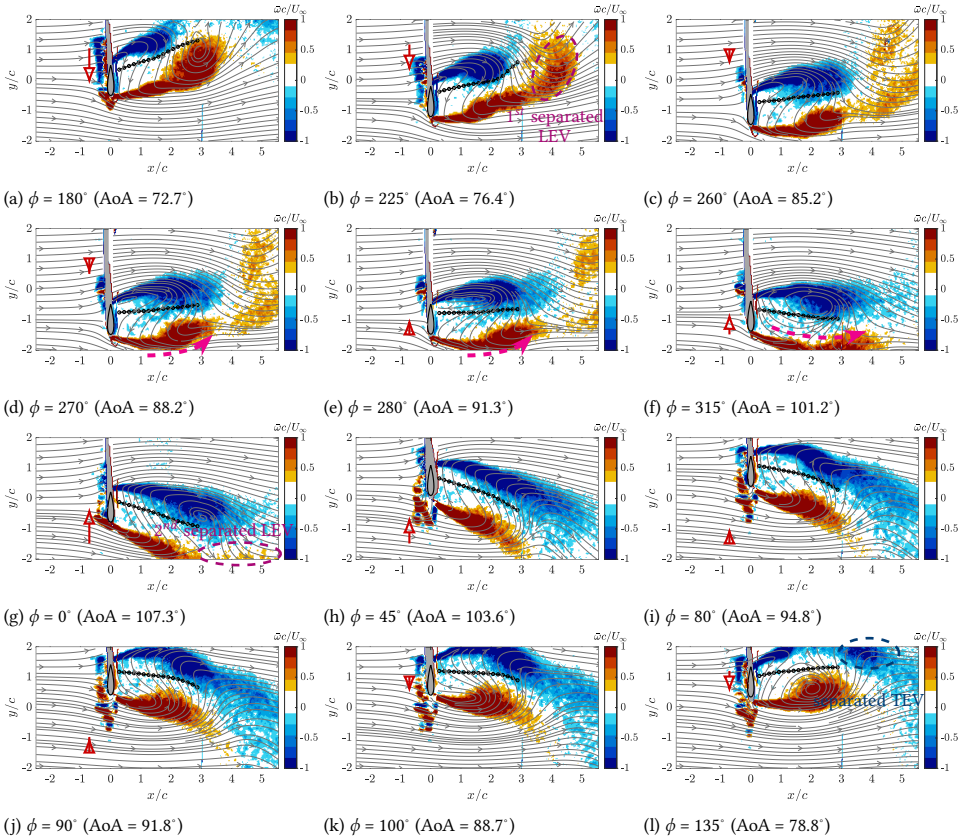

(a) ϕ = 180° (AoA = 72.7°) (b) ϕ = 225° (AoA = 76.4°) (c) ϕ = 260° (AoA = 85.2°)

(d) ϕ = 270° (AoA = 88.2°) (e) ϕ = 280° (AoA = 91.3°) (f) ϕ = 315° (AoA = 101.2°)

(g) ϕ = 0° (AoA = 107.3°) (h) ϕ = 45° (AoA = 103.6°) (i) ϕ = 80° (AoA = 94.8°)

(j) ϕ = 90° (AoA = 91.8°) (k) ϕ = 100° (AoA = 88.7°) (l) ϕ = 135° (AoA = 78.8°)

Figure 5.7: Contours of the phase-averaged spanwise vorticity component superimposed with streamlines. Vortex identified using Γ_1 method for the $k = 0.19$ surging case. The red arrow represents the scaled motion velocity $\dot{h}$. The wake center line is marked by the black circled line.

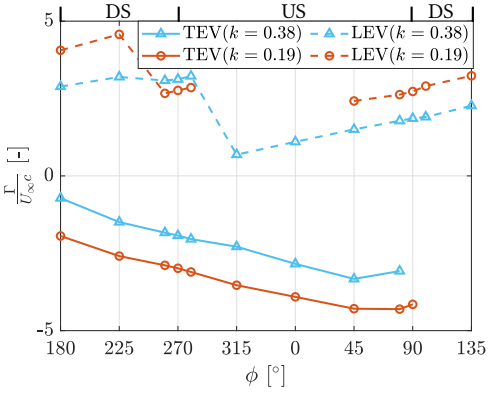

Figure 5.8: Non-dimensionalized circulation $\frac{\Gamma}{U_\infty c}$ of the LEV and TEV at different phases in a cycle. The upstroke (US) and downstroke (DS) periods are marked on top of the figures with US defined as the wing moving up and DS as the wing moving down.

its detachment. As a result, this LEV separation occurs at the part of the LEV of approximately $x/c = 3$. After this process, the TEV develops further (with $\frac{\Gamma}{U_\infty c}$ decreasing to −4.3), as illustrated at $\phi = 45^\circ$ (Figure 5.7h).

Therefore, during a plunging cycle at $k = 0.19$, the airfoil exhibits periodic vortex shedding characterized by two distinct events: a primary vortex pair (one LEV and one TEV) separates from the front part during the downstroke, followed by an additional LEV separation during the upstroke. During this second event, the TEV continues to grow, fed by the separating boundary layer rather than shedding into the wake. This behavior indicates that at this reduced frequency and frequency ratio ($f/f_{st,90} = 0.39$), vortex shedding follows a more complex mechanism instead of locking into the motion frequency. This result contrasts with the surging case at the same k reported in Chapter 4, where lock-in occurs. In surging motion, the purely streamwise oscillation modulates only the effective velocity amplitude while maintaining a constant angle of attack, preserving flow symmetry and enabling synchronization between vortex shedding and motion. In contrast, plunging motion introduces a transverse velocity component that causes a time-varying effective angle of attack (see Figure 5.4). The resulting flow asymmetry leads to complex vortex dynamics and multiple separation events per cycle, including the additional LEV separation observed here. Furthermore, based on previous studies (Figure 1.4), $f/f_{st,90} = 0.39$ lies in a regime where lock-in is less likely compared to higher f/f_{st} values (close to 1). Consequently, while the surging case exhibits subharmonic lock-in, this phenomenon fails to emerge in the plunging case due to the inherent flow asymmetry and continuous variation in the effective angle of attack.

The high frequency case: $k = 0.38$

The velocity contour for $k = 0.38$ ($f/f_{st,90} = 0.78$) case is shown in Figure 5.9. The wake centers are plotted using a black circled line, with the calculation starting at $x/c = 0.1$ and extending up to $x/c = 2$. The streamwise velocity field exhibits a different wake characteristic compared to the $k = 0.19$ case. A notable difference lies in the spatial difference of velocity magnitudes. For $k = 0.38$, the wake velocity peaks in the immediate near-wake region (approximately within $1c$ downstream), while for $k = 0.19$, the high-magnitude region extends further up to approximately $4c$ from the airfoil. This difference arises from the larger variation in motion velocity and AoA at $k = 0.38$. The corresponding high oscillation frequency shortens the streamwise wavelength of the vortex structures, effectively confining them to a shorter region downstream. This manifests as a concentrated near-wake local velocity gradient. Conversely, the milder AoA variations at $k = 0.19$ allow vortices to convect further downstream, resulting in a larger area of reverse flow region and a more elongated wake.

In addition, at the higher frequency ($k = 0.38$), the wake displays a wavier pattern with discontinuous structures in the near-wake region ($x/c \approx 1.8$), as evident from Figure 5.9c to Figure 5.9e. The wake skew angles γ at $k = 0.38$ are plotted in Figure 5.6b for their streamwise distribution. It shows much higher overall variations between −66° to 66° within a shorter x/c range of 0 to 2, while that for $k = 0.19$ is confined between −40° and 50° over a longer wake extent of 0 to 3. For each phase, the variations of the wake skew angle are substantially higher compared to the $k = 0.19$ case. The highest variation at the high frequency case occurs at $\phi = 315^\circ$ with the standard deviation of ±33.8°, which

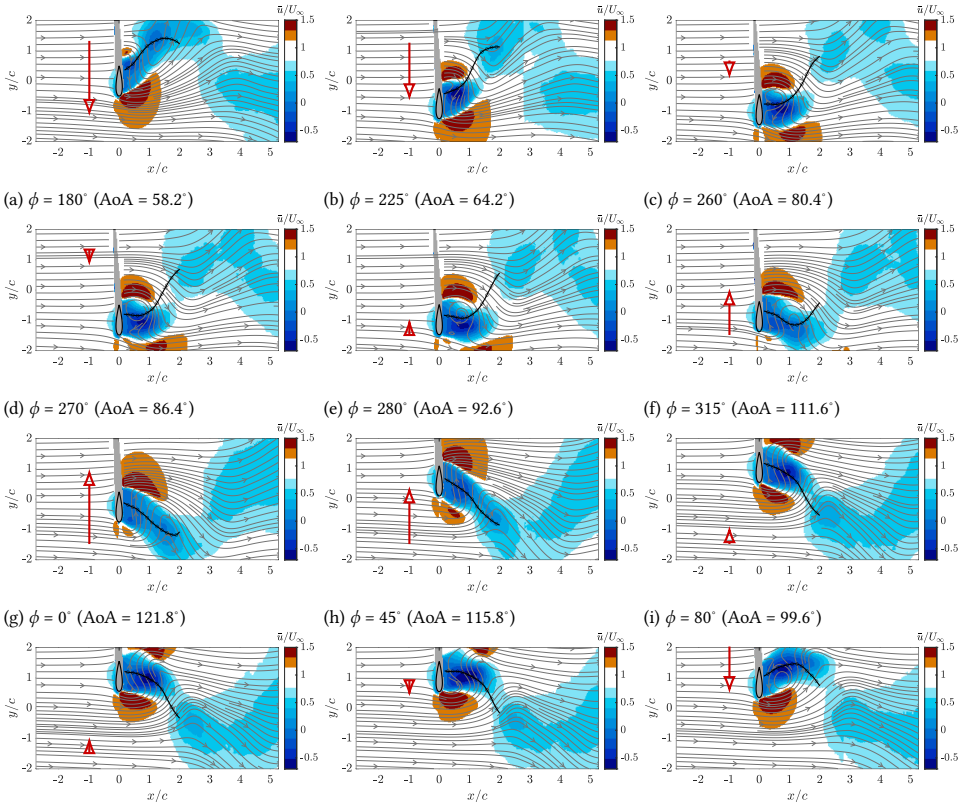

(a) ϕ = 180° (AoA = 58.2°) (b) ϕ = 225° (AoA = 64.2°) (c) ϕ = 260° (AoA = 80.4°)

(d) ϕ = 270° (AoA = 86.4°) (e) ϕ = 280° (AoA = 92.6°) (f) ϕ = 315° (AoA = 111.6°)

(g) ϕ = 0° (AoA = 121.8°) (h) ϕ = 45° (AoA = 115.8°) (i) ϕ = 80° (AoA = 99.6°)

(j) ϕ = 90° (AoA = 93.6°) (k) ϕ = 100° (AoA = 87.3°) (l) ϕ = 135° (AoA = 68.4°)

Figure 5.9: Streamwise velocity field $\bar{u}/U_\infty$ for k = 0.38 plunging case at all measured phases. The red arrow represents the scaled motion velocity $\dot{h}$. The wake center line is marked by the black circled line.

is approximately 2.1 times higher than the low frequency case. The wavier and more irregular wake at $k = 0.38$ results from a higher crossflow aerodynamic force (not shown here) compared to the $k = 0.19$ case, which in turn arises from stronger vortex interactions driven by rapid changes in effective angle of attack and increased flow unsteadiness. In Figure 5.10, the variation of γ with AoA in the near wake region is shown for both cases. For both cases, the γ at $x/c = 0.5$ is selected to plot as γ becomes very unstable after $x/c = 0.6$ for the higher frequency case, as shown in Figure 5.6b. Compared to the $k = 0.19$ case, the variation of AoA at $k = 0.38$ is about 1.8 times higher. Meanwhile, the variation of γ for the $k = 0.38$ case is approximately 2 times higher relative to $k = 0.19$. Therefore, the overall variation of the wake skew angle γ scales roughly proportionally with the variation of AoA, caused by the difference in k.

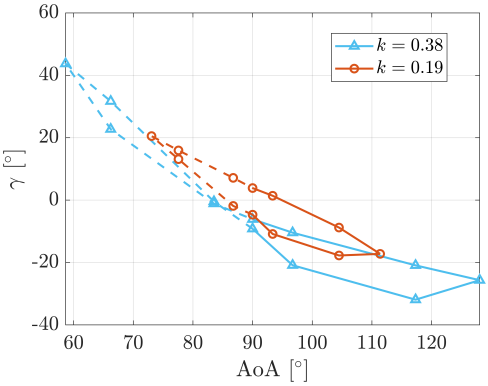

Figure 5.10: Wake skew angle γ as a function of AoA at $x/c = 0.5$. The solid line indicates the upstroke process and the dashed lines indicate the downstroke process.

Figure 5.11 presents the spanwise vorticity contour at $k = 0.38$, following the TEV formation and shedding order. At $\phi = 180^\circ$ (near the center of travel, moving down), the TEV starts to grow, with $\frac{\Gamma}{U_\infty c}$ starting from −0.7, as shown in Figure 5.8. When the airfoil moves down to the lowest point ($\phi = 270^\circ$, Figure 5.11d) and then moves up to $\phi = 280^\circ$ (Figure 5.11e), the TEV remains close to the airfoil, with the most downstream boundary near $x/c = 1.5$. During this period, $\frac{\Gamma}{U_\infty c}$ from the TEV steadily decreases to approximately −2.0. As the airfoil continues its upward plunge to $\phi = 315^\circ$ and $\phi = 0^\circ$ (Figure 5.11f and Figure 5.11g), the TEV elongates streamwise and downward (marked by the dashed arrow), stretched by the high relative velocity due to the airfoil's upstroke motion. Then, as the airfoil pitches up to $\phi = 80^\circ$ (Figure 5.11i), the TEV becomes distorted near $x/c = 1.8$, nearly separating apart under the influence of the strengthening LEV, which is convecting downstream towards it (marked by the dashed arrow). As the airfoil moves up to $\phi = 90^\circ$ (Figure 5.11j) and $\phi = 100^\circ$ (Figure 5.11k), the rear part of the TEV gradually detaches from the front part. This occurs because the fluid in this region has low momentum (close-to-zero velocity near $x/c \approx 2.3$, $y/c \approx -0.5$, as shown in Figure 5.9j and Figure 5.9k) and responds slowly to the rapidly changing motion of the airfoil ($\ddot{h} \approx -60.5$ m/s^2 at $\phi = 90^\circ$ and 100°), preventing the rear vortex from immediately following the upstream flow and

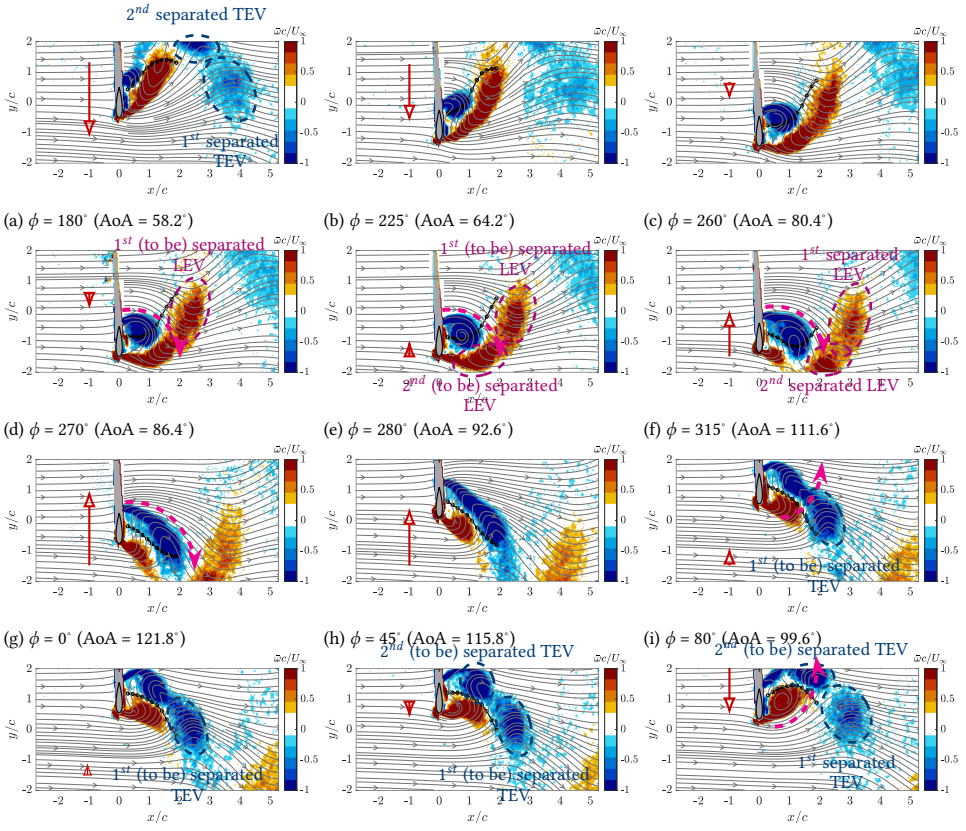

(a) ϕ = 180° (AoA = 58.2°) (b) ϕ = 225° (AoA = 64.2°) (c) ϕ = 260° (AoA = 80.4°)

(d) ϕ = 270° (AoA = 86.4°) (e) ϕ = 280° (AoA = 92.6°) (f) ϕ = 315° (AoA = 111.6°)

(g) ϕ = 0° (AoA = 121.8°) (h) ϕ = 45° (AoA = 115.8°) (i) ϕ = 80° (AoA = 99.6°)

(j) ϕ = 90° (AoA = 93.6°) (k) ϕ = 100° (AoA = 87.3°) (l) ϕ = 135° (AoA = 68.4°)

Figure 5.11: Contours of the phase-averaged spanwise vorticity component superimposed with streamlines. Vortex identified using Γ_1 method for the k = 0.38 surging case The red arrow represents the scaled motion velocity $\dot{h}$. The wake center line is marked by the black circled line.

leading to its apparent separation. Meanwhile, when the airfoil moves further down to $\phi = 135^{\circ}$ (Figure 5.11l), the growing LEV elongates in the direction of the TEV (marked by the dashed arrow), which starts to separate the remaining rear part of the TEV. This separation process is finished at $\phi = 180^{\circ}$. At this phase, the airfoil has the highest speed (pointing down), which also facilitates the shedding as the rear part has a relatively low speed compared to the airfoil. At this phase, the two rear parts of the TEV (including the one that remains stagnant between $\phi = 90^{\circ}$ and 100°) shed simultaneously, and a new TEV formation cycle begins.

On the other hand, a similar pattern can be found for the LEV development at $k = 0.38$. Instead, the growth of the LEV starts at $\phi = 315^{\circ}$ where the $\frac{\Gamma}{U_{\infty}c}$ is 0.68. During the upstroke period until $\phi = 90^{\circ}$ (the most top location), the LEV accumulates strength while maintaining close to the leading edge (the most downstream boundary maintains smaller than $x/c \approx 1.6$). Once the airfoil starts to move down from $\phi = 100^{\circ}$ and onward, the LEV tilted upwards and elongates in the same direction (as shown in the dashed arrow in Figure 5.11l). During this downstroke period between $\phi = 100^{\circ}$ and $\phi = 270^{\circ}$, the wake skew angle changes accordingly from -32.0° (tilting down) to 34.0° (tilting up). When the airfoil moves down to $\phi = 270^{\circ}$ (the bottom-most location), the growth of the TEV similarly separates the rear part of the LEV (marked by the dashed arrow). Due to the fluid momentum in this region (low local velocity near $x/c \approx 2.5$, $y/c \approx 0$, shown in Figure 5.9d and Figure 5.9e), this rear portion cannot immediately follow the rapid motion of the airfoil ($\ddot{h} \approx 60.5$ m/s^2 at $\phi = 270^{\circ}$ and 280°), and it remains nearly stationary in the wake until $\phi = 280^{\circ}$. As the airfoil moves up to $\phi = 315^{\circ}$ (Figure 5.11f), the rear part of the remaining LEV (the 2^{nd} separated LEV) detaches due to the growing TEV, and sheds in the wake together with the first (stagnant) rear part of the vortex (the 1^{st} separated LEV), as also partially shown at $\phi = 0^{\circ}$ (Figure 5.11g).

Therefore, during a plunging cycle at $k = 0.38$, the large angle of attack variations characteristic of this motion generate complex LEV-TEV interactions, resulting in a highly distorted wake structure. This higher motion frequency also leads to smaller circulation magnitudes compared to the $k = 0.19$ case (Figure 5.8). This strong flow interaction causes mutual separation of both the LEV and TEV by their counterpart vortices prior to final detachment, where the frequency lock-in is manifested through the synchronized separation of two vortex pairs into the wake.

Compared to the surging motion discussed in Chapter 4, both surging and plunging motions at $k = 0.38$ exhibit frequency lock-in with the imposed oscillation frequency, consistent with previous studies [106–108] for high frequency ratios. However, their distinct kinematics produce fundamentally different vortex shedding patterns. For the surging motion (streamwise oscillation), the fixed angle of attack at 90° leads to nominally symmetric development of the LEV and TEV, resulting in similar vortex structures and synchronous shedding. In contrast, the plunging motion (crossflow oscillation) induces a continuously varying angle of attack. This kinematic asymmetry amplifies the inherent geometric asymmetry between the rounded leading edge and sharp trailing edge: while the sharp trailing edge enforces immediate separation, the rounded leading edge allows partial flow attachment before separation. As a result, the timing of vortex formation and shedding differs between the two edges. Consequently, the LEV and TEV evolve with unequal strengths and distinct shapes (with additional LEV separation occurring at the lower reduced fre-

quency case) and shed asynchronously, resulting in a consecutive vortex street. While this wake pattern bears some resemblance to those reported in oscillating cylinder studies, such as Lin et al. [118], the present results reveal distinct differences arising from the airfoil kinematics. At higher k, the edge effect is minimized, producing two well-separated vortex pairs, whereas at lower k, additional LEV separation leads to imbalanced vortex shedding and prevents lock-in.

5.3.2 Load estimation

The load estimation approach introduced in Section 2.4.2 is applied to the plunging airfoil PIV flow field to estimate aerodynamic forces. The control boundary, illustrated in Figure 2.14, is defined as a rectangular region enclosing the airfoil. The rectangular geometry was selected arbitrarily, serving as a convenient and consistent boundary for the control-volume analysis. For both frequency cases, a total of 14 different control boundaries were employed to compute averaged quantities and their associated uncertainties. The boundary dimensions were varied such that $d_1 = d_2 = d_3 = d_4$, ranging from $10\,dx$ to $23\,dx$ with an interval of dx, where $dx = 0.027c$ denotes the vector spacing within the measured FoV.

5

The streamwise force coefficient, C_x, is plotted against the phase for the two motion frequencies, as shown in Figure 5.12. The upstroke (US) and downstroke (DS) periods are indicated at the top of the plot. For reference, the static drag coefficient at 90° angle of attack, $C_d = 0.95$ (Chapter 4), is shown as a grey line. At the higher reduced frequency ($k = 0.38$), C_x ranges from 1.2 to 3.5, exceeding the static value throughout the cycle. In contrast, at the lower frequency ($k = 0.19$), C_x varies between 0.8 and 1.8, remaining closer to the static reference. The force fluctuation amplitude at $k = 0.38$ is more than twice that at $k = 0.19$, consistent with the increased flow unsteadiness observed in the corresponding velocity fields.

To better understand the origin of the force coefficients, the individual contributions in Equation (2.22), namely the mean momentum convection (MC) term, the pressure (press) term, the time-derivative (TD) term, and the turbulence momentum transfer (TMT) term, are shown in Figure 5.13a and 5.13b for the two reduced frequency cases at each phase for the plunging motion. The mean viscous stress term is omitted due to its negligible magnitude. For the streamwise force contribution, the pressure term dominates the overall loading, while the MC term provides the second-largest contribution, varying in phase with the motion. In general, each force contribution is greater at $k = 0.38$ than at $k = 0.19$. For example, the maximum pressure contribution at $k = 0.38$ (occurring at $\phi = 90^\circ$) exceeds the corresponding maximum at $k = 0.19$ (occurring at $\phi = 260^\circ$) by more than 55%. This is related to the relative location between the vortex pair and the airfoil surface. For $k = 0.19$ case, the LEV and TEV pair is extended to more than $3c$ downstream (Figure 5.7), while for the higher frequency case, the vortex pair stays closer to the airfoil surface (on average stays within $3c$, see Figure 5.11), which leads to higher pressure, and overall high C_x.

It is seen in Figure 5.12 that for both frequencies, C_x peaks near the transition between upstroke and downstroke, which are near $\phi = 90^\circ$ and 270°. At these two extreme plunging locations, the wake vortices are developed with relatively high circulations. As shown in Figure 5.8, near $\phi = 90^\circ$, TEV develops the most, with the next phase being vortex separation. Meanwhile, at this phase, the LEV is also developed with a high vorticity and circulation ($\frac{\Gamma}{U_\infty c} = 1.9$ at $k = 0.38$ and 2.7 at $k = 0.19$). Similarly, at $\phi = 270^\circ$, the LEV devel-

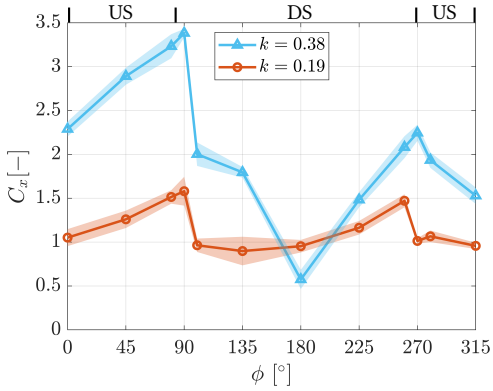

Figure 5.12: (a) streamwise force coefficient C_x at each plunging phase for the two motion cases. The shaded area indicates the 95% confidence interval from different boundary tests. The US and DS period is marked on top of the figure. The solid gray line indicates the static drag coefficient at 90° angles of attack.

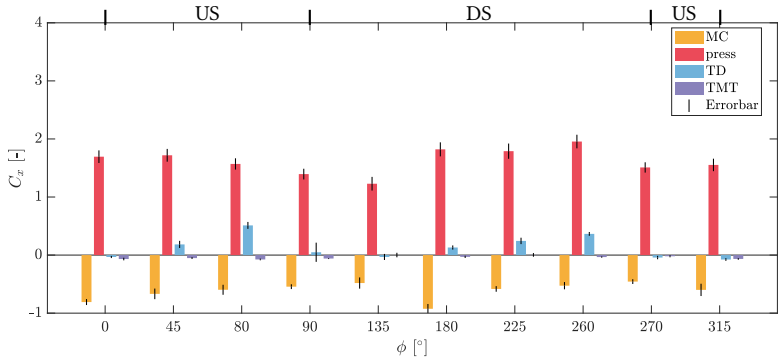

(a) k = 0.19, plunging

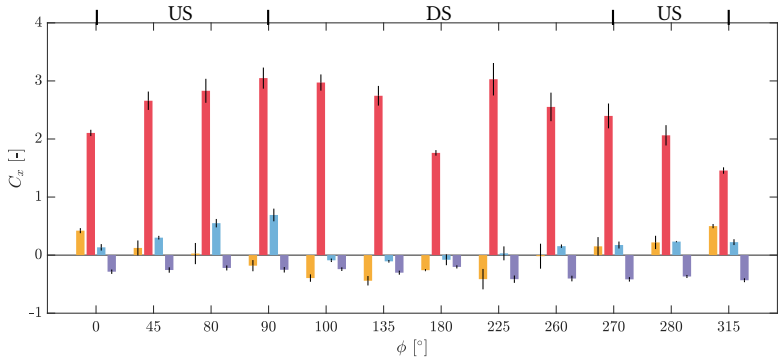

(b) k = 0.38, plunging

Figure 5.13: (Continued)

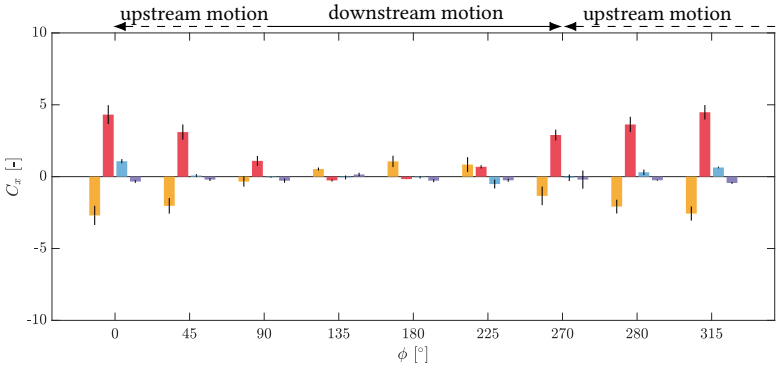

(c) k = 0.19, surging

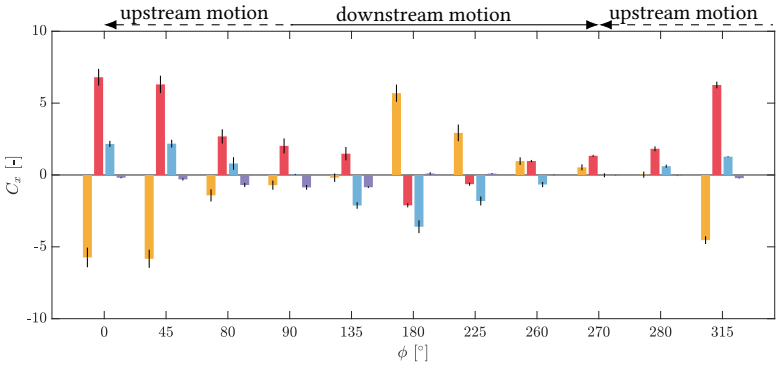

(d) k = 0.38, surging

Figure 5.13: Streamwise aerodynamic force contribution at k = 0.19 and k = 0.38 from mean convection (MC), pressure (press), turbulent momentum transfer (TMT), and time derivative (TD) for both the plunging and surging cases. The definitions of each term are shown from Equation (2.23) to Equation (2.26). The errorbar height represents the 95% confidence intervals from different boundary tests.

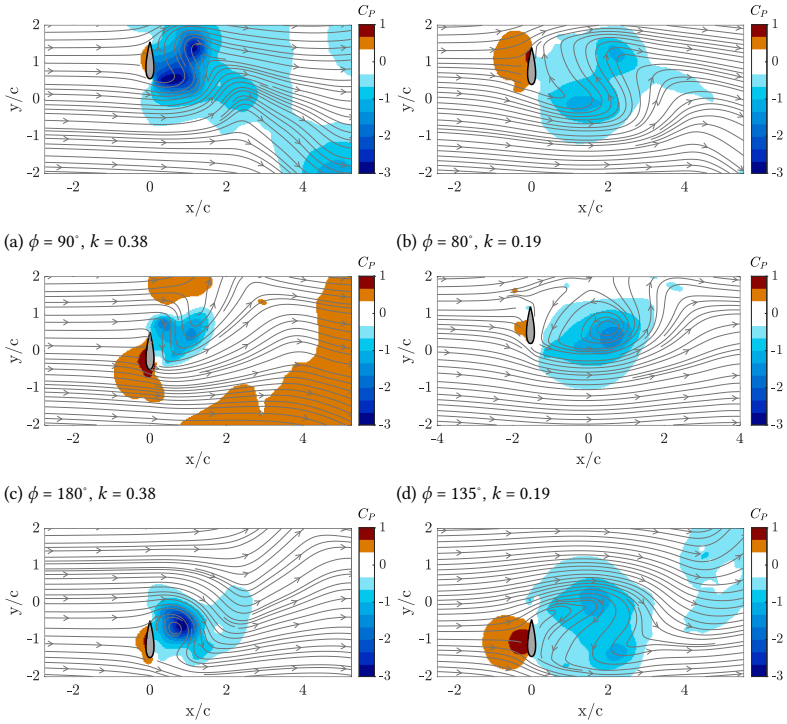

(a) $\phi = 90^{\circ}$, $k = 0.38$

(b) $\phi = 80^{\circ}$, $k = 0.19$

(c) $\phi = 180^{\circ}$, $k = 0.38$

(d) $\phi = 135^{\circ}$, $k = 0.19$

(e) $\phi = 270^{\circ}$, $k = 0.38$

(f) $\phi = 260^{\circ}$, $k = 0.19$

Figure 5.14: Pressure field C_p at representative phases at the two reduced frequencies.

ops with a high circulation: at $k = 0.38$, $\frac{\Gamma}{U_\infty c} = 3.1$, and the separation of the rear part of the LEV happens shortly after ($\phi = 280^\circ$); similarly at $k = 0.19$, $\frac{\Gamma}{U_\infty c} = 2.8$ at $\phi = 270^\circ$. Overall, the developed vortex pairs near the transition between the upstroke and downstroke lead to the highest circulatory force on the airfoil, which is demonstrated as the force peaks as shown in Figure 5.12.

Interestingly, at $k = 0.38$, C_x also presents a local minimum value of 1.2 at $\phi = 180^\circ$. In contrast, the C_x distribution does not display a pronounced local minimum, but rather two comparable maxima at $\phi = 80^\circ$ and $\phi = 260^\circ$. The smallest value appears at $\phi = 135^\circ$ ($C_x = 0.7$), yet it is not substantially lower than those in the adjacent phases. In order to compare the different performance at the two reduced frequencies, the pressure coefficient field C_p is plotted together for $\phi = 90^\circ$ (the highest C_x at $k = 0.38$), $\phi = 180^\circ$, and $\phi = 270^\circ$ at $k = 0.38$, and $\phi = 80^\circ$, $\phi = 135^\circ$, and $\phi = 260^\circ$ (the highest C_x at $k = 0.19$) at $k = 0.19$, as shown in Figure 5.14.

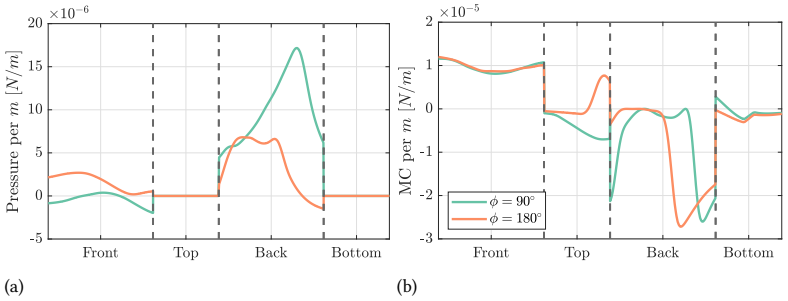

Figure 5.15: (a) pressure term and (b) MC in the streamwise direction in Eq.2.22 for $\phi = 90^\circ$ and $\phi = 180^\circ$ at $k = 0.38$. The curves start from the bottom-left of the control contour as shown in Figure 2.14.

As shown in the vorticity plots at $k = 0.38$ at $\phi = 90^\circ$ (Figure 5.11j) and $\phi = 180^\circ$ (Figure 5.11a), the TEV has just shed at $\phi = 180^\circ$, whereas at $\phi = 90^\circ$ the exhibited vortices contribute to lower circulation (higher magnitude), with the non-dimensionalized value decreasing from approximately −0.7 to −3 (illustrated in Figure 5.8). Consequently, in the wake region, $\phi = 90^\circ$ exhibits a much lower pressure coefficient (higher magnitude, as shown in Figure 5.14a), with a minimum of approximately −3, compared to $\phi = 180^\circ$, where the negative C_p region is smaller with the minimum value near −1.8. For these two phases, the two most dominant force contributions (pressure term and MC) on the control boundary are shown in Figure 5.15. The control contour presented here has a fixed 20 dx distance from each boundary of the airfoil surface. The curves start from the bottom-left of the control contour, with the four sides marked in Figure 2.14. In the pressure contour plot (Figure 5.15a), although the front contour shows a similar pressure contribution at both phases, the back contour at $\phi = 90^\circ$ exhibits significantly higher pressure contribution.

At $k = 0.38$, another noticeable difference is observed between the two extreme phases at $\phi = 90^\circ$ (Figure 5.14a) and $\phi = 270^\circ$ (Figure 5.14e). At $\phi = 90^\circ$, two suction regions are located at the LEV and TEV in the wake, while at $\phi = 270^\circ$, the suction is smaller and concentrated mainly at the TEV. To better understand the relationship between the vorticity field and the pressure, these two fields were analyzed with a higher C_p range between −4

and 4 (not shown). The analysis shows that the TEVs are well developed at both phases, each containing a fully reversed flow region. In contrast, the LEV exhibits a strong dependence on the instantaneous angle of attack: at $\phi = 90^\circ$, the LEV vorticity is high ($\bar{\omega}c/U_\infty \geq 4$), whereas at $\phi = 270^\circ$, it is weaker ($\bar{\omega}c/U_\infty \approx 2$). This demonstrates that at high k, the high frequency motion alters the shear layer evolution, leading to different vorticity flux and vortex roll-up between phases

However, at the lower reduced frequency ($k = 0.19$), the distinction between the highest C_x phase ($\phi = 260^\circ$, peak C_x) and the lowest C_x phase ($\phi = 135^\circ$) becomes less pronounced. This is evident in the pressure coefficient fields (Figure 5.14f and 5.14d), which both show a similar high-pressure region on the upwind side and comparable low-pressure regions in the wake (with the minimum reaching approximately $C_p = -1.2$). The same trend can be observed between the two extreme phases at $\phi = 80^\circ$ and $\phi = 260^\circ$, where the wake contains two local suction regions associated with the LEV and TEV. At $\phi = 80^\circ$, the suction is slightly stronger near the LEV, while at $\phi = 260^\circ$ (Figure 5.7c) it shifts toward the TEV. In the meantime, the suction in the upwind side of the airfoil is higher at $\phi = 260^\circ$ than at $\phi = 80^\circ$. Overall, at low k, the smaller angle of attack variations result in a less varied flow topology and pressure distribution between different phases, producing smaller force variations compared to the high-k case.

The MC term, shown in Figure 5.15b, exhibits similar contributions at both phases at $k = 0.38$ along the front and bottom boundaries. The streamwise velocity plots (Figure 5.9j and Figure 5.9a) indicate that the incoming flow from the left, combined with the accelerated flow induced by the airfoil motion and the lower boundary layer, generates comparable flow dynamics in these regions. However, the difference between these two phases lies in the top and back control boundaries. As shown in the second term on the right-hand side of Equation (2.22), the MC term is primarily governed by the product of streamwise and crossflow velocities. The crossflow velocity distributions $\bar{v}/U_\infty$ at these two phases are presented in Figure 5.16, where the black rectangle denotes the force integration contour around the airfoil. At $\phi = 90^\circ$, the airfoil reaches the end of the upstroke, and the wake retains upward inertia, producing positive $\bar{v}/U_\infty$ in the near wake. In contrast, during the downstroke at $\phi = 180^\circ$, negative $\bar{v}/U_\infty$ develops in the wake. This phase-dependent difference in crossflow velocity accounts for the distinct MC contributions from the top and back boundaries. As a result, as shown in Figure 5.13b, the MC contribution at $\phi = 90^\circ$ and $\phi = 180^\circ$ presents opposite contributions.

Overall, due to the higher vorticity magnitude and the more horizontally oriented near wake, the streamwise force distribution at $\phi = 90^\circ$ exhibits a much stronger pressure contribution together with a positive MC term. In contrast, at $\phi = 180^\circ$, the pressure contribution is weaker and the MC term becomes negative as a result of the skewed wake. Consequently, when combined with the minor TD and TMT terms, $\phi = 90^\circ$ corresponds to the maximum streamwise force within the cycle, whereas $\phi = 180^\circ$ corresponds to the minimum.

The drag and lift coefficients, C_d and C_l, are plotted against ϕ in Figure 5.17a and Figure 5.17b, respectively. These coefficients are obtained from the effective angle of attack, together with the force coefficients C_x and C_y (crossflow force coefficient), using the relations $C_d = C_x \sin(\text{AoA}) + C_y \cos(\text{AoA})$ and $C_l = C_x \cos(\text{AoA}) - C_y \sin(\text{AoA})$. C_d is in the same direction as U_{rel} as shown in Figure 5.3, and C_l is perpendicular to it. The static

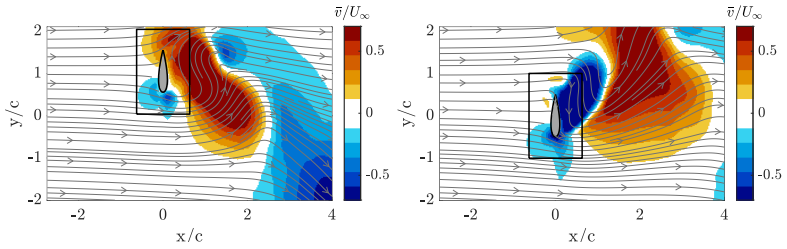

(a) $\phi = 90^\circ$ (b) $\phi = 180^\circ$

Figure 5.16: Crossflow velocity $\bar{v}/U_\infty$ for (a) $\phi = 90^\circ$ and (b) $\phi = 180^\circ$ at $k = 0.38$. The black rectangle represents the force integration contour. Note that the shadow region on the top of the airfoil is interpolated for load integration purposes.

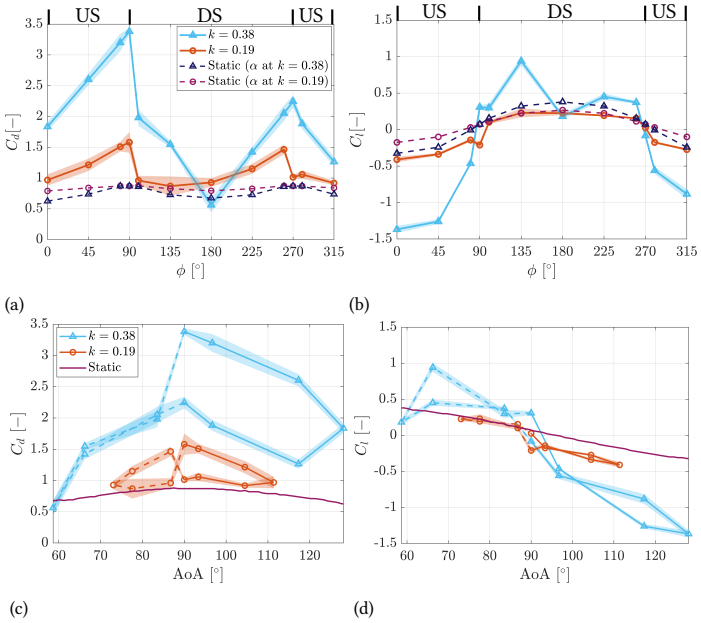

Figure 5.17: Aerodynamic coefficients plotted with phase ((a) and (b)) and effective angle of attack ((c) and (d)). Note that the static results are interpolated from the wind tunnel measurement from Holst et al. [105].

results reported by Holst et al. [105] were interpolated based on the AoA at each phase for the two motion cases and are shown as dashed lines for comparison. Overall, with the static C_d varying between 0.68 and 0.88, the plunging motion produces substantially higher drag values in both cases. Similar to C_x, the peak C_d during the plunging cycle is approximately four times higher than the static case at $k = 0.38$ and more than twice as high at $k = 0.19$. The largest deviations between the plunging and static results occur when the acceleration is highest, near $\phi = 90^\circ$ and $\phi = 270^\circ$.

For the lift coefficient, C_l, the plunging motion generally follows the trend of the static case, particularly for $k = 0.19$. Between $\phi = 0^\circ$ and 90°, and between $\phi = 270^\circ$ and 315°, the angle of attack exceeds 90°, resulting in negative C_l, whereas between $\phi = 90^\circ$ and 270°, AoA < 90° produces positive C_l. Especially at $k = 0.19$, the plunging C_l closely matches the static values. In contrast, at $k = 0.38$, the negative C_l regions exhibit much lower values (approximately −1.45) compared to the static case (approximately −0.3). In the positive C_l region, however, the overall trend remains similar, though with larger peaks around $\phi = 135^\circ$ and $\phi = 225^\circ$.

These results indicate that plunging motion fundamentally alters the aerodynamic forces relative to the static case. While C_l retains some resemblance to the static behavior, particularly at lower reduced frequency ($k = 0.19$), the increasing deviations at higher k highlight the importance of vortex dynamics and flow unsteadiness induced by motion with varying accelerations. In contrast, the consistently elevated C_d compared to the static cases demonstrates that plunging introduces substantial additional drag through unsteady vortex shedding, which cannot be captured by a static polar.

The coefficients C_d and C_l are also plotted against the angle of attack, forming hysteresis loops as shown in Figure 5.17c and Figure 5.17d. The static values from Holst et al. [105] are indicated by the purple line in each plot. In the hysteresis plots, the solid line corresponds to the mean values during the upstroke period, while the dashed line represents those during the downstroke.

For both reduced frequency cases, the C_l hysteresis loops remain close to the static values, especially for the $k = 0.19$ case. At $k = 0.38$, the C_l values diverge from the static results outside the AoA close to 90° region. However, the variations between the increasing angle of attack phases and decreasing angle of attack phases are small, which is consistent with the inherent small lift values in this angle range.

In contrast, the C_d hysteresis loops show pronounced differences between the increasing and decreasing angle of attack phases. For $k = 0.38$, the strongest hysteresis occurs during the upstroke period, where AoA varies between 90° and 128° (corresponding to phases $\phi = 0^\circ$–90° and $\phi = 270^\circ$–315°; see Figure 5.4). This behavior arises because, at $k = 0.38$, the LEV and TEV grow and shed at different phases during the upstroke period: the LEV sheds between $\phi = 270^\circ$ and 0° (Figure 5.11d to Figure 5.11g), while the TEV sheds between $\phi = 0^\circ$ and 90° (Figure 5.11g to Figure 5.11j). The resulting strong variations in vorticity, circulation, and force lead to the pronounced C_d hysteresis during the upstroke. In contrast, during the downstroke ($\phi = 90^\circ$–270°; see Figure 5.11j to Figure 5.11l and Figure 5.11a to Figure 5.11d), both the LEV and TEV continue to grow without shedding from the airfoil. As a result, the force variations are smaller, and the hysteresis in C_d is much weaker compared to the upstroke period. The presence of maximum hysteresis during the upstroke is consistent with the findings of [57] and [119]. Although their operating

conditions (k = 0.25, maximum effective angle of 22°) resulted in a correspondingly lower maximum C_d of approximately 0.4, the fundamental asymmetry in the hysteresis loop closely mirrors the behavior observed in the present study.

However, for the low frequency case at k = 0.19, the differences in magnitudes between the increasing and decreasing angle of attack phases are most evident near AoA = 85.2° (during downstroke, the peak on the dashed line) and 94.8° (during upstroke, the peak on the solid line), corresponding to the transition phases between upstroke and downstroke ($\phi = 260°-270°$ and $\phi = 80°-100°$ respectively), as shown in Figure 5.4. Because the plunging acceleration reaches its maximum at these stroke reversal points, this result indicates that at lower reduced frequencies, where circulatory forces from the vortices are weaker, the hysteresis is primarily governed by non-circulatory effects from the added mass forces.

Comparison between the plunging motion and the surging motion

In order to compare the aerodynamic performance between the surging motion (discussed in Chapter 4) and the present plunging motion, the force terms listed from Equation (2.23) to Equation (2.26) are computed with the same control boundary condition ($d_1 = d_2 = d_3 = d_4$, ranging from 10 dx to 23 dx with an interval of dx, Figure 2.14) for the surging cases to match those for the plunging cases. The results are shown in Figure 5.13.

Compared with the surging motion, three main differences are observed in the overall force variations and individual force contributions:

- Overall force variation: In surging motion, the airfoil moves parallel to the incoming wind, so the angle of attack remains fixed at 90°. Due to the direct effect of the wind in the vertical direction, C_x (equaling C_d for the surging case) exhibits much larger variations, ranging from approximately −1.5 to 3, compared to 0.8 to 3.5 for the plunging motion. In addition, because plunging involves variations in AoA, forces are generated outside the x direction, and C_l shows noticeable variations (between −1.3 and 1 at k = 0.38) despite the inherently small static values near AoA = 90°.

- Force contributions in the streamwise direction: The results for the selected control boundaries tests for the surging cases are shown in Figure 5.13c and 5.13d. Overall, the result of the selected control boundaries for the surging case shows similar mean values and confidence intervals compared to the higher range results in Chapter 4. Compared to surging, the variation of the pressure and MC terms in plunging is smaller within a cycle. For plunging, the pressure term ranges from 1.2 to 3.0 and the MC term from −0.9 to 0.4, accounting for both reduced frequency cases. By contrast, for surging (Figure 5.13c and 5.13d), the variation at k = 0.19 is 0 to 5 for the pressure term and −3 to 0.5 for the MC term. At k = 0.38, the variation is even greater: approximately 50% higher for the pressure term and 130% higher for the MC term compared to the low frequency case. This difference is attributed to the motion direction: in surging, the direct alignment with the incoming wind enhances pressure and MC variations, whereas in plunging, the varying AoA leads to a lower variation of the relative speed experienced by the airfoil, thus leading to lower variations of the individual load terms.

- Relative importance of MC and pressure terms: In plunging, the MC term is much smaller than the pressure term, whereas in surging, both are comparable in mag-

nitude. This is because, in surging, the horizontal motion at a constant 90° angle of attack generates vortex shedding with a symmetric, fully reversed pattern. The wake, therefore, extends into a larger region of strong reverse flow ($\bar{u}/U_\infty < -0.5$), where significant velocity gradients produce strong momentum convection. As a result, the MC term becomes comparable to the pressure gradient term, and both contribute substantially to the local momentum balance. In contrast, plunging involves predominantly crossflow motion. The vertical acceleration of the airfoil induces large instantaneous pressure gradients that dominate the momentum balance, while the wake is shorter and less sustained. The reverse flow region is smaller and weaker (Figure 5.5 and 5.9), leading to reduced momentum convection. Meanwhile, the shorter wake requires momentum to be restored over a smaller distance, which leads to larger pressure gradients and higher pressure magnitudes near the airfoil. Consequently, the pressure term dominates the momentum balance in plunging, whereas in surging, both the convective and pressure terms contribute comparably.

Overall, these differences show that, under the same motion amplitude, frequency, and incoming wind speed, the surging motion produces larger streamwise force variations, strongly influenced by the competing contributions of the pressure and MC terms. By contrast, in plunging, the streamwise force coefficient is dominated by pressure variations, and additional force is generated due to the crossflow motion.

5.4 Conclusion

In this study, the plunging motion of an airfoil has been experimentally investigated with emphasis on vortex dynamics, frequency lock-in, and intra-cycle aerodynamic force variations. To enable direct comparison with the surging motion presented in Chapter 4, identical incoming flow conditions, motion amplitudes, and frequencies were used, and the angle of attack was fixed at 90°.

Phase-locked PIV measurements captured the flow fields at 12 phases for two reduced frequencies, $k = 0.19$ and $k = 0.38$. At the lower reduced frequency ($k = 0.19$), the rear part of one LEV–TEV pair was separated and convected downstream during the downstroke, while an additional LEV was generated during the upstroke. In this regime, the TEV dissipated into the wake rather than causing separation near the rear of the airfoil, thereby preventing the vortex shedding frequency from synchronizing with the motion frequency. Thus, unlike the surging case, lock-in did not occur. This difference arises because surging only changes the effective flow speed (with AoA = 90° constant), promoting synchronization, whereas plunging continuously alters the effective angle of attack, introducing asymmetry that generates extra vortical structures and disrupts lock-in.

At the higher reduced frequency ($k = 0.38$), two rear parts of the LEV–TEV pair were separated and convected into the downstream wake each cycle, with one pair formed by the interaction with the counter vortex. This result leads to frequency lock-in. However, the wake at this condition was shorter and contained a lower circulation magnitude compared to $k = 0.19$, due to the broader variation of the effective angle of attack. Comparing plunging with surging at this reduced frequency reveals that, while both motions exhibit frequency lock-in, their distinct kinematics produce fundamentally different shedding patterns. The cross-flow motion requires a higher motion frequency to overcome asymmetric

shedding vortices, highlighting that lock-in depends on both frequency and motion kinematics.

The aerodynamic load analysis further shows that the maximum streamwise force occurs during transitions between upstroke and downstroke, reaching $C_x \approx 3.5$ at $k = 0.38$, which is almost four times higher than the static value at $\alpha = 90^\circ$. Relative to the static measurement data from Holst et al. [105], the plunging motion yields substantially higher C_d, especially near $\phi = 90^\circ$ and 270°, where values are up to four times larger. For C_l, plunging at $k = 0.19$ closely follows the static case, but at $k = 0.38$ the increased unsteadiness produces higher C_l.

Finally, comparing the load estimation results with surging motion highlights three main distinctions. First, plunging produces smaller streamwise force variations within a cycle, with contributions dominated by pressure, whereas in surging, both pressure and mean convection terms play comparable roles. Second, plunging wakes are less sustained, producing weaker reverse flow regions in the wake, while surging wakes are more symmetric and show higher reverse flow magnitudes. Third, the different motion kinematics fundamentally alter the vortex dynamics and therefore the balance of force contributions. Under identical flow conditions and airfoil kinematics (frequency and amplitude of motion), surging motion generates larger and more balanced force variations, while plunging motion is primarily pressure-driven with reduced overall force variation but enhanced sensitivity to unsteady vortex dynamics.

6

Pitch motion: airfoil dynamic stall under reverse flow conditions

In the previous two chapters, the translational motions of an airfoil were examined, where the resulting force variations, lock-in effects, and vortex dynamics were shown to depend strongly on both motion kinematics and motion frequency. In this chapter, the focus shifts to the rotational motion of an airfoil, specifically pitching under reverse flow conditions. This configuration is of particular interest because it closely relates to the VIV experienced by wind turbine blades, yet limited research has investigated the associated vortex dynamics and force variations. More than 40 test cases with different mean angles of attack, pitching amplitudes, and frequencies were conducted, from which a universal trend in suction side pressure distribution was identified and analyzed. Furthermore, the dominant flow features, whether governed by the DSV or the TEV, are discussed as a function of the mean angle of attack. In addition, the initiation time detection method of the DSV and TEV is also proposed and compared against existing methods, demonstrating an average difference of less than 2.4% of the cycle period compared to the POD method . Overall, this chapter provides a deep understanding of the unsteady aerodynamics of the pitching airfoil under reverse flow conditions, where the data and interpretation compared to the conventional dynamic stall cases can be incorporated into future numerical simulations and engineering models.

This chapter is based on

G. Xu, A. Sciacchitano, C. Simão Ferreira, W. Yu, *Dynamic stall of a pitching airfoil under reverse flow conditions*, Physics of Fluids, **37**, (1), 32, 2025 [120].

G. Xu, A. Sciacchitano, W. Yu, *Vortex initiation detection and evolution analysis on a pitching airfoil under reverse flow conditions*, Physics of Fluids, *under review.*

6.1 Introduction

Dynamic stall is a critical unsteady aerodynamic phenomenon characterized by flow separation, vortex formation, and severe unsteady loads. It has been extensively studied under conventional flow conditions, particularly for applications such as helicopters, maneuvering aircraft, and wind turbines.

Pioneering works [62, 63, 65–68] established the fundamental understanding of this regime and introduced influential semi-empirical models. Building on this foundation, more recent studies [70–73] have provided deeper insights into the specific roles of vortex dynamics, boundary-layer behavior, and the influence of parameters such as Reynolds number and reduced frequency.

However, research on dynamic stall in reverse flow, where the trailing edge faces the incoming flow, remains limited despite its relevance for applications such as parked wind turbines and retreating rotor blades in helicopters. Reverse flow introduces immediate leading edge separation and potentially distinct vortex dynamics compared to conventional cases, but its underlying mechanisms are not yet well understood. Experimental work by Lind and Jones [79] suggests multiple vortex formation events per cycle, but comprehensive flow-field analysis is still lacking.

A significant challenge in this domain, even for conventional stall, is the accurate detection of Dynamic Stall Vortex (DSV) and Trailing Edge Vortex (TEV) initiation. Predicting these critical timings is crucial for designing unsteady wings and refining aerodynamic models. Several approaches exist for identifying DSV initiation under conventional conditions. Ramesh et al. [121] introduced the leading edge suction parameter (LESP), correlating DSV release with a threshold in peak suction. Sudharsan et al. [122] developed a more conservative boundary enstrophy flux (BEF) criterion using wall-resolved large-eddy simulations. More recently, Li and Feng [123] proposed the spatial distribution coefficient of pressure (SDCP) and high-order central moment of pressure (HCMP), together with the modulated location of peak pressure (MLPP) as an indicator of DSV detachment. In addition, Mulleners and Raffel [70] utilized POD to identify the DSV detachment time, linking POD mode structures to the physical development of vortices. While these methods significantly advanced the prediction of critical timing events in conventional dynamic stall, none have yet been evaluated for reverse flow conditions, where the vortex dynamics differ from conventional cases.

Beyond mere detection, there is a need to quantitatively examine the evolution of the dynamic stall vortex under reverse flow. For conventional cases, the development and evolution of the dynamic stall vortex have been extensively investigated across a wide range of scenarios. Through high-fidelity simulations, Visbal [57] demonstrated that the formation, roll-up, and convection of the leading edge dynamic stall vortex govern the dominant unsteady aerodynamic loads during deep dynamic stall. Gupta and Ansell [72] further demonstrated experimentally that the onset of dynamic stall is preceded by the evolution of the LSB and leading edge instabilities, which grow into the DSV. Zhu et al. [124] demonstrated that the timing and character of dynamic stall on vertical-axis wind turbine blades depend strongly on Reynolds number and reduced frequency, where a higher Reynolds number and reduced frequency lead to the delay of dynamic stall onset. To quantify this development, Mulleners and Raffel [71] utilized the average chord-normal height of vortical structures, while Buchner et al. [125] correlated the formation of discrete vor-

tices with dimensionless centrifugal instability. It remains to be seen how these evolution metrics translate to the reverse flow regime.

Consequently, this chapter addresses two primary objectives for dynamic stall under reverse flow conditions:

Experimental investigation: To investigate the dynamic stall phenomenon under reverse flow conditions, aiming to deepen the understanding of vortex dynamics, surface pressure distribution, and force variation. This includes analyzing the impact of key pitching parameters, specifically the mean angle of attack, pitching amplitude, and reduced frequency.

Vortex initiation detection criterion development: To develop a robust method for detecting the initiation timings of both the DSV and TEV in reverse flow dynamic stall, and to explore the application of this method for evaluating the subsequent development of the DSV.

6.2 Methodology: definition and experimental setup

6.2.1 Definitions and nomenclature in reverse flow dynamic stall conditions

To analyze reverse-flow dynamic stall systematically and to better compare with conventional dynamic stall cases, it is essential to define the key parameters and conventions for a pitching airfoil under reverse flow conditions.

First of all, the reverse flow angle of attack during a reverse flow dynamic stall condition $\mathrm{AoA_r}$ is defined as $\mathrm{AoA_r} = 180^\circ - \mathrm{AoA}$, where AoA is defined in Chapter 1. In this paper, the different cases are named as $\overline{\mathrm{AoA_r}}a_1\Delta a_2 k a_3$ (or $\overline{\mathrm{AoA}}a_1\Delta a_2 k a_3$ for conventional dynamic stall cases), where a_1, a_2, and a_3 are the values of the mean angle of attack ($\overline{\mathrm{AoA_r}}$ or $\overline{\mathrm{AoA}}$), pitching amplitude ($\Delta\mathrm{AoA_r}$ or $\Delta\mathrm{AoA}$), both in degrees, and reduced frequency (k) of this test case, respectively. k is defined as $2\pi f * (c/2)/U_\infty$ [48], where f is the pitching frequency in Hz, c is the chord length in meters, and U_∞ is the incoming wind speed in meters per second.

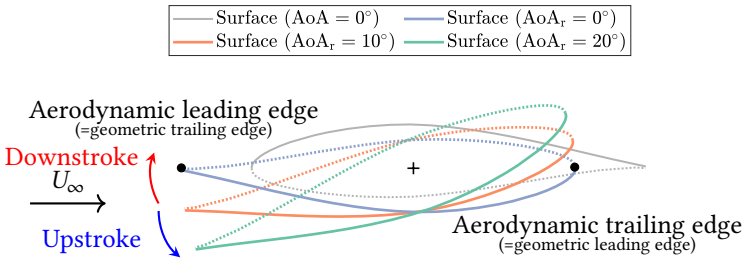

Figure 6.1: Schematic plot of airfoil orientation at case $\overline{\mathrm{AoA_r}}10\Delta10k0.1$. Solid lines represent the suction side of the airfoil surface, while the dotted lines represent the pressure side. Arrows indicate pitching motion directions. The aerodynamic leading and trailing edges are indicated with black dots.

Figure 6.1 shows the schematic plot of the airfoil orientation at case $\overline{\mathrm{AoA_r}}10\Delta10k0.1$ compared to a reference orientation where AoA= 0°. The pitching airfoil reaches the minimum angle of $\mathrm{AoA_r} = 0^\circ$ and the maximum angle of $\mathrm{AoA_r} = 20^\circ$. The cross in the figure

represents the location of the physical pitching axis, which is at $x_c/c = 0.4012$. x_c denotes the chordwise coordinate along the airfoil, where $x_c/c = 0$ is the geometric leading edge. The wind comes from the left. Under this reverse flow condition, the geometric trailing edge becomes the aerodynamic leading edge. For clarification, if not specified, the leading edge and trailing edge mentioned in the rest of the paper are referred to as the aerodynamic leading edge and aerodynamic trailing edge, respectively. In addition, in order to make a fair comparison with conventional dynamic stall cases, in the reverse flow dynamic stall condition, the upstroke motion is defined as when $\mathrm{AoA_r}$ increases (aerodynamic leading edge moving down), and the downstroke motion is defined as when $\mathrm{AoA_r}$ decreases (aerodynamic leading edge moving up).

During the pitching motion of the airfoil, two coordinate systems are defined as shown in Fig. 6.2, where x and y are the global coordinate system with x aligning with the free-stream direction, and x_c and y_c follow the airfoil coordinate system, where x_c aligns with the chordline of the airfoil. The origin in the airfoil coordinate system is located at the geometric leading edge, which aligns with the conventional airfoil convention. Instead, the origin of the global coordinate system is positioned at the location of the geometric trailing edge when $\mathrm{AoA_r} = 0^\circ$ ($\mathrm{AoA} = 180^\circ$).

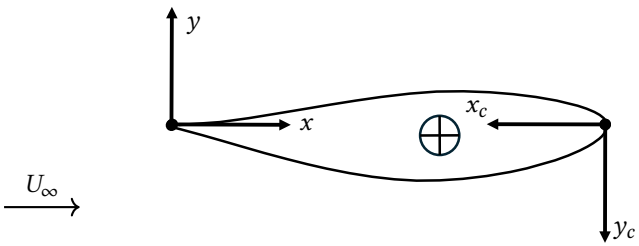

Figure 6.2: illustration of the two coordinate systems used in the study.

The aerodynamic lift coefficient C_l and the aerodynamic moment coefficient C_m are analyzed in this study. These results are obtained by integrating the measured pressure using the equations reported in Anderson's book [126].

6.2.2 Experimental design and setup

Wind tunnel and model

The experiments were conducted in the Low-Speed Low Turbulence Tunnel (LTT) at the Delft University of Technology in the Netherlands. The LTT is a closed-test section, closed-circuit wind tunnel with a nominal turbulence intensity varying from 0.015% at 20 m/s to 0.07% at 75 m/s and an octagonal test section 1.80 m wide, 1.25 m high, and 2.60 m long. A wing with a NACA 643418 profile was used in the experiments. The wing spans the entire vertical dimension of the test section (1.25 m) and has a chord of 250 mm, leading to an aspect ratio of 5. A total of 49 pressure sensors were used to measure the static pressure over the airfoil surface. The airfoil geometry and pressure tap locations are shown in Figure 2.3.

Pressure measurement

The surface pressure was measured using the Digital Temperature Compensation (DTC) Initium electronic pressure scanning system, which supports up to 8 DTC scanners to facilitate as many as 512 channels of pressure measurements. The accuracy is ±0.05% for a full-scale range (> 5 psid) measurement. The system can measure at a maximum frequency of 1200 Hz when scanning 16 channels per scanner. In this campaign, the acquisition frequency was set to 300 Hz.

The test matrix for reverse flow dynamic stall conditions is shown in Table 6.1, where the chord-based Reynolds number Re was set at 2.5×10^5 and the free stream velocity (U_∞) is approximately 14.9 m/s. The design of the test matrix is explained in Appendix D.1. Additionally, a few conventional cases are also tested, with the test matrix shown in Table 6.2. The number of cycles required for each test case was determined through a convergence study. One pitching case was measured over a duration of 299 cycles, with each cycle consisting of one upstroke and one downstroke. The standard deviation was evaluated for comparisons between 50 and 298 cycles. Note that the first cycle was excluded from the standard deviation calculation to avoid transient effects in the measurement. Further details can be found in Appendix D.1.1. Based on the study, 150 cycles were selected for each test case to ensure high accuracy while minimizing test duration. The results presented in this study are based on the 149 cycles following the excluded first cycle.

Table 6.1: Test matrix of the experimental campaign for reverse flow conditions.

$\overline{\mathrm{AoA_r}}$ (°)	$\Delta\mathrm{AoA_r}$ (°)	f (Hz)	k (-)
5, 10, 15, 20, 25	5	1, 2, 3, 4	0.05, 0.1, 0.16, 0.21
	10	1, 1.5, 2, 2.5, 3, 3.5	0.05, 0.08, 0.1, 0.13, 0.16, 0.18
	15	1, 2, 3	0.05, 0.1, 0.16[1]

Table 6.2: Test matrix of the experimental campaign for conventional cases.

$\overline{\mathrm{AoA}}$ (°)	$\Delta\mathrm{AoA}$ (°)	f (Hz)	k (-)
5, 10, 15	5	1, 2, 3, 4	0.05, 0.1, 0.16, 0.21
	10,15[2]	1, 2, 3	0.05, 0.1, 0.16

To represent the uncertainty of the pressure measurement, we calculate the 95% confidence interval for the mean value of lift coefficient C_l and moment coefficient C_m over 149 cycles. The following procedure shows an example for uncertainty calculation for C_l.

First of all, the standard deviation of C_l (σ_{C_l}) is calculated as:

$$\sigma_{C_l} = \sqrt{\frac{1}{n-1}\sum_{i=1}^{n}\left(C_{l,i} - \overline{C_l}\right)^2}$$

[1]The case with $k = 0.16$ at $\Delta\mathrm{AoA_r} = 15^\circ$ was only tested at $\overline{\mathrm{AoA_r}} = 20^\circ$ and 25° due to experimental constraints.
[2]Instead of $\Delta\mathrm{AoA_r} = 15^\circ$, the case with $\overline{\mathrm{AoA}} = 15^\circ$ was tested with $\Delta = 14^\circ$ due to experimental constraints.

where n is the number of cycles, $C_{l,i}$ is the C_l time series at the i's cycle, and $\overline{C_l}$ is the cycle-averaged C_l.

Then the standard error (SE) of the mean value is calculated as:

$$\mathrm{SE} = \frac{\sigma_{C_l}}{\sqrt{n}}$$

Assuming the data is approximately normally distributed, the 95% confidence interval for the mean $\overline{C_l}$ is given by:

$$C_{l_{95\%}} = \overline{C_l} \pm t_{0.975,\,df} \cdot \mathrm{SE}$$

where $t_{0.975,\,df}$ is the critical value from the Student's t-distribution [127], with $df = n - 1$ degrees of freedom (reflecting the number of independent observations used to estimate the variance), corresponding to the two-sided 95% confidence interval. For $n = 149$, this value is $t_{0.975,\,df} = 1.976$.

Particle Image Velocimetry (PIV)

PIV measurements were conducted using the apparatus shown schematically in Figure 6.3. The flow inside the tunnel was seeded with water-glycol droplets of 1 μm median diameter produced by a SAFEX smoke generator. The flow was illuminated by two Quantel Evergreen Nd:YAG lasers (200 mJ pulse energy, maximum 15 Hz repetition rate, 532 nm wavelength), shooting from the two sides of the test section to illuminate both pressure and suction sides of the airfoil. Flow field imaging was conducted using two LaVision Imager sCMOS cameras (2560 × 2160 pixel, 16 bit, 6.5 × 6.5 μm pixel size) equipped with 50 mm Nikon lenses; the lens numerical aperture was set to $f_\# = 8$. The optical magnification was $M = 0.03$, yielding a digital image resolution of 4.94 pixels/mm. The cameras were controlled by a LaVision programmable timing unit PTU X, where precise pulses are triggered and synchronized for cameras and lasers.

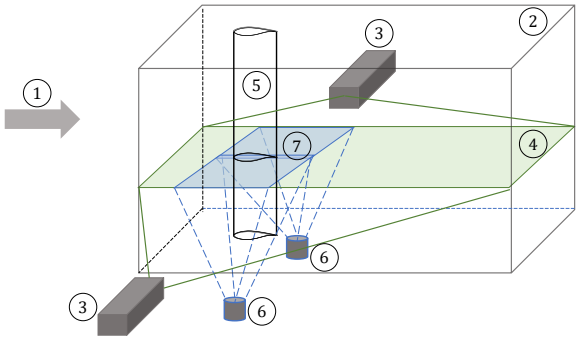

Figure 6.3: Schematic plot of the PIV setup with reference directions. The components of the measurement are: 1: incoming wind 2: test section 3: lasers 4: illumination plane 5: airfoil model 6: cameras 7: field of view.

Based on the convergence analysis shown in the appendix in Figure D.1, 50 cycles yield a low standard deviation of less than 2.5%. Therefore, in order to maintain a high

efficiency while measuring, for PIV measurements, 50 pairs of images were taken for each phase. The field of view (FoV) has a size of approximately 430 mm ×363 mm. The images were first filtered with a Butterworth high-pass filter [128] with a filter length of 7 images. Then the vector calculation is performed with two rounds of passes: the initial pass has an interrogation window size of 128 px ×128 px, with an overlap ratio of 50%; the second pass has an interrogation window size of 32 px ×32 px, with an overlap ratio of 75%. The last pass gives the vector pitch of 1.343 mm.

The uncertainty in the PIV measurements is determined based on the ensemble data size and the flow velocity fluctuations, as outlined by Ye et al. [109]. For each measured phase, 50 uncorrelated snapshots were collected, resulting in the standard uncertainty of the phase-averaged flow velocity being given by:

$$\varepsilon_{\overline{u}} = \frac{\sigma_u}{U_\infty \sqrt{N}} \tag{6.1}$$

σ_u is the representative standard deviation value of the streamwise velocity component (σ_u/U_∞ is approximately 0.1 in the airfoil's wake) and N represents the number of uncorrelated samples. This equation yields $\varepsilon_{\overline{u}} \approx 1.4\%$ for the present experiment.

The uncertainty of the Root Mean Square of the velocity fluctuations is estimated as (Sciacchitano and Wieneke [110]):

$$\varepsilon_{u'} = \frac{\sigma_u}{U_\infty \sqrt{2(N-1)}} \tag{6.2}$$

The expression yields $\varepsilon_{u'} \approx 0.1\%$.

6.3 Results and discussion: experimental investigation

6.3.1 Pressure, force and vortex dynamics during dynamic stall under reverse flow conditions

The analysis begins with a comprehensive examination of pressure fields, integrated aerodynamic forces, and flow structures across all test cases. A detailed discussion is presented of two representative cases: $\overline{\mathrm{AoA_r}}10\Delta10k0.1$ and $\overline{\mathrm{AoA_r}}20\Delta10k0.1$, characterized by a different number of suction regions on the airfoil surface.

Localized suction region case: $\overline{\mathbf{AoA_r}}10\Delta10k0.1$

This section discusses the case $\overline{\mathrm{AoA_r}}10\Delta10k0.1$, where the airfoil is operated at $\overline{\mathrm{AoA_r}} = 10^\circ$, $\Delta\mathrm{AoA_r} = 10^\circ$, and $k = 0.1$. Figure 6.4a presents the cycle-averaged pressure coefficient C_p on the suction side of the airfoil. From left to right of the plot, the colormap indicates the value of C_p during the upstroke period from $\mathrm{AoA_r} = 0^\circ$ to 20° and then downstroke to $\mathrm{AoA_r} = 0^\circ$. A schematic airfoil is plotted on the left of the figure with the leading edge ($x_c/c = 1$) and trailing edge ($x_c/c = 0$) aligned with the y axis. This airfoil is oriented at $\mathrm{AoA_r} = 0^\circ$, and the suction side is marked by the solid line. In the colormap, grey isolines indicate the C_p-levels in increments of $\Delta C_p = 0.25$. Meanwhile, the measured PIV phases are marked with vertical dashed lines where the vorticity fields are shown in Figure 6.5. During the initial upstroke motion from phase a (0°) until approximately phase c (4.0°), the

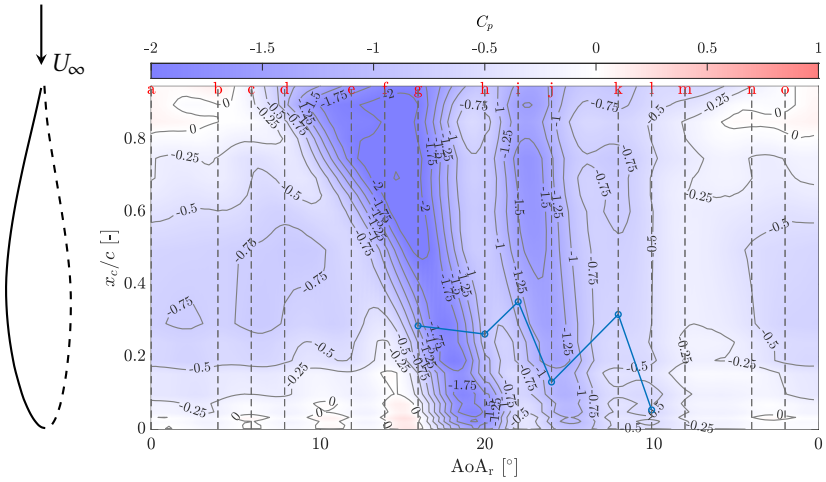

(a) Cycle-averaged pressure coefficient C_p on the suction surface over a pitching cycle. The vertical dashed lines represent measured PIV phases. The blue curve indicates the DSV core location in the chordwise direction, identified using the Γ_1 method [89, 90].

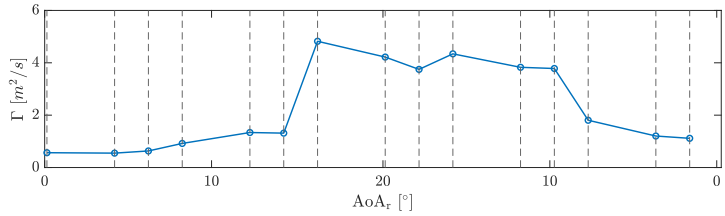

(b) Circulation of the DSV at the measured PIV phases.

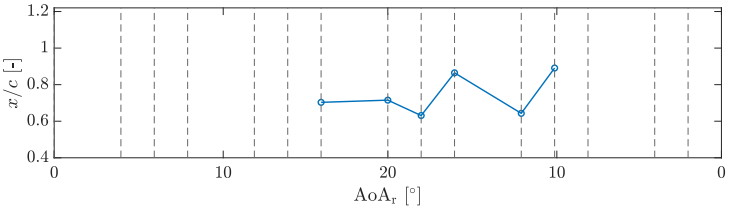

(c) Streamwise location of the DSV core

Figure 6.4: Pressure and DSV information at case $\overline{\text{AoA}_r}10\Delta10k0.1$: $\overline{\text{AoA}_r}$ = 10°, ΔAoA_r = 10°, and k = 0.1.

flow remains attached to the airfoil surface, with the lowest C_p near the highest thickness region ($x_c/c \approx 0.4$). The vorticity fields from the PIV measurement during these phases are shown from Figure 6.5a to 6.5d. Likewise, no major flow event happens, and the flow remains fully attached. The high vorticity in proximity to the airfoil surface is representative of the boundary layers forming on both the pressure and suction sides. Starting approximately at phase *d* and starting from the leading edge, C_p decreases to below zero. This is ascribed to the initiation of the DSV, which grows from the leading edge, where the flow separation (FS) can be seen from the suction side near the leading edge (from phase *d* to *f*). As the suction region grows larger, the DSV is formed as shown at phase

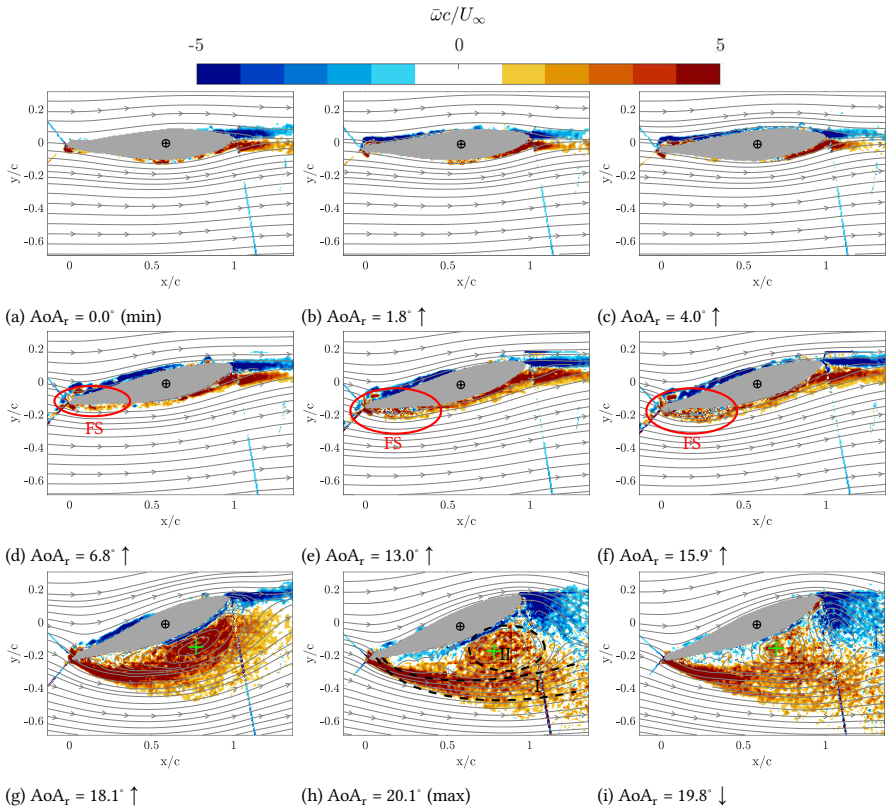

Figure 6.5: (continued)

g (AoA$_r$ = 18.1°, Figure 6.5g). At this phase, the DSV core (x_c/c = 0.28, marked by the blue curve in Figure 6.4a) is visible, which is close to the maximum thickness region of the airfoil. The vortex core location is evaluated using the Γ_1 method [89, 90]. The circulation of the DSV is shown in Figure 6.4b, which is obtained by integrating the positive vorticity in the wake of the airfoil region, thus excluding the negative vorticity, which is associated with the TEV. The result shows that Γ is initially relatively low until phase f and then increases sharply to a local maximum at phase g. It is noted that from phase a to g, the FoV of the PIV measurements is large enough to cover almost the full area of the vortex evolution; instead, from phase h onward, part of the vorticity from the DSV and TEV exits the field of view, yielding an under-estimation of Γ. At the same time, the C_p colormap indicates that during this upstroke period, the suction region (C_p below zero, blue areas) on the airfoil surface extends from less than 40% (phase e) to more than 90% (phase g) of the chord length.

Meanwhile, the pressure coefficient fields were derived from the PIV velocity measurements. The results are obtained by applying the Reynolds Averaged Navier–Stokes

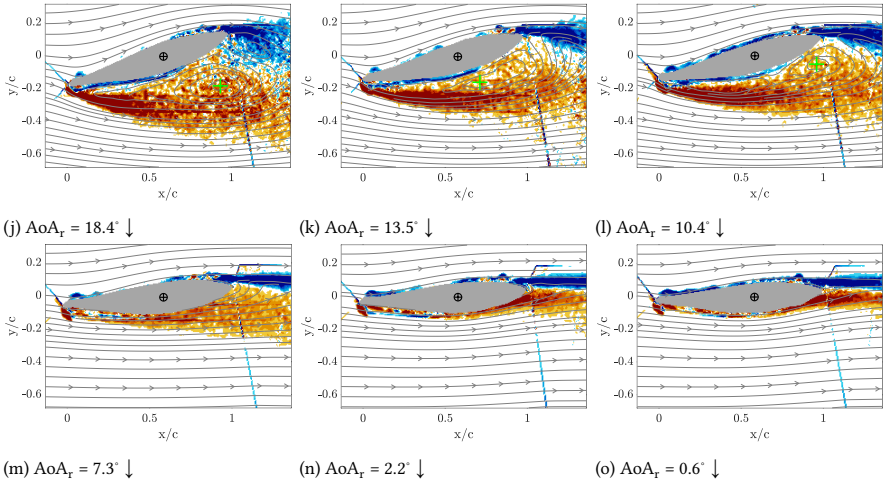

Figure 6.5: Vorticity field $\overline{\omega}c/U_\infty$ for case $\overline{\text{AoA}_r}10\Delta10k0.1$: $\overline{\text{AoA}_r}$ = 10°, ΔAoA_r = 10°, k = 0.1. Green cross represents the location of DSV core center, identified using Γ_1 method [89, 90]. FS: flow separation.

6

equation, and then solving for the static pressure using the Poisson equation formulation (see Section 2.4.2). The boundary conditions adopted in the computations are specified as follows. At the inlet (left boundary of the PIV flow field), a Dirichlet boundary condition is imposed, with the pressure value determined from the Bernoulli equation. For the remaining boundaries, including the top, bottom, and right boundaries of the PIV flow field as well as the boundary of the airfoil, Neumann boundary conditions are applied, where the pressure gradients are obtained from the Navier–Stokes equations. As shown in Figure 6.6, as the airfoil pitches up from phase *a* to *c* (aerodynamic leading edge moving down), a low-pressure region is present only on the airfoil suction (bottom) side, near the location of maximum thickness ($x_c/c \approx 0.4$). At phase *d*, the low-pressure region is concentrated at both the leading edge and the maximum thickness region. As the airfoil pitches up, higher suction takes place near the leading edge (phases *e* and *f*), and then the suction region grows bigger and reaches the maximum at phase *g*, where it covers the entire suction side of the airfoil, with the minimum C_p approaching −2. For higher angles of attack (phases *h* and *i*), the low-pressure region moves to the aerodynamic trailing edge, indicating the shedding of the DSV. Hence, it can be concluded that, during reverse flow dynamic stall, the DSV development follows a characteristic pressure propagation: first the leading edge experiences high suction, then (at $\text{AoA}_r \approx 18^\circ$) the suction region extends to the entire suction side of the airfoil, and finally (at $\text{AoA}_r \approx 20^\circ$) the vortex is shed downstream, resulting in the lower pressure near the aerodynamic trailing edge. This DSV-induced pressure fluctuation is widely recognized as the most dominant feature of dynamic stall and can be found in many works in the literature [72, 129, 130] for conventional dynamic stall. Similarly, for reverse flow cases, Datta et al. [74] and Potsdam et al. [75] also documented the reverse flow DSV-induced pressure wave for helicopters. A comparison of the DSV-induced pressure wave from conventional and reverse flow dynamic stall will be discussed later in this section.

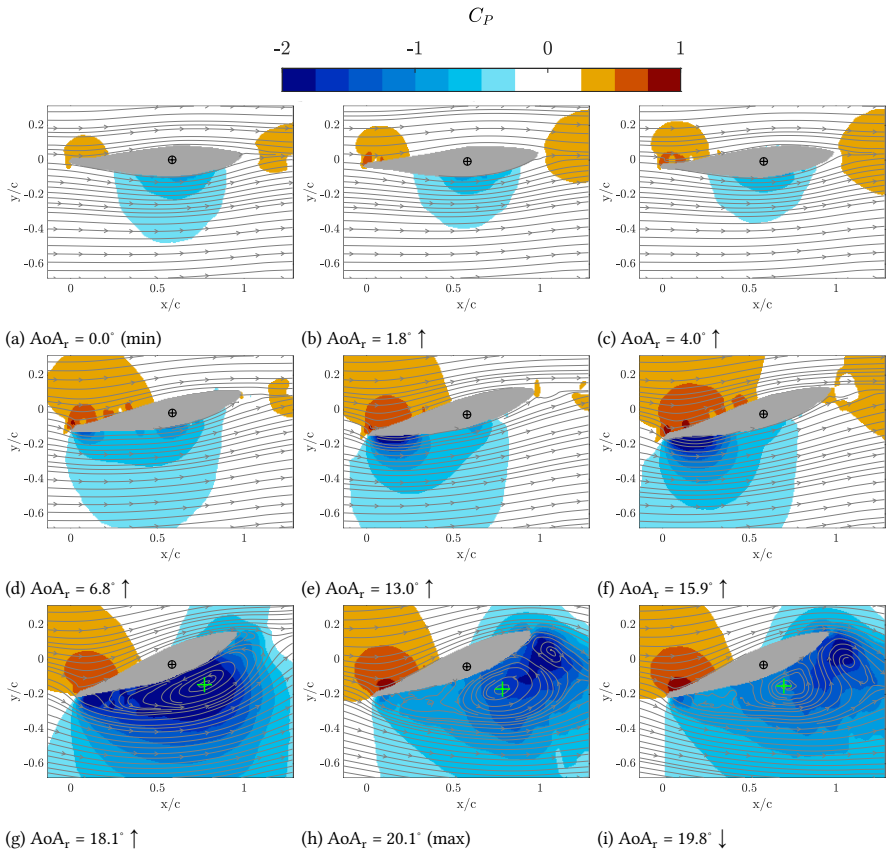

Figure 6.6: (continued)

Successively, when the airfoil pitches up to the largest AoA$_r$ of 20.1° (phase *h*, Figure 6.5h), it is observed that the negative vorticity at the trailing edge increases (larger blue area). At phase *g*, the local circulatory flow shows signs of TEV formation. This TEV is induced by the upstroke motion and the convection of the DSV towards the trailing edge, which both lead to the increase of adverse pressure gradient near the trailing edge. When the airfoil pitches to the maximum angle at phase *h*, the TEV grows bigger, which causes a higher suction near the trailing edge region. At the same time, from phase *g* to *h*, the DSV partially separates from the airfoil surface (marked by region I in Figure 6.5h). Meanwhile, the inner part of the DSV remains attached to the airfoil, which is marked by region II in Figure 6.5h. Overall, this partial separation leads to a decrease of Γ within the FoV (Figure 6.4b). After reaching the maximum AoA$_r$, the airfoil starts to pitch down (aerodynamic trailing edge moving down) and the vorticity field is shown from phase *i* (Figure 6.5i) to phase *o* (Figure 6.5o). As AoA$_r$ decreases to 19.8° (phase *i*, Figure 6.5i), the TEV grows larger. Together with the downstroke movement of the airfoil, the recirculating part of the DSV moves upstream, as shown in Figure 6.4c from x/c = 0.72 (phase *h*)

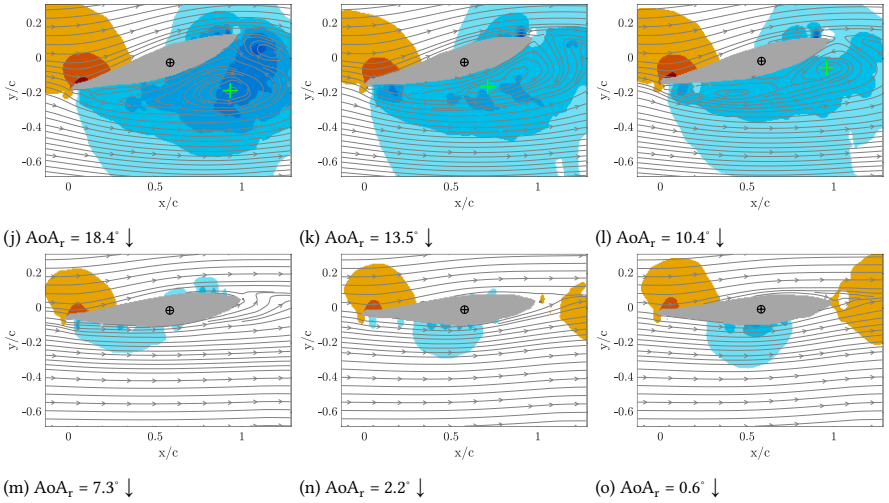

Figure 6.6: Pressure coefficient field C_p for case $\overline{\text{AoA}_r}10\Delta10k0.1$ derived from PIV measured velocity fields.

to x/c = 0.63 (phase *i*). Due to the upstream motion of the DSV during this period, the negative C_p region at phase *i* expands towards the upstream location, while for the previous phase (*h*), the negative C_p region concentrates at the trailing edge region, which can be seen in Figure 6.4a. Following the partial separation phases of *h* and *i*, at phase *j* (Figure 6.5j), the attached DSV grows, fed by the boundary layer separating at the aerodynamic leading edge. This growth is facilitated by the TEV shedding, which allows the DSV to develop unimpeded. This leads to an increase in circulation measured inside the FoV. As the airfoil continues pitching down to approximately 7.3° (phase *m*), the DSV moves away from the trailing edge, and the flow begins to reattach onto the airfoil surface progressively. During this period, the circulation within the FoV drops sharply and returns to a value close to zero by the end of the cycle.

The aerodynamic force and moment during the pitching process for this case are also examined. The results are obtained through the integration of the measured pressure. The hysteresis loops of the lift coefficient C_l and pitching moment coefficient C_m are shown in Figure 6.7. Solid lines indicate the upstroke motion, while the dashed lines represent the downstroke motion. These two lines represent the cycle averaged value, while the red shaded area (very thin in the plot) represents the 95% confidence interval level. The measured PIV phases are also marked on the lines. As the airfoil pitches up from phase *a* to phase *c*, the flow remains attached; thus, both C_l and C_m vary approximately linearly with the angle of attack. From phase *c* to phase *g*, C_l keeps decreasing, owing to the increasing suction from the growing DSV. In this period from phase *c* to phase *f*, as the airfoil pitches up, the DSV-induced suction at the leading edge generated ahead of the pitching axis (as shown in Figure 6.6d to Figure 6.6f) creates a counter-clockwise (negative) moment on the airfoil. At the same time, the suction near the trailing edge only has a minor impact on generating the clockwise (positive) moment. Thus from phase *c* to phase *f*, C_m decreases. At phase *g*, the DSV causes the huge suction region over 90% of the airfoil length from the

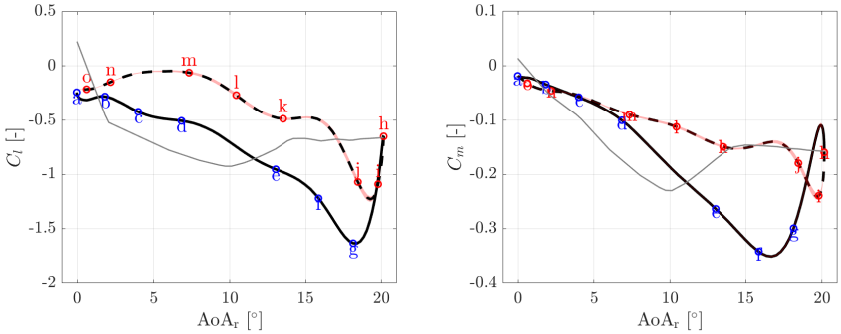

(a) (b)

Figure 6.7: Hysteresis loop of the lift coefficient C_l, and pitching moment coefficient C_m for case $\overline{\text{AoA}_r}10\Delta10k0.1$. Line styles and confidence intervals as described in the text. PIV phases are marked on the curves.

leading edge (see Figure 6.4a). This suction, centered on the downstream (right-hand) side of the airfoil pitching axis, creates a clockwise (positive) moment. This is the reason for the increase of C_m at phase g. Meanwhile, at phase g, C_l reaches the maximum absolute value while the DSV is still attached and features maximum strength. Between phases g and h, the partial detachment of the DSV leads to a drop in C_l. Between these two phases, C_m also decreases due to the decrease in suction on the airfoil surface. Afterward, as the airfoil pitches up (phases h to phase j), both C_l and C_m first feature an increase in magnitude due to the higher suction induced by the attached (partial) DSV (phases h to i), and then (phases i to j) a decrease in magnitude as the DSV convects away from the airfoil. As the airfoil pitches further down from phase j to phase o until the end of the downstroke cycle, the DSV convects further away from the trailing edge, and C_l and C_m decrease in magnitude. Overall, the hysteresis loops indicate two times the sharp increase of C_l and C_m magnitude, which are related to the DSV initial growth (phases d to g) and the attached DSV moving upstream (phases h to i), respectively. The second increase in C_l and C_m is smaller compared to the first one, as (1) the strength of the attached DSV is smaller compared to the original DSV, (2) the second increase happens during the downstroke period, therefore the DSV decreases in strength when AoA_r returns back to 0.

The static C_l measurement is marked as the grey line in Figure 6.7a. During the range of the pitching angles from 0° to 20° (AoA from 180° to 160°), C_l decreases to the minimum of −0.93 at 10.1°. Afterwards, the C_l magnitude decreases due to flow separation. After 14.2°, the steady C_l curve remains relatively constant at approximately −0.67. The C_p distributions on the airfoil surface from 10° to 20° are shown in Figure 6.8a. The suction side is represented as a solid line and the pressure side as a dashed line. Initially from 10° to 13°, the suction side has a C_p peak region near the aerodynamic leading edge ($x_c/c = 1$, which is the geometric trailing edge), which is ascribed to the flow separation near the sharp leading edge. From 14° to 20°, the flow on the suction side remains fully separated, with only minor changes near the trailing edge ($x_c/c = 0$) for the pressure side. This leads to the stable C_l after 14.2°.

Compared to the steady C_l, during pitching (Figure 6.7a), the upstroke motion leads

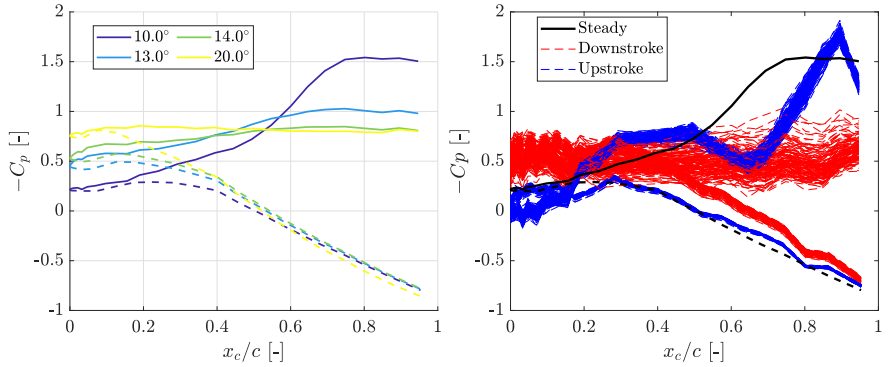

Figure 6.8: C_p distribution with $\mathrm{AoA_r}$ (a) from 10° to 20° for steady measurement (solid lines represent suction side and dashed lines represent pressure side) and (b) at 10° for both the steady and unsteady cases.

to a higher magnitude and a delayed magnitude drop near phase g. Similarly, compared to the static C_m (the grey curve in Fig. 6.7b), dynamic C_m presented at this pitching case also shows a lower minimum from approximately −0.22 (static) to −0.35 (dynamic) and a delayed magnitude recovery. This aligns with conventional dynamic stall results, where a lift and moment overshoot is reported [64, 66]. Meanwhile, it is also shown that for $\mathrm{AoA_r}$ between 1.2° and 12.6°, both upstroke and downstroke motions lead to a lower C_l magnitude compared to the static case. The C_p distributions compared to the steady C_l at 10° are shown in Figure 6.8b. For the steady measurement, the suction side is marked as the black solid line, and the pressure side is marked as the black dashed line. For the pitching cases, lines of C_p distribution when $|\mathrm{AoA_r} - 10| \leq 0.2$ are plotted. The pressure side C_p remains close to the steady case, with the main differences lying in the suction side C_p. During the downstroke motion, the flow remains fully separated from the airfoil surface, which creates the low flat C_p on the suction side. This uniform C_p is also shown in Figure 6.4a (marked by line *o*) and C_p map (Figure 6.6l). These results contribute to a lower C_l compared to the steady measurement during the downstroke period. During the upstroke period, strong suction regions are observed near the leading edge and around the pitching axis location ($x_c/c = 0.4$), as evidenced in Figure 6.6d and 6.6e. The lower $-C_p$ magnitude outside these regions leads to the deviation from the suction side of the steady result, leading to an overall decrease in C_l values.

Through the examination of all DSV-present cases, suction side C_p in a reverse flow condition shows distinct patterns where multiple suction regions can be found. Appendix Figure D.6 reports the results for all the tested cases. In order to compare the difference between conventional and reverse flow dynamic stall, a conventional dynamic stall case tested in this campaign is shown in Figure 6.9, where $\overline{\mathrm{AoA}} = 10°$, $k = 0.16$, and $\Delta\mathrm{AoA} = 10°$. The phases measured by PIV are marked by vertical dashed lines, and the corresponding vorticity fields are shown in Figure D.8 in the Appendix D.5. Note that the colormap and colorbar range are modified in order to match the result as shown in Visbal and Benton [129]. In their research, large eddy simulation was performed on a NACA 0012 airfoil at angles of attack ramped up from a minimum value of AoA = 4° to a maximum of AoA = 30°

[131]. During the upstroke period, the conventional test case in this campaign shows similar patterns to the reverse-flow case, where the suction starts from the leading edge and extends towards the trailing edge as the airfoil pitches up. However, the leading edge is characterized by extremely low pressure ($C_p < -5$) between approximately AoA = 10° to a maximum of AoA = 20°. This extremely low pressure is ascribed to the development and burst of the laminar separation bubble (LSB) [131].

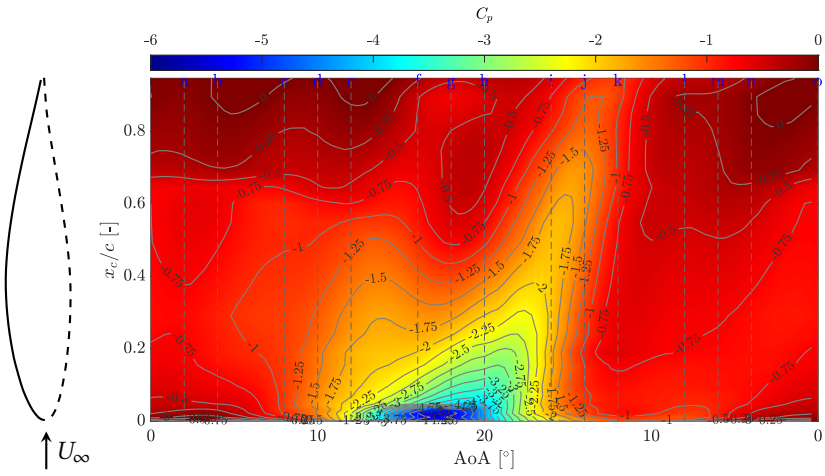

Figure 6.9: Cycle-averaged pressure coefficient C_p on the suction surface at case $\overline{\text{AoA}}10\Delta10k0.16$. The PIV measured phases are marked by vertical dashed lines and the vorticity fields of which are shown in Figure D.8.

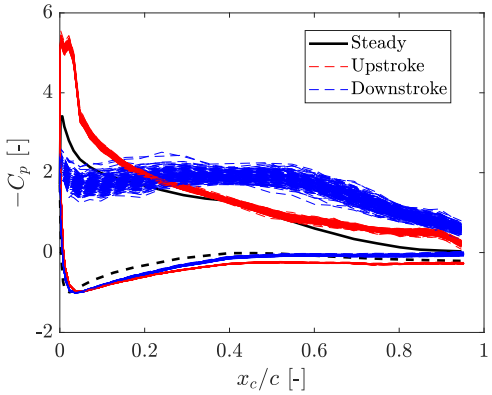

Figure 6.10: C_p distribution at 18° for both the steady and unsteady cases for the conventional dynamic stall case $\overline{\text{AoA}}10\Delta10k0.16$.

For this conventional (non-reverse) flow case, the C_p distribution on the airfoil surface at AoA = 18° (phase f for the upstroke) is shown in Figure 6.10. The unsteady cases are plotted for $|\text{AoA} - 18| \leq 0.2$ because achieving the exact integer angle of 18° is not possible from the pitching motion. The result shows that at phase f (the red curves), C_p from

the suction side exceeds the value from the steady measurement. Especially at the leading edge region (between x_c/c = 0.002 and 0.03), the C_p overshoot leads to a plateau near $-C_p$ = 5.3, which indicates the presence of a leading edge separation bubble. From the PIV vorticity field, it is shown that from phase *d* (Figure D.8d) to phase *f* (Figure D.8f), the flow separation occurs near the trailing edge of the airfoil's suction side. From phase *g* (Figure D.8g) to phase *i* (Figure D.8i), the trailing edge separation leads to the roll-up of the boundary layer and eventually to the formation of the DSV at phase *i*. Therefore, for conventional cases, the LSB at the leading edge plays an important role, which creates abrupt pressure drops prior to the DSV development. Similar spatial-temporal suction side C_p pattern can be found in many previous works in the literature [72, 129, 130]. In contrast, reverse flow conditions exhibit a more gradual pressure decrease during the initial DSV formation period, as consistently observed across all DSV-present cases (Appendix Figure D.6). In forward flow, the streamlined leading edge accelerates the flow smoothly, creating a suction peak just downstream of $x_c/c \approx 0.002$, followed by a deceleration. In reverse flow, the sharp leading edge triggers immediate separation even at a small angle of attack, resulting in a flat, low-pressure plateau ($-C_p \approx 1.5$) in the separated flow region (Figure 6.8). This lack of acceleration/deceleration contrasts sharply with the C_p dynamics of forward flow.

Overall, during one pitching cycle of case $\overline{\text{AoA}_\text{r}}10\Delta10k0.1$, a single DSV is shed at the end of the downstroke, while partial flow separation occurs once during the upstroke due to the increasing angle of attack. This experimental observation captures the detailed vortex evolution throughout the entire pitching cycle in a reverse flow dynamic stall scenario. It suggests that the DSV shedding process is influenced by the interactions with the boundary layer emanating from the sharp leading edge, which continues to feed into the still-attached portion of the DSV. In comparison, Hodara et al. [132] observed two DSVs in one pitching cycle during their reverse flow dynamic stall experiments using a NACA 0012 airfoil at $\overline{\text{AoA}_\text{r}} = -8.9^\circ$, $\Delta\text{AoA}_\text{r} = 9.9^\circ$, $Re = 3.3 \times 10^5$, and $k = 0.16$. Their C_p maps indicated two distinct suction regions, and instantaneous PIV images showed that the second DSV formed during the downstroke. Notably, the vortices in their study were fully separated, in contrast to the partially attached vortices observed in the present work. Such partially attached vortices are not only linked to additional force fluctuations but also influence flow reattachment dynamics and the unsteady aerodynamic loading. Additionally, in conventional dynamic stall cases, the dynamic stall development typically involves an initial instability stage followed by the formation of a DSV [71], which differs from the behavior observed under reverse flow conditions. The present research provides a detailed physical understanding of the DSV development mechanism in reverse flow, showing that (1) the flow separation at the initial stage of DSV development leads to a gradual C_p decrease compared to the conventional dynamic stall case, where the LSBs lead to a suction peak before the DSV forms. (2) Moreover, the partial DSV attachment and the boundary layers feeding of the attached DSV lead to additional force fluctuations during the pitching cycle.

Extended suction region case: $\overline{\text{AoA}_\text{r}}20\Delta10k0.1$

This section discusses the flow physics of case $\overline{\text{AoA}_\text{r}}20\Delta10k0.1$, where only the mean pitching angle is changed to 20° compared to the previous case (case $\overline{\text{AoA}_\text{r}}10\Delta10k0.1$). The

suction side C_p and DSV evolution are shown in Figure 6.11, the PIV vorticity fields are shown in Figure 6.12, and C_p obtained from the PIV flow field are present in Figure D.7.

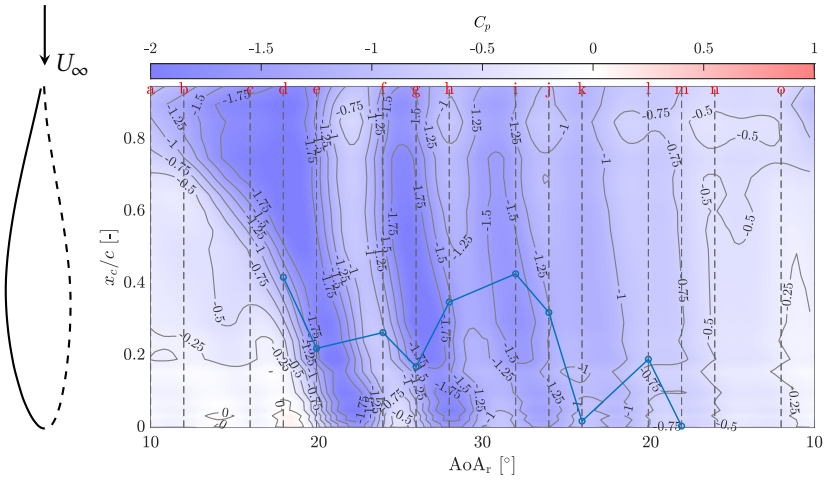

(a) Cycle-averaged pressure coefficient C_p on the suction surface over a pitching cycle. The blue curve indicates the DSV core location in the chordwise direction, identified using the Γ_1 method [89, 90].

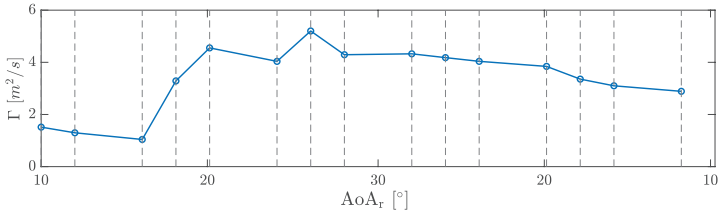

(b) Circulation of the DSV at the measured PIV phases.

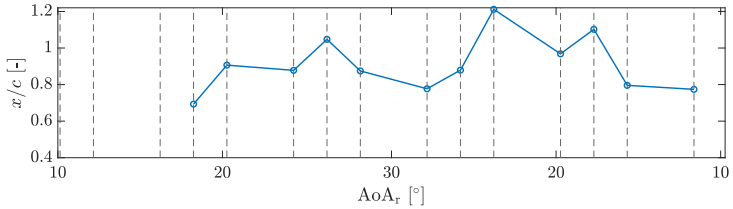

(c) Streamwise location of the DSV core.

Figure 6.11: Pressure and DSV information at case $\overline{\text{AoA}_r}20\Delta10k0.1$: $\overline{\text{AoA}_r}$ = 20°, ΔAoA_r = 10°, and k = 0.1.

Two major differences in pressure imprint can be found between these two cases. First, the suction region persists over a significantly larger portion of the pitching cycle in case $\overline{\text{AoA}_r}20\Delta10k0.1$ compared to $\overline{\text{AoA}_r}10\Delta10k0.1$. While the lower angle case ($\overline{\text{AoA}_r}10\Delta10k0.1$) exhibits the maximum suction near mid-cycle (phase *g*, corresponding to AoA$_r$ = 18.1°), the higher angle case ($\overline{\text{AoA}_r}20\Delta10k0.1$) develops suction immediately at the minimum pitch angle of 10°, maintaining it throughout the motion. Examples can be seen from phase *a* (Figure 6.12a and Figure D.7a) and *b* (Figure 6.12b and Figure D.7b), where the leading edge flow separation is present at both phases, yielding a suction pres-

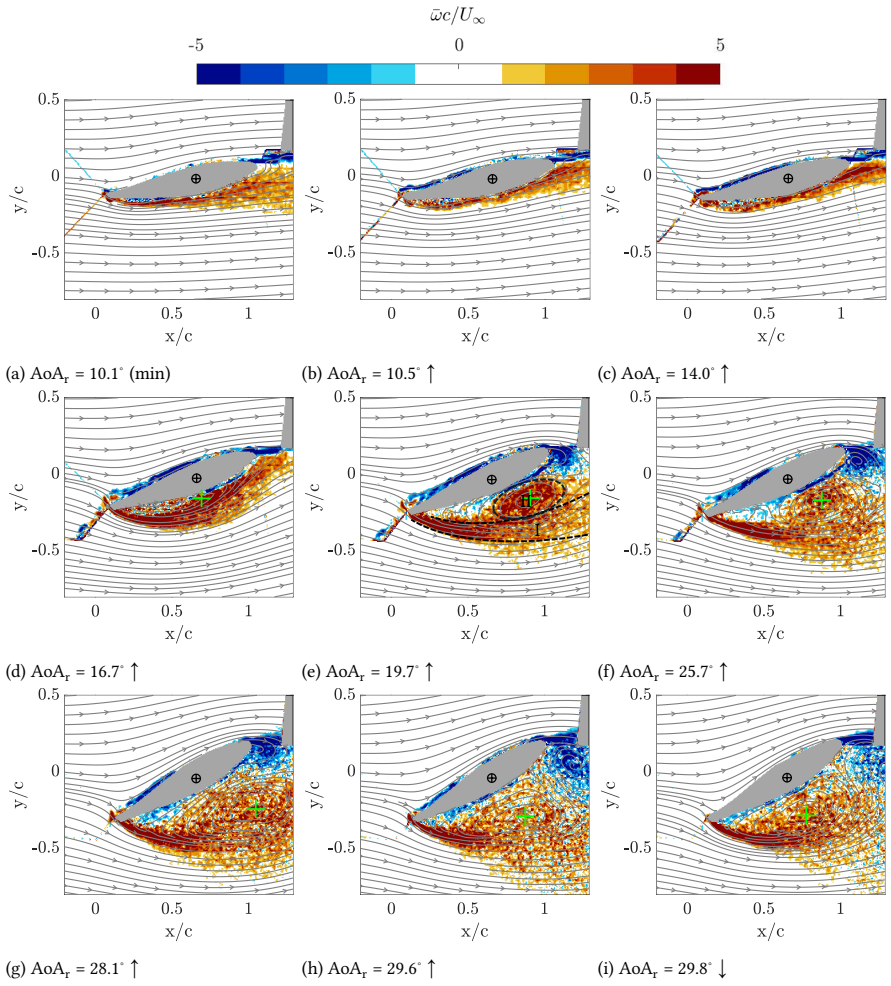

Figure 6.12: (continued)

sure growth at the beginning of the upstroke cycle. It is also noticed from phase *o*, the last captured downstroke phase, that the boundary layer emanating from the aerodynamic leading edge is still detached from the airfoil surface (Figure 6.12o), which indicates that the growth of the DSV starts from the previous cycle at the end of the downstroke period. Overall, this wider suction region on the airfoil surface is inherent for case $\overline{\text{AoA}_\text{r}}20\Delta10k0.1$ as it has a higher AoA$_\text{r}$ during pitching. As a result, C_l and C_m for case $\overline{\text{AoA}_\text{r}}20\Delta10k0.1$ (Figure 6.13) already feature large variations with the angle of attack near the small AoA$_\text{r}$ region (from phase *o* to *a* to *b*).

Secondly, unlike case $\overline{\text{AoA}_\text{r}}10\Delta10k0.1$, where the partial separation of the DSV happens once, the C_p map of case $\overline{\text{AoA}_\text{r}}20\Delta10k0.1$ shows three major enclosed suction areas on the

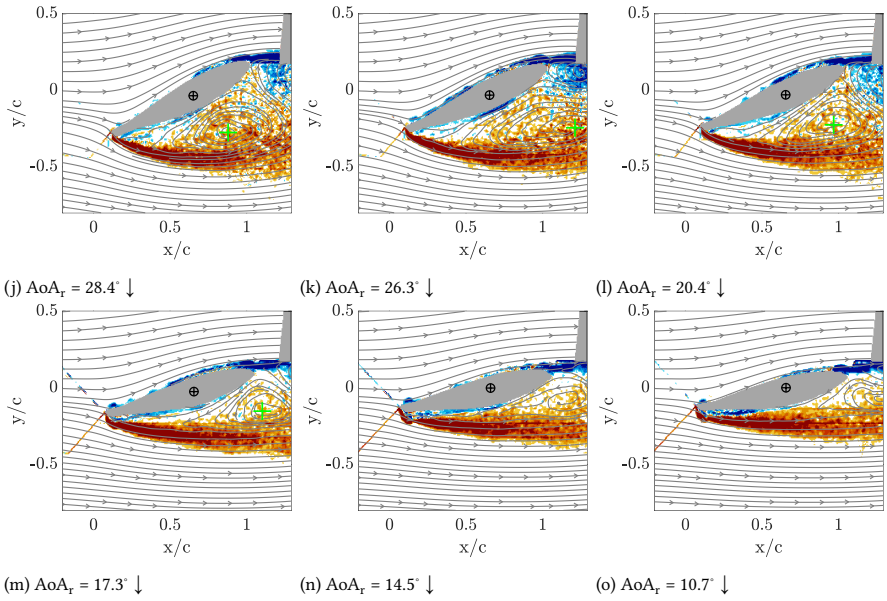

Figure 6.12: Vorticity field $\overline{\omega}c/U_\infty$ for case $\overline{\text{AoA}_r}20\Delta10k0.1$: $\overline{\text{AoA}_r}$ = 20°, ΔAoA_r = 10°, k = 0.1. Green cross represents the location of DSV core center, identified using Γ_1 method [89, 90].

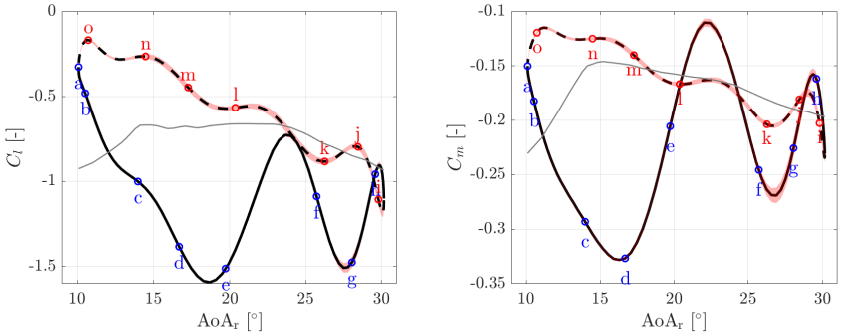

Figure 6.13: Hysteresis loop of the lift coefficient C_l, and pitching moment coefficient C_m at case $\overline{\text{AoA}_r}20\Delta10k0.1$. Line styles and confidence intervals as described in the text. PIV phases are marked on the curves.

airfoil suction side, which are linked to the multiple partially separated DSV. Initially, from phase *a* (Figure 6.12a) to phase *d* (Figure 6.12d), the DSV starts forming from the leading edge, becoming fully visible at phase *d*. During this period, the DSV remains attached to the airfoil surface; Γ is initially low up to phase *c*, and then it increases at phase *d* due to the vorticity feeding from the boundary layer. As the airfoil pitches up from phase *d* to phase *e* (Figure 6.12e) and *f* (Figure 6.12f), the DSV starts to detach from the airfoil surface. Similar to case $\overline{\text{AoA}_r}10\Delta10k0.1$, the DSV is partially shed, marked by the region

I in Figure 6.12e, while the inner part remains attached to the airfoil surface (marked by region II). Different from case $\overline{\text{AoA}_\text{r}}10\Delta10k0.1$, this interaction happens during the early stage of the upstroke period, which is attributed to the higher AoA_r for this case.

Similarly, from phase *g* to phase *h*, from phase *i* to phase *j*, and from phase *k* to phase *l*, the same partial separation can be observed: at the earlier phase of the two (phase *g*, *i* or *k*), the C_p distribution on the suction surface (Figure 6.11a) reaches the local minimum, with the vorticity field featuring a round-contour DSV, which is attached to the airfoil surface; At the latter phase (phase *h*, *j* or *l*), the boundary layer does not fully recirculate back towards the surface; instead, its outer part sheds into the wake. Owing to this, phases *e*, *g*, *i*, and *k* lie roughly near the local peak of C_l, and the C_l recovery happens at the corresponding following phases, as shown in Figure 6.13a.

Apart from the hysteresis of C_l, the hysteresis of C_m also exhibits similar characteristics compared to case $\overline{\text{AoA}_\text{r}}10\Delta10k0.1$, where the location of the DSV highly influences the variation of the C_m value. For example, during the initial DSV formation period, the low pressure region starts from the leading edge (phase *a*, (Figure 6.12a and D.7a) and then extends to close to the pitching axis (Figure 6.12d and D.7d). As a result, it creates a counter-clockwise moment, which leads to the decrease in C_m. After the DSV development in phase *d*, at phase *e* (Figure 6.12e and D.7e), the partially attached DSV is located on the right-hand side of the pitching axis, generating a clockwise motion, which increases C_m.

Therefore, compared to the single partial separation observed in case $\overline{\text{AoA}_\text{r}}10\Delta10k0.1$, case $\overline{\text{AoA}_\text{r}}20\Delta10k0.1$ presents four partial separations, which is a more complex flow dynamics due to the higher pitching angles. Although previous research on conventional dynamic stall also focused on the development of the DSV [71, 133, 134], the influence of the partial separation was not discussed. Our experimental campaign reveals that the partial separation leads to the secondary growth of the DSV, which can happen multiple times during the pitching cycle, depending on different pitching parameters (as shown in Figure D.6). This partial separation extends the overall DSV development time and delays the time at which the DSV detaches. In addition, the DSV vortex formation leads to an increased magnitude of the aerodynamic lift, followed by a reduction when partial DSV separation occurs; as indicated before, this process occurs multiple times (specifically for case $\overline{\text{AoA}_\text{r}}20\Delta10k0.1$, four times) during the oscillation cycle.

6.3.2 POD analysis

As established, dynamic stall under reverse flow conditions presents a complex aerodynamic phenomenon marked by multiple (partial) separations and shedding of the DSV. Building on previous POD analyses of conventional dynamic stall [70, 77, 123], we employ Proper Orthogonal Decomposition (POD) of the pressure coefficient Cp on the suction side of the airfoil, across all cases where a DSV is present, to identify the dominant flow features characterizing the reverse flow conditions. The methodology is introduced in Section 2.4.1. The energy contents from the first two POD modes are shown in Table 6.3, clearly indicating that the first two modes together contribute to about 90% of the total energy. The results are grouped by $\overline{\text{AoA}_\text{r}}$. For cases with $\overline{\text{AoA}_\text{r}} = 5^\circ$, a single dominant mode captures more than of 76% of the total energy, suggesting that the flow is highly

dominated by one distinct flow pattern. For the other cases with $\overline{\text{AoA}_\text{r}}$ = 10°, 15° and 20°, the first mode decreases its dominance, with the lowest value 46.9% of the total energy. This indicates that for larger $\overline{\text{AoA}_\text{r}}$, two prominent flow patterns coexist, suggesting a more complex flow dynamics compared to the single-mode dominance observed at lower angles. The different flow regimes are color-coded, which will be explained at the end of this section.

Table 6.3: Energy distribution of the most dominant mode(s) across all cases, grouped by $\overline{\text{AoA}_\text{r}}$. The flow regimes are color-coded as follows: orange for DSV-dominated flow, black for TEV-dominated flow, and blue for mixed-energy cases where both vortices contribute significantly. The classification criteria for these regimes are discussed later in this section.

Case	E_1 [%]	E_2 [%]	Case	E_1 [%]	E_2 [%]	Case	E_1 [%]	E_2 [%]
$\overline{\text{AoA}_\text{r}}$5Δ10$k$0.05	84.6	8.9	$\overline{\text{AoA}_\text{r}}$10Δ10$k$0.13	57.9	33.2	$\overline{\text{AoA}_\text{r}}$15Δ15$k$0.05	62.3	28.1
$\overline{\text{AoA}_\text{r}}$5Δ10$k$0.08	84.4	9.2	$\overline{\text{AoA}_\text{r}}$10Δ10$k$0.16	58.3	32.6	$\overline{\text{AoA}_\text{r}}$15Δ15$k$0.1	54.9	37.9
$\overline{\text{AoA}_\text{r}}$5Δ10$k$0.1	85.6	8.1	$\overline{\text{AoA}_\text{r}}$10Δ10$k$0.18	58.8	31.4	$\overline{\text{AoA}_\text{r}}$20Δ10$k$0.05	69.7	26.9
$\overline{\text{AoA}_\text{r}}$5Δ10$k$0.13	87.7	6.5	$\overline{\text{AoA}_\text{r}}$10Δ15$k$0.05	75.9	18.4	$\overline{\text{AoA}_\text{r}}$20Δ10$k$0.08	57.6	38.1
$\overline{\text{AoA}_\text{r}}$5Δ10$k$0.16	89.9	4.7	$\overline{\text{AoA}_\text{r}}$10Δ15$k$0.1	65.3	28.8	$\overline{\text{AoA}_\text{r}}$20Δ10$k$0.1	58.4	35.9
$\overline{\text{AoA}_\text{r}}$5Δ10$k$0.18	91.2	4.3	$\overline{\text{AoA}_\text{r}}$15Δ5$k$0.05	90.9	7.8	$\overline{\text{AoA}_\text{r}}$20Δ10$k$0.13	54.8	39.1
$\overline{\text{AoA}_\text{r}}$5Δ15$k$0.05	80.8	14.2	$\overline{\text{AoA}_\text{r}}$15Δ5$k$0.1	63.6	32.2	$\overline{\text{AoA}_\text{r}}$20Δ10$k$0.16	55.8	38.2
$\overline{\text{AoA}_\text{r}}$5Δ15$k$0.1	76.6	18.3	$\overline{\text{AoA}_\text{r}}$15Δ5$k$0.16	52.4	40.9	$\overline{\text{AoA}_\text{r}}$20Δ10$k$0.18	57.5	35.8
$\overline{\text{AoA}_\text{r}}$10Δ5$k$0.05	56.9	31.9	$\overline{\text{AoA}_\text{r}}$15Δ5$k$0.21	60.4	32.1	$\overline{\text{AoA}_\text{r}}$20Δ15$k$0.05	67.7	26.4
$\overline{\text{AoA}_\text{r}}$10Δ5$k$0.1	60.6	28.2	$\overline{\text{AoA}_\text{r}}$15Δ10$k$0.05	54.4	36.7	$\overline{\text{AoA}_\text{r}}$20Δ15$k$0.1	54.2	39.1
$\overline{\text{AoA}_\text{r}}$10Δ5$k$0.16	68.7	20.8	$\overline{\text{AoA}_\text{r}}$15Δ10$k$0.08	54.1	38.2	$\overline{\text{AoA}_\text{r}}$20Δ15$k$0.16	51.0	40.8
$\overline{\text{AoA}_\text{r}}$10Δ5$k$0.21	75.9	14.4	$\overline{\text{AoA}_\text{r}}$15Δ10$k$0.1	52.6	39.7	$\overline{\text{AoA}_\text{r}}$25Δ10$k$0.18	75.7	21.0
$\overline{\text{AoA}_\text{r}}$10Δ10$k$0.05	57.8	27.6	$\overline{\text{AoA}_\text{r}}$15Δ10$k$0.13	46.9	45.2	$\overline{\text{AoA}_\text{r}}$25Δ15$k$0.05	71.7	25.5
$\overline{\text{AoA}_\text{r}}$10Δ10$k$0.08	59.7	28.4	$\overline{\text{AoA}_\text{r}}$15Δ10$k$0.16	50.3	42.0	$\overline{\text{AoA}_\text{r}}$25Δ15$k$0.1	60.6	33.9
$\overline{\text{AoA}_\text{r}}$10Δ10$k$0.1	59.2	30.9	$\overline{\text{AoA}_\text{r}}$15Δ10$k$0.18	53.6	37.9	$\overline{\text{AoA}_\text{r}}$25Δ15$k$0.16	55.1	38.2

To investigate the spatial location of these high-energy activities, the mode shapes ϕ of the first mode for all the cases are shown in Figure 6.14, where each sub-figure contains the result from the cases with the same $\overline{\text{AoA}_\text{r}}$. Since POD mode shapes are determined up to an arbitrary sign, we analyze their absolute peak values to identify the most dominant flow features.

For $\overline{\text{AoA}_\text{r}}$ = 5° and 10° cases (Figure 6.14a and Figure 6.14b), the first mode shapes exhibit uniform peaks near the aerodynamic leading edge (x_c/c = 1), indicating that the most dominant modes are concentrated in this region. This peak in the mode shape is likely associated with the dynamics, namely formation and growth, of the DSV. Conversely, for $\overline{\text{AoA}_\text{r}}$ = 15°, the mode shapes become less monotonic; in general, two local maxima are present, one at the leading edge and one at the trailing edge, respectively. For example, for the case $\overline{\text{AoA}_\text{r}}$15Δ10$k$0.1 (the red curve in Figure 6.14c), the mode shape is relatively flat, with the value of −0.24 at x_c/c = 0.69 and −0.25 at x_c/c = 0.19. This means that, in such a case, the flow contains equally significant energy at the leading edge and trailing

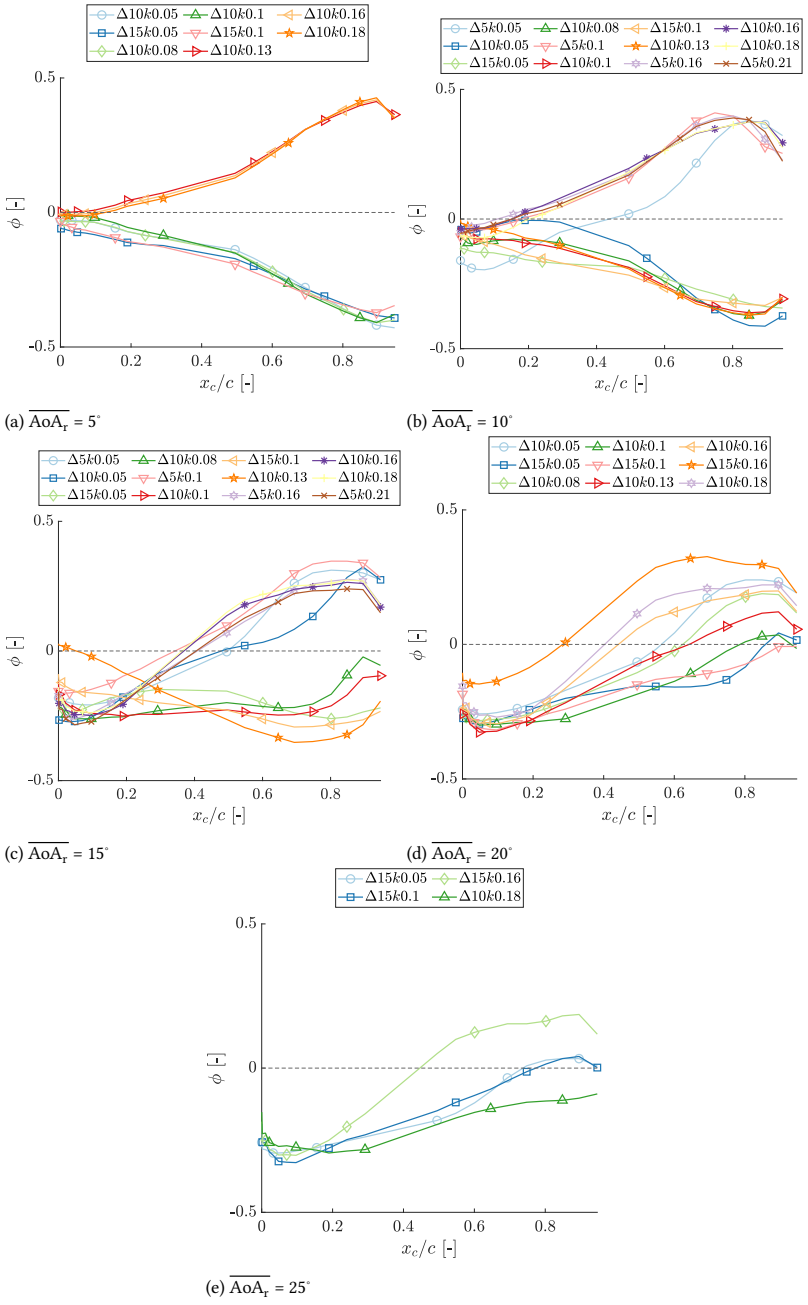

Figure 6.14: POD mode shapes of the most dominant mode (mode 1) for each $\overline{\text{AoA}_r}$ case.

edge, which suggests that the DSV and the TEV contribute equally to the flow dynamics. When $\overline{\text{AoA}_\text{r}} = 20^\circ$ and 25°, even though some cases still shows a mixture of energy from both the leading edge and trailing edge, the other cases (including $\overline{\text{AoA}_\text{r}}20\Delta10k0.1$, $\overline{\text{AoA}_\text{r}}20\Delta10k0.13$, $\overline{\text{AoA}_\text{r}}20\Delta15k0.05$, $\overline{\text{AoA}_\text{r}}20\Delta15k0.1$, $\overline{\text{AoA}_\text{r}}25\Delta10k0.18$, $\overline{\text{AoA}_\text{r}}25\Delta15k0.05$, and $\overline{\text{AoA}_\text{r}}25\Delta15k0.1$) start to exhibit dominance from the trailing edge only. This result suggests that, at higher mean angles of attack, the flow is dominated by the dynamics of the TEV.

To validate the assumption that links mode shapes to vortex dynamics, the rest of this section analyzes examples of DSV-dominated and TEV-dominated flows using POD.

DSV-dominated flow

As a representative case, we consider case $\overline{\text{AoA}_\text{r}}10\Delta10k0.1$, where the most dominant mode exhibits a pronounced peak in the leading edge region. The first two mode shapes (ϕ_1 and ϕ_2) and the time average C_p (ϕ_0) at each chordwise location are shown in Figure 6.15. The temporal coefficient of the first two modes, along with the cycle-averaged Cp variation at chordwise location $x_c/c = 0.05$ and 0.95, are presented in Figure 6.16. These two locations are chosen since they are the peak locations of ϕ_1 and ϕ_2.

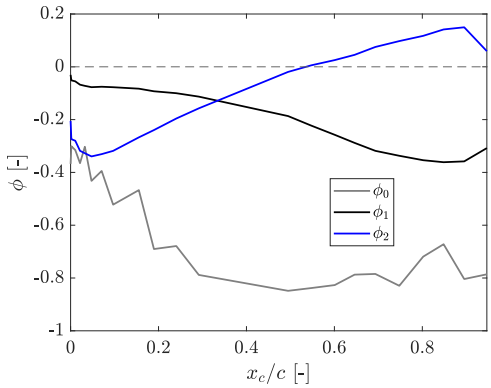

Figure 6.15: POD mode shapes of the time averaged C_p (ϕ_0) and the first two modes(ϕ_1 and ϕ_2) at case $\overline{\text{AoA}_\text{r}}10\Delta10k0.1$.

Overall, ϕ_0 experiences a decreasing trend from the trailing edge to the leading edge, which is representative of a large flow separation occurring from the leading edge and covering most of the suction side of the airfoil. While ϕ_1 exhibits a peak near the leading edge ($x_c/c = 1$), ascribed to the formation and growth of the DSV, ϕ_2 has a local peak near the trailing edge region, which is attributed to the TEV dynamics. From the perspective of the temporal coefficient (Figure 6.16), mode 1's temporal coefficient exhibits an increasing trend during the upstroke cycle; during this period, the formation of the DSV leads to an increasing leading edge suction. Consequently, the first peak of mode 1's temporal coefficient coincides with the suction peak of C_p near the leading edge ($x_c/c = 0.9$). Similarly, the second peak of mode 1's temporal coefficient coincides with the suction peak at the same chordwise location during the downstroke period; this suction peak is due to the

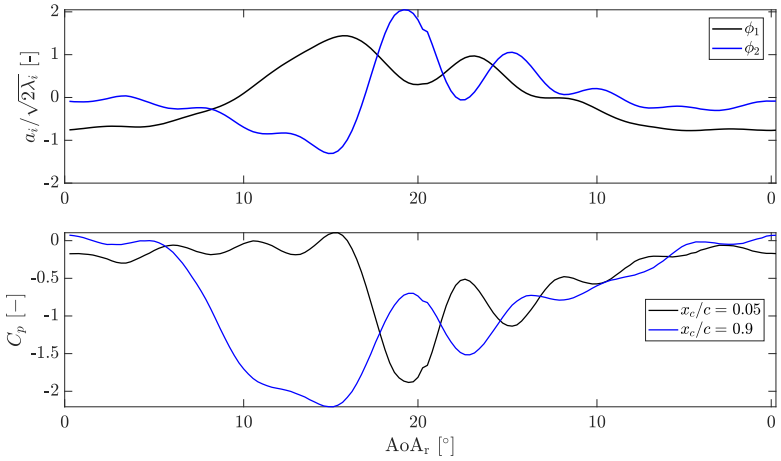

Figure 6.16: Temporal coefficient of the first two dominant modes (top) and suction side C_p (bottom) at case $\overline{\text{AoA}_r}10\Delta10k0.1$.

secondary development of the attached DSV. Likewise, for the second mode, the temporal coefficient starts to increase when C_p at $x_c/c = 0.05$ starts to decrease near AoA$_r$ = 17° during upstroke. The two peaks in mode 2's temporal coefficient align with the two C_p suction peaks at $x_c/c = 0.05$. As a result, the first mode correlates with the dynamics of the DSV. Similarly, the temporal-spatial correspondence strongly indicates that mode 2 physically represents the dynamics of TEV development during dynamic stall.

In order to further investigate the physical meaning of each mode, C_p is reconstructed based on the first two modes. The results are shown in Figure 6.17 with chordwise distribution in the left column and spatial-temporal field in the right column. ϕ_1 (times a constant h) is added/subtracted to/from the mean C_p (ϕ_0); the result is shown in Figure 6.17a. By adding (or subtracting) ϕ_1, the mean C_p shows decreasing (or increasing) values separately. The variation is the highest close to the leading edge ($x_c/c > 0.6$), and gradually diminishes closer to the trailing edge; when $x_c/c < 0.2$, the variation is the minimum. Meanwhile, the spatial-temporal C_p reconstructed from mode 1 (Figure 6.17b) presents two suction regions near the leading edge, which correspond to the DSV and the secondary development of the DSV, respectively. Based on the reconstructed C_p, it can be concluded that mode 1 is correlated with the growth and decay of the DSV.

The reconstructed C_p from mode 2 is shown in Figure 6.17c and Figure 6.17d. Contrary to mode 1, by adding (or subtracting) this mode, C_p shows decreasing (or increasing) values, stemming from the middle of the airfoil ($x_c/c = 0.5$) towards the trailing edge ($x_c/c = 0$). At the same time, C_p in the leading edge region increases or decreases, opposite to the variation in the trailing edge region. The spatial-temporal plot (Figure 6.17d) shows that the reconstructed C_p from mode 2 creates two trailing edge suction areas, which are correlated with the TEV development. Meanwhile, a high-pressure region is present near the leading edge at the same phases, which increases the leading edge pressure in mode 2. Therefore, mode 2 is related to two physical activities: first, it is highly correlated with the growth and decay of the trailing edge vortex. Second, as a minor effect, it is also related to the

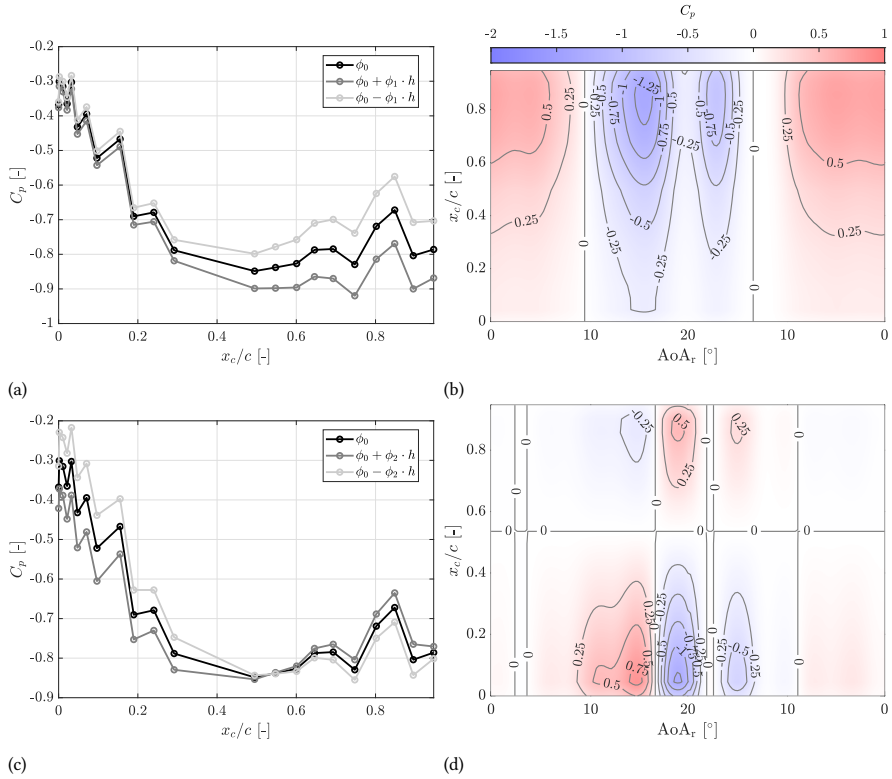

Figure 6.17: Reconstructed C_p chordwise distribution (left column) and reconstructed C_p spatial-temporal field (right column) from the first two modes (the first and second row separately) for case $\overline{\text{AoA}_r}10\Delta10k0.1$.

growth (or the pressure recovery) of the DSV, as a consequence of the decay (or growth) of the TEV.

TEV-dominated flow

The case $\overline{\text{AoA}_r}20\Delta10k0.1$ is selected as representative of TEV-dominated flow dynamics. The dominating mode shapes are shown in Figure 6.18, with the mean C_p also shown for comparison. Compared to the previous case, the mean C_p distribution presents lower values, with $C_p < -0.5$ even at the trailing edge, indicating a large flow separation affecting the entire suction side of the airfoil. As already discussed, in this case, the first mode peaks near the trailing edge region, opposite to $\overline{\text{AoA}_r}10\Delta10k0.1$, and the second mode has a wider peak region on the airfoil center region, but still peaks at approximately 30% from the leading edge.

The temporal coefficient of the first two modes, together with the phased-averaged suction side C_p at x_c/c = 0.05, 0.69, 0.6, 0.8, and 0.9, are shown in Figure 6.19. The two chordwise locations at x_c/c = 0.05 and 0.69 correspond to the mode shape peaks as shown in Figure 6.18. The other locations at x_c/c = 0.6, 0.8, and 0.9 are plotted to explain the reason why the first mode shape peaks at x_c/c = 0.69, which will be discussed later. The variations

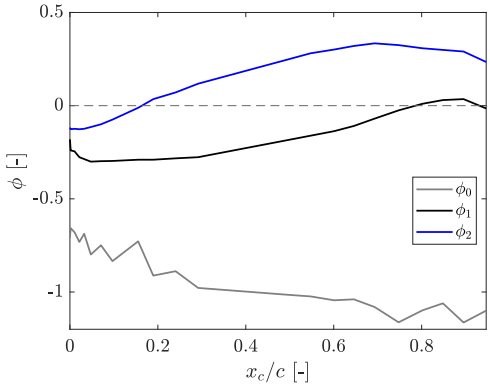

Figure 6.18: POD mode shapes of the time averaged C_p (ϕ_0) and the first two modes(ϕ_1 and ϕ_2) at case $\overline{\text{AoA}_\text{r}}20\Delta10k0.1$.

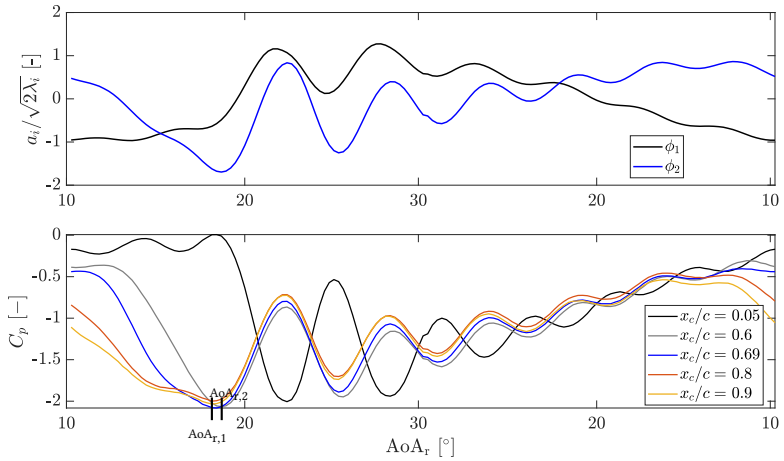

Figure 6.19: Temporal coefficient of the first two dominant modes (top) and suction side C_p (bottom) at case $\overline{\text{AoA}_\text{r}}20\Delta10k0.1$. $\text{AoA}_{\text{r},1}$ is the angle where the suction peak occurs between $x_c/c = 0.9$ and $x_c/c = 0.69$. $\text{AoA}_{\text{r},2}$ is the angle where the suction peak occurs at $x_c/c = 0.6$.

of C_p and the temporal coefficient are related to multiple DSV separations and sheddings, as discussed in the previous section. It is observed in Figure 6.19 that the first mode starts to increase sharply when C_p at $x_c/c = 0.05$ starts to decrease near $\text{AoA}_\text{r} = 17^\circ$ during upstroke. When C_p reaches the local minimum at $x_c/c = 0.05$, mode 1 reaches the local peak values simultaneously. This means that mode 1 is correlated with the development of the TEV. The reconstructed C_p from mode 1 is shown in Figure 6.20a and Figure 6.20b for its chordwise distribution and spatial-temporal distribution, respectively. By adding (or subtracting) ϕ_1, the C_p distribution decreases (or increases) accordingly, with the largest variations occurring in the trailing edge region ($x_c/c = 0.02$ to 0.5), and almost no variation in the leading edge region (from $x_c/c = 0.75$ and onward). The reconstructed C_p from this

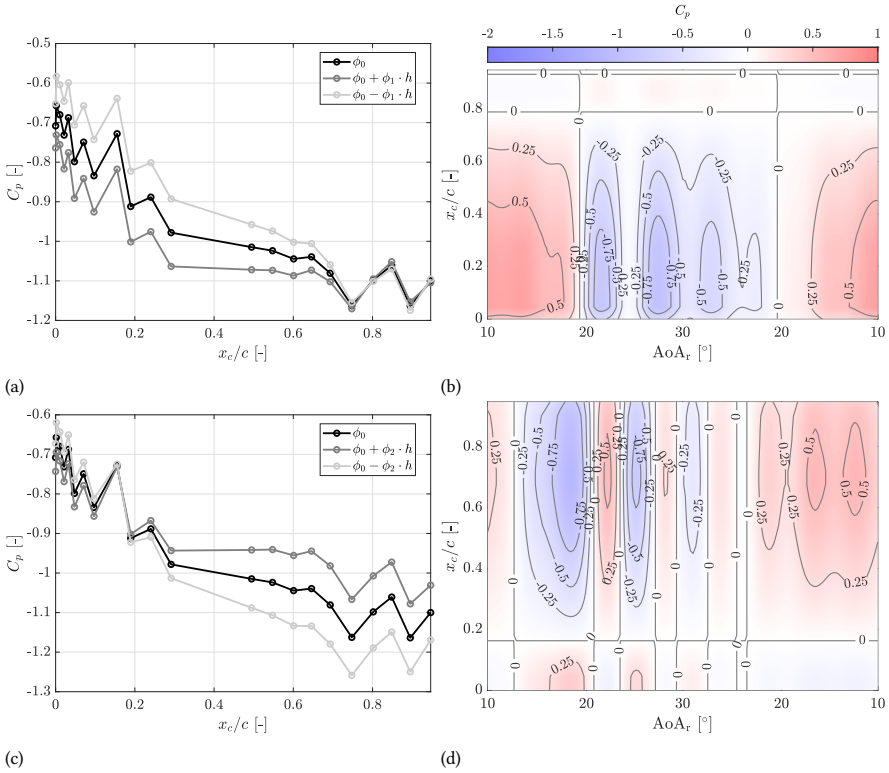

Figure 6.20: Reconstructed C_p chordwise distribution (left column) and reconstructed C_p spatial-temporal field (right column) from the first mode (the first row) and the second mode (the second row) for case $\overline{\text{AoA}_r}20\Delta10k0.1$.

mode shows a concentration of suction areas near the trailing edge region, extending up to approximately $x_c/c = 0.75$. The multiple suction regions are associated with the dynamics of the DSV, and in particular, its formation and the subsequent secondary effect from the partially attached DSVs. The large value of mode 1 in the trailing edge region and the high correlation between its temporal coefficient and the pressure coefficient near the trailing edge allow us to conclude that mode 1 is related to the growth and decay of the TEV. By comparing the vorticity field from the two cases (Figure 6.5 and Figure 6.12), it is shown that, in the latter case, the TEV is formed much earlier during the upstroke period and its size is much bigger, which indicates its stronger impact on the overall flow dynamics.

Instead, mode 2 presents (negative) peaks when C_p at $x_c/c = 0.69$ reaches the local minimum, indicating that this mode represents the dynamics of the energy from $x_c/c = 0.69$ the most. In order to examine the physical meaning of this mode, the reconstructed C_p chordwise distribution and space-temporal distribution are shown in Figure 6.20c and Figure 6.20d. This mode presents the maximum C_p fluctuation from the leading edge ($x_c/c = 1$) up until $x_c/c = 0.19$. No major fluctuation is seen near the trailing edge region by adding or subtracting the normalized ϕ_2. In the spatial-temporal field, it is shown that the suction areas are located near the leading edge, which indicates that mode 2 represents the

growth and decay of the DSV. In the previous case ($\overline{\text{AoA}_\text{r}}10\Delta10k0.1$, Mode 1), the highest energy concentrations associated with the DSV appear near the leading edge, indicating strong flow instability initiation there. However, in this case, the dominant energy peaks shift to a different region (closer to mid-chord at $x_c/c = 0.69$), suggesting a different DSV development pattern. From the temporal coefficient and C_p plot (Figure 6.19), it is shown that the lowest C_p is obtained at the same time in the entire region from the leading edge ($x_c/c = 0.9$) until $x_c/c = 0.69$, at $\text{AoA}_{\text{r}1} = 17.1^\circ$ marked in the plot. Afterwards, due to the initiation of the TEV, the development of the DSV is hindered, which brings a later suction peak at $x_c/c = 0.6$ at $\text{AoA}_{\text{r}2} = 17.5^\circ$ marked in the plot. This also explains the high mode shape values of mode 2 between $x_c/c = 0.6$ towards the leading edge; at the moment the TEV starts to initiate, the DSV develops the most, and the temporal coefficient of mode 2 reaches the highest value.

6.3.3 Trend from POD analysis for reverse flow dynamic stall

Overall, the two cases presented above showcase two different flow regimes, which are either DSV-dominated or TEV-dominated. In order to investigate the flow regimes for all the test cases in Table 6.3, the following procedure is followed:

1. A reconstruction of the suction side C_p field is performed based on the first mode, similar to what is shown in Figure 6.17 and Figure 6.20.
2. If the reconstruction field represents the dynamics from only the DSV or the TEV (i.e., the C_p increases or decreases centered at the leading edge or trailing edge region),
   - If $E_1 - E_2 \geq 25\%$, then the first mode is the most dominant mode and represents one single dominant dynamics from the DSV or the TEV. These two flow regimes are marked by orange and black separately.
   - If $E_1 - E_2 < 25\%$, then the first two modes are both considered important in the flow. Then, an additional reconstruction of C_p is performed based on the second mode. For all the relevant cases, the second mode represents the dynamics of the TEV or the DSV, respectively. Therefore, these cases are classified as a mixed type of energy, marked by blue.
3. If the reconstruction field represents the dynamics from both the DSV and the TEV, these cases are also classified as mixed energy type (blue).

The classification of the flow regimes is shown in Table 6.3. Overall, the trend is clear: at low mean angles of 5° and 10°, the flow is DSV dominated, where the growth and decay of the DSV determine the majority of the force variation. When the mean angle increases to 15°, the DSV loses its dominance, and the flow starts to show a mixture of energy from both the DSV and the TEV. When the mean angle increases to 20° and 25°, although a mixture of energy is still present, more cases are dominated by the dynamics of the TEV. These results indicate that, across the studied reduced frequency range (k from 0.05 to 0.21) and pitching amplitude range ($\Delta\text{AoA}_\text{r}$ from 5° to 15°), $\overline{\text{AoA}_\text{r}}$ emerges as the governing parameter for determining dominant flow regimes identified through POD analysis. For $\overline{\text{AoA}_\text{r}} = 5^\circ$, the low mean angle results in suction-side C_p distributions (Appendix D.3

Figure D.6) that lack a distinct suction peak near the trailing edge, indicating underdeveloped TEV. As the mean angle increases to $\overline{\text{AoA}_\text{r}} = 10^\circ$, while the dominant mode still captures the DSV dynamics (Figure 6.14b), the second mode gains substantially more energy (minimum 14.4%), which primarily reflects the growing influence from the TEV on the flow structure. However, for higher mean angles of 15°, 20°, and 25°, multiple separation and shedding events disrupt the DSV development. Together with the initiation of competing TEV structures, they lead to a mixture of both DSV and TEV energy or even a TEV-only-dominant flow regime.

Despite this $\overline{\text{AoA}_\text{r}}$-dependent trend, within the cases with the same $\overline{\text{AoA}_\text{r}}$ of 15°, 20°, and 25°, variations can be found. For example, at $\overline{\text{AoA}_\text{r}} = 20^\circ$ and $\Delta\text{AoA}_\text{r} = 10^\circ$, both $k = 0.1$ and 0.13 cases exhibit TEV-dominated flow (Figure 6.14b), while the remaining four cases ($k = 0.05$, 0.08, 0.16, and 0.18) are dominated by both DSV and TEV. The C_l hystereses of these cases are plotted in Figure 6.21. All cases present negative peak(s) during the upstroke period (solid lines). As discussed in the previous section, the decrease in C_l during the upstroke is due to the formation of the DSV, while the increase in C_l is due to its partial detachment from the airfoil's surface. As the reduced frequency increases, C_l reaches its peak at a later time (or angle) during the upstroke period, which causes an enlargement in the hysteresis loop. This trend with k aligns with previous literature with conventional dynamic stall cases [65, 76].

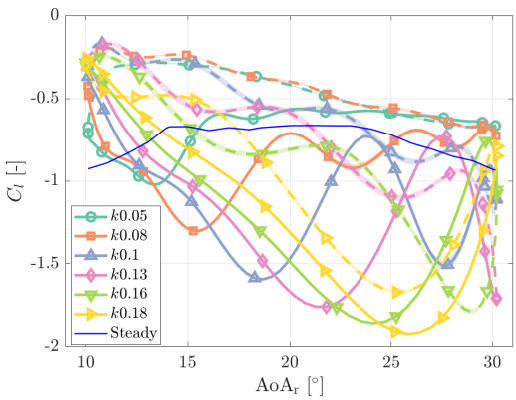

Figure 6.21: C_l hystereses loops at different k values at $\overline{\text{AoA}_\text{r}} = 20^\circ$ and $\Delta\text{AoA}_\text{r} = 10^\circ$. The 95% confidence intervals are plotted together for each case as a shaded area. Due to very low uncertainty, these shaded areas are thin. The upstroke period is plotted in solid lines, and the downstroke period is plotted in dashed lines.

In cases $\overline{\text{AoA}_\text{r}}20\Delta10k0.05$ and $\overline{\text{AoA}_\text{r}}20\Delta10k0.08$, the upstroke period presents peaks with smaller amplitudes compared to the remaining four cases. The spatial-temporal evolution of C_p for these two cases, as shown in Figure D.6y and D.6z, presents underdeveloped DSV and TEV. Therefore, the dominant energy for these two cases comes from a mixture of both DSV and TEV. It is also interesting to note that even at the lowest frequency ($k = 0.05$), which is considered as a quasi-steady condition [48], the unsteady loop differs from the steady curve. This indicates that the transition between quasi-steady and unsteady behavior in reverse flow dynamic stall may occur at frequencies lower than $k = 0.05$, where

the discrepancy between steady and unsteady responses becomes minimal. On the contrary, cases $\overline{\text{AoA}_\text{r}}20\Delta10k0.1$ and $\overline{\text{AoA}_\text{r}}20\Delta10k0.13$ each present two negative peaks in the hysteresis loop, both with larger amplitudes. The spatial-temporal C_p of these two cases (Figure D.6aa and D.6ab) exhibits two DSV-induced suction regions during the upstroke period, which indicates multiple separations during upstroke. Furthermore, these cases feature fully developed TEVs. Consequently, the DSV dynamics are suppressed by both the DSV intermittent separation and the strong TEV influence, resulting in TEV-dominated flow characteristics for these conditions.

At higher reduced frequencies (cases $\overline{\text{AoA}_\text{r}}20\Delta10k0.16$ and $\overline{\text{AoA}_\text{r}}20\Delta10k0.18$), the hysteresis loops exhibit a single dominant peak during the upstroke. The corresponding spatio-temporal C_p distributions (Figure D.6ac and D.6ad) reveal an extensive DSV-induced suction region persisting throughout the upstroke. Simultaneously, the TEV development generates comparable suction levels (average $C_p = -2.5$). The competing energy contributions from both vortices result in a mixed flow regime.

Therefore, at a mean angle of $\overline{\text{AoA}_\text{r}} = 20^\circ$ and $\Delta\text{AoA}_\text{r} = 10^\circ$, the dominant flow regime is characterized by contributions from both the DSV and TEV, depending on k. For low values of k, both vortices are underdeveloped, while high k values lead to strong, competing DSV and TEV structures. In both cases, the resulting flow reflects a mixture of energies from the two vortices. In contrast, at intermediate k, multiple DSV separations occur, leading to a flow regime dominated by the TEV. Similarly, at both $\overline{\text{AoA}_\text{r}}20\Delta15k0.16$ (Figure D.6ag) and $\overline{\text{AoA}_\text{r}}25\Delta15k0.16$ (Figure D.6ak) cases, the flow reflects a comparable mixture of energies, arising from the competition between the DSV and TEV.

It is important to note that the influence of k on the flow behavior is not universal but case-dependent. For instance, the case $\overline{\text{AoA}_\text{r}}15\Delta5k0.1$ exhibits a DSV-dominated flow, in contrast to the other three cases with the same mean angle and amplitude ($\overline{\text{AoA}_\text{r}}15\Delta5k0.05$, $\overline{\text{AoA}_\text{r}}15\Delta5k0.16$, and $\overline{\text{AoA}_\text{r}}15\Delta5k0.21$), which all display a mixed vortex regime. The spatial-temporal C_p distributions of these four cases are shown from Figure D.6ap to D.6as. In the mixed-mode cases, the C_p fields reveal either underdeveloped DSV and TEV structures (as in $\overline{\text{AoA}_\text{r}}15\Delta5k0.05$) or strong, competing contributions from both vortices (as in $\overline{\text{AoA}_\text{r}}15\Delta5k0.16$ and $\overline{\text{AoA}_\text{r}}15\Delta5k0.21$). In contrast, for $\overline{\text{AoA}_\text{r}}15\Delta5k0.1$, the TEV remains underdeveloped while the DSV exhibits a well-defined suction region throughout its formation period, indicating dominance of the DSV dynamics. This case demonstrates that flow regime transitions are governed not solely by k, but by the combined effects of all three pitching parameters: mean angle of attack, amplitude, and reduced frequency.

In addition, it is also interesting to notice that at a very low reduced frequency of 0.05, both $\overline{\text{AoA}_\text{r}}20\Delta15k0.05$ (Figure D.6ae) and $\overline{\text{AoA}_\text{r}}25\Delta15k0.05$ (Figure D.6ai) exhibit a TEV-dominated flow. For these cases, due to larger pitching amplitudes, the trailing edge region experiences a longer suction period due to flow separation, even though the TEV is not present.

From this analysis, it can be concluded that the mean angle of attack is the main parameter that determines the dominant flow regime. In contrast, the effects of reduced frequency (k) and pitching amplitude ($\Delta\text{AoA}_\text{r}$) are also important, but their influence is neither direct nor linear. Instead, the dominant flow regime emerges from the specific combination of pitching parameters, which governs the development patterns of the DSV

and TEV on the airfoil surface. These patterns, such as underdeveloped vortices, multiple separation events, or strong competing DSV and TEV structures, directly define the prevailing flow regime.

6.3.4 Comparison with POD analysis from conventional dynamic stall

In order to further investigate the difference between conventional and reverse flow dynamic stall, the POD analysis was conducted on conventional dynamic stall cases tested in this campaign. Similar to the reverse flow case, the suction side C_p distribution was used in the analysis. Table 6.4 shows the energy content of the first two dominant modes for all conventional dynamic stall cases. The result shows a universal trend across all tested conventional dynamic stall cases: the first mode has a dominant energy content of more than 75% of the total energy, while the second mode has much less energy, with a maximum of less than 20%. This means that for conventional dynamic stall cases, the pitching parameters of mean angle of attack, pitching amplitude, and pitching frequency do not alter the most energetic flow feature.

Table 6.4: Energy distribution of the most dominant mode(s) across conventional dynamic stall cases, grouped by $\overline{\text{AoA}}$.

Case	E_1 [%]	E_2 [%]	Case	E_1 [%]	E_2 [%]	Case	E_1 [%]	E_2 [%]
$\overline{\text{AoA}}5\Delta10k0.05$	96.7	2.8	$\overline{\text{AoA}}10\Delta5k0.21$	95.0	4.0	$\overline{\text{AoA}}15\Delta5k0.16$	83.8	9.8
$\overline{\text{AoA}}5\Delta10k0.1$	97.2	2.2	$\overline{\text{AoA}}10\Delta10k0.05$	89.8	6.3	$\overline{\text{AoA}}15\Delta5k0.21$	82.8	10.0
$\overline{\text{AoA}}5\Delta10k0.16$	97.4	2.1	$\overline{\text{AoA}}10\Delta10k0.1$	88.7	6.9	$\overline{\text{AoA}}15\Delta10k0.05$	78.7	14.4
$\overline{\text{AoA}}5\Delta15k0.05$	87.7	7.0	$\overline{\text{AoA}}10\Delta10k0.16$	89.2	6.0	$\overline{\text{AoA}}15\Delta10k0.1$	75.7	17.0
$\overline{\text{AoA}}5\Delta15k0.1$	90.3	4.0	$\overline{\text{AoA}}10\Delta15k0.05$	85.7	9.5	$\overline{\text{AoA}}15\Delta10k0.16$	79.1	13.5
$\overline{\text{AoA}}5\Delta15k0.16$	93.0	2.6	$\overline{\text{AoA}}10\Delta15k0.1$	85.4	9.4	$\overline{\text{AoA}}15\Delta14k0.05$	76.1	17.8
$\overline{\text{AoA}}10\Delta5k0.05$	96.7	2.1	$\overline{\text{AoA}}10\Delta15k0.16$	87.5	7.1	$\overline{\text{AoA}}15\Delta14k0.1$	76.5	16.5
$\overline{\text{AoA}}10\Delta5k0.1$	95.7	3.0	$\overline{\text{AoA}}15\Delta5k0.05$	88.9	6.1	$\overline{\text{AoA}}15\Delta14k0.16$	81.1	12.0
$\overline{\text{AoA}}10\Delta5k0.16$	95.1	3.7	$\overline{\text{AoA}}15\Delta5k0.1$	85.0	8.9			

From the energy distribution, it is confirmed that the first mode is the dominant mode for conventional cases. The mode shape of the first mode for all conventional cases is shown in Figure 6.22. Across all cases, the mode shapes of the first modes all present the same pattern, where the peak is shown at the leading edge with high concentration. In order to further confirm the relationship between the mathematical structures of the dominant POD mode (mode 1) and the physical dynamics in the flow field, the suction side C_p at case $\overline{\text{AoA}}10\Delta10k0.16$ is reconstructed with the first mode. The result is shown in Figure 6.23. The reconstructed C_p in the chordwise distribution (Figure 6.23a) exhibits decreasing (or increasing) C_p from near the mid chord ($x_c/c = 0.6$) to the leading edge ($x_c/c = 0$), and the variation is the largest close to the leading edge. The spatial-temporal reconstructed field shows low C_p concentration stemming from the leading edge, appearing between AoA = 11° during upstroke and AoA = 16° during downstroke. This range also

aligns with the extreme low-pressure region (LSB) shown at the leading edge in Figure 6.9. Therefore, it is concluded that the dominant mode (mode 1) is related to the growth and decay of the leading edge negative pressure. Similar flow patterns can also be found in the conventional dynamic stall analysis from Li and Feng [123].

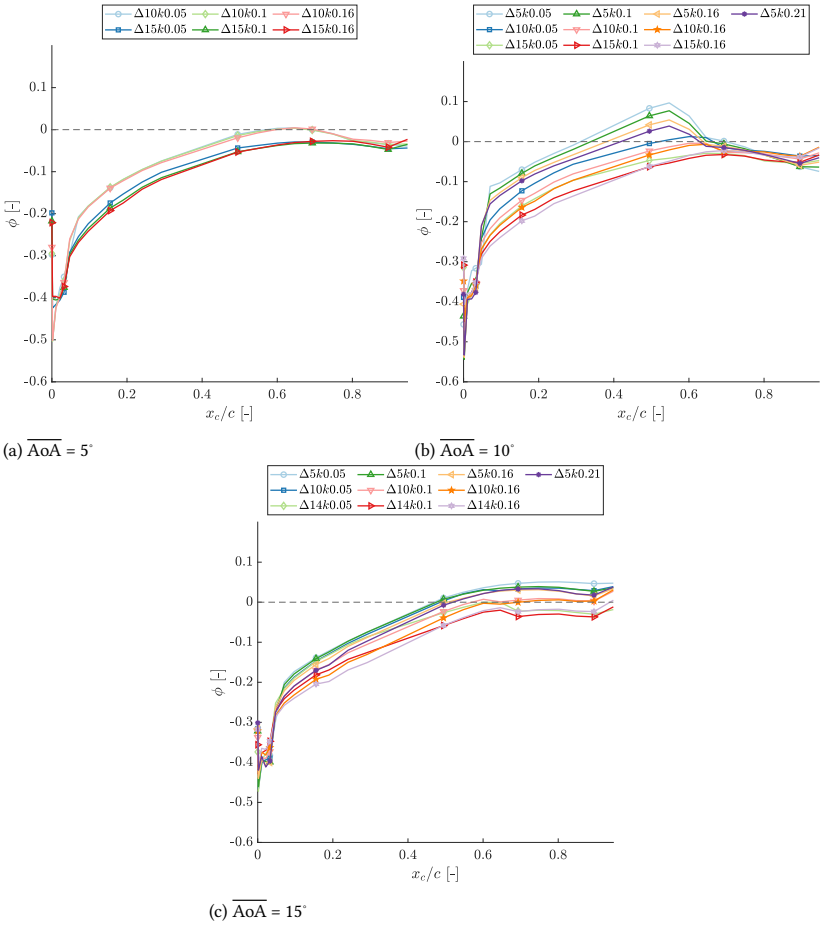

Figure 6.22: POD mode shapes of the most dominant mode (mode 1) for conventional dynamic stall cases.

Therefore, due to the presence of the LSBs, the dominant flow pattern exhibits uniform dominance dynamics near the leading edge for conventional dynamic stall cases. This result differs from the reverse flow dynamic stall cases, where the dominant energy can come from the dynamics of the DSV, TEV, or a mixture of both energies. This difference is fundamentally owing to the high suction from the LSB for conventional cases, and the gradual decrease of C_p at the initial stage of DSV formation for the reverse flow conditions.

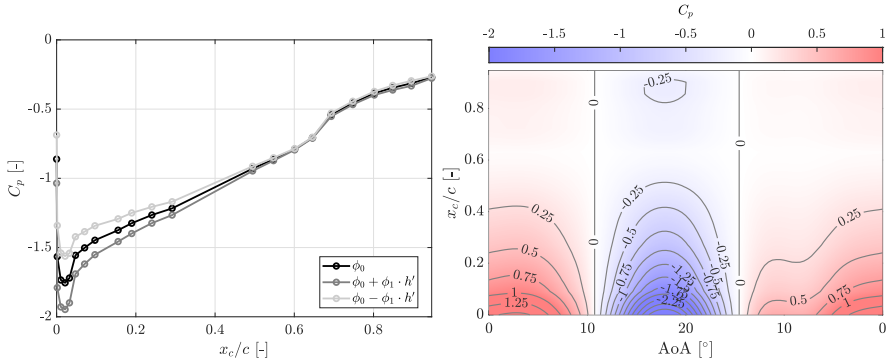

(a) (b)

Figure 6.23: Reconstructed C_p chordwise distribution (left) and reconstructed C_p spatial-temporal field (right) from the first mode for case $\overline{\text{AoA}}10\Delta10k0.16$.

6.4 Method development: assessment of existing detection criteria and development of a new method

6.4.1 Validity of existing DSV initiation detection method under reverse flow conditions

First, we examine whether the existing DSV initiation detection method under conventional conditions is valid for reverse flow conditions. In this section, the existing DSV initiation time detection method from [123] is analysed. In their study, two parameters are defined for DSV initiation, namely, the spatial distribution coefficient of pressure (SDCP) and the high-order central moment of pressure (HCMP). The POD-based method is also introduced here, which has been applied by a few previous studies [70, 120, 123]. A brief introduction of these methods is summarized in Table 6.5, and the methods in detail are discussed in the following sections together with their validity under reverse flow conditions.

Table 6.5: DSV initiation detection method overview.

Name & Meaning	Ref.	Input	Detection Point	Valid under Rev. Flow?
SDCP Spatial distribution coefficient of pressure	[123]	Time series of suction side surface pressure; pressure measurement location	Global peak	No
HCMP High-order central moment of pressure	[123]		Global peak	No
POD Proper orthogonal decomposition	[135]		Local peak (or trough)	Yes

SDCP method

SDCP is defined as [123]:

$$\mathrm{SDCP}(t) = \sum_{n=1}^{N_s-1} [C_{p,n+1}(t) - C_{p,n}(t)] \times \left(1 - \frac{x_{c,n}}{c}\right)^{\mathrm{sgn}(C_{p,n+1}(t)-C_{p,n}(t))} \left(\frac{x_{c,n}}{c}\right)^{1-\mathrm{sgn}(C_{p,n+1}(t)-C_{p,n}(t))} \tag{6.3}$$

where N_s is the total number of pressure transducers, x_c is the chordwise location of the pressure measurement, and sgn is the standard symbolic function, which is defined as:

$$\mathrm{sgn}(x) = \begin{cases} 1, & \text{if } x \geq 0. \\ 0, & \text{if } x < 0\ . \end{cases} \tag{6.4}$$

Alternatively, SDCP can be defined as:

$$\mathrm{SDCP}(t) = \sum_{n=1}^{N_s-1} f_n(t) \tag{6.5}$$

where

$$f_n(t) = \begin{cases} [C_{p,n+1}(t) - C_{p,n}(t)]\left(1 - \frac{x_{c,n}}{c}\right), & C_{p,n+1}(t) \geq C_{p,n}(t), \\ [C_{p,n+1}(t) - C_{p,n}(t)]\left(\frac{x_{c,n}}{c}\right), & C_{p,n+1}(t) < C_{p,n}(t). \end{cases} \tag{6.6}$$

A schematic plot of this method is shown in Figure 6.24 where the application at $t = t_1$ is demonstrated. The absolute peak values of SDCP are used to identify the onset of LSBs and the initiation of DSV, where the peak from the DSV initiation time occurs later and contains a higher value compared to the peak from the LSBs. The definition of SDCP is based on three physical fluid dynamics that the suction side pressure presents during conventional dynamic stall conditions [123]: first, the concentration of the suction peak in the leading edge region, i.e., suction increases as time proceeds near the leading edge. Second, the downstream movement of the suction peak, i.e., the DSV-induced pressure wave from the leading edge towards the trailing edge. Third, small-amplitude fluctuations in pressure. The value of SDCP increases with the leading edge pressure concentration, decreases with the downstream movement of the suction peak, and increases with an increase in the fluctuation.

The reverse flow case $\overline{\mathrm{AoA_r}}10\Delta10k0.1$ is used to validate this method. Specifically, the cycle-averaged suction side pressure coefficient distribution is applied to Equation (6.3). The SDCP curve is shown in Figure 6.25. This result indicates that the DSV initiation time, as marked by the global peak in the figure, is located near the PIV measured phase *h* (Figure 6.5h). At this phase. The PIV results at phase *h* show that the DSV is already formed, with part of it separated to the downstream. However, the analysis of the PIV flow fields reported in Figure 6.5 shows that the formation of the DSV occurs between phases *f* and *g*: hence, it can be concluded that the SDCP method fails to identify the DSV initiation under reverse flow conditions.

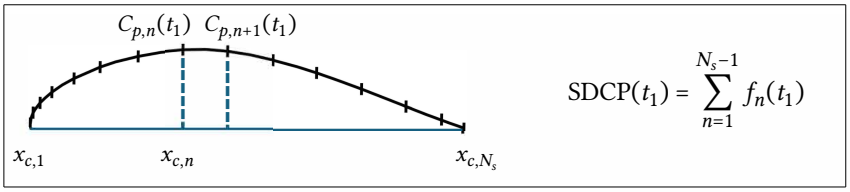

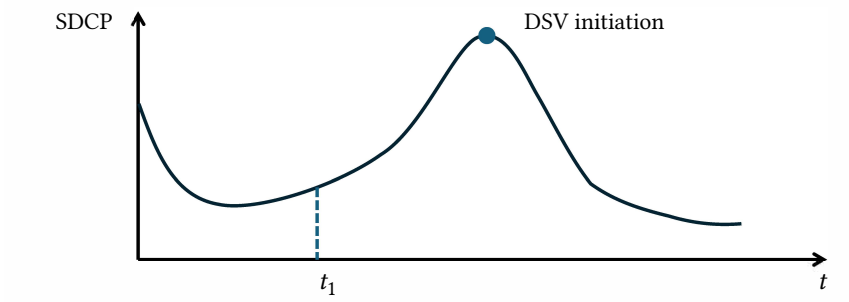

Figure 6.24: Schematic plot of the SDCP method.

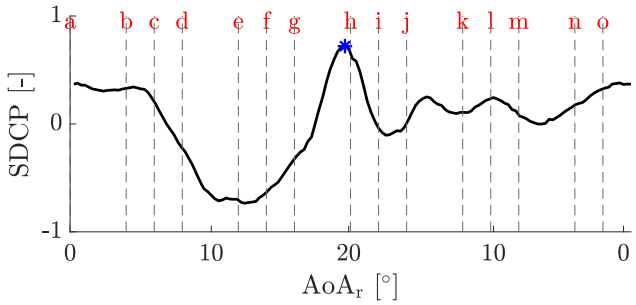

Figure 6.25: Application of the SDCP method on a reverse flow case $\overline{\mathrm{AoA_r}}10\Delta10k0.1$. Phases from PIV measurements are marked by the dashed vertical lines.

HCMP method

The HCMP method proposed by [123] is defined as follows:

$$\mathrm{HCMP}(t) = \frac{1}{N_s}\sum_{n=1}^{N_s}\left[-C_{p,n}(t) - \left(-\overline{C_p(t)}\right)\right]^m$$

where m is the order of the moment, which is a positive integer. $\overline{C_p(t)}$ is the averaged C_p at a certain measurement time t over the airfoil suction surface:

$$\overline{C_p(t)} = \frac{1}{N_s}\sum_{n=1}^{N_s} C_{p,n}(t)$$

It is found in Li and Feng's study [123] that, when $m = 2$, the maximum value in HCMP cannot correctly reflect the DSV initiation time. However, when $m \geq 3$, the maximum value in HCMP is always around the DSV initiation time. Based on their result, in the present study, m is selected as 4.

The HCMP method is applied to the reverse flow case $\overline{\mathrm{AoA_r}}10\Delta10k0.1$ and the result is shown in Figure 6.26. The peak of HCMP shows between phase f and g, during which the DSV is already partially separated from the airfoil, as marked by the red circles with "FS" (flow separation) label shown in the PIV measurement field in Figures 6.5d to 6.5f. Therefore, HCMP also cannot accurately predict the DSV initiation point under reverse flow conditions.

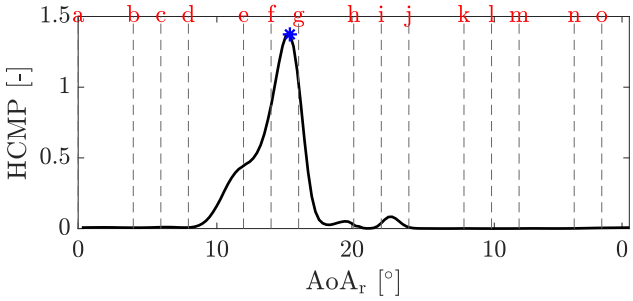

Figure 6.26: Application of the HCMP method on a reverse flow case $\overline{\mathrm{AoA_r}}10\Delta10k0.1$. Phases from PIV measurements are marked by the dashed vertical lines.

POD method

As discussed in Section 6.3.2, the temporal coefficient of the DSV mode increases in magnitude as the DSV-induced pressure increases in magnitude. Therefore, the beginning of the sharp increase from this temporal coefficient is the DSV initiation point. Therefore, the DSV initiation point is defined as the beginning point of the first large increase (or decrease) during the upstroke period in the temporal coefficient of the DSV mode.

Through the analysis of the relative energy of the first two modes and of the reconstruction of the first two modes, all test cases can be categorized into DSV-dominated flow at low mean angles $\overline{\mathrm{AoA_r}} = 5^\circ$ and 10°, mixed energy from both the DSV and TEV at moderate mean angles of $\overline{\mathrm{AoA_r}} = 15^\circ$, and more TEV-dominated flow at higher angles $\overline{\mathrm{AoA_r}} = 20^\circ$ and 25°. Hence, three representative cases from these three categories are shown in Figure 6.27.

For all three cases, the non-dimensional temporal coefficient $a/\sqrt{2\lambda}$ corresponds to the associated DSV mode. Meanwhile, the $a/\sqrt{2\lambda}$ is ordered with the upstroke-downstroke sequence. The green point, located at the local peak or trough, indicates the detected DSV initiation point, marking the beginning of a sustained increase in magnitude for this temporal coefficient. By comparing these three detected locations with the associated PIV-measured flow fields for the first two, as shown in Figure 6.5 and Figure 6.12, and the pressure field for the last case (Figure D.6c), the POD method provides accurate detection results. Because POD operates based on the pressure distribution, it directly captures the

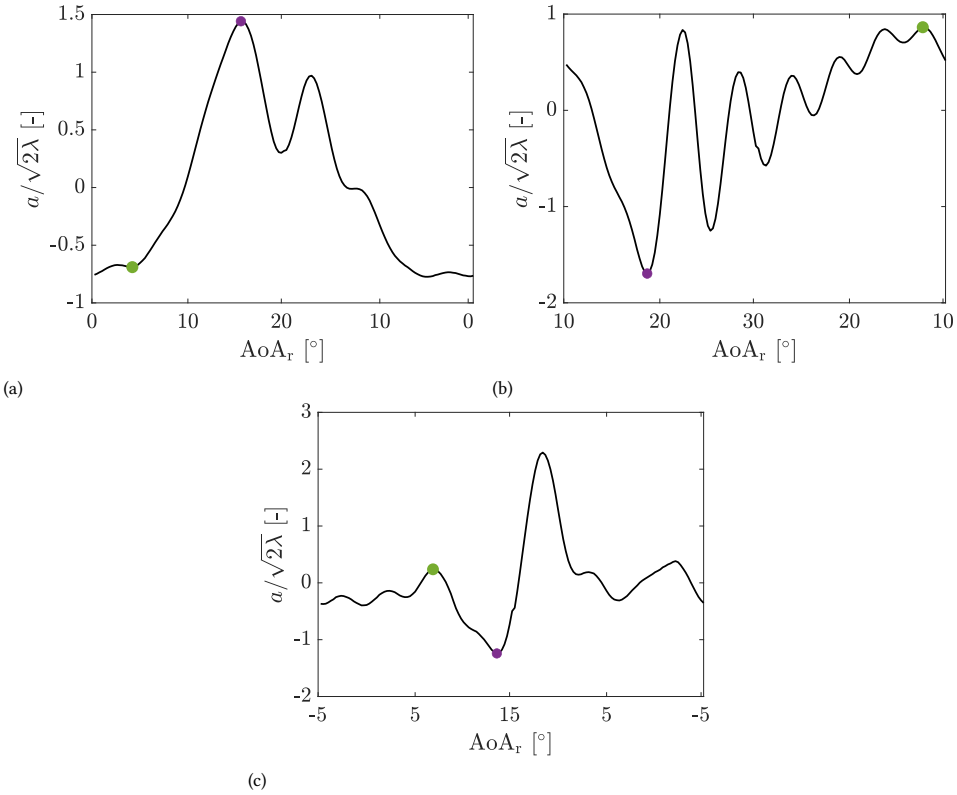

Figure 6.27: Demonstration of the POD-based method for three flow categories using the temporal coefficient related to the DSV mode: (a) DSV-dominated flow at case $\overline{\text{AoA}_r}10\Delta10k0.1$, (b) TEV-dominated flow at case $\overline{\text{AoA}_r}20\Delta10k0.1$, and (c) mixed energy flow from both the DSV and TEV at case $\overline{\text{AoA}_r}5\Delta10k0.1$. The green point is the detected point for DSV initiation by the POD method, with the definition given in Section 6.4.1. The purple point is the detected point for TEV initiation obtained by the POD method, with the definition given in Section 6.4.2.

pressure signatures induced by DSV/TEV formation, thereby providing a robust detector of vortex initiation. It is also noted that the DSV initiation time can be either during upstroke (Figure 6.27a and Figure 6.27c) or downstroke (Figure 6.27b). This characteristic will be further discussed in the proposed detection method in Figure 6.31.

6.4.2 Validity of existing TEV initiation detection method under reverse flow conditions

This section aims to examine the existing methods for detecting the TEV initiation time. Note that we mainly consider the first TEV initiation detection for the reverse flow condition, even though partial separation and regrowth may happen later. In Section 6.3.1, it is found that TEV initiation occurs at the time when DSV has fully developed and begins to detach. Therefore, we examine the existing DSV detachment method for the purpose of TEV initiation. Here, two methods are examined, namely the modulated location of peak

pressure (MLPP) [123] and the POD method. A brief summary of these methods is shown in Table 6.6.

Table 6.6: TEV initiation detection method overview.

Name & Meaning	Ref.	Input	Detection Point	Valid under Rev. Flow?
MLPP Modulated location of peak pressure	[123]	Time series of suction side surface pressure; pressure measurement location	Global peak	No
POD Proper orthogonal decomposition	[135]		Local peak (or trough)	Yes
HCMP High-order central moment of pressure	[123]		global peak	To be validated in Section 6.5.2

MLPP method

In Li and Feng's study, MLPP is defined to determine the DSV detachment time [123]. MLPP is defined as the product between the m_r-th power of the local root mean square of C_p ($C_{p,rms}$) and the location of peak pressure (LPP):

$$\mathrm{MLPP}(t) = \mathrm{LPP}(t) \times \sum_{n=1}^{N_s} \left[C_{p,rms}(x_{c,n}, t) \right]^{m_r} \tag{6.7}$$

The LPP is defined as the weighted average chordwise coordinates of the 10% measurement point with the strongest negative pressure [123]. The $C_{p,rms}$ is defined as [123]:

$$C_{p,rms}(x_{c,n}, t) = \sqrt{\frac{1}{\delta t} \int_{t-\delta t}^{t} [C_p(x_{c,n}, t) - \overline{C_p(x_{c,n}, t)}]^2 dt} \tag{6.8}$$

where $\overline{C_p(x_{c,n}, t)}$ is the moving average of C_p at chordwise location $x_{c,n}$ during the preset time period of δt. The power exponent m_r is the empirical parameter for $C_{p,rms}$ to modulate LPP, and is chosen to be 3 in Li and Feng's study. In the present study, we also used the same number for m_r. According to Li and Feng's study, MLPP can successfully predict the DSV deteachment time, owing to the fact that for classic dynamic stall, the $C_{p,rms}$ reaches the maximum during the DSV detachment period [123].

We tested the MLPP method on the reverse flow cases. In reverse flow conditions, multiple partial separation events frequently do not align with the typical full separation patterns for conventional cases, as shown in Figure 6.9. Consequently, the peaks of the RMS of C_p sometimes deviate from the expected DSV detachment region. As an example, the $C_{p,rms}$ for case $\overline{\mathrm{AoA_r}}20\Delta10k0.1$ is shown in Figure 6.28.

While the first TEV initiation occurs near phase e (marked by the red circle in Figure 6.28 with the PIV velocity field shown in Figure 6.12), the light yellow regions in Figure 6.28 indicate that the $C_{p,\mathrm{rms}}$ peaks instead appear during the second DSV regrowth

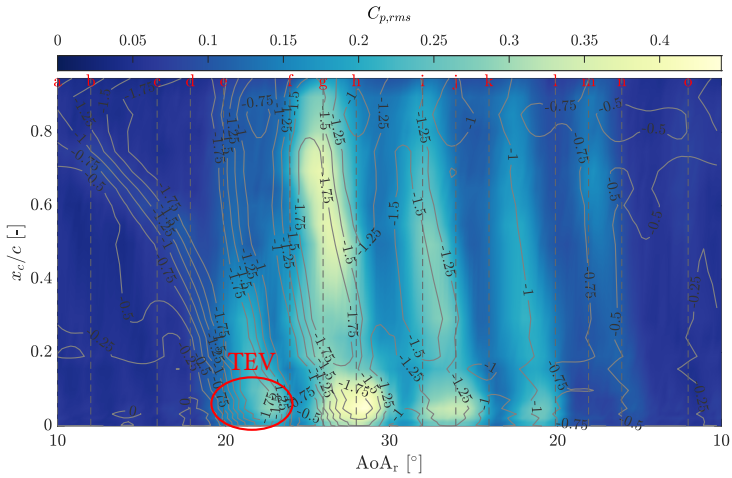

Figure 6.28: $C_{p,rms}$ on the suction side at case $\overline{\mathrm{AoA_r}}20\Delta10k0.1$. PIV phases are marked by dashed vertical lines, TEV indicated by a circle.

stage, between phases f and h. In particular, the prominent $C_{p,\mathrm{rms}}$ peak near the leading edge at phase g deviates significantly from the actual first TEV initiation location identified in the PIV fields. Moreover, the strong $C_{p,\mathrm{rms}}$ signals during phases f–h dominate the overall pressure fluctuation field, masking other relatively smaller partial detachment events and thereby reducing the accuracy of vortex detection.

The highest $C_{p,\mathrm{rms}}$ levels observed between phases f and h correspond to the largest pitching angles, where the flow experiences more severe separation compared to the earlier phase e, when the angle of attack is smaller, and the TEV is smaller and low in strength (Figure 6.12). As a result, the MLPP of this case, shown in Figure 6.29, indicates that the global maximum lies in phase g, which is later than the TEV initiation time marked in Figure 6.28.

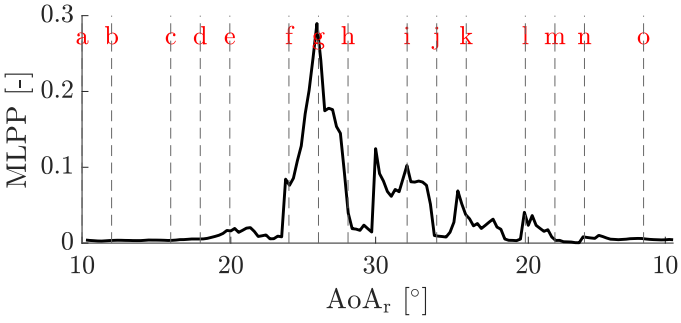

Figure 6.29: Application of the MLPP method on a reverse flow case $\overline{\mathrm{AoA_r}}20\Delta10k0.1$. Phases from PIV measurements shown in Figure 6.12 are marked by the dashed vertical lines.

POD method

In Section 6.4.1, the DSV initiation time is characterized by the first point when the temporal coefficient of the DSV mode starts to increase (or decrease) sharply. Conveniently, as discussed in Section 6.3.1, the initiation time of the TEV can be easily identified from the POD analysis, also using the DSV mode. Specifically, the DSV is the most developed during the upstroke period when the temporal coefficient of the DSV-related mode reaches the peak (or trough) of its first sharp increase during upstroke. Meanwhile, it is shown that the trailing edge C_p begins to decrease at this peak (or trough), indicating that this peak (or trough) marks the onset of TEV formation. Therefore, the local peak (or trough) for this first sharp increase during the upstroke is defined as the TEV initiation time. In fact, a similar application of POD for identifying TEV initiation has been demonstrated by Mulleners and Raffel [70], which confirms its reliability. The detected TEV initiation time is marked with a purple dot, as shown in Figure 6.27, for the three representative cases. Compared with the PIV flow fields (Figure 6.5 and Figure 6.12) and the suction surface pressure coefficient field shown in Figure D.6c, the result from POD demonstrates accurate alignment.

However, it is worth noting that for vortex detection using POD analysis, spatially resolved surface pressure distributions covering the entire suction side are required. This necessitates high-resolution instrumentation during measurement and results in massive datasets. This limitation leaves room for a more practical approach that utilizes sparse sensor data, such as measurements limited to the leading and trailing edges.

HCMP method

As discussed in Section 6.4.1, HCMP cannot detect the DSV under reverse flow conditions, either. However, based on the statistical interpretation, a high HCMP means a higher variation from the mean value. This, on the contrary, fits the TEV initiation criteria discussed in Section 6.4.2, where the TEV initiates when the DSV develops the most with the highest overall suction on the airfoil surface. Therefore, instead of predicting the DSV initiation time, HCMP can be a suitable candidate for predicting the TEV initiation time under reverse flow conditions. The accuracy will be discussed in Section 6.5.2.

Summary

The validity of the examined method for the DSV and TEV initiation detection is summarized in the last column of Table 6.5 and Table 6.6. To summarize, as discussed in Section 6.3.1, in conventional dynamic stall, the LSB exhibits the highest suction on the airfoil surface. When the LSB bursts and the DSV develops, the suction pressure gradually recovers. Therefore, it is reasonable that the global peak in SDCP and HCMP represents the DSV initiation point. In contrast, under reverse flow conditions, the suction pressure increases progressively during DSV development, where the lowest region in C_p actually means its initiation. This difference in vortex dynamics proves that the global peak point in SDCP and HCMP does not coincide with DSV initiation in reverse flow cases, as the rising suction pressure occurs after the DSV initiation.

Meanwhile, the MLPP methods fail in detecting the corresponding vortex initiation time for the reverse flow condition. This failure is due to the nature of multiple separations from the reverse flow conditions, where, for conventional cases, the vortex shedding

is usually complete. Due to these multi-separation events, the peak value in MLPP is typically detected at other event locations where C_p exhibits higher variations. The physics implied by HCMP is reasonable for TEV initiation detection, as discussed in Section 6.4.2; however, its validity still needs to be verified.

Lastly, the POD method is effective for both DSV and TEV initiation detection under reverse flow conditions, as it decomposes the surface pressure field into dominant coherent modes. These modes reflect the underlying physics embedded in the C_p distribution, which allows the distinct signatures associated with DSV- and TEV-induced pressure variations to be clearly isolated.

6.4.3 The modified SDCP method for DSV initiation time detection under reverse flow conditions

As discussed in Section 6.3.1, under reverse flow dynamic stall conditions, the process of DSV formation and the evolution of suction side pressure exhibit several characteristics in common with the conventional case. First, the suction peak occurs at the (aerodynamic) leading edge and increases in amplitude. Second, DSV travels downstream, towards the direction of the (aerodynamic) trailing edge. Third, the reverse flow dynamic stall condition exhibits small amplitude fluctuations in pressure. These three similarities form the basis of the SDCP method and suggest that it should, in principle, remain compatible with the underlying flow physics of reverse flow dynamic stall. However, because of the differences between conventional flow and reverse flow outlined in Section 6.3.1, the SDCP method fails to identify the DSV initiation point for reverse flow cases. Accordingly, in this section, we investigate potential modifications to the SDCP method to enable accurate DSV detection under reverse flow conditions.

First of all, the order of the airfoil coordinate is reversed from the aerodynamic leading edge to the aerodynamic trailing edge, i.e, at the leading edge, the index is $n = N_s$ while at the trailing edge, the index is $n = 1$. This also means that part of the integrand $C_{p,n+1}(t) - C_{p,n}(t)$ in Equation (6.6) needs to switch sign. Under this condition, the pressure difference is properly calculated in the reverse flow condition. Second, for the original SDCP method, the integration starts from the leading edge towards the second-to-last of the pressure ports. In the revere flow condition, the same integration range should be matched, which should be from $n = N_s$ to $n = 2$. Since the direction of integration does not influence the final result, the modified SDCP method mSDCP for the reverse flow condition is written as:

$$\mathrm{mSDCP}(t) = \sum_{n=2}^{N_s} [C_{p,n-1}(t) - C_{p,n}(t)] \times \left(1 - \frac{x_{c,n}}{c}\right)^{\mathrm{sgn}(C_{p,n}(t) - C_{p,n-1}(t))} \left(\frac{x_{c,n}}{c}\right)^{1-\mathrm{sgn}(C_{p,n}(t) - C_{p,n-1}(t))} \tag{6.9}$$

Apart from the two above-mentioned differences compared to the original SDCP method, the most important difference lies in the detection location. For the classic dynamic stall condition, the suction peak occurs at the very beginning of DSV initiation. Therefore, the global peak in SDCP represents the DSV initiation time. However, for reverse flow

dynamic stall cases, local flow separation near the leading edge region does not lead to large C_p variation before the DSV formation, and no LSBs are formed. Instead, C_p gradually decreases thereafter and reaches its maximum as the DSV fully develops. Therefore, for reverse flow dynamic stall cases, the initial point where the mSDCP starts to increase, rather than the peak value, is defined as the DSV initiation point.

6.4.4 The proposed C_p method for DSV and TEV initiation detection

In this section, the time determination for the DSV and the first TEV initiation for the reverse flow condition, based on the suction side C_p, is defined, which is referred to as the C_p method.

The proposed C_p method is developed from the universal flow features observed across all tested reverse flow dynamic stall cases. As discussed in Section 6.3.1, the vortex dynamics in this regime are primarily governed by two dominant structures: the DSV, acting as the leading-edge vortex (LEV), and the TEV. Since no other prominent vortical structures, such as the LSBs present in conventional dynamic stall, are observed, the suction side C_p distribution becomes particularly effective for capturing the essential flow physics from these two vortices for reverse flow conditions.

Definitions for DSV initiation detection

Two important parameters involved in this method are the aerodynamic leading edge pressure coefficient, denoted as $C_p^{LE}(t)$, and the time derivative of the leading edge pressure coefficient, denoted as $dC_p^{LE}(t)/dt^*$. The nondimensional time t^* is defined as $t^* = tU_\infty/c$, where $t \in [0, T]$ and T is the pitching period.

For the DSV initiation detection, two scenarios may happen: The DSV may either initiate during the upstroke period or at the end of the previous downstroke period, depending on the mean pitch angle, as discussed in Section 6.3.1. For the first scenario, the DSV initiation time t_D is defined as the first instant (the minimum value) when $C_p^{LE}(t)$ starts a sustained decrease: specifically, dC_p^{LE}/dt^* must remain below a negative threshold $-\theta$ for at least a duration of P:

$$t_D = \min\left\{t \in [0, T] \ : \ dC_p^{LE}(\tau)/dt^* \le -\theta \ \text{ for all } \ \tau \in [\, t, t+P\,]\right\} \tag{6.10}$$

It is important to note that for practical implementation, the C_p time series should be arranged sequentially through the upstroke (increasing angle of attack) and downstroke (decreasing angle of attack) phases to ensure consistent detection of these critical events.

For DSV initiation detection, the following values of the parameters θ and P are chosen: $\theta = 2\% \cdot [\max(dC_p^{LE}/dt^*) - \min(dC_p^{LE}/dt^*)]$ and $P = 10\%T$. θ is defined based on the trial and error from all the reverse flow test cases. These constraints mainly filter out minor flow instabilities, as well as measurement noise, which will be discussed based on the example shown in Figure 6.30a. Meanwhile, the definition of P is based on the portion of the duration of the DSV-induced pressure on the overall duration of the pitching period shown in Figure D.6. For all test cases, the DSV-induced suction always takes up less than 10% of the total pitching period for each case. Therefore, this duration constraint enables the long decrease characterized by the DSV-induced pressure, rather than small pressure fluctuations.

For the second scenario, where the DSV begins to form during the downstroke phase, the C_p method for DSV initiation detection is further reinforced by applying a backward search. Specifically, if the forward detection procedure identifies the DSV initiation at the first sample of the downstroke (i.e. if $t_D = 0$), then the algorithm restarts the detection from the end of the time series and proceeds backward in time. The backward search evaluates the interval $[\,T - P_i,\, T\,]$ for successive window lengths $P_i = i\Delta t$ with $i = 0, 1, 2, 3, \ldots$ and Δt being the measurement time interval. This backward search algorithm accepts each window length as long as the negative slope condition $dC_p^{LE}/dt^* \le -\theta$ continues to hold throughout the entire P_i interval. This process continues until the condition is violated, at which point the largest valid window is selected and the DSV initiation time is defined as $t_D = -P_{i^*}$, where i^* is the maximum index.

Therefore, the complete DSV initiation detection using the C_p method is:

$$t_f = \min\left\{t \in [0, T] \,:\, \frac{dC_p^{LE}(\tau)}{dt^*} \le -\theta \text{ for all } \tau \in [t,\, t+P]\right\}, \tag{6.11}$$

$$i^* = \max\left\{i \ge 0 \,:\, \frac{dC_p^{LE}(\tau)}{dt^*} \le -\theta \text{ for all } \tau \in [T - P_i,\, T]\right\}, \tag{6.12}$$

$$t_D = \begin{cases} t_f, & \text{if } t_f > 0, \\ -P_{i^*}, & \text{else if } t_f = 0. \end{cases} \tag{6.13}$$

Note that in the second scenario, where the DSV initiates near the end of the downstroke, the underlying detection criterion remains unchanged. The two-part formula in Equation (6.13) is used solely to accommodate the predefined ordering of the time series.

Definitions for TEV initiation detection

Similarly, the TEV initiation time is defined based on two parameters: the trailing edge pressure coefficient $C_p^{TE}(t)$ and the time derivative of the trailing edge pressure coefficient $dC_p^{TE}(t)/dt^*$.

The TEV initiation time t_T is identified as the first instant (the minimum value) when $C_p^{TE}(t)$ starts a sustained decrease: specifically, dC_p^{TE}/dt^* must remain below a negative threshold $-\theta$ for at least a duration of P:

$$t_D = \min\left\{t \in [0, T] \;:\; dC_p^{TE}(\tau)/dt^* \le -\theta \;\text{ for all }\; \tau \in [\,t,\, t+P\,]\right\} \tag{6.14}$$

For TEV initiation detection, the following values are selected: $\theta = 2\% \cdot [\max(dC_p^{TE}/dt^*) - \min(dC_p^{TE}/dt^*)]$ and $P = 5\%T$. The value of θ matches the value for DSV initiation detection, while the predefined duration P is different because TEV takes a shorter period to develop during a pitching cycle. This period is less than $5\%T$ for all the reverse flow test cases, as shown in Figure D.6. Note that throughout the reverse flow test cases, the TEV always initiates during upstroke or during the early downstroke, and no pressure fluctuation is caused by TEV development (or partial separation) before the nominal upstroke–downstroke sequence. Consequently, for the purpose of detecting TEV initiation in this dataset, no additional treatment (such as a backward search) is required.

Demonstration of the C_p method

First, an example is shown in Figure 6.30, which illustrates the TEV initiation detection at $\overline{\text{AoA}_\text{r}}15\Delta5k0.1$. Three detecting scenarios are shown: Figure 6.30a, no constraint on θ (i.e., $\theta = 0$) while $P = 5\%T$; Figure 6.30b, no constraint on P (i.e., $P = 0$) while $\theta = 2\% \cdot [\max(dC_p^{TE}/dt^*) - \min(dC_p^{TE}/dt^*)]$; Figure 6.30c, both constraints on θ and P are properly applied.

For all three scenarios, dC_p^{TE}/dt^* is calculated using a forward difference, as shown by the solid green curve. Meanwhile, the threshold $-\theta$ is marked by the green dashed horizontal line.

The TEV initiation time detected by the C_p method is marked as the yellow solid dot. The detection by the POD method is marked with a black cross. The first two figures both provide false detection where the detection TEV initiation point, marked by the yellow dot, is much earlier than the actual sustained decrease location detected from the POD method (the black cross). The successful detection (within 4% relative time difference) only happens when constraints on θ and P are both properly applied. This correct detection is shown in Figure 6.30c. Thus, if any of the constraints from the C_p method is ignored, the TEV initiation time cannot be detected correctly.

Two representative cases, $\overline{\text{AoA}_\text{r}}10\Delta10k0.1$ and $\overline{\text{AoA}_\text{r}}20\Delta10k0.1$, are presented in Figure 6.31 to illustrate the application of the C_p method for detecting DSV initiation under the two scenarios. First, the detection of the DSV initiation time for case $\overline{\text{AoA}_\text{r}}10\Delta10k0.1$ is illustrated in Figure 6.31a. C_p at the location closest to the leading edge ($x_c/c = 0.95$) is selected for the detection. First, t_f is calculated using Equation (6.11), which gives a result of 0.047s (1.6° during upstroke). This value is larger than 0; thus, it falls inside the first scenario where the DSV initiates during the upstroke period. This point is marked by the yellow point in the figure, which successfully indicates the time at which C_p starts to drop, fulfilling the aforementioned requirement. This detection shows the same result from the POD method, which is marked by the black cross.

In order to demonstrate the cases where the DSV initiates from the end of the previous cycle, examples at case $\overline{\text{AoA}_\text{r}}20\Delta10k0.1$ are shown and the corresponding C_p and dC_p/dt at $x/c = 0.95$ are plotted in Figure 6.31b. It is shown that C_p continues to decrease since the beginning of the downstroke cycle, which gives the calculation of $t_\text{f} = 0$ in Equation (6.11). In this scenario, the backward search is applied using Equation (6.12), and the maximum i^* is found with the result marked by the orange point. The point in Figure 6.31b also successfully pinpointed the start of C_p decrease at $x_c/c = 0.95$, which is 0.47 s (11.0° during downstroke). Note that the DSV initiation point detected by the POD method (marked by the black cross) also provides the same result.

Meanwhile, one may also argue that the DSV initiation location obtained from the proposed C_p is at $x_c/c = 0.95$ instead of at the absolute leading edge, as the impact of DSV should initiate at the most upstream position. To verify this, C_p over time for case $\overline{\text{AoA}_\text{r}}10\Delta10k0.1$ at the three closest pressure ports near the leading edge are plotted in Figure 6.32. The points where C_p starts to fulfill the C_p method are marked by the corresponding-colored dots, which shows a delay as x_c/c decreases (towards the trailing edge), with the detected C_p decrease at $x_c/c = 0.95$ being 0.05 s (1.6° during upstroke) and that at $x_c/c = 0.85$ being 0.07 s (3.2° during upstroke). As AoA_r increases, the DSV-induced pressure propa-

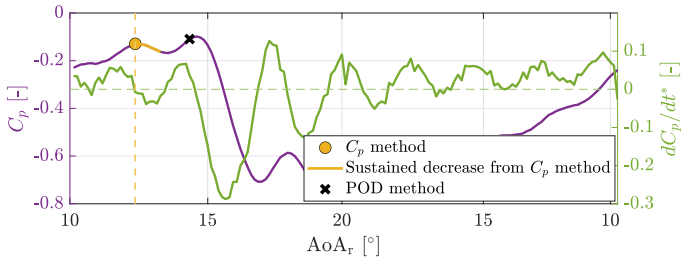

(a) Fault detection ($\theta = 0$, $P = 5\%T$)

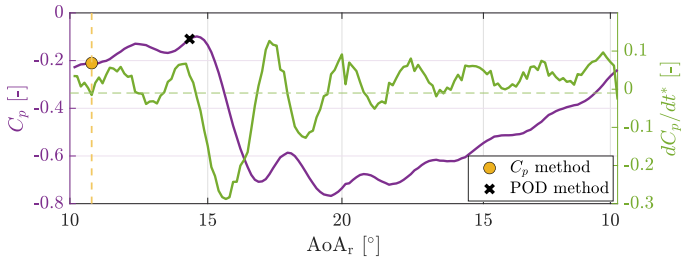

(b) Fault detection ($\theta = 2\% \cdot [\max(dC_p^{TE}/dt^*) - \min(dC_p^{TE}/dt^*)]$, $P = 0$)

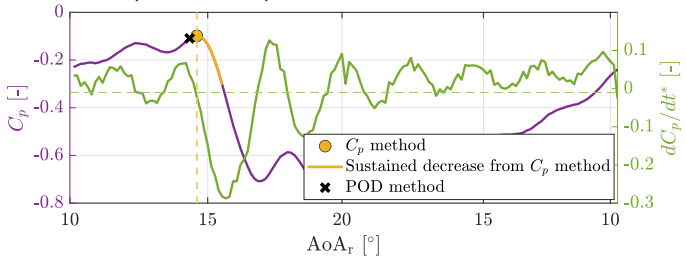

(c) Correct detection ($\theta = 2\% \cdot [\max(dC_p^{TE}/dt^*) - \min(dC_p^{TE}/dt^*)]$, $P = 5\%T$)

Figure 6.30: C_p (purple curve) and dC_p/dt^* (green curve) at the trailing edge location ($x_c/c = 0$) for the reverse flow dynamic stall case $\overline{\text{AoA}_r}15\Delta5k0.1$. The TEV initiation time detected by the (wrongly or correctly implemented) C_p method is marked as the yellow solid dot. While that detected by the POD method is marked with a black cross.

gates downstream, which fulfills the flow physics discussion in Section 6.3.1. As the acquisition of C_p data ranges from $x_c/c = 0$ to $x_c/c = 0.95$ during the experiment, one can also extrapolate the information and obtain the DSV initiation time at the absolute leading edge ($x_c/c = 1$). However, it is important to note that the SDCP method relies on C_p data across all chordwise locations to accurately resolve flow features. Since C_p measurements are unavailable at the absolute leading edge ($x_c/c = 1$), the mSDCP results cannot be directly compared against the interpolated DSV initiation time at $x_c/c = 1$ from the C_p method. To ensure a consistent comparison, the DSV initiation times derived from both methods are instead evaluated at $x_c/c = 0.95$ (up to $x_c/c = 0.95$ for the mSDCP method), the closest available pressure port to the leading edge.

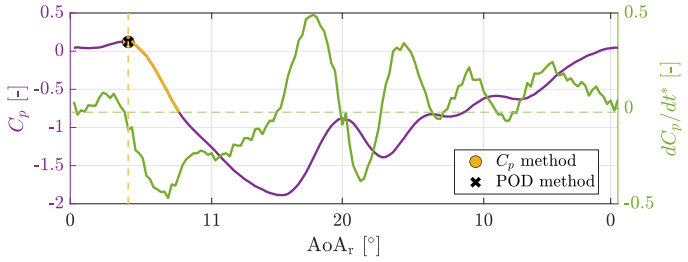

(a) $\overline{\text{AoA}_r}10\Delta10k0.1$

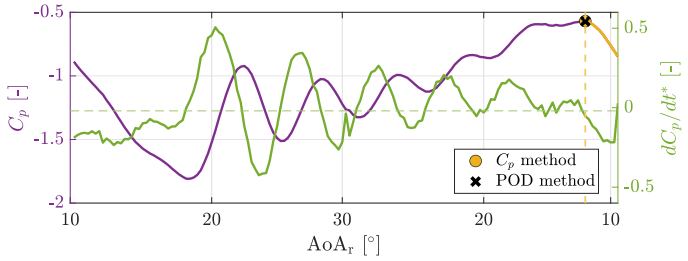

(b) $\overline{\text{AoA}_r}20\Delta10k0.1$

Figure 6.31: C_p (purple curve) and dC_p/dt^* (green curve) at the measure port location closest to the leading edge (x_c/c = 0.95) for reverse flow dynamic stall cases where DSV initiates during upstroke (top) and during downstroke (bottom). The DSV initiation time detected by the C_p method is marked as the yellow solid dot. The detection by the POD method is marked with a black cross.

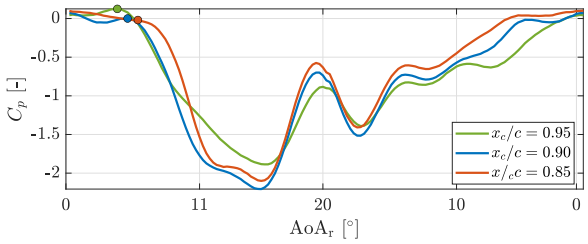

Figure 6.32: C_p at three port locations near the leading edge with the start of C_p decreasing detected from C_p method for case $\overline{\text{AoA}_r}10\Delta10k0.1$.

6.5 Results and discussions: validation of the proposed methods and the DSV development under reverse flow conditions

In this section, the validity of the modified methods and the proposed methods are examined and compared with the POD-based method. The POD method is considered the closest to the ground truth, and the error (δ_t) and relative error ($|\delta_t|/T$) in time are computed for all the reverse flow test cases. Table 6.7 and Table 6.8 present the list of methods to be validated for DSV initiation detection and TEV initiation detection, respectively.

Table 6.7: Validation for the modified DSV initiation detection methods and the proposed C_p method.

Method	Input	Detection point	Reference
mSDCP	Time series of suction side surface pressure; pressure measurement location	Global peak	POD
C_p	Time series of the aerodynamic leading edge pressure	The first point of the sharp decrease	POD

Table 6.8: Validation for the modified TEV initiation detection methods and the proposed C_p method.

Method	Input	Detection point	Reference
HCMP	Time series of suction side surface pressure; pressure measurement location	Global peak	POD
C_p	Time series of the aerodynamic trailing edge pressure	The first point of the sharp decrease	POD

6.5.1 Time determination of DSV initiation

The DSV initiation time is determined using both the C_p method and the mSDCP method. The difference in time δ_t and relative difference ($|\delta_t|/\mathrm{T}$) compared to the reference POD-based method are shown in table Table 6.9 and Table 6.12, respectively, for the mSDCP and the C_p method. For δ_t, the positive value means the prediction from the mSDCP method or the C_p method is later than the prediction from the POD method, and vice versa.

Overall, the average relative error of the mSDCP method is $|\delta_t|/T = 3.1\%$, while that of the C_p method is $|\delta_t|/T = 2.4\%$, compared to the POD-based method. These results indicate that both approaches can reliably estimate the DSV initiation time. Notably, Table 6.12 shows that the C_p method yields more exact matches ($|\delta_t|/T < 0.1\%$). While the maximum relative difference remains 8% for the proposed C_p method, that value reaches 12% for the mSDCP method. As reported in Table 6.9, this case ($\overline{\mathrm{AoA_r}}10\Delta5k0.21$) corresponds to a high reduced frequency of 0.21, which gives a shorter pitching period compared to the other cases, despite the same absolute time difference compared to, e.g., case $\overline{\mathrm{AoA_r}}10\Delta5k0.1$.

These overall performance results indicate that both approaches are comparable and can reliably estimate the DSV initiation time. A further practical advantage of the C_p method is that it requires only pressure information near the leading edge, which is easier to obtain compared to the full suction-side pressure distribution that the mSDCP method requires.

6.5.2 Time determination of TEV initiation

The TEV initiation time obtained from the HCMP method and the C_p method is compared against the POD method, with results summarized in Table 6.11 and Table 6.12, respectively. The time difference δt and relative difference $|\delta t|/T$ are reported, where similarly, a positive δt indicates that the prediction from the HCMP method or the C_p method occurs later than that from the POD method, and vice versa. Overall, both method shows strong agreement with the POD-based method, where the averaged $|\delta t|/T = 1.5\%$ for the

Table 6.9: Absolute and relative time difference between the mSDCP method and the POD method in predicting the DSV initiation time.

Case	δ_t [s]	$\lvert\delta_t\rvert/T$ [%]	Case	δ_t [s]	$\lvert\delta_t\rvert/T$ [%]	Case	δ_t [s]	$\lvert\delta_t\rvert/T$ [%]
$\overline{\text{AoA}_\text{r}}5\Delta10k0.05$	−0.007	0.7	$\overline{\text{AoA}_\text{r}}10\Delta10k0.13$	−0.010	2.5	$\overline{\text{AoA}_\text{r}}15\Delta15k0.05$	0.057	5.7
$\overline{\text{AoA}_\text{r}}5\Delta10k0.08$	−0.013	2.0	$\overline{\text{AoA}_\text{r}}10\Delta10k0.16$	−0.007	2.0	$\overline{\text{AoA}_\text{r}}15\Delta15k0.1$	0.023	4.7
$\overline{\text{AoA}_\text{r}}5\Delta10k0.1$	−0.040	8.0	$\overline{\text{AoA}_\text{r}}10\Delta10k0.18$	−0.007	2.3	$\overline{\text{AoA}_\text{r}}20\Delta10k0.05$	−0.003	3.3
$\overline{\text{AoA}_\text{r}}5\Delta10k0.13$	−0.007	1.7	$\overline{\text{AoA}_\text{r}}10\Delta15k0.05$	0.077	7.7	$\overline{\text{AoA}_\text{r}}20\Delta10k0.08$	−0.007	1.0
$\overline{\text{AoA}_\text{r}}5\Delta10k0.16$	−0.003	1.0	$\overline{\text{AoA}_\text{r}}10\Delta15k0.1$	−0.033	6.7	$\overline{\text{AoA}_\text{r}}20\Delta10k0.1$	−0.003	0.7
$\overline{\text{AoA}_\text{r}}5\Delta10k0.18$	−0.007	2.3	$\overline{\text{AoA}_\text{r}}15\Delta5k0.05$	−0.030	3.0	$\overline{\text{AoA}_\text{r}}20\Delta10k0.13$	−0.010	2.5
$\overline{\text{AoA}_\text{r}}5\Delta15k0.05$	0.023	2.3	$\overline{\text{AoA}_\text{r}}15\Delta5k0.1$	−0.033	6.7	$\overline{\text{AoA}_\text{r}}20\Delta10k0.16$	0.023	7.0
$\overline{\text{AoA}_\text{r}}5\Delta15k0.1$	−0.007	1.3	$\overline{\text{AoA}_\text{r}}15\Delta5k0.16$	−0.013	4.0	$\overline{\text{AoA}_\text{r}}20\Delta10k0.18$	−0.003	1.2
$\overline{\text{AoA}_\text{r}}10\Delta5k0.05$	0.010	1.0	$\overline{\text{AoA}_\text{r}}15\Delta5k0.21$	0.007	2.7	$\overline{\text{AoA}_\text{r}}20\Delta15k0.05$	−0.063	6.3
$\overline{\text{AoA}_\text{r}}10\Delta5k0.1$	−0.030	6.0	$\overline{\text{AoA}_\text{r}}15\Delta10k0.05$	0.013	1.3	$\overline{\text{AoA}_\text{r}}20\Delta15k0.1$	−0.020	4.0
$\overline{\text{AoA}_\text{r}}10\Delta5k0.16$	−0.020	6.0	$\overline{\text{AoA}_\text{r}}15\Delta10k0.08$	0	0	$\overline{\text{AoA}_\text{r}}20\Delta15k0.16$	0.003	1.0
$\overline{\text{AoA}_\text{r}}10\Delta5k0.21$	−0.030	12.0	$\overline{\text{AoA}_\text{r}}15\Delta10k0.1$	0.013	2.7	$\overline{\text{AoA}_\text{r}}25\Delta10k0.18$	0.007	2.3
$\overline{\text{AoA}_\text{r}}10\Delta10k0.05$	0.013	1.3	$\overline{\text{AoA}_\text{r}}15\Delta10k0.13$	−0.010	2.5	$\overline{\text{AoA}_\text{r}}25\Delta15k0.05$	−0.003	0.3
$\overline{\text{AoA}_\text{r}}10\Delta10k0.08$	0.013	2.0	$\overline{\text{AoA}_\text{r}}15\Delta10k0.16$	0.003	1.0	$\overline{\text{AoA}_\text{r}}25\Delta15k0.1$	−0.007	1.3
$\overline{\text{AoA}_\text{r}}10\Delta10k0.1$	0.013	2.6	$\overline{\text{AoA}_\text{r}}15\Delta10k0.18$	−0.007	2.3	$\overline{\text{AoA}_\text{r}}25\Delta15k0.16$	0.003	1.0

Table 6.10: Absolute and relative time difference between the C_p method and the POD method in predicting the DSV initiation time.

Case	δ_t [s]	$\lvert\delta_t\rvert/T$ [%]	Case	δ_t [s]	$\lvert\delta_t\rvert/T$ [%]	Case	δ_t [s]	$\lvert\delta_t\rvert/T$ [%]
$\overline{\text{AoA}_\text{r}}5\Delta10k0.05$	−0.027	2.7	$\overline{\text{AoA}_\text{r}}10\Delta10k0.13$	−0.023	5.8	$\overline{\text{AoA}_\text{r}}15\Delta15k0.05$	0.027	2.7
$\overline{\text{AoA}_\text{r}}5\Delta10k0.08$	−0.433	6.5	$\overline{\text{AoA}_\text{r}}10\Delta10k0.16$	−0.007	2.0	$\overline{\text{AoA}_\text{r}}15\Delta15k0.1$	0.013	2.7
$\overline{\text{AoA}_\text{r}}5\Delta10k0.1$	−0.040	8.0	$\overline{\text{AoA}_\text{r}}10\Delta10k0.18$	−0.003	1.2	$\overline{\text{AoA}_\text{r}}20\Delta10k0.05$	−0.017	1.7
$\overline{\text{AoA}_\text{r}}5\Delta10k0.13$	0	0	$\overline{\text{AoA}_\text{r}}10\Delta15k0.05$	−0.010	1.0	$\overline{\text{AoA}_\text{r}}20\Delta10k0.08$	0.003	0.5
$\overline{\text{AoA}_\text{r}}5\Delta10k0.16$	−0.020	6.0	$\overline{\text{AoA}_\text{r}}10\Delta15k0.1$	0.013	2.7	$\overline{\text{AoA}_\text{r}}20\Delta10k0.1$	0	0
$\overline{\text{AoA}_\text{r}}5\Delta10k0.18$	−0.020	7.0	$\overline{\text{AoA}_\text{r}}15\Delta5k0.05$	0	0	$\overline{\text{AoA}_\text{r}}20\Delta10k0.13$	0	0
$\overline{\text{AoA}_\text{r}}5\Delta15k0.05$	0	0	$\overline{\text{AoA}_\text{r}}15\Delta5k0.1$	0.020	4.0	$\overline{\text{AoA}_\text{r}}20\Delta10k0.16$	0.017	5.0
$\overline{\text{AoA}_\text{r}}5\Delta15k0.1$	−0.017	3.3	$\overline{\text{AoA}_\text{r}}15\Delta5k0.16$	−0.020	6.0	$\overline{\text{AoA}_\text{r}}20\Delta10k0.18$	−0.003	1.2
$\overline{\text{AoA}_\text{r}}10\Delta5k0.05$	0.020	2.0	$\overline{\text{AoA}_\text{r}}15\Delta5k0.21$	0.007	2.7	$\overline{\text{AoA}_\text{r}}20\Delta15k0.05$	0.003	0.3
$\overline{\text{AoA}_\text{r}}10\Delta5k0.1$	−0.017	3.3	$\overline{\text{AoA}_\text{r}}15\Delta10k0.05$	0.013	1.3	$\overline{\text{AoA}_\text{r}}20\Delta15k0.1$	−0.003	0.7
$\overline{\text{AoA}_\text{r}}10\Delta5k0.16$	−0.017	5.0	$\overline{\text{AoA}_\text{r}}15\Delta10k0.08$	−0.010	1.5	$\overline{\text{AoA}_\text{r}}20\Delta15k0.16$	0.017	5.0
$\overline{\text{AoA}_\text{r}}10\Delta5k0.21$	−0.007	2.7	$\overline{\text{AoA}_\text{r}}15\Delta10k0.1$	0.010	2.0	$\overline{\text{AoA}_\text{r}}25\Delta10k0.18$	0.003	1.2
$\overline{\text{AoA}_\text{r}}10\Delta10k0.05$	−0.013	1.3	$\overline{\text{AoA}_\text{r}}15\Delta10k0.13$	0	0	$\overline{\text{AoA}_\text{r}}25\Delta15k0.05$	0.003	0.3
$\overline{\text{AoA}_\text{r}}10\Delta10k0.08$	−0.013	0.5	$\overline{\text{AoA}_\text{r}}15\Delta10k0.16$	0.007	2.0	$\overline{\text{AoA}_\text{r}}25\Delta15k0.1$	−0.007	1.3
$\overline{\text{AoA}_\text{r}}10\Delta10k0.1$	0	0	$\overline{\text{AoA}_\text{r}}15\Delta10k0.18$	−0.010	3.5	$\overline{\text{AoA}_\text{r}}25\Delta15k0.16$	0.010	3.0

HCMP method and 1.0% for the C_p method. For both methods, the TEV initiation times are evaluated more accurately than the DSV initiation times.

This result indicates that while the HCMP method cannot identify the precise moment of DSV initiation under reverse flow conditions, it accurately captures the TEV initiation time. This is because the TEV initiates immediately after the suction side C_p reaches its minimum, which is a state driven by the initial full development of the DSV. Consequently, the HCMP method detects the strong pressure variations associated with the developed DSV, which temporally aligns with the onset of the TEV rather than the DSV in cfor the reverse flow cases.

While the maximum relative difference from the C_p method is as small as 4.7% at case $\overline{\text{AoA}_\text{r}20\Delta10k0.18}$, the maximum relative difference for the HCMP method reaches 18% (at case $\overline{\text{AoA}_\text{r}25\Delta15k0.1}$). Recall from Section 6.4.2 that HCMP is the product between the $C_{p,rms}$ (Equation (6.8)) and the LPP. In this case, both the $C_{p,rms}$ and the LPP reach their maximum values after the first partial separation of the DSV and the TEV initiation (not shown in the dissertation), and the HCMP method predicts the subsequent TEV initiation (after the secondary growth of the DSV) instead. Therefore, when multiple separation and regrowth events occur, the HCMP method becomes less reliable than the C_p method.

Overall, validation against POD analysis confirms that both the HCMP and C_p methods provide reliable estimations of TEV initiation time under reverse flow conditions. Notably, the C_p method offers a distinct advantage in terms of simplicity, as it requires data from only a single pressure port.

Table 6.11: HCMP method compared with the POD method regarding the TEV initiation time.

Case	δ_t [s]	$\lvert\delta_t\rvert/T$ [%]	Case	δ_t [s]	$\lvert\delta_t\rvert/T$ [%]	Case	δ_t [s]	$\lvert\delta_t\rvert/T$ [%]
$\overline{\text{AoA}_\text{r}5\Delta10k0.05}$	−0.007	0.7	$\overline{\text{AoA}_\text{r}10\Delta10k0.13}$	−0.003	0.8	$\overline{\text{AoA}_\text{r}15\Delta15k0.05}$	0	0
$\overline{\text{AoA}_\text{r}5\Delta10k0.08}$	−0.007	1.0	$\overline{\text{AoA}_\text{r}10\Delta10k0.16}$	−0.003	1.0	$\overline{\text{AoA}_\text{r}15\Delta15k0.1}$	0	0
$\overline{\text{AoA}_\text{r}5\Delta10k0.1}$	−0.007	1.3	$\overline{\text{AoA}_\text{r}10\Delta10k0.18}$	0	0	$\overline{\text{AoA}_\text{r}20\Delta10k0.05}$	−0.047	4.7
$\overline{\text{AoA}_\text{r}5\Delta10k0.13}$	−0.007	1.7	$\overline{\text{AoA}_\text{r}10\Delta15k0.05}$	−0.023	2.3	$\overline{\text{AoA}_\text{r}20\Delta10k0.08}$	−0.013	2.0
$\overline{\text{AoA}_\text{r}5\Delta10k0.16}$	−0.007	2.0	$\overline{\text{AoA}_\text{r}10\Delta15k0.1}$	−0.003	0.7	$\overline{\text{AoA}_\text{r}20\Delta10k0.1}$	−0.003	0.7
$\overline{\text{AoA}_\text{r}5\Delta10k0.18}$	−0.007	2.3	$\overline{\text{AoA}_\text{r}15\Delta5k0.05}$	−0.010	1.0	$\overline{\text{AoA}_\text{r}20\Delta10k0.13}$	−0.007	1.7
$\overline{\text{AoA}_\text{r}5\Delta15k0.05}$	−0.007	0.7	$\overline{\text{AoA}_\text{r}15\Delta5k0.1}$	0	0	$\overline{\text{AoA}_\text{r}20\Delta10k0.16}$	−0.013	4.0
$\overline{\text{AoA}_\text{r}5\Delta15k0.1}$	0	0	$\overline{\text{AoA}_\text{r}15\Delta5k0.16}$	−0.003	1.0	$\overline{\text{AoA}_\text{r}20\Delta10k0.18}$	−0.017	5.8
$\overline{\text{AoA}_\text{r}10\Delta5k0.05}$	−0.020	2.0	$\overline{\text{AoA}_\text{r}15\Delta5k0.21}$	0.003	1.3	$\overline{\text{AoA}_\text{r}20\Delta15k0.05}$	−0.003	0.3
$\overline{\text{AoA}_\text{r}10\Delta5k0.1}$	−0.007	1.3	$\overline{\text{AoA}_\text{r}15\Delta10k0.05}$	0	0	$\overline{\text{AoA}_\text{r}20\Delta15k0.1}$	0	0
$\overline{\text{AoA}_\text{r}10\Delta5k0.16}$	−0.003	1.0	$\overline{\text{AoA}_\text{r}15\Delta10k0.08}$	0	0	$\overline{\text{AoA}_\text{r}20\Delta15k0.16}$	0.003	1.0
$\overline{\text{AoA}_\text{r}10\Delta5k0.21}$	−0.007	2.7	$\overline{\text{AoA}_\text{r}15\Delta10k0.1}$	0	0	$\overline{\text{AoA}_\text{r}25\Delta10k0.18}$	0	0
$\overline{\text{AoA}_\text{r}10\Delta10k0.05}$	−0.003	0.3	$\overline{\text{AoA}_\text{r}15\Delta10k0.13}$	−0.003	0.8	$\overline{\text{AoA}_\text{r}25\Delta15k0.05}$	−0.007	0.7
$\overline{\text{AoA}_\text{r}10\Delta10k0.08}$	−0.010	1.5	$\overline{\text{AoA}_\text{r}15\Delta10k0.16}$	0	0	$\overline{\text{AoA}_\text{r}25\Delta15k0.1}$	−0.090	18.0
$\overline{\text{AoA}_\text{r}10\Delta10k0.1}$	−0.003	0.7	$\overline{\text{AoA}_\text{r}15\Delta10k0.18}$	0	0	$\overline{\text{AoA}_\text{r}25\Delta15k0.16}$	−0.003	1.0

Table 6.12: C_p method compared with the POD method regarding the TEV initiation time.

Case	δ_t [s]	$\lvert\delta_t\rvert/T$ [%]	Case	δ_t [s]	$\lvert\delta_t\rvert/T$ [%]	Case	δ_t [s]	$\lvert\delta_t\rvert/T$ [%]
$\overline{\mathrm{AoA_r}}5\Delta10k0.05$	0.003	0.3	$\overline{\mathrm{AoA_r}}10\Delta10k0.13$	0	0	$\overline{\mathrm{AoA_r}}15\Delta15k0.05$	0.007	0.7
$\overline{\mathrm{AoA_r}}5\Delta10k0.08$	0	0	$\overline{\mathrm{AoA_r}}10\Delta10k0.16$	0.003	1.0	$\overline{\mathrm{AoA_r}}15\Delta15k0.1$	0.007	1.3
$\overline{\mathrm{AoA_r}}5\Delta10k0.1$	0.010	2.0	$\overline{\mathrm{AoA_r}}10\Delta10k0.18$	0.003	1.2	$\overline{\mathrm{AoA_r}}20\Delta10k0.05$	0.003	0.3
$\overline{\mathrm{AoA_r}}5\Delta10k0.13$	0.007	1.7	$\overline{\mathrm{AoA_r}}10\Delta15k0.05$	−0.007	0.7	$\overline{\mathrm{AoA_r}}20\Delta10k0.08$	−0.007	1.0
$\overline{\mathrm{AoA_r}}5\Delta10k0.16$	0.007	2.0	$\overline{\mathrm{AoA_r}}10\Delta15k0.1$	0	0	$\overline{\mathrm{AoA_r}}20\Delta10k0.1$	0.003	0.7
$\overline{\mathrm{AoA_r}}5\Delta10k0.18$	0.003	1.2	$\overline{\mathrm{AoA_r}}15\Delta5k0.05$	0	0	$\overline{\mathrm{AoA_r}}20\Delta10k0.13$	−0.003	0.8
$\overline{\mathrm{AoA_r}}5\Delta15k0.05$	0	0	$\overline{\mathrm{AoA_r}}15\Delta5k0.1$	0.007	1.3	$\overline{\mathrm{AoA_r}}20\Delta10k0.16$	−0.010	3.0
$\overline{\mathrm{AoA_r}}5\Delta15k0.1$	0	0	$\overline{\mathrm{AoA_r}}15\Delta5k0.16$	0.007	2.0	$\overline{\mathrm{AoA_r}}20\Delta10k0.18$	−0.013	4.7
$\overline{\mathrm{AoA_r}}10\Delta5k0.05$	0.023	2.3	$\overline{\mathrm{AoA_r}}15\Delta5k0.21$	0.007	2.7	$\overline{\mathrm{AoA_r}}20\Delta15k0.05$	0	0
$\overline{\mathrm{AoA_r}}10\Delta5k0.1$	0.007	1.3	$\overline{\mathrm{AoA_r}}15\Delta10k0.05$	0.007	0.7	$\overline{\mathrm{AoA_r}}20\Delta15k0.1$	0.003	0.7
$\overline{\mathrm{AoA_r}}10\Delta5k0.16$	0.003	1.0	$\overline{\mathrm{AoA_r}}15\Delta10k0.08$	0.007	1.0	$\overline{\mathrm{AoA_r}}20\Delta15k0.16$	0.007	2.0
$\overline{\mathrm{AoA_r}}10\Delta5k0.21$	0.007	2.7	$\overline{\mathrm{AoA_r}}15\Delta10k0.1$	0	0	$\overline{\mathrm{AoA_r}}25\Delta10k0.18$	−0.003	1.2
$\overline{\mathrm{AoA_r}}10\Delta10k0.05$	0.007	0.7	$\overline{\mathrm{AoA_r}}15\Delta10k0.13$	0	0	$\overline{\mathrm{AoA_r}}25\Delta15k0.05$	0	0
$\overline{\mathrm{AoA_r}}10\Delta10k0.08$	−0.003	0.5	$\overline{\mathrm{AoA_r}}15\Delta10k0.16$	0.007	2.0	$\overline{\mathrm{AoA_r}}25\Delta15k0.1$	0	0
$\overline{\mathrm{AoA_r}}10\Delta10k0.1$	0	0	$\overline{\mathrm{AoA_r}}15\Delta10k0.18$	0.007	2.3	$\overline{\mathrm{AoA_r}}25\Delta15k0.16$	0	0

6

6.5.3 Extended application of the proposed C_p method: DSV development tracking

As has been validated, for dynamic stall under reverse flow conditions, the DSV initiation time can be accurately tracked by examining the sudden decrease of C_p at the leading edge using the proposed C_p method. Similarly, by tracking the (first) sharp decrease of the C_p in space from the leading edge to the trailing edge, one can examine the development of the DSV in the chordwise direction, as when the suction impact extends to the specific chordwise location after the leading edge. To compare with different cases, the chordwise location at which the first decrease in C_p occurs is plotted against the tracked non-dimensional time t/T. To quantify how rapidly the DSV suction footprint spreads downstream, including the growth and convection, the gradient of this location–time curve ($d(x_c/c)/(d(t/T))$) is calculated for all the cases and is defined as the chordwise evolution rate of the DSV. In this section, the influence of k and $\overline{\mathrm{AoA_r}}$ on the DSV development, as well as on the chordwise evolution rate, is discussed separately based on selected cases. Note that the trailing edge 10% is excluded from the plot, as in that region the TEV dominates the pressure.

Influence of k on the DSV development and chordwise evolution rate

Figure 6.33 includes six DSV development subplots that present cases with the same $\overline{\mathrm{AoA_r}}$ and $\Delta\mathrm{AoA_r}$ combination ($\overline{\mathrm{AoA_r}}5\Delta10$, $\overline{\mathrm{AoA_r}}10\Delta10$, $\overline{\mathrm{AoA_r}}15\Delta10$, $\overline{\mathrm{AoA_r}}20\Delta10$, $\overline{\mathrm{AoA_r}}10\Delta5$, and $\overline{\mathrm{AoA_r}}15\Delta5$) but different k values in each subplot. The y-axis represents the location where DSV suction first sharply decreases at a specific time on the x-axis.

Overall, the development trends indicate that for a given combination of mean angle of attack $\overline{\mathrm{AoA_r}}$ and amplitude $\Delta\mathrm{AoA_r}$, the DSV-induced impact initiates at the leading edge ($x_c/c \approx 1$) and gradually expands toward the trailing edge as the airfoil pitches. Based

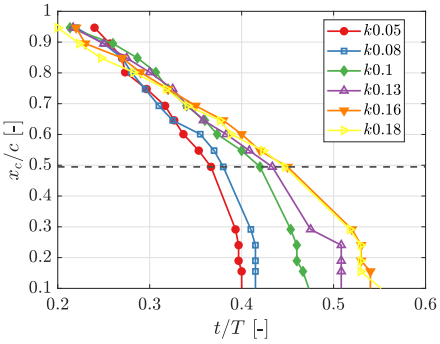

(a) $\overline{\text{AoA}_\text{r}}$5Δ10 (DSV-dominated flow)

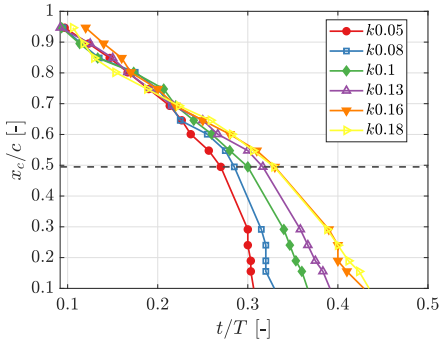

(b) $\overline{\text{AoA}_\text{r}}$10Δ10 (DSV-dominated flow)

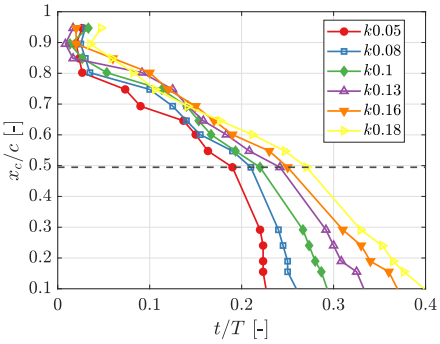

(c) $\overline{\text{AoA}_\text{r}}$15Δ10 (comparable DSV-TEV domination)

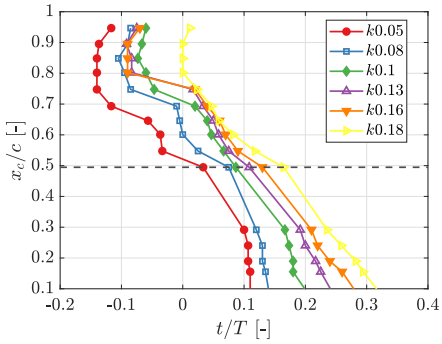

(d) $\overline{\text{AoA}_\text{r}}$20Δ10 (comparable DSV-TEV domination and TEV-dominated flow)

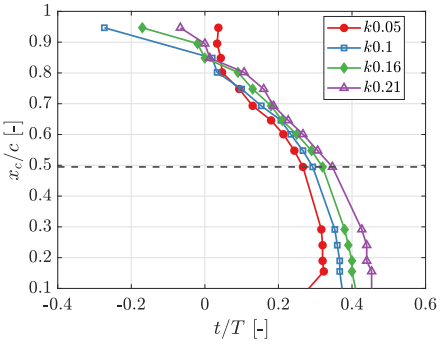

(e) $\overline{\text{AoA}_\text{r}}$10Δ5 (DSV-dominated flow)

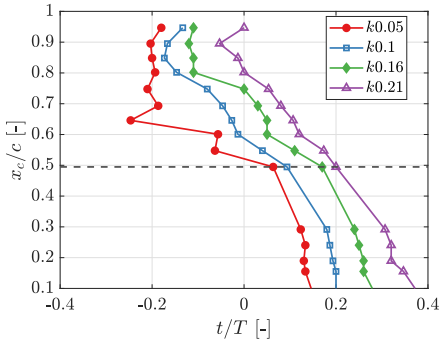

(f) $\overline{\text{AoA}_\text{r}}$15Δ5 (comparable DSV-TEV domination)

Figure 6.33: DSV development in the chordwise direction as a function of non-dimensional time t/T - influence of k. The dashed horizontal line is located at $x_c/c = 0.5$.

on the evolution rate (discussed in Figure 6.34), a two-stage development of the DSV is observed for each $\overline{\text{AoA}_\text{r}}$ and $\Delta\text{AoA}_\text{r}$ combination:

1. **Phase 1:** From the leading edge to $x_c/c = 0.5$ (marked by dashed horizontal lines in

Figure 6.33).

2. **Phase 2:** Between $x_c/c = 0.5$ and $x_c/c = 0.1$.

During Phase 1, development is primarily governed by the underlying flow topology rather than kinematic unsteadiness. As discussed in the POD analysis (Section 6.3.2), the flow physics near the pitching airfoil can be categorized into DSV-dominated flow (lower $\overline{\text{AoA}_r}$), mixed DSV-TEV flow, and TEV-dominated flow (higher $\overline{\text{AoA}_r}$). For DSV-dominated cases (e.g., Figures 6.33a and 6.33b), the development curve is approximately linear. This linearity corresponds to the initial boundary layer separation from the sharp leading edge, where the reverse flow, as long as the DSV core near the airfoil surface, is not formed (see case $\overline{\text{AoA}_r}10\Delta10k0.1$ at phase d (Figure 6.5d) to f (Figure 6.5f)).

In contrast, cases with mixed or TEV-dominated flows (e.g., Figures 6.33c and 6.33d) exhibit a sharp slope near the leading edge. This behavior is linked to the hysteresis of the flow field. In these high angle cases, the flow is already separated near the leading edge at the start of the cycle ($t/T \approx 0$). Consequently, the DSV does not form from a clean boundary layer but evolves within an existing separation region (e.g., case $\overline{\text{AoA}_r}20\Delta10k0.1$ at phase o Figure 6.12o), leading to a rapid (almost instantaneous) initial evolution of the suction footprint.

Quantitatively, the evolution rate $d(x_c/c)/d(t/T)$ is obtained at $x_c/c = 0.7$ (near the center of Phase 1), as shown in Figure 6.34a. The overall rate ranges from −3.6 to −0.9 across all relevant cases. Crucially, for DSV-modinated flow cases of $\text{AoA}_r10\Delta5$ (the blue curve) and $\text{AoA}_r10\Delta10$ cases (the red curve), the evolution rate amplitude decreases with increasing k. However, for mixed-energy flows or TEV-dominated flows ($\text{AoA}_r15\Delta10$, $\text{AoA}_r20\Delta10$, and $\text{AoA}_r15\Delta5$), this rate shows fluctuations with no clear monotonic trend with k. This result further demonstrates that, during the initial boundary layer separation, for mixed energy or TEV-dominated flow cases, the effective angle of attack (from the combined effect of the pitching amplitude and the mean pitching angle) plays a larger role, with the linear DSV development region occurring after the initial separation near the leading edge.

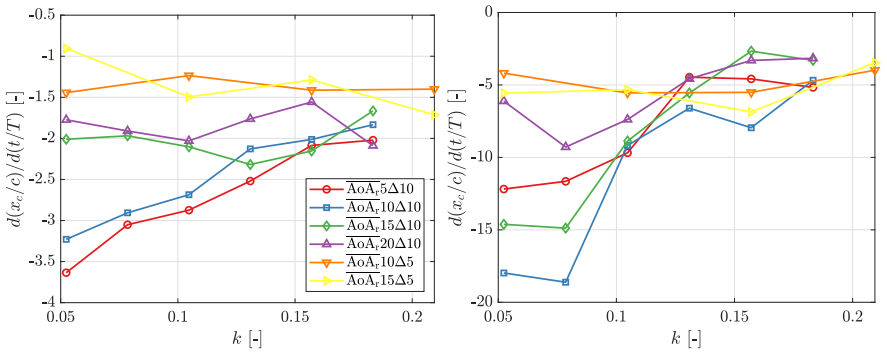

(a) Phase 1 ($x_c/c = 0.7$)

(b) Phase 2 ($x_c/c = 0.3$)

Figure 6.34: DSV chordwise evolution rate in the chordwise direction $d(x_c/c)/d(t/T)$ at phase 1 ($x_c/c = 0.7$) and phase 2 ($x_c/c = 0.3$).

As the DSV extends beyond mid-chord (Phase 2), the location of the DSV-induced suction shows a stronger dependence on k across all cases. In Figure 6.33, the development curve follows a second-order polynomial form. Therefore, a second-order polynomial fit of t/T versus x_c/c was performed, and the result at $x_c/c = 0.3$ (near the center of this region) is presented in Figure 6.34b. In this phase, the DSV evolution rate is much higher than in Phase 1, with the maximum magnitude near 20. As k increases, the magnitude of the DSV evolution rate decreases dramatically. The largest reduction occurs at $\overline{\text{AoA}_\text{r}}10\Delta10$, where $d(x_c/c)/d(t/T)$ changes from almost −20 at $k = 0.05$ to −5 at $k = 0.21$. This variation is significantly larger than in phase 1 (Figure 6.34a) and largely determines the delayed DSV development at higher k. Surface pressure measurements for the $\overline{\text{AoA}_\text{r}}10\Delta10$ case in Figure D.6 further illustrate this trend: increasing k strengthens the DSV-induced suction peak (more negative C_p) and delays its occurrence in time. At low reduced frequencies ($k = 0.05, 0.08$), the DSV forms and convects rapidly, with peak suction ($C_p \approx -1.75$ to -2.0) largely confined to the upstroke. At the highest k value (0.18), DSV formation is prolonged, resulting in a stronger suction ($C_p < -2.5$) that extends into the downstroke. Thus, for a lower k condition, the separation extent is lower due to low unsteadiness, which leads to a shorter time for full development. However, when k values are higher, the peak suction pressure increases in magnitude where the full DSV development takes a longer time. These observations align with previous studies (e.g., [76]), but here the effect of k is explicitly interpreted in terms of DSV development dynamics.

Therefore, the delay observed at high k is not a delay in initiation, but a delay in downstream propagation caused by the prolonged accumulation of vorticity. High unsteadiness facilitates a stronger, more coherent vortex structure that dominates the airfoil surface for a longer duration, albeit with a slower rate of spatial evolution.

Influence of $\overline{\text{AoA}_\text{r}}$ on the DSV development and chordwise evolution rate

Figure 6.35 presents the DSV development in the chordwise direction as a function of non-dimensional time t/T for varying mean angle of attack $\overline{\text{AoA}_\text{r}}$ from 5° to 25° for three distinct dynamic cases: $\Delta10k0.18$ (Figure 6.35a), $\Delta15k0.05$ (Figure 6.35b), and $\Delta15k0.11$ (Figure 6.35b).

The most prominent feature across all cases is that the DSV development curves for different $\overline{\text{AoA}_\text{r}}$ are almost parallel. This indicates that the mean angle of attack $\overline{\text{AoA}_\text{r}}$ has a negligible influence on the rate of vorticity accumulation once the DSV starts to grow. Instead, the primary role of $\overline{\text{AoA}_\text{r}}$ is to control the starting time for DSV formation. At a high $\overline{\text{AoA}_\text{r}}$, the instantaneous angle of attack AoA_r exceeds the critical static stall angle and the DSV initiates much earlier: for $\overline{\text{AoA}_\text{r}} = 25°$ cases at both $\Delta15k0.05$ and $\Delta15k0.11$, and $\overline{\text{AoA}_\text{r}} = 20°$ case at $\Delta15k0.11$, the DSV even starts formation from the end of the previous downstroke cycle, where the initial tracked locations has $t/T < 0$. This leads to an earlier onset of DSV formation and an earlier ending of its evolution. Conversely, at a low $\overline{\text{AoA}_\text{r}}$ (e.g., $\overline{\text{AoA}_\text{r}} = 5°$), the airfoil operates far below its stall condition for most of the cycle, which means a more substantial upstroke motion with a high pitching amplitude is required to reach the critical stall AoA_r for boundary layer rolling-up. This results in a delayed onset of DSV formation, which, in turn, develops at a later stage.

In summary, the mean angle of attack $\overline{\text{AoA}_\text{r}}$ does not influence the overall DSV evo-

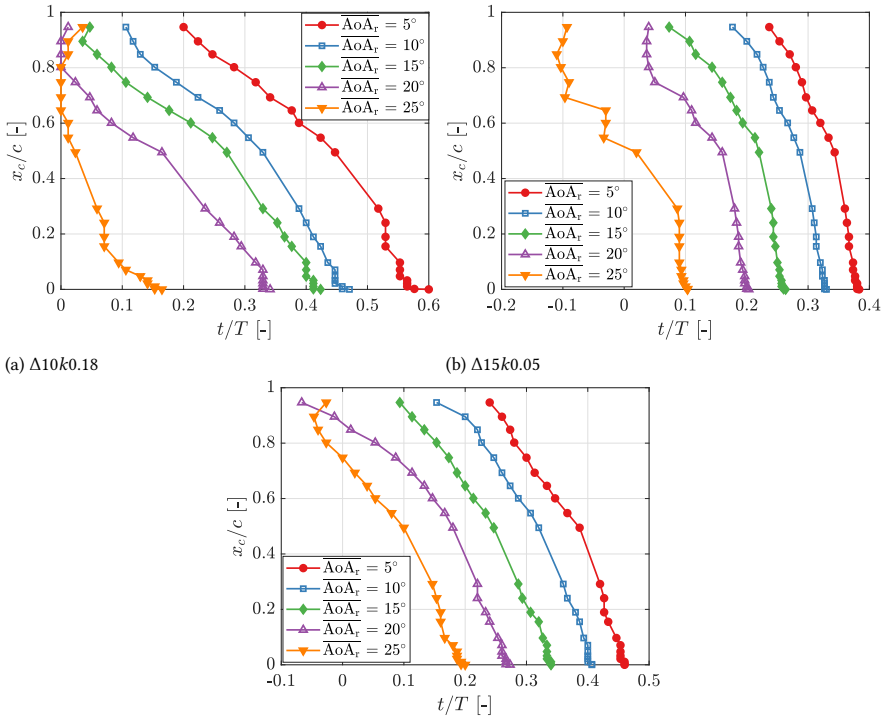

(a) $\Delta 10k0.18$

(b) $\Delta 15k0.05$

(c) $\Delta 15k0.1$

Figure 6.35: DSV development in the chordwise direction as a function of non-dimensional time t/T — influence of $\overline{\mathrm{AoA_r}}$.

lution rate, but instead, acts as a phase-shift parameter for the dynamic stall process. It determines the specific point in the oscillation cycle at which the boundary layer separates, thereby shifting the entire life cycle of the DSV earlier or later without altering its intrinsic chordwise evolution character.

6.6 Conclusion

The dynamic stall of a pitching airfoil under reverse flow conditions is experimentally studied under different test parameters of mean angle of attack, reduced frequency, and pitching amplitude. Combining both surface pressure measurements and PIV flow field measurements, the analysis targets the relation between vortex evolution and aerodynamic force variation and the strong dominant flow features under different pitching cases.

Combined surface pressure and PIV flow fields provide detailed information on the vortex dynamics and their influence on the surface pressure. The multiple suction peaks on the airfoil suction side, instead of representing the number of DSVs generated during one pitching cycle, indicate that multiple DSV separations and shedding happen during a pitching cycle, which shows a universal trend among all the test cases. These separations are only partial: the outer part of the boundary layer is shed downstream, while the inner

part remains attached and feeds the circulation of the dynamic stall vortex. As a result, the force coefficient exhibits multiple peaks due to (1) DSV formation and partial separation, and (2) the secondary growth of the attached DSV(s) and separation. Compared to conventional dynamic stall cases, the flow separation at the initial stage of DSV development causes a gradual decrease in the pressure coefficient. Instead, for conventional dynamic stall cases, the presence of the laminar separation bubbles leads to the suction peak near the leading edge region, before the DSV forms [72, 129, 130].

POD analysis was conducted across all test cases to identify the dominant flow features. Over the tested parameter range ($k \in [0.05, 0.21]$, $\Delta\mathrm{AoA}_\mathrm{r} \in [5^\circ, 15^\circ]$), the type of flow regime, and in particular which vortex dominates the flow dynamics, depends mainly on the mean angle of attack $\overline{\mathrm{AoA}_\mathrm{r}}$: (1) for low mean angle ($\overline{\mathrm{AoA}_\mathrm{r}} = 5^\circ$ and 10°), the DSV development dominates the flow; for $\overline{\mathrm{AoA}_\mathrm{r}} = 5^\circ$ cases, the TEV remains underdeveloped, with no discernible trailing-edge pressure peak. (2) For moderate mean angles ($\overline{\mathrm{AoA}_\mathrm{r}} = 15^\circ$), the energy partitions comparably between DSV and TEV. (3) For high mean angle ($\overline{\mathrm{AoA}_\mathrm{r}} = 20^\circ$ and 25°), multiple flow separations trigger robust TEV development, enabling more cases to have TEV dominance. Despite these $\overline{\mathrm{AoA}_\mathrm{r}}$-dependent variations in modal dominance, all dominant POD modes share a consistent physical interpretation: they capture the growth or decay of DSV and TEV structures.

In addition, a POD analysis comparison was made between the conventional and reverse flow dynamic stall cases. It is shown that, similar to the literature [123], for conventional dynamic stall cases, the most dominant energy (mode 1) represents the growth and decay of the leading edge negative pressure, which is highly related to the dynamics of the LSB(s). This most dominant energy shows the same pattern for all the conventional cases with different mean angles of attack, pitching amplitudes, and reduced frequencies. This result reveals the fundamental difference in the flow physics between conventional and reverse flow dynamic stall. Such differences have important implications for real-world applications: for example, the strong partially attached DSVs or the TEV development under reverse flow can influence unsteady loading, vibration, and fatigue on parked wind turbine blades, propellers, and helicopter rotors, where reverse flow conditions are encountered.

The characteristic of reverse flow vortex dynamics, where dominant features are limited to DSV and TEV development, enables robust vortex initiation detection via the C_p method. This approach monitors single-port pressure at either the leading or trailing edge, avoiding the need for full-surface measurements. Validation against established techniques confirms its accuracy: the C_p method agrees with the POD method for DSV initiation time (averaged relative difference of 2.4% of cycle period) and aligns accurately for TEV initiation time (averaged relative difference of 1.0%).

While existing methods developed for conventional dynamic stall cases, such as SDCP and HCMP [123], struggle to detect DSV initiation under reverse flow conditions, and the MLPP method [123] fails to consistently detect TEV initiation, the C_p method offers a robust alternative. Notably, the modified SDCP (mSDCP) method is capable of predicting DSV initiation with a relative error of 3.1%. Furthermore, the HCMP method, applied as a pure statistical parameter without modification, successfully predicts TEV initiation (instead of DSV) with a relative error of 1.5%. However, the C_p method retains a distinct advantage due to its use of a single pressure port, making it ideal for applications with

limited instrumentation.

Furthermore, the extended C_p method allows for straightforward tracking of DSV evolution along the airfoil suction surface when pressure measurements are available all along the chordwise direction. Detection is achieved by applying the C_p method at every single pressure port from the leading edge to the trailing edge. The results demonstrate that DSV development categorizes into two distinct phases for any $\overline{\mathrm{AoA_r}}$ and $\Delta\mathrm{AoA_r}$ combination: an initial phase (Phase 1) dominated by immediate boundary layer separation, and a major evolution phase (Phase 2) driven by reduced frequency. In the major evolution phase (Phase 2), a higher k leads to slower development but results in a stronger DSV. Conversely, in Phase 1, increasing k results in a milder evolution rate for only DSV-dominated flows; in other cases, the effective angle of attack dominates the development, leaving the evolution rate insensitive to k. Finally, the mean angle of attack, $\overline{\mathrm{AoA_r}}$, acts primarily as a phase-shift parameter, advancing or delaying the DSV life cycle without altering its intrinsic chordwise evolution behavior.

IV

Conclusion

7

Conclusion

This research aims to investigate the unsteady aerodynamics of static and oscillating airfoils at large angles of attack through experimental methods. In this chapter, the conclusions are summarized based on the airfoil motion, with the aim of answering the research questions listed in Chapter 1. Finally, the outlook for future research is proposed.

7.1 Conclusion

7.1.1 Static airfoil behavior at large angles of attack

A static DU91-W2-150 airfoil was tested across a wide range of angles of attack, up to 310°, at three Reynolds numbers with the order of 10^5. Experimental results from PIV and surface pressure measurements reveal that forward and reverse flow conditions produce distinct unsteady aerodynamic responses.

Answer to research question 1: Forward vs. reverse flow effects

Research question 1
How do unsteady aerodynamic phenomena influence the forces and flow dynamics of static and oscillating airfoils at high angles of attack?

Under forward flow, separation develops gradually with increasing angle of attack, resulting in relatively smooth fluctuations in lift and drag. Vortex shedding remains coherent, and the shedding frequency is largely independent of Reynolds number, reflecting fully stalled flow. In reverse flow, instantaneous separation occurs at the aerodynamic leading edge, generating larger unsteady force fluctuations. Despite this, the Strouhal number is not influenced by the forward flow or reverse flow condition; instead, the airfoil surfaces are more critical: the Strouhal number is slightly higher when the angle of attack exceeds 180°, because an airfoil with a convex curvature in the upwind direction has less effect on wake expansion, resulting in a higher shedding frequency. These observations demonstrate that reverse flow amplifies unsteady loading and modifies vortex dynamics, whereas forward flow produces smoother aerodynamic forces. This fundamental distinction carries over to forced airfoil motions, and understanding forward and reverse flow effects in the static airfoil provides a critical foundation for interpreting and predicting the unsteady aerodynamic behavior of airfoils under various forced motions.

7.1.2 Oscillating airfoil behavior at large angles of attack

This dissertation investigates the vortex dynamics and aerodynamic response of airfoils undergoing three types of forced motion: surge (streamwise motion), plunge (cross-flow motion), and pitch (rotational motion). This section summarizes the experimental findings and their implications for aerodynamic performance, frequency lock-in, reverse flow effect, and DSV onset detection.

Surge Motion

Surge motion was studied at a fixed angle of attack of 90° with two reduced frequencies, $k = 0.19$ and $k = 0.38$.

Answer to research question 2: Vortex dynamics and aerodynamic performance

Research question 2
How do the evolution and interaction of vortices in various forced motions affect aerodynamic performance?

At the lower k, vortices remain confined to the downwind side, forming elongated, turbulence-dominated structures that contribute to small variations in aerodynamic force. At the higher k, a vortex pair forms in the upwind direction during the downstream motion and sheds simultaneously with the wake vortices at the end of the downwind motion. This synchronized shedding produces large, periodic fluctuations in drag.

Answer to research question 3: Effect of motion frequency on lock-in

> **Research question 3**
> How does motion frequency alter the formation, interaction, and synchronization of vortices, and what is its role in driving frequency lock-in?

Surging exhibits clear frequency lock-in at both tested k cases. At the higher k, where the motion frequency is close to the natural shedding frequency, two vortex pairs grow out of phase but shed simultaneously; at the lower k, a single pair of wake vortices forms and sheds per cycle, matching the imposed motion frequency. While the former is validated against prior findings [106–108] for standard VIV conditions, the latter demonstrates that lock-in can also occur under subharmonic conditions [114], when the motion frequency is much lower than the natural static shedding frequency. In our experiments, the high imposed motion amplitude appears to play a key role in enabling this subharmonic lock-in.

Plunge Motion

Plunge motion was also studied at 90° geometric angle of attack with $k = 0.19$ and $k = 0.38$.

Answer to research question 2: Vortex dynamics and aerodynamic performance

Plunging motion modulates the instantaneous angle of attack, generating fundamentally different vortex behavior compared to a surging case. At the lower k, a single LEV–TEV pair forms during the downstroke, with an additional LEV shedding during the upstroke, resulting in irregular vortex interactions and lower force variation. At the higher k, two strong LEV–TEV pairs form per cycle, including one created via the separation from a counter-rotating vortex. This leads to higher aerodynamic forces and variations within a cycle. Compared to surging motion, plunging generates less coherent vortices due to additional force in the crossflow direction, and the vortex shedding performance is highly sensitive to the reduced frequency.

Answer to research question 3: Effect of motion frequency on lock-in

At the lower k, irregular LEV–TEV shedding prevents synchronization between vortex shedding and motion frequency. At the higher k, two LEV–TEV pairs are shed per cycle, achieving lock-in. However, the synchronized states differ from surging: surging produces alternating vortex pairs on both upwind and downwind sides, whereas plunging generates vortex pairs exclusively downstream. Overall, the lock-in phenomenon from both the surging and plunging motion suggests that the cross-flow motion requires a higher motion frequency to overcome asymmetric shedding vortices, which indicates that lock-in depends on both frequency and motion kinematics.

Pitch Motion

Pitching motion under reverse flow conditions introduces complex unsteady flow due to the strong dynamic stall effect. The sharp trailing edge faces the incoming flow, triggering DSV formation in an early stage.

Answer to research question 2: Vortex dynamics and aerodynamic performance

Among all the DSV-present cases, the surface pressure and PIV measurements show that the DSV partially detaches during the upstroke period, with the outer shear layer shed downstream while the core remains attached. This mechanism sustains lift over multiple cycles and produces multiple peaks in aerodynamic force due to the secondary growth of the attached DSV. POD analysis demonstrates that the dominant flow structures (based on the dominant mode and the pressure reconstruction of the dominant mode) depend on mean reverse pitching angle of attack $\overline{\mathrm{AoA_r}}$: lower $\overline{\mathrm{AoA_r}}$ (5°–10°) is DSV-dominated; moderate $\overline{\mathrm{AoA_r}}$ (15°) exhibits mixed DSV and TEV influence; and higher $\overline{\mathrm{AoA_r}}$ (20°–25°) leads to TEV-dominated flow structure.

Answer to research question 4: Forward vs. reverse flow effects

> **Research question 4**
> How do reverse flow conditions influence the aerodynamic response of a pitching airfoil compared to the conventional cases?

Under forward flow, dynamic stall begins with a LSB near the leading edge, producing a strong suction peak before DSV formation [72, 129, 130]. The bursting of the LSB triggers rapid DSV growth and a sharp lift overshoot. However, in reverse flow, early separation occurs directly from the trailing edge without LSB formation, leading to a gradual pressure coefficient decrease and multiple force peaks rather than a single overshoot. This altered mechanism changes the timing and strength of aerodynamic loading, which indicates that predictive models based on forward flow dynamic stall cannot be applied directly to reverse flow conditions.

Answer to research question 5: DSV/TEV onset detection

> **Research question 5**
> What approach can be developed to accurately identify the onset of DSV and TEV formation during dynamic stall under reverse flow?

To address this question, this study developed the single-port pressure coefficient (C_p) method. By monitoring this distinct pre-DSV/TEV pressure evolution at a single leading- or trailing-edge port, the C_p method provides a robust detection mechanism without the need for full-surface measurements. Validation against the POD method confirms its accuracy, yielding averaged relative differences of 2.5% for DSV initiation and 1.0% for TEV initiation. Furthermore, applying the extended C_p method across chordwise pressure ports enables the tracking of DSV evolution, revealing two distinct phases: an initial separation phase and a major expansion phase. The reduced frequency is the primary driver during the expansion phase, where a higher reduced frequency decreases the development rate,

correlating with increased vortex strength. In contrast, the mean angle of attack acts solely as a phase-shift parameter, temporally advancing or delaying the DSV life cycle without altering its intrinsic spatial expansion behavior.

7.2 Outlook

The findings of this dissertation highlight several areas that require further investigation to advance the understanding and prediction of unsteady aerodynamic phenomena and unsteady aeroelastic studies, particularly in the context of wind turbine applications where large-scale, high-angle-of-attack flows are increasingly relevant. While the present study provides detailed findings into vortex dynamics and reverse flow effects using forced motion experimental methods, future work should extend these findings to fully coupled aeroelastic systems. VIV of wind turbine blades remains a complex, three-dimensional fluid–structure interaction problem, and bridging the gap between controlled forced motion and realistic aeroelastic responses requires new experimental and computational approaches. To this end, the following directions are recommended:

- **Aeroelastic testing:** Instead of using a stiff wing/blade model, the aeroelastic testing, which includes the well-designed model structure, should be initiated. Initial investigations could employ a single-degree-of-freedom (SDOF) setup to isolate the fundamental fluid–structure coupling mechanisms. This means that the model is constrained to a specific direction of motion (plunging, surging, or pitching) through a particular mechanical design. Such an approach has been demonstrated numerically by Fernandez-Aldama et al. [136]. Building upon the SDOF configuration, some research also examines the two-degree-of-freedom setup. Examples can be found in Srinil et al. [137] when the motion of the cylinder is limited to two degrees of freedom motion using two pairs of coil strings. A detailed review related to two degrees of freedom VIV on cylinders can be found in Rashki et al. [138].

  Subsequent studies should adopt fully elastic mountings with multiple degrees of freedom to capture the complete dynamic response, including aerodynamic damping, cross-coupling, and energy transfer effects. Until now, the aeroelastic study regarding VIV is mainly limited to numerical simulations [17, 20, 24]. Therefore, the aeroelastic measurement will provide valuable validation data for further modelling improvement.

- **Scaling and design considerations:** A major challenge for conducting wind tunnel VIV experiments on wind turbine blades lies in designing a representative scaled blade model. Although several studies have addressed wind turbine blade scaling for experimental use [139–142], the problem remains non-trivial. To downscale the blade to a wind turbine level, many parameters need to be considered so that it can match a full-scale wind turbine reference. A direct geometric downscaling is straightforward but often insufficient due to aerodynamic, structural, and manufacturing constraints [141]. In the context of VIV studies, however, the simplified case of a parked blade allows rotation-related similarity requirements (e.g., tip-speed ratio) to be omitted, which may simplify the design matrix.

For aeroelastic blade models, key nondimensional parameters must be preserved to ensure similarity with a full-scale turbine. Based on Buckingham Π theory [143], relevant governing parameters include the Reynolds number (inertial versus viscous forces), Froude number (flow inertia versus gravity), Lock number (aerodynamic versus inertial forces), nondimensional natural frequency, and nondimensional time. Previous work indicates that VIV can induce significant edgewise and flapwise aerodynamic work [17], and results from this dissertation further show that VIV can be triggered under both plunging and surging motions. Consequently, matching the first edgewise and flapwise structural modes should be prioritized when designing a wind-tunnel-scale aeroelastic blade.

- **Three-dimensional effects:** Real wind turbine blades feature three-dimensional geometric variations in chord, twist, and pitch along the span. These features lead to the shedding of spanwise vortices, including dominant tip vortices, that interact with the wake in a complex manner (Pirrung et al. [17]). Characterizing these dynamics remains challenging with conventional planar measurements. Therefore, advanced volumetric techniques such as large-scale three-dimensional Lagrangian Particle Tracking (Schröder et al. [144]) should be explored to capture the spatial evolution of unsteady vortical structures. Such investigations could enable more accurate modelling of turbine wake development and improved prediction of unsteady blade loading.

In parallel, the extensive unsteady data generated in this study can support the refinement of existing engineering models. For example, more than 40 cases of dynamic stall under reverse flow conditions were tested. Since the primary difference between conventional and reverse flow dynamic stall lies in the onset of DSV formation, future modeling efforts should prioritize accurate prediction of the initiation phase of DSV development. But ultimately, reliable prediction of VIV in large-scale wind turbine blades will require fully coupled aeroelastic simulations validated against both forced-motion and free-response experiments.

Additionally, two aspects should be considered during future investigations. First, aerodynamic damping should be quantified more comprehensively, as it governs the stability of aeroelastic responses. Recent studies by Bowles et al. [145] and the review by Corke and Thomas [146] indicate that instantaneous aerodynamic damping can be extracted from airfoil surface-pressure data using Hilbert transforms. This approach is particularly promising for aeroelastic experiments involving pressure instrumentation on blades. Second, inflow turbulence should be incorporated into future VIV studies, as it can significantly modify vortex synchronization compared to uniform inflow conditions. Cylinder experiments [147] show that increasing freestream turbulence accelerates wake recovery, reduces vortex coherence, promotes self-similarity in velocity statistics, and alters instantaneous wake structures. In a wind tunnel, an active grid provides a practical means of generating controlled turbulence levels for such future investigations.

Lastly, although many research papers have addressed VIV on wind turbine blades, the scarcity of publicly available field measurement data related to VIV remains a significant obstacle. From a researcher's perspective, without access to this industrial data, it is challenging to validate the extent of these VIV conditions, leaving it unclear whether the

predicted severity from research aligns with physical reality or remains an academic curiosity. Consequently, it would be extremely valuable if the industry could share its data with research institutes, enabling us to collaborate and mitigate this potential problem.

V

Appendices

A

Convergence analysis and PIV uncertainity of the static airfoil measurement

A

A.1 Convergence analysis of PIV measurement

Since obtaining the mean flow field is the main goal of this PIV setup, it is of vital importance to check the convergence of the result to obtain good-quality data. At small angles of attack of 0˚, 100 images were sampled while at the other AoA values, 200 images were sampled. Figure A.1 shows the evolution of mean flow velocity and Reynolds stresses with regard to the number of samples at $Re = 5 \times 10^5$. The maximum number of samples at AoA = 0˚ is 100 while that for AoA = 90˚ is 200. The mean flow velocity at 0˚ converges quickly and the Reynolds stresses remain at a very low value close to 0. This means that 100 samples will keep a good quality of 0˚ cases. At AoA = 90˚, the convergence happens after the averaging of 100 samples while a bit unstable for the Reynolds stresses R_{yy}, which the periodic vortex shedding disturbs heavily in the cross flow direction. Considering both accuracy and processing efficiency, 200 samples were deemed sufficient.

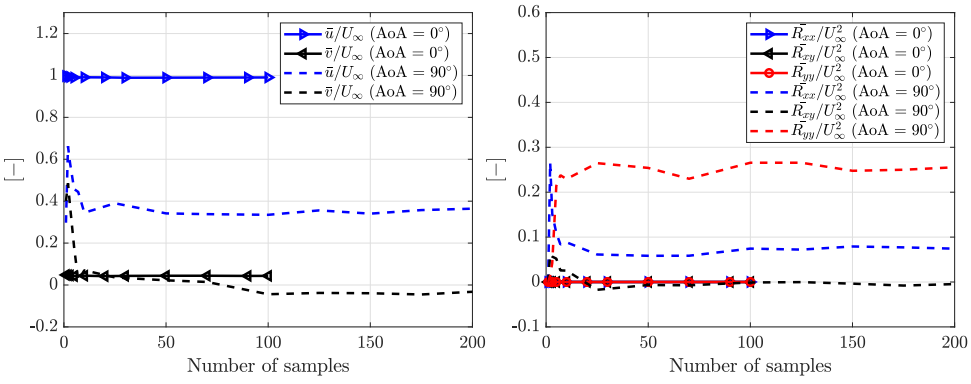

(a) (b)

Figure A.1: Evolution of the statistical (a) average velocity and (b) Reynolds stresses at $Re = 5 \times 10^5$ at AoA = 0˚ and 90˚.

A.2 PIV uncertainty

The standard uncertainty of the PIV measurements can be estimated from the ensemble data size and the flow velocity fluctuation [109]. For AoA = 0˚, 100 uncorrelated snapshots were taken, while for the rest of the α values, 200 uncorrelated snapshots were taken; hence, the standard uncertainty of the phase-average flow velocity is equal to:

$$\varepsilon_u = \frac{\sigma_u}{U_\infty \sqrt{N}} \tag{A.1}$$

σ_u is the representative standard deviation value of the streamwise velocity component (σ_u/U_∞ is approximately 0.1 in the wake of the wing) and N represents the number of uncorrelated samples. The standard uncertainty for the measurement cases are listed in Table A.1.

The uncertainty of the Root Mean Square (RMS) of the velocity fluctuations is esti-

Table A.1: Uncertainty of the PIV measurements.

Re	ε_u		$\varepsilon_{u'}$	
	AoA = 0°	AoA ≠ 0°	AoA = 0°	AoA ≠ 0°
2×10^5	1%	0.7%	0.7%	0.5%
5×10^5	1%	0.7%	0.7%	0.5%
8×10^5	1%	0.7%	0.7%	0.5%

mated as [110]:

$$\varepsilon_{u'} = \frac{\sigma_u}{U_\infty \sqrt{2(N-1)}} \tag{A.2}$$

And the uncertainty of the RMS of the velocity fluctuations for the measured cases is listed in Table A.1.

B

Uncertainty and non-dimensionalization issue of the surging airfoil experiment

B

B.1 Uncertainty of the added mass term

To evaluate the uncertainties of the measured wing displacement, velocity, and accelerations, and in turn the uncertainty of the added mass term (Equation (2.30)), an imposed sinusoidal curve is compared with the actual motion of the airfoil. The comparison is presented at the top of Figure B.1. Then, the motion velocity ($\dot{h}$) and acceleration ($\ddot{h}$) were calculated by analytical derivation in time. The results show very good agreement between the measured and the imposed values for both position and velocity (root mean square of the difference equal to 0.008 m and 0.37 m/s for k = 0.38 (0.18 m/s for k = 0.19), respectively). Instead, $\ddot{h}$ exhibits larger differences, especially at phases 45°, 90°, 270° and 315° at k = 0.38, where the uncertainty reaches maximum 57% of the measured value. Consequently, it is expected that the total C_d has the largest relative difference for these cases.

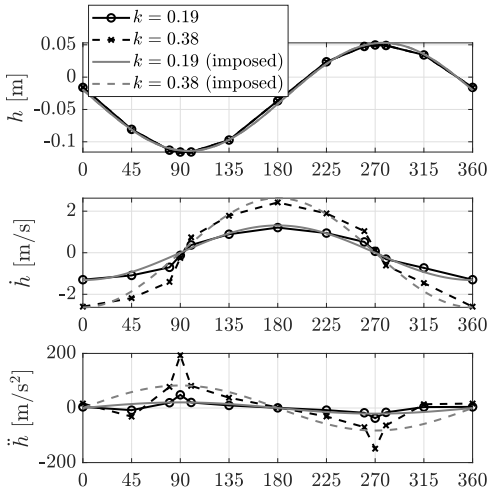

Figure B.1: Real and imposed motion (h) of the airfoil (top), and the corresponding motion velocity ($\dot{h}$) and acceleration ($\ddot{h}$).

The total C_d based on the theoretical added mass term obtained from the imposed h - curve is compared with the C_d where the added mass term is calculated from the actual motion. The root mean square uncertainty is calculated and is shown in Figure B.2. Overall, the added mass term on average contributes to 1.9% (k = 0.19) and 2.2% (k = 0.38) of the overall C_d. This results in a minimal change in the overall C_d value for most of the cases. On the one hand, the added mass term is inherently small due to the small wing model (small cross-section area). On the other hand, other force terms, such as the mean convection term, pressure term, etc., have a larger influence on the total C_d. Therefore, the $\ddot{h}$ calculated from the measured airfoil motion is adopted for the analysis.

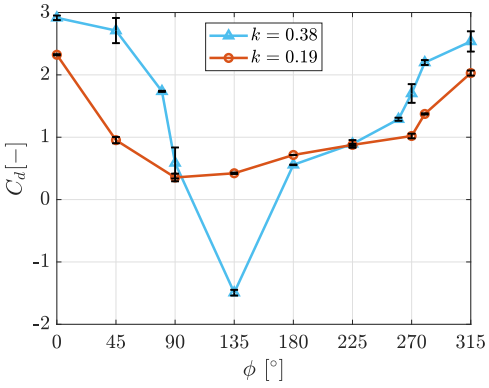

Figure B.2: Averaged total drag force coefficient C_d with the uncertainty from the added mass term marked as the black bars.

B.2 C_d non-dimensionalization issue

During the analysis, it is observed that the relative wind speed experienced by the airfoil significantly influences vortex dynamics. Therefore, in the section, the drag coefficient with the drag force (D) non-dimensionalized by the incoming wind (C_d) and the one non-dimensionalized by the relative wind (C_d^*) are compared, which is shown in Figure B.3.

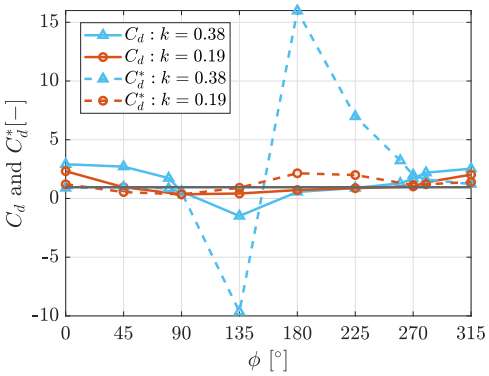

Figure B.3: Comparison between C_d (= $D/(1/2\rho U_\infty^2 c)$) and C_d^* (= $D/(1/2\rho U_{rel}^2 c)$).The static C_d is marked as the grey horizontal line.

The results show that when the airfoil moves upstream (between ϕ = 0° and 90°, and between ϕ = 270° and 315°), C_d^* is smaller than C_d due to a higher relative wind speed compared to the incoming wind speed. For different k cases, this difference reflects the relative effect of varying vortex dynamics. Vice versa, when the airfoil moves downstream, C_d^* is higher than C_d for both cases due to the lower relative wind speed compared to the incoming wind velocity. Additionally, when moving downstream, the influence of the relative wind speed on the vortex dynamics becomes less significant compared to that of the downwind flow velocity. Consequently, the C_d^* during this period will provide a less

insightful comparison to C_d. To ensure a valid comparison of C_d throughout the entire surging cycle, the drag force non-dimensionalized by the incoming wind speed is used in this paper.

C

Additional results from the plunging airfoil experiment

C

C.1 Vorticity field $\bar{\omega}c/U_\infty$ with a larger colorbar range

The vorticity field $\bar{\omega}c/U_\infty$ at the two extreme plunging locations is plotted with a higher colorbar range of −4 to 4 to show the vortex structures more clearly.

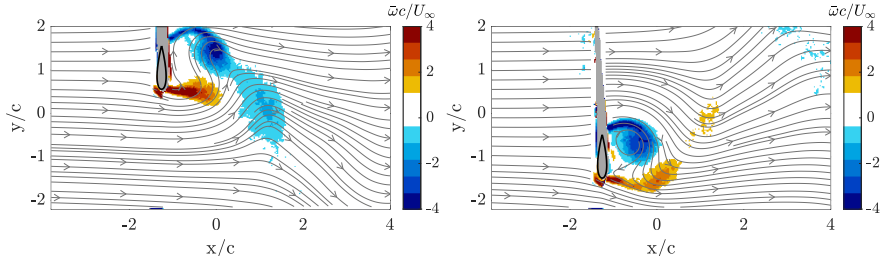

(a) ϕ = 90° (AoA = 90.0°) (b) ϕ = 270° (AoA = 90.0°)

Figure C.1: The vorticity field $\bar{\omega}c/U_\infty$ at the two extreme locations for the high reduced frequency (k = 0.38) case.

C.2 The reliability of the plunging motion

In order to ensure the data reliability of the presented phase-lock PIV, the airfoil location at each phase was constantly checked throughout the wind tunnel test. To quantify the motion reliability, in Figure C.2 we present the location of the airfoil trailing edge on each measured image (200 in total for each phase) under the high reduced frequency case (k = 0.38), from the most upstroke (ϕ = 90°) and most downstroke (ϕ = 270°) position.

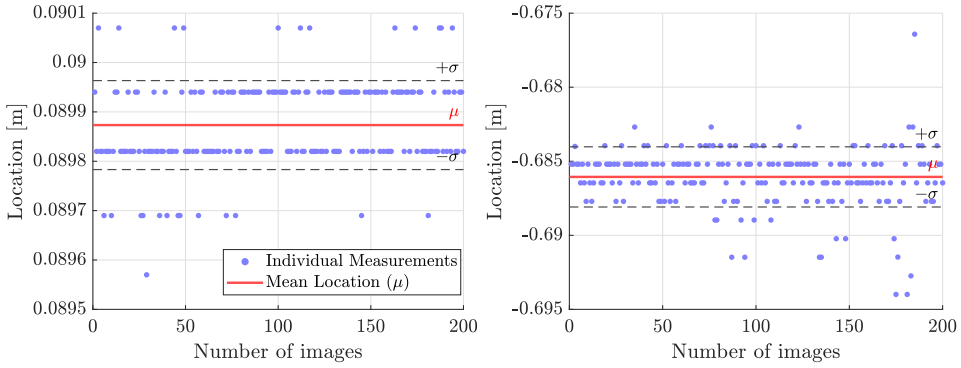

(a) ϕ = 90° (the most upstroke position) (b) ϕ = 270° (the most downstroke position)

Figure C.2: The location of the leading edge at the most upstroke and most downstroke position at the high frequency (k = 0.38) case.

At these two extreme locations, the standard deviation (σ) remains minimum, which is 9×10^{-5} m and 0.002 m for the most upstroke and most downstroke, respectively. This low level of variance demonstrates that the motion is highly repeatable and robust.

D

Experimental design and additional results of the pitching airfoil experiment

D.1 Experiment design

D.1.1 Convergence analysis of pressure measurement

The NACA 643418 airfoil is selected for the pitching test. First, it is an asymmetric airfoil, which allows for a more representative simulation of wind turbine blade sections compared to symmetric sections. Second, this airfoil has been previously employed in wind energy with a few related studies[148, 149], providing a valuable benchmark and facilitating comparison of the present results with established research.

In order to determine the adequate cycle for data acquisition, a 299-cycle long measurement was performed for case $\overline{\text{AoA}} = 40^{\circ}$, $\Delta\text{AoA} = 5^{\circ}$, $k = 0.11$. The trailing edge measurement point with cycles in the range between 50 and 298 was examined. Note that the first cycle is eliminated to avoid the transient effect from the measurement. The corrected C_p variations are shown in Figure D.1a. Assuming the 298-cycle case is the closest result compared with the ground truth, the standard deviation (σ) compared to the 298-cycle case is calculated and shown in Figure D.1b. Overall, even for 50-cycle case, the lowest cycle tested, the RMS is within 0.025, which shows great repeatability of the pitching cycle. In order to sustain high efficiency during measuring while maintaining σ lower than 0.01, 150-cycle measurement was decided as the optimal acquisition cycle for pressure measurement, and 50-cycle measurement was decided for PIV measurement.

D.1.2 Determination of Reynolds number

In order to minimize the influence of Re on the aerodynamic performance, a test on the static airfoil was carried out in the first step by varying Re values. The Re was ranged from 0.8×10^5 to 1×10^6. The pressure data was corrected under both dynamic response correction and wind tunnel wall correction, as discussed in Chapter 2. The corrected C_l and C_d polars are shown in Figure D.2. Except $Re = 1 \times 10^6$ where AoA varies from 0°

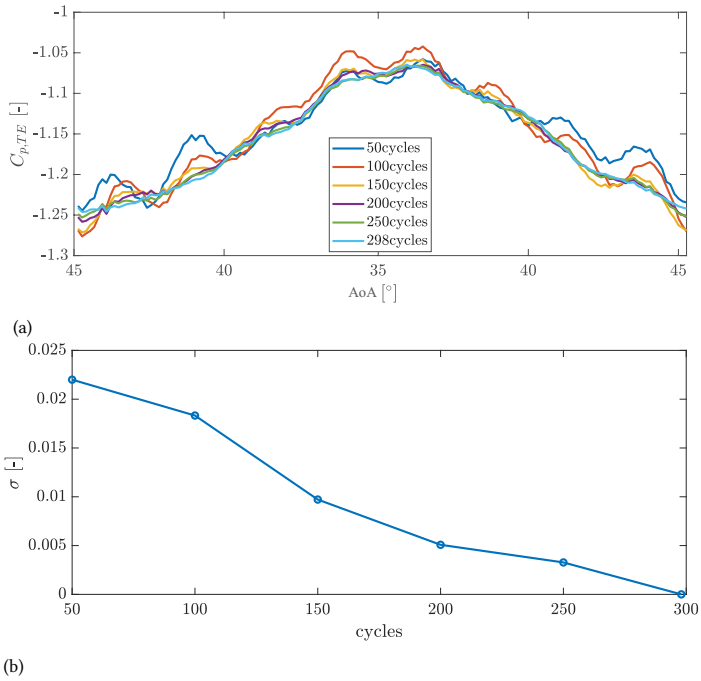

Figure D.1: Convergence analysis based on the trailing edge C_p at case $\overline{\text{AoA}}$ = 40°, ΔAoA = 5°, k = 0.11

to 44°, the rest test ranges are from 0° to 180°. It is distinct that the result at 0.8×10^5 deviates the most from the rest at all the measured AoA. C_l is even close to zero at this Re when AoA = 0°, while for the other Re cases C_l is approximately 0.4. The C_p distribution at AoA = 0° is compared between $Re = 0.8 \times 10^5$ and $Re = 2.5 \times 10^5$, as shown in Figure D.3. Unlike $Re = 2.5 \times 10^5$, where the suction side and pressure side present pressure differences before $x_c/c = 0.7$, C_p remains relatively the same for the two sides for $Re = 0.8 \times 10^5$ after $x_c/c = 0.2$. This leads to the near-zero C_l at $Re = 0.8 \times 10^5$, different from the values with the other Re cases.

When $Re = 1.5 \times 10^5$, a visible difference can be seen from 40° to 60° and from 120° to 140° for C_l, and from 40° to 60° and from 40° to 150° for C_d. Nevertheless, as Re increases, the stall region becomes smoother. In this study, the primary angles of investigation are above the normal stall region, and the result at $Re = 2.5 \times 10^5$ is considered to be a good condition for the unsteady pressure measurement without having significant Re effects.

D.1.3 Design of pitching amplitude and pitching frequency

In order to determine pitching amplitude and frequency for the campaign, aero-elastic simulations (unsteady Blade Element Momentum method together with Ritz method) were conducted on an NREL 5 MW wind turbine [150]. To make a quick and rather accurate investigation of wind turbine blades under VIV conditions, a semi-empirical VIV force model is integrated in the simulations, based on the method proposed in Eurocode 1 [16].

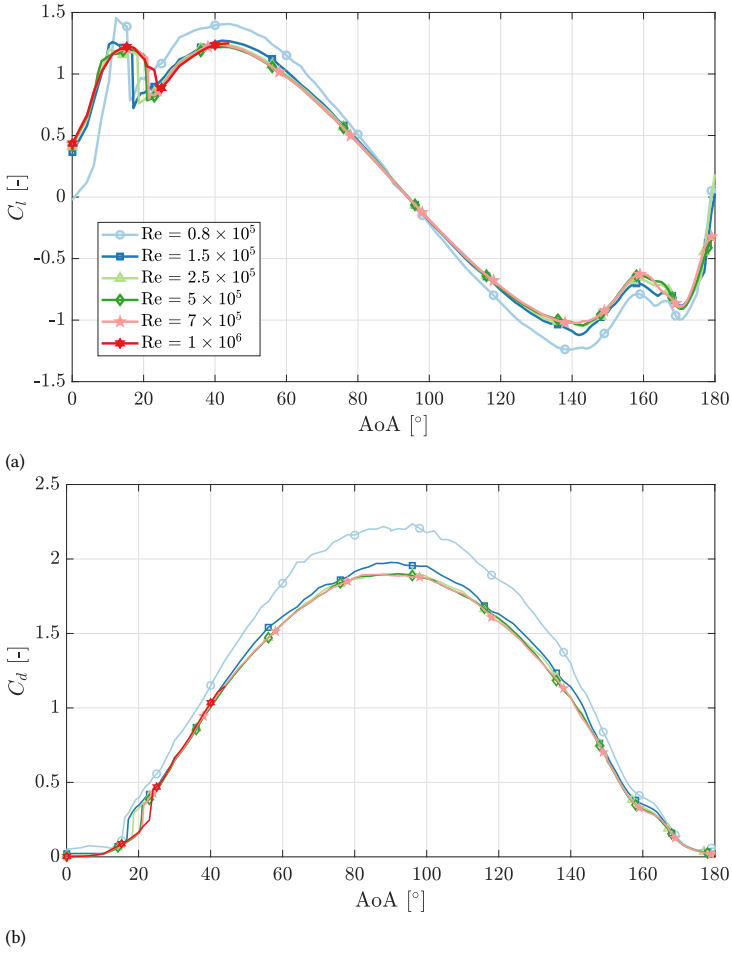

Figure D.2: Corrected polars for all the tested *Re* cases.

This method has been previously applied by Manolas et al. [15]. Served as an added force in the load, a lift coefficient increment ΔC_l is defined:

$$\Delta C_l = \min(\max(3 - 2.4\frac{V_{crit,i}}{V_{m,Li}}), 1)C_{lat,0} \tag{D.1}$$

where $V_{crit,i}$ is the critical wind velocity for bending vibration mode n_i, defined as $\frac{Dn_i}{St}$, where D is the projected chord length in the wind direction, n_i is the natural frequency of each mode i, and St is the Strouhal number. $V_{m,Li}$ is the mean wind velocity at the center of each blade section. $C_{lat,0}$ is the base value of the lateral force coefficient, defined in Eurocode 1 [16], which is dependent on the Reynolds numbers.

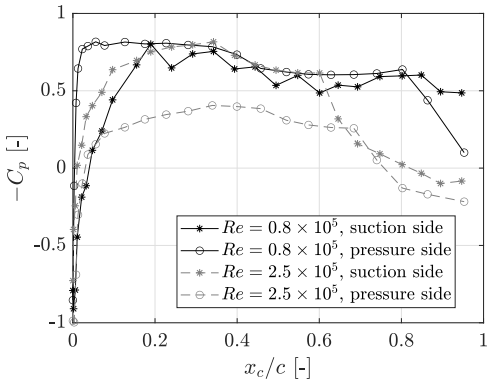

D

Figure D.3: C_p distribution at AoA = 0° for $Re = 0.8 \times 10^5$ and $Re = 2.5 \times 10^5$.

Then, the total lift force l as a function of time t is calculated as:

$$l(t) = \frac{1}{2}\rho U_\infty^2 D \Delta C_l \cos(\Omega t) + \frac{1}{2}\rho U_\infty^2 D C_l \tag{D.2}$$

where ρ is the air density, U_∞ is the free stream wind speed, Ω is the angular speed corresponding to the St, and C_l is the lift coefficient at the corresponding angle of attack at each t.

Four sets of simulations are tested during wind turbine parked condition, with blade pitch angle 35°, 90°, 135°, and 160° separately, and the corresponding wind speed U_∞ equals 24.1 m/s, 42.0 m/s, 15.9 m/s, and 14.4 m/s. The selection of these wind speeds is to satisfy the condition of St approximately 0.16 for large angle of attack cases, which was discussed in Chapter 3. The test cases are listed in Table D.1.

Table D.1: Aeroelastic simulation test cases.

Test case	$\overline{\text{AoA}}$ [°]	U_∞ [m/s]	St
1	35	24.1	0.16
2	90	42.0	0.16
3	135	15.9	0.16
4	160	14.4	0.16

We focus mainly on the angular variation of the wind turbine blade tip. The standard deviation of the blade tip pitch angle change is shown in Table D.2 together with the dominant frequency that appears in the pitch angle time series and the reduced frequency at the blade tip. The angle variation shows the highest standard deviation (3.9°) when the airfoil is pitched by 90° and the lowest value (0.4°) when the airfoil is pitched by 160°. The reduced frequency ranges from 0.111 to 0.307.

Table D.3 lists the relevant wind turbine natural frequencies provided by the NREL 5 MW wind turbine model [150]. Compared with the dominant frequency from the pitch angle time series, it shows a large amount of overlap from the 1^{st} Drivetrain Torsion mode

Table D.2: Standard deviation δ of the blade tip pitch angle change and the location of the frequency peak of the angle time series in the frequency domain

Test case	δ [°]	Peak frequency [Hz]	k
1	1.0	0.6,1.03	0.111,0.191
2	3.9	1.87	0.198
3	1.2	1.0	0.280
4	0.4	0.97	0.307

to the 2^{nd} Blade Asymmetric Flapwise Pitch mode. These cases indicate the potential VIV problem on the wind turbine blade. Therefore, in order to mimic the same vibration effect of a real wind turbine during VIV in the angular and reduced frequency perspective, the testing pitching amplitudes were set as 5°, 10°, and 15° for each mean angle of attack case (if the pitching mechanism is allowed). The testing frequencies are set to be between 1 and 4 Hz, where the corresponding k are between 0.05 and 0.21. Note that the pitching frequency could not go higher due to the limitation of the pitching mechanism in the wind tunnel. The final test matrix is shown in Table 6.1 and 6.2.

Table D.3: Relevant natural frequencies of the NREL 5 MW reference wind turbine.

Mode	Name	Frequency [Hz]
1	1^{st} Drivetrain Torsion	0.6205
2	1^{st} Blade Asymmetric Flapwise Yaw	0.6664
3	1^{st} Blade Asymmetric Flapwise Pitch	0.6675
4	1^{st} Blade Collective Flap	0.6993
5	1^{st} Blade Asymmetric Edgewise Pitch	1.0793
6	1^{st} Blade Asymmetric Edgewise Yaw	1.0898
7	2^{nd} Blade Asymmetric Flapwise Yaw	1.9337
8	2^{nd} Blade Asymmetric Flapwise Pitch	1.9223

D.2 Streamwise velocity field at two representative cases

Figure D.4 and Figure D.5 present the streamwise velocity field $\overline{U}/U_\infty$ at case $\overline{\text{AoA}_\text{r}}10\Delta10k0.1$ and $\overline{\text{AoA}_\text{r}}20\Delta10k0.1$ respectively in order to provide more information apart from the vorticity field shown from Figure 6.5 and Figure 6.12. For both cases, the results show that as the airfoil pitches up, the wake becomes wider: at case $\overline{\text{AoA}_\text{r}}10\Delta10k0.1$, a thin layer of reverse flow region (deep blue color) occurs on the suction side (see phase j and h), while for the high mean angle case of $\overline{\text{AoA}_\text{r}}20\Delta10k0.1$, the suction region occurs earlier from phase d and the wake is also wider. During the downstroke period, the wake in case $\overline{\text{AoA}_\text{r}}10\Delta10k0.1$ recovers quickly, while for case $\overline{\text{AoA}_\text{r}}20\Delta10k0.1$, the wake remains wide until the end of the downstroke cycle due to a high angle of attack. This PIV result also matches the pressure measurement in that, due to a high mean angle, the suction pressure

is higher for $\overline{\text{AoA}_\text{r}}20\Delta10k0.1$ (Fig. 6.11a), which also leads to a higher aerodynamic force (Fig. 6.13). Noticeably, the reverse flow region is concentrated near the trailing edge for case $\overline{\text{AoA}_\text{r}}20\Delta10k0.1$ at phase f, g, and k, for example, while no strong reverse flow can be found near the trailing edge at case $\overline{\text{AoA}_\text{r}}10\Delta10k0.1$. This result further indicates that in case $\overline{\text{AoA}_\text{r}}20\Delta10k0.1$, the TEV has a stronger strength, which leads to the TEV domination as discussed in Section 6.3.2.

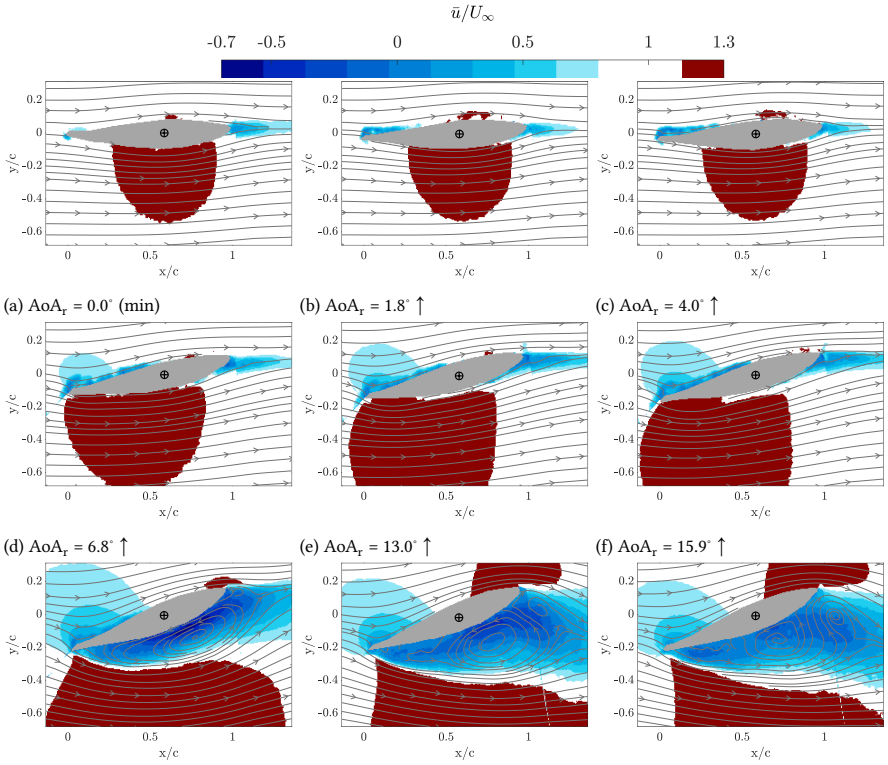

Figure D.4: (continued)

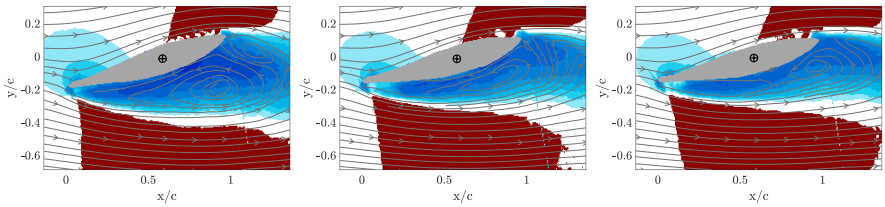

(j) $\mathrm{AoA_r} = 18.4^\circ \downarrow$ (k) $\mathrm{AoA_r} = 13.5^\circ \downarrow$ (l) $\mathrm{AoA_r} = 10.4^\circ \downarrow$

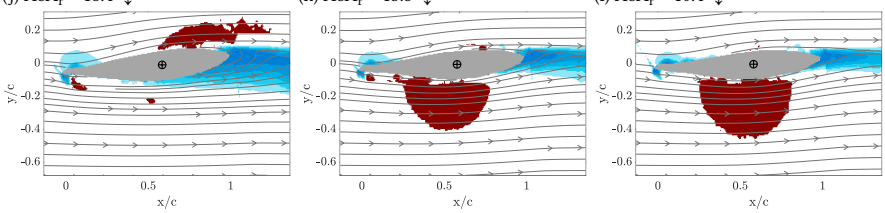

(m) $\mathrm{AoA_r} = 7.3^\circ \downarrow$ (n) $\mathrm{AoA_r} = 2.2^\circ \downarrow$ (o) $\mathrm{AoA_r} = 0.6^\circ \downarrow$

Figure D.4: Streamwise velocity field $\overline{U}/U_\infty$ for case $\overline{\mathrm{AoA_r}}10\Delta10k0.1$.

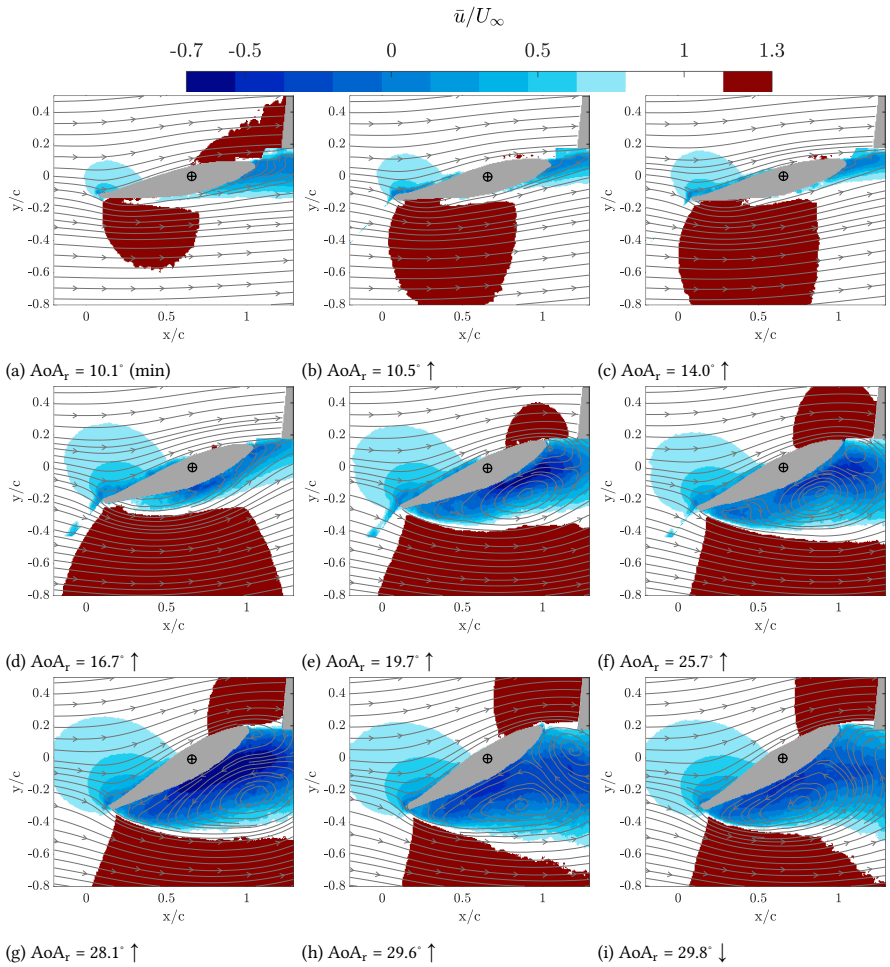

(a) $AoA_r = 10.1^\circ$ (min) (b) $AoA_r = 10.5^\circ \uparrow$ (c) $AoA_r = 14.0^\circ \uparrow$

(d) $AoA_r = 16.7^\circ \uparrow$ (e) $AoA_r = 19.7^\circ \uparrow$ (f) $AoA_r = 25.7^\circ \uparrow$

(g) $AoA_r = 28.1^\circ \uparrow$ (h) $AoA_r = 29.6^\circ \uparrow$ (i) $AoA_r = 29.8^\circ \downarrow$

Figure D.5: (continued)

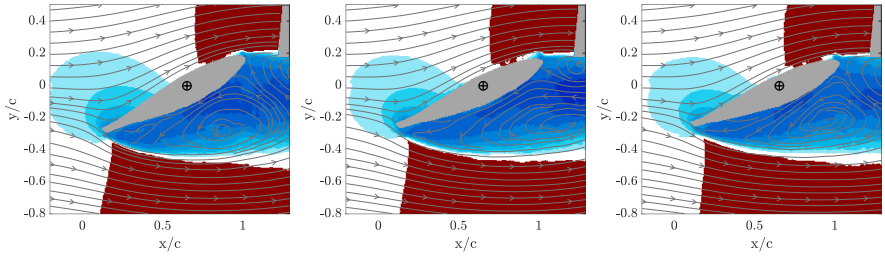

(j) $AoA_r = 28.4^\circ \downarrow$ (k) $AoA_r = 26.3^\circ \downarrow$ (l) $AoA_r = 20.4^\circ \downarrow$

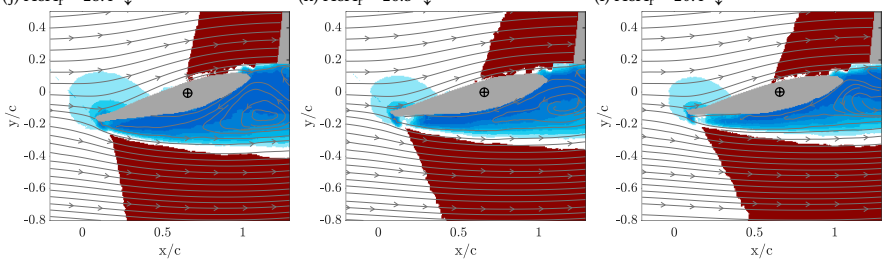

(m) $AoA_r = 17.3^\circ \downarrow$ (n) $AoA_r = 14.5^\circ \downarrow$ (o) $AoA_r = 10.7^\circ \downarrow$

Figure D.5: Streamwise velocity field $\overline{U}/U_\infty$ for case $\overline{\text{AoA}_\text{r}}20\Delta10k0.1$.

D.3 Spatial-temporal field of suction side C_p for all the test cases

In this section, the cycle-averaged suction side C_p for all test cases are presented in Figure D.6. The maps are plotted with a universal C_p range from −2 to 1. The gray contour lines indicate the C_p magnitude with an increment of 0.25.

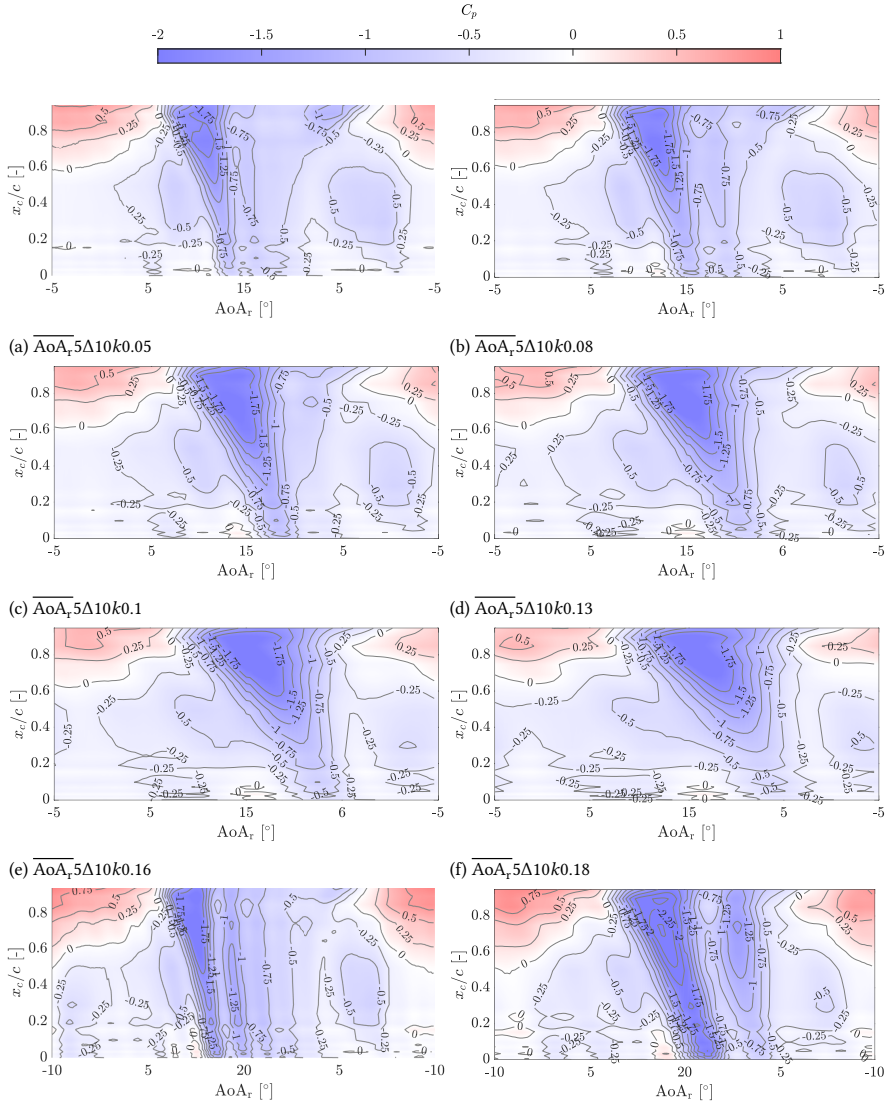

(a) $\overline{\text{AoA}_r}5\Delta10k0.05$ (b) $\overline{\text{AoA}_r}5\Delta10k0.08$

(c) $\overline{\text{AoA}_r}5\Delta10k0.1$ (d) $\overline{\text{AoA}_r}5\Delta10k0.13$

(e) $\overline{\text{AoA}_r}5\Delta10k0.16$ (f) $\overline{\text{AoA}_r}5\Delta10k0.18$

(g) $\overline{\text{AoA}_r}5\Delta15k0.05$ (h) $\overline{\text{AoA}_r}5\Delta15k0.1$

Figure D.6: (continued)

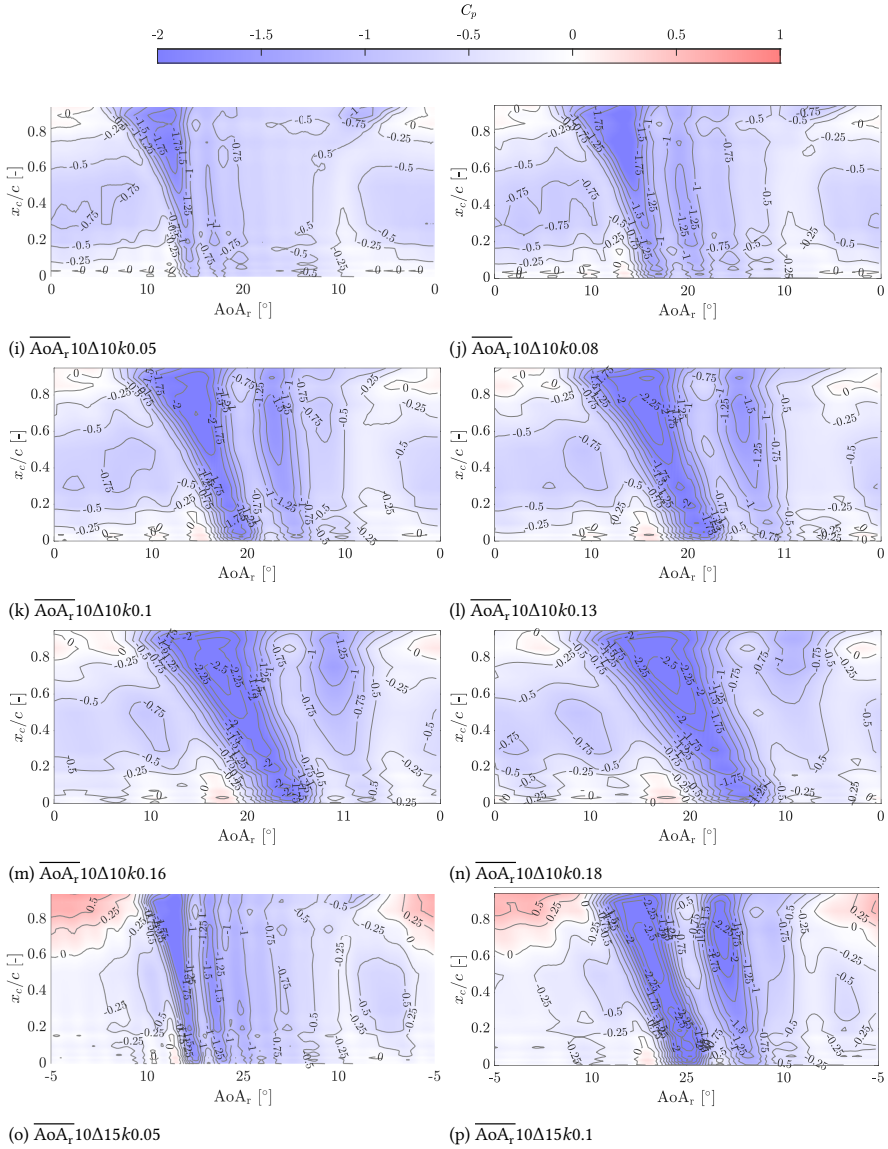

(i) $\overline{\text{AoA}_r}10\Delta10k0.05$ (j) $\overline{\text{AoA}_r}10\Delta10k0.08$

(k) $\overline{\text{AoA}_r}10\Delta10k0.1$ (l) $\overline{\text{AoA}_r}10\Delta10k0.13$

(m) $\overline{\text{AoA}_r}10\Delta10k0.16$ (n) $\overline{\text{AoA}_r}10\Delta10k0.18$

(o) $\overline{\text{AoA}_r}10\Delta15k0.05$ (p) $\overline{\text{AoA}_r}10\Delta15k0.1$

Figure D.6: (continued)

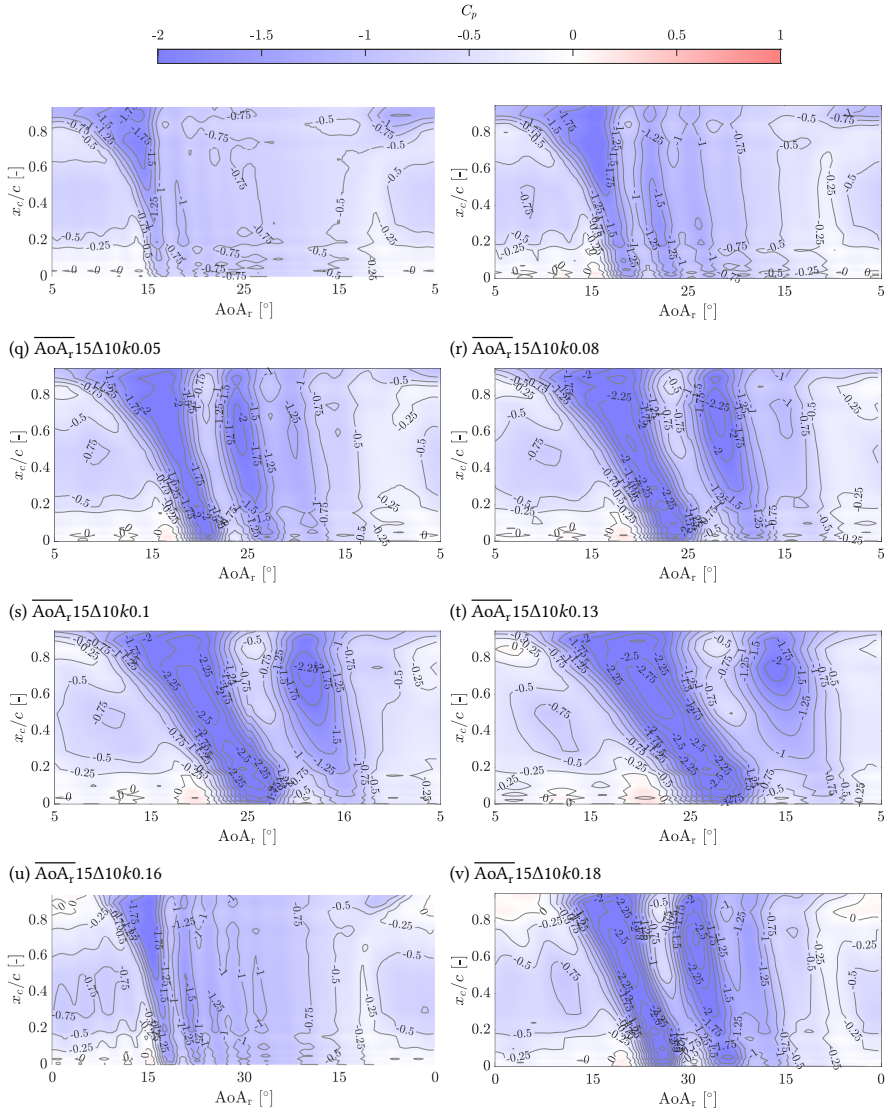

(q) $\overline{\text{AoA}_r}15\Delta10k0.05$ (r) $\overline{\text{AoA}_r}15\Delta10k0.08$

(s) $\overline{\text{AoA}_r}15\Delta10k0.1$ (t) $\overline{\text{AoA}_r}15\Delta10k0.13$

(u) $\overline{\text{AoA}_r}15\Delta10k0.16$ (v) $\overline{\text{AoA}_r}15\Delta10k0.18$

(w) $\overline{\text{AoA}_r}15\Delta15k0.05$ (x) $\overline{\text{AoA}_r}15\Delta15k0.1$

Figure D.6: (continued)

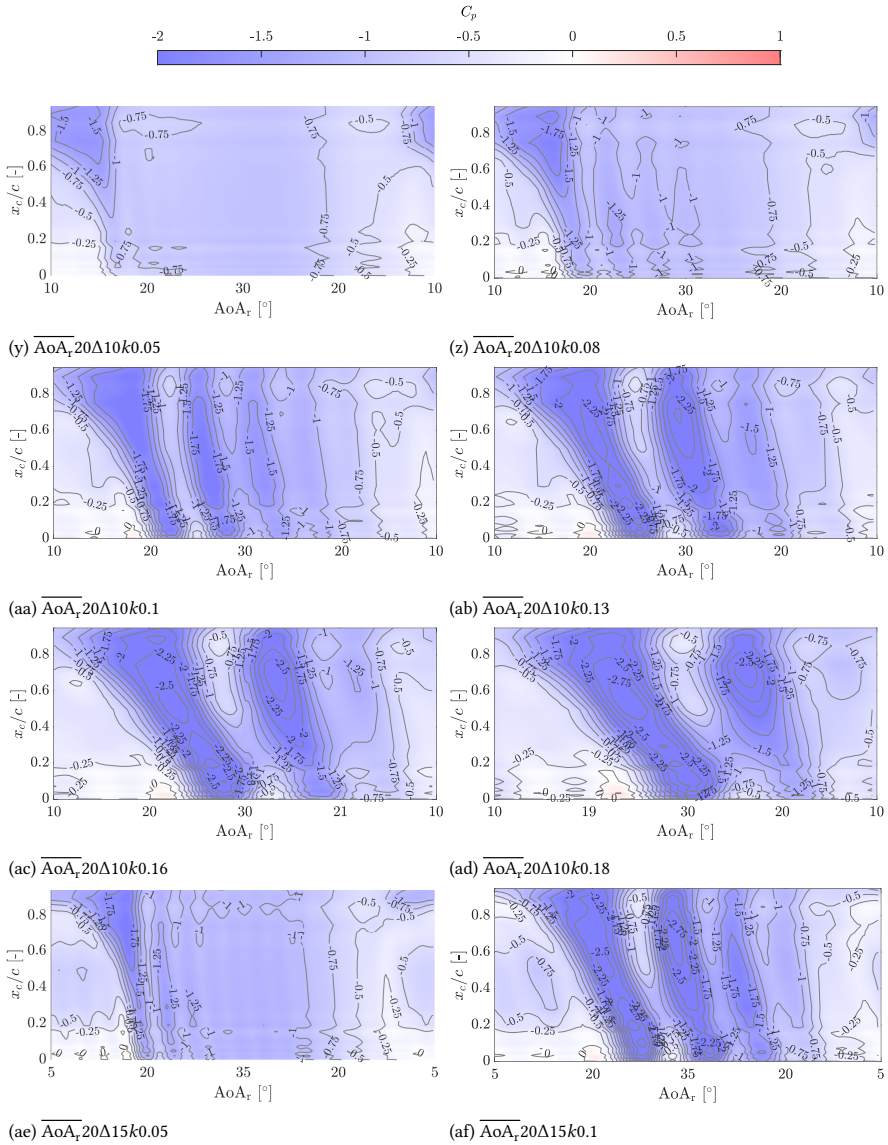

(y) $\overline{\text{AoA}_r}20\Delta10k0.05$ (z) $\overline{\text{AoA}_r}20\Delta10k0.08$

(aa) $\overline{\text{AoA}_r}20\Delta10k0.1$ (ab) $\overline{\text{AoA}_r}20\Delta10k0.13$

(ac) $\overline{\text{AoA}_r}20\Delta10k0.16$ (ad) $\overline{\text{AoA}_r}20\Delta10k0.18$

(ae) $\overline{\text{AoA}_r}20\Delta15k0.05$ (af) $\overline{\text{AoA}_r}20\Delta15k0.1$

Figure D.6: (continued)

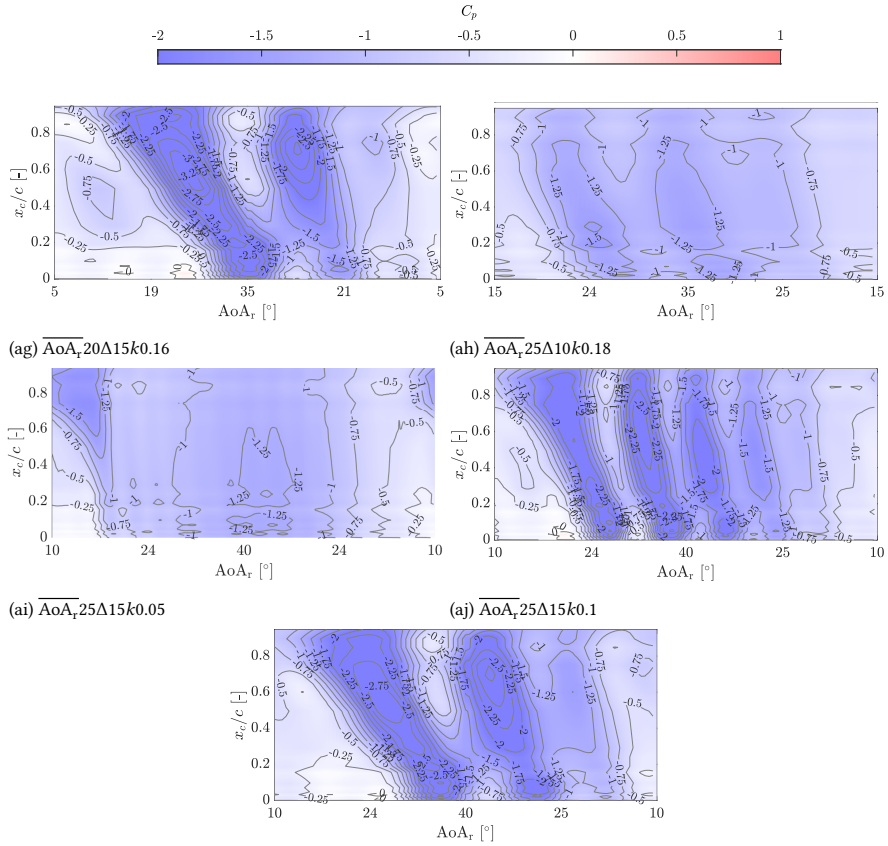

(ag) $\overline{\text{AoA}_r}20\Delta15k0.16$

(ah) $\overline{\text{AoA}_r}25\Delta10k0.18$

(ai) $\overline{\text{AoA}_r}25\Delta15k0.05$

(aj) $\overline{\text{AoA}_r}25\Delta15k0.1$

(ak) $\overline{\text{AoA}_r}25\Delta15k0.16$

Figure D.6: (continued)

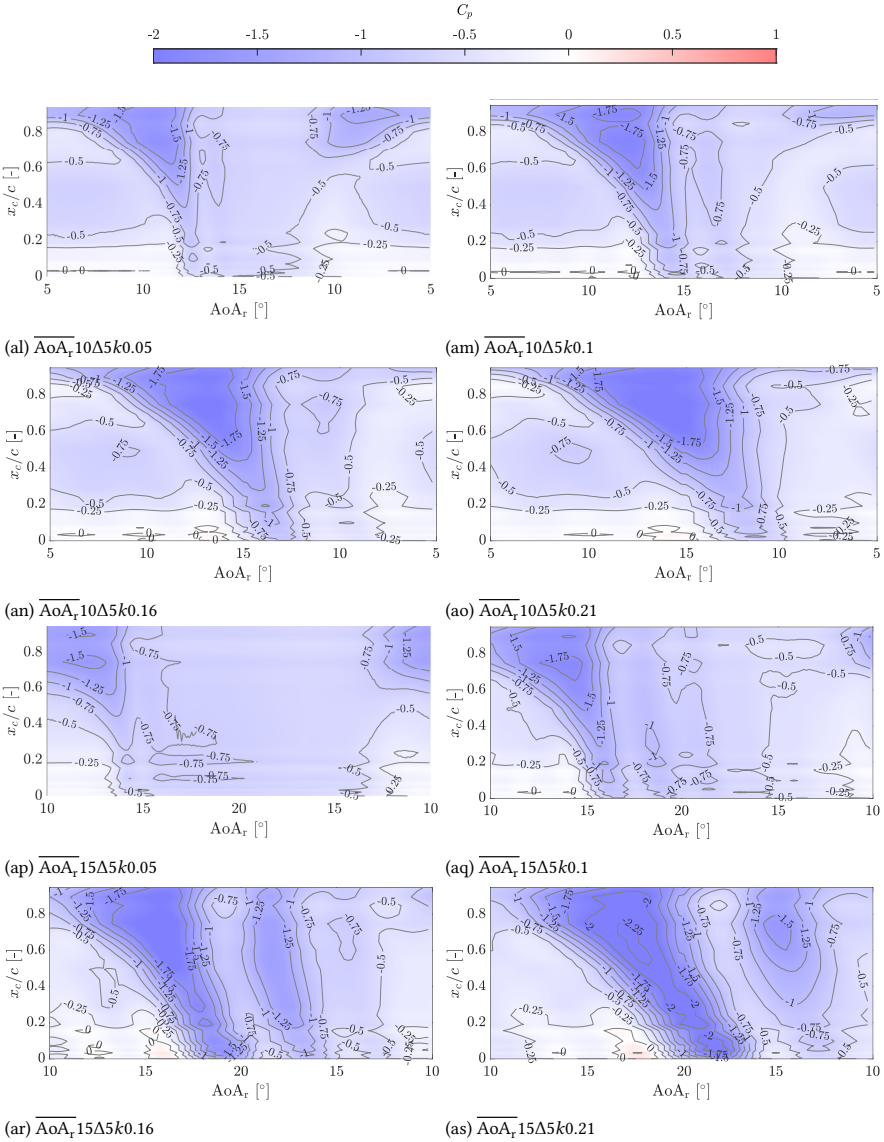

(al) $\overline{\text{AoA}_r}10\Delta5k0.05$ (am) $\overline{\text{AoA}_r}10\Delta5k0.1$

(an) $\overline{\text{AoA}_r}10\Delta5k0.16$ (ao) $\overline{\text{AoA}_r}10\Delta5k0.21$

(ap) $\overline{\text{AoA}_r}15\Delta5k0.05$ (aq) $\overline{\text{AoA}_r}15\Delta5k0.1$

(ar) $\overline{\text{AoA}_r}15\Delta5k0.16$ (as) $\overline{\text{AoA}_r}15\Delta5k0.21$

Figure D.6: Spatial-temporal field of suction side surface pressure coefficient C_p.

D.4 C_p field derived from PIV measurement for case $\overline{\mathbf{AoA_r}}20\Delta10k0.1$

Figure D.7 presents the C_p field at case $\overline{\text{AoA}_\text{r}}20\Delta10k0.1$ extracted from the PIV measurement.

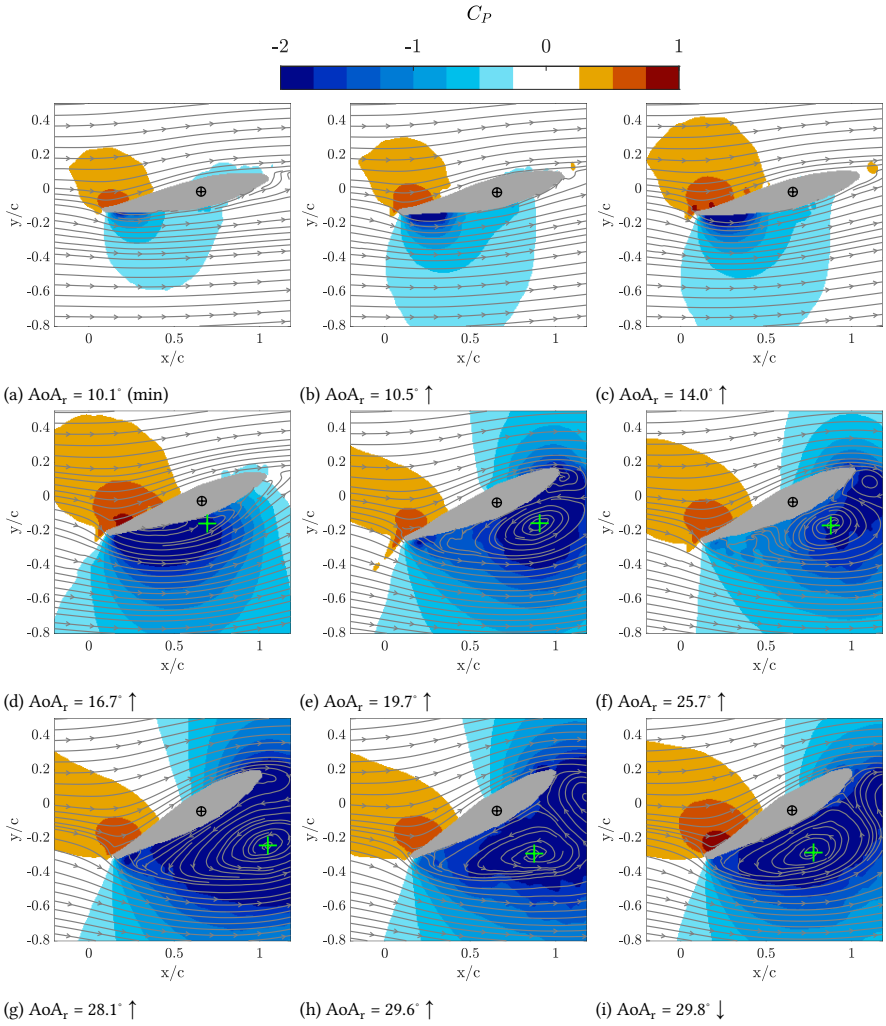

(a) $\text{AoA}_\text{r} = 10.1^\circ$ (min) (b) $\text{AoA}_\text{r} = 10.5^\circ \uparrow$ (c) $\text{AoA}_\text{r} = 14.0^\circ \uparrow$

(d) $\text{AoA}_\text{r} = 16.7^\circ \uparrow$ (e) $\text{AoA}_\text{r} = 19.7^\circ \uparrow$ (f) $\text{AoA}_\text{r} = 25.7^\circ \uparrow$

(g) $\text{AoA}_\text{r} = 28.1^\circ \uparrow$ (h) $\text{AoA}_\text{r} = 29.6^\circ \uparrow$ (i) $\text{AoA}_\text{r} = 29.8^\circ \downarrow$

Figure D.7: (continued)

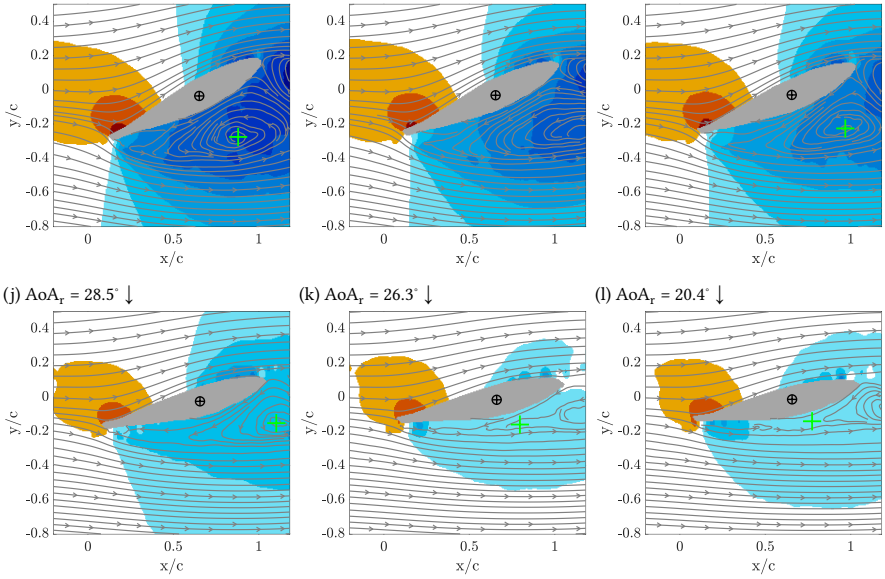

(j) AoA_r = 28.5° ↓ (k) AoA_r = 26.3° ↓ (l) AoA_r = 20.4° ↓

(m) AoA_r = 17.3° ↓ (n) AoA_r = 14.5° ↓ (o) AoA_r = 10.7° ↓

Figure D.7: Pressure coefficient field C_p for case $\overline{\text{AoA}_\text{r}}20\Delta10k0.1$ derived from PIV measured velocity fields. Green cross represents the location of DSV core center, identified using the Γ_1 method [89, 90].

D.5 Vorticity field $\overline{\omega}c/U_\infty$ at a conventional dynamic stall case $\overline{\textbf{AoA}}10\Delta10k0.16$: $\overline{\textbf{AoA}}$ = 10°, $\Delta\textbf{AoA}_\textbf{r}$ = 10°, k = 0.16

The vorticity field of the conventional dynamic stall case $\overline{\text{AoA}}10\Delta10k0.16$ is presented in Figure D.8.

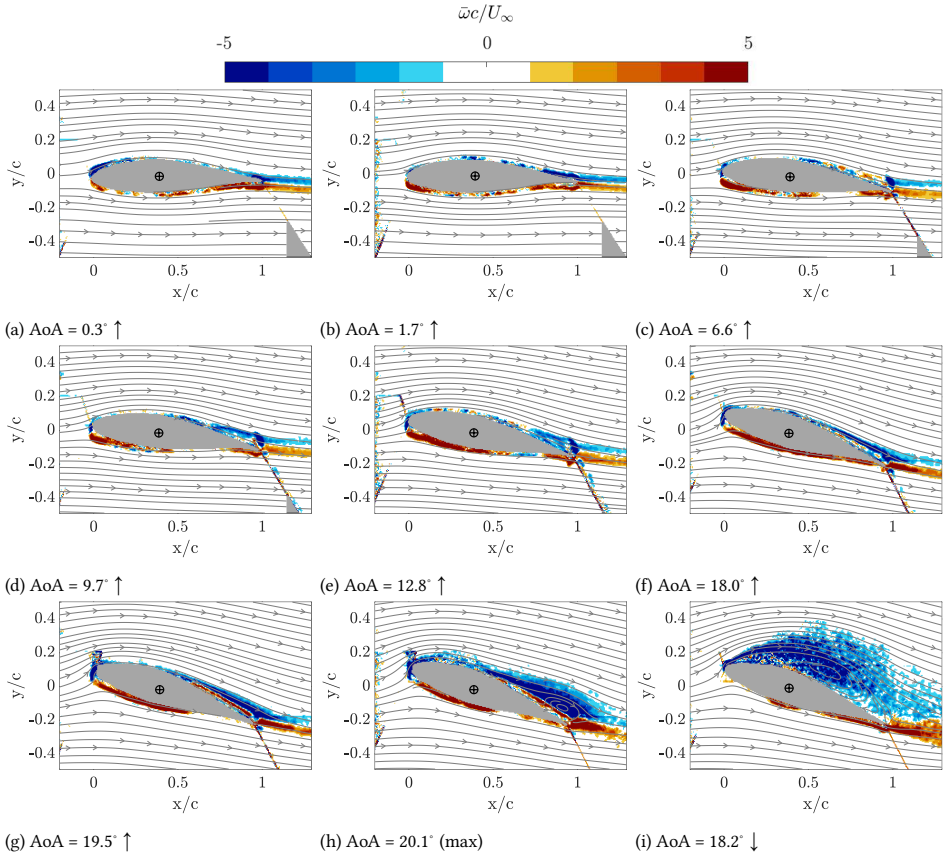

(a) AoA = 0.3° ↑ (b) AoA = 1.7° ↑ (c) AoA = 6.6° ↑

(d) AoA = 9.7° ↑ (e) AoA = 12.8° ↑ (f) AoA = 18.0° ↑

(g) AoA = 19.5° ↑ (h) AoA = 20.1° (max) (i) AoA = 18.2° ↓

Figure D.8: (continued)

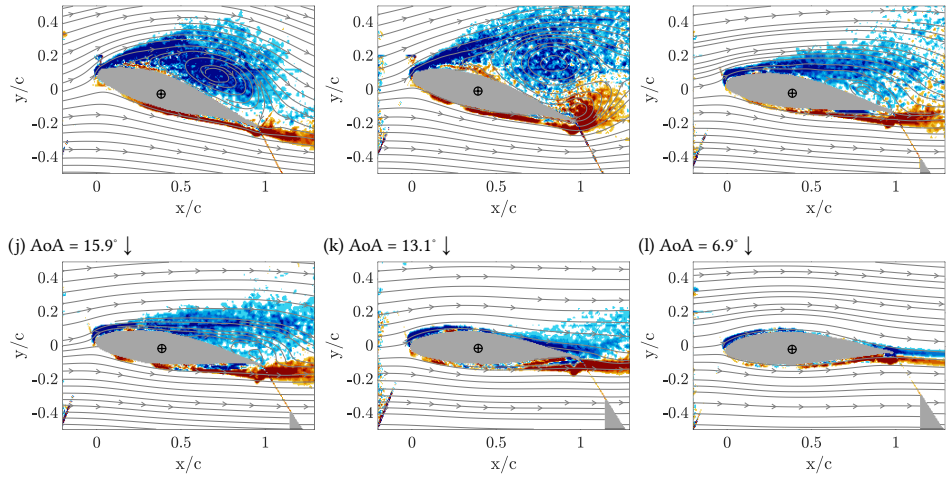

(j) AoA = 15.9° ↓ (k) AoA = 13.1° ↓ (l) AoA = 6.9° ↓

(m) AoA = 4.1° ↓ (n) AoA = 1.9° ↓ (o) AoA = −0.1° (min)

Figure D.8: Vorticity field $\overline{\omega}c/U_\infty$ for case $\overline{\text{AoA}}$ = 10°, ΔAoA = 10°, k = 0.16.

D.6 The second POD mode shapes for all the reverse flow test cases

Figure D.9 shows the mode shape from the second mode for all reverse flow test cases. The results are grouped by the mean pitching angle. Note that the mode shapes at $\overline{\text{AoA}_\text{r}} = 5^\circ$ are not shown here as the second mode is less than 10% of the total energy.

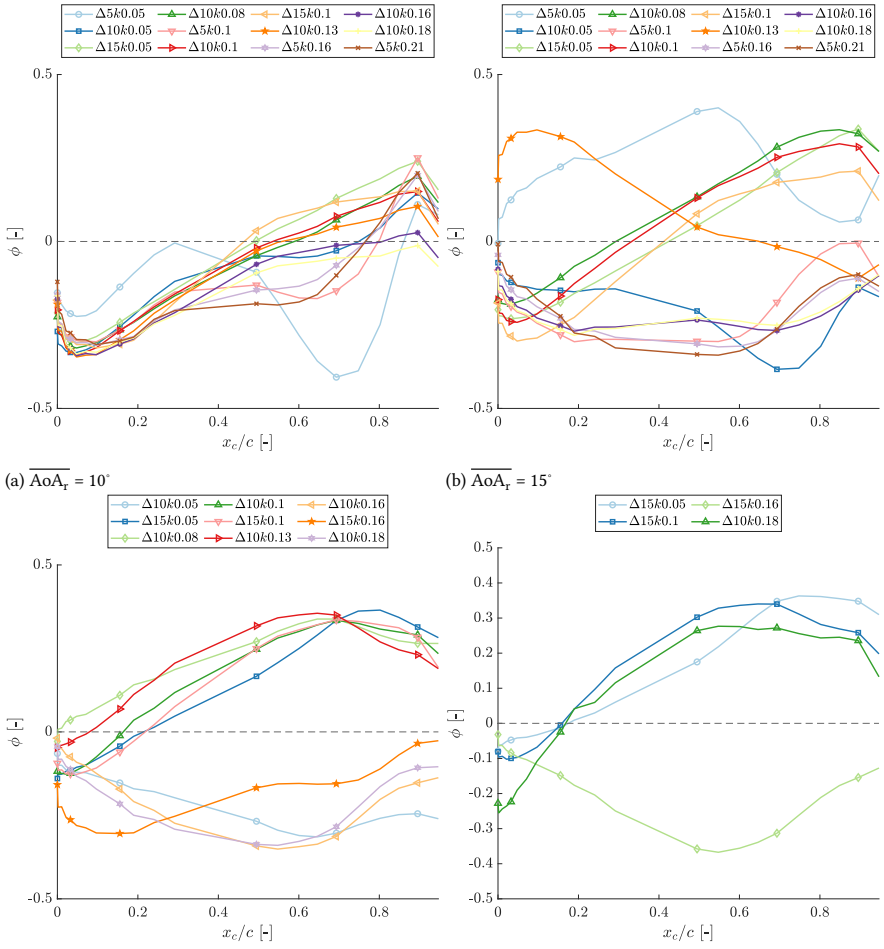

(a) $\overline{\text{AoA}_\text{r}} = 10^\circ$ (b) $\overline{\text{AoA}_\text{r}} = 15^\circ$

(c) $\overline{\text{AoA}_\text{r}} = 20^\circ$ (d) $\overline{\text{AoA}_\text{r}} = 25^\circ$

Figure D.9: POD mode shapes of the second dominant mode (mode 2) for each case.

Bibliography

References

[1] U.S. Department of Energy. How Wind Energy Became Integral to the Modern Grid, 2023.

[2] GWEC. Global wind report 2024. Technical report, Brussels, 2024.

[3] UNFCCC. The Kyoto Protocol.

[4] European Commission. What is the EU ETS?

[5] Manfred Hafner and Giacomo Luciani. The Palgrave Handbook of International Energy Economics. Technical report.

[6] IEA (2024). Renewables 2023. Technical report, Paris.

[7] WWEA. WWEA Annual Report 2024. Technical report, 2025.

[8] Paul Veers, Carlo L. Bottasso, Lance Manuel, Jonathan Naughton, Lucy Pao, Joshua Paquette, Amy Robertson, Michael Robinson, Shreyas Ananthan, Thanasis Barlas, Alessandro Bianchini, Henrik Bredmose, Sergio González Horcas, Jonathan Keller, Helge Aagaard Madsen, James Manwell, Patrick Moriarty, Stephen Nolet, and Jennifer Rinker. Grand challenges in the design, manufacture, and operation of future wind turbine systems, 7 2023.

[9] C. H.K. Williamson and R. Govardhan. Vortex-induced vibrations. *Annual Review of Fluid Mechanics*, 36:413–455, 2004.

[10] P W Bearman. Vortex shedding from oscillating bluff bodies. *Ann. Rev. Fluid Mech*, 16:195–222, 1984.

[11] C H K Williamson and A Roshko. Vortex formation in the wake of an oscillating cylinder. *Journal of Fluids and Structures*, 2:355–381, 1988.

[12] T. Sarpkaya. A critical review of the intrinsic nature of vortex-induced vibrations. *Journal of Fluids and Structures*, 19(4):389–447, 2004.

[13] Rasoul Shirzadeh, Wout Weijtjens, Patrick Guillaume, and Christof Devriendt. The dynamics of an offshore wind turbine in parked conditions: A comparison between simulations and measurements. *Wind Energy*, 18(10):1685–1702, 10 2015.

[14] Max Bouwmeesters. Stall and vortex induced vibrations in large wind turbines. Technical report.

[15] Dimitris I. Manolas, Panagiotis K. Chaviaropoulos, and Vasilis A. Riziotis. Assessment of Vortex Induced Vibrations on wind turbines. In *Journal of Physics: Conference Series*, volume 2257. Institute of Physics, 5 2022.

[16] EN 1991-1-4: Eurocode 1: Actions on structures - Part 1-4: General actions - Wind actions. Technical report, European Committee for Standardization, 2005.

[17] Georg Raimund Pirrung, Christian Grinderslev, Niels Nørmark Sørensen, and Riccardo Riva. Vortex-induced vibrations of wind turbines: From single blade to full rotor simulations. *Renewable Energy*, 226:960–1481, 2024.

[18] Pietro Bortolotti, Helena Canet Tarres, Katherine Dykes, Karl Merz, Latha Sethuraman, David Verelst, and Frederik Zahle. IEA Wind TCP Task 37 Systems Engineering in Wind Energy-WP2.1 Reference Wind Turbines. Technical report, 2019.

[19] Jun Leng, Gen Li, and Lei Duan. The impact of extreme wind conditions and yaw misalignment on the aeroelastic responses of a parked offshore wind turbine. *Ocean Engineering*, 313, 12 2024.

[20] Qingshen Meng, Wei Yu, Faming Wu, Xugang Hua, and Chao Chen. Stall-induced aeroelastic instability of floating offshore wind turbines: Comparison of frequency domain and time domain quasi-steady approaches. *Renewable Energy*, 251, 10 2025.

[21] S G Horcas, N N Sørensen, F Zahle, N N Sørensen, G R Pirrung, and T Barlas. Vibrations of wind turbine blades in standstill: Mapping the influence of the inflow angles. *Phys. Fluids*, 34:54105, 2022.

[22] S. G. Horcas, T. Barlas, F. Zahle, and N. N. Sørensen. Vortex induced vibrations of wind turbine blades: Influence of the tip geometry. *Physics of Fluids*, 32(6):065104, 6 2020.

[23] Joachim C. Heinz, Niels N. Sørensen, Frederik Zahle, and Witold Skrzypiński. Vortex-induced vibrations on a modern wind turbine blade. *Wind Energy*, 19(11):2041–2051, 11 2016.

[24] Witold Skrzypiński, Mac Gaunaa, and Joachim Heinz. Modelling of Vortex-Induced Loading on a Single-Blade Installation Setup. *Journal of Physics: Conference Series*, 753(8), 10 2016.

[25] S.G. Horcas, M.H.A. Madsen, N.N. Sørensen, and F. Zahle. Suppresing Vortex Induced Vibrations of Wind Turbine blades with flaps. In *the 7th European Conference on Computational Fluid Dynamics (ECFD 7) European Community on Computational Methods in Applied Sciences*, number 7, 2018.

[26] D. E. Raveh and E. H. Dowell. Frequency lock-in phenomenon for oscillating airfoils in buffeting flows. *Journal of Fluids and Structures*, 27(1):89–104, 1 2011.

[27] Christian Grinderslev, Felix Houtin-Mongrolle, Niels Nørmark Sørensen, Georg Raimund Pirrung, Pim Jacobs, Aqeel Ahmed, and Bastien Duboc. Forced-motion simulations of vortex-induced vibrations of wind turbine blades-a study of sensitivities. *Wind Energ. Sci*, 8:1625–1638, 2023.

[28] Witold Skrzypiński, Mac Gaunaa, Niels Sørensen, Frederik Zahle, and Joachim Heinz. Vortex-induced vibrations of a DU96-W-180 airfoil at 90° angle of attack. *Wind Energy*, 17(10):1495–1514, 2013.

[29] R. S. Ehrmann, K. M. Loftin, S. Johnson, and E. B. White. Lock-in of elastically mounted airfoils at a 90° angle of attack. *Journal of Fluids and Structures*, 44:205–215, 1 2014.

[30] Fanny M. Besem, Joshua D. Kamrass, Jeffrey P. Thomas, Deman Tang, and Robert E. Kielb. Vortex-induced vibration and frequency lock-in of an airfoil at high angles of attack. *Journal of Fluids Engineering, Transactions of the ASME*, 138(1), 1 2016.

[31] Bridget M. Benner, Daniel W. Carlson, Banafsheh Seyed-Aghazadeh, and Yahya Modarres-Sadeghi. Vortex-Induced Vibration of symmetric airfoils used in Vertical-Axis Wind Turbines. *Journal of Fluids and Structures*, 91:102577, 11 2019.

[32] Ping Hu, Chong Sun, Xiaocheng Zhu, and Zhaohui Du. Investigations on vortex-induced vibration of a wind turbine airfoil at a high angle of attack via modal analysis. *Journal of Renewable and Sustainable Energy*, 13(3):033306, 6 2021.

[33] Craig Meskell and Alberto Pellegrino. Vortex shedding lock-in due to pitching oscillation of a wind turbine blade section at high angles of attack. *International Journal of Aerospace Engineering*, 2019, 2019.

[34] F. Zou, V. A. Riziotis, S. G. Voutsinas, and J. Wang. Analysis of vortex-induced and stall-induced vibrations at standstill conditions using a free wake aerodynamic code. *Wind Energy*, 18(12):2145–2169, 12 2015.

[35] Franck Bertagnolio, Helge Aa Madsen, Andreas Fischer, and Christian Bak. A semi-empirical airfoil stall noise model based on surface pressure measurements. *Journal of Sound and Vibration*, 387:127–162, 1 2017.

[36] Nicholas J. Kay, Peter J. Richards, and Rajnish N. Sharma. Influence of turbulence on cambered and symmetrical airfoils at low Reynolds numbers. *AIAA Journal*, 58(5):1913–1925, 2020.

[37] Lance W. Traub and Evan Cooper. Experimental investigation of pressure measurement and airfoil characteristics at low Reynolds numbers. *Journal of Aircraft*, 45(4):1322–1333, 2008.

[38] Serhiy Yarusevych and Michael S H Boutilier. Vortex Shedding of an Airfoil at Low Reynolds Numbers. 2011.

[39] Ryan Gerakopulos and Serhiy Yarusevych. Novel time-resolved pressure measurements on an airfoil at a low Reynolds number. *AIAA Journal*, 50(5):1189–1200, 5 2012.

[40] K E Swalwell, J Sheridan, and W H Melbourne. Frequency analysis of surface pressures on an airfoil after stall. In *21st AIAA Applied Aerodynamics Conference*, 2003.

[41] W A Timmer. Aerodynamic characteristics of wind turbine blade airfoils at high angles-of-attack. In *TORQUE 2010: The science of making torque from wind*, pages 71–78, 2010.

[42] Andrew H. Lind and Anya R. Jones. Vortex shedding from airfoils in reverse flow. *AIAA Journal*, 53(9):2621–2633, 2015.

[43] Andrew H. Lind and Anya R. Jones. Unsteady airloads on static airfoils through high angles of attack and in reverse flow. *Journal of Fluids and Structures*, 63:259–279, 5 2016.

[44] Theodore Theodorsen. General theory of aerodynamic instability and the mechanism of flutter. Technical report, NACA, 1935.

[45] William Rees Sears. *A systematic presentation of the theory of thin airfoils in non-uniform motion*. PhD thesis, California Institute of Technology, 1938.

[46] J. Mayo Greenberg. Airfoil in sinusoidal motion in a pulsating stream. Technical report, NACA, 1947.

[47] Jeesoon Choi, Tim Colonius, and David Williams. Dynamics and energy extraction of a surging and plunging airfoil at low Reynolds number. In *51st AIAA Aerospace Sciences Meeting including the New Horizons Forum and Aerospace Exposition*, page 672, 2013.

[48] Gordon J Leishman. *Principles of helicopter aerodynamics*. Cambridge university press, Cambridge, 2006.

[49] Wenbo Zhu, Matthew H. McCrink, Jeffrey P. Bons, and James W. Gregory. The unsteady Kutta condition on an airfoil in a surging flow. *Journal of Fluid Mechanics*, 2020.

[50] C. Strangfeld, H. F. Müller-Vahl, C. N. Nayeri, C. O. Paschereit, and D. Greenblatt. Airfoil synchronous surging and pitching. *Journal of Fluid Mechanics*, 1009, 4 2025.

[51] Philip B. Kirk and Anya R. Jones. Vortex formation on surging aerofoils with application to reverse flow modelling. *Journal of Fluid Mechanics*, 859:59–88, 1 2018.

[52] J Young and J C S Lai. Oscillation frequency and amplitude effects on the wake of a plunging airfoil. *AIAA Journal*, 42(10), 2004.

[53] John Young and Joseph C S Lai. Vortex lock-in phenomenon in the wake of a plunging airfoil. *AIAA Journal*, 45, 2 2007.

[54] Idil Fenercioglu and Oksan Cetiner. Categorization of flow structures around a pitching and plunging airfoil. *Journal of Fluids and Structures*, 31:92–102, 5 2012.

[55] Chang Kwon Kang, Hikaru Aono, Yeon Sik Baik, Luis P. Bernal, and Wei Shyy. Fluid dynamics of pitching and plunging flat plate at intermediate Reynolds numbers. *AIAA Journal*, 51(2):315–329, 2 2013.

[56] Johannes Kissing, Jochen Kriegseis, Zhenyao Li, Lihao Feng, Jeanette Hussong, and Cameron Tropea. Insights into leading edge vortex formation and detachment on a pitching and plunging flat plate. *Experiments in Fluids*, 61(9):1–18, 9 2020.

[57] Miguel R. Visbal. Numerical investigation of deep dynamic stall of a plunging airfoil. *AIAA Journal*, 49(10):2152–2170, 10 2011.

[58] A Gross, M Agate, J Little, and H F Fasel. Numerical Simulation of Plunging Wing Section at High Angles of Attack. *AIAA Journal*, (56), 2018.

[59] Victor Troshin and Avraham Seifert. Modeling of a pitching and plunging airfoil using experimental flow field and load measurements. *Experiments in Fluids*, 59(1):1–14, 11 2017.

[60] Chang-Kwon Kang, Yeon Sik Baik, Luis Bernal, Michael V Ol, and Wei Shyy. Fluid dynamics of pitching and plunging airfoils of Reynolds number between 1×10^4 and 6×10^4. In *47th AIAA Aerospace Sciences Meeting Including The New Horizons Forum and Aerospace Exposition*, 2009.

[61] Yeon Sik Baik, Jonathan M Rausch, Luis P Bernal, and Michael V Ol. Experimental Investigation of Pitching and Plunging Airfoils at Reynolds Number between 1×10^4 and 6×10^4. In *39th AIAA Fluid Dynamics Conference*, 6 2009.

[62] Lawrence W. Carr. Progress in analysis and prediction of dynamic stall. *Journal of Aircraft*, 25(1):6–17, 1988.

[63] W J McCroskey and Richard K. Fisher. Detailed Aerodynamic Measurements on a Model Rotor in the Blade Stall Regime. *Journal of the American Helicopter Society*, 1 1972.

[64] W J McCroskey. The Phenomenon of Dynamic Stall. *National Aeronautics and Space Administration*, 1981.

[65] Kenneth W McAlister, Lawrence W Carr, and William J Mccroskey. Dynamic Stall Experiments on the NACA 0012 Airfoil. Technical report, 1978.

[66] J G Leishman and T S Beddoes. A Semi-Empirical Model for Dynamic Stall. *Journal of the American Helicopter society*, 34:3–17, 1989.

[67] V K Truong. A 2-D Dynamic Stall Model Based on a Hopf Bifurcation. Technical report, 1993.

[68] C T Tran and D Petot. Semi-empirical model for the dynamic stall of airfoils in view to the application to the calculation of responses of a helicopter blade in forward flight. In *Sixth European Rotorcraft and Powered Lift Aircraft Forum*, 9 1980.

[69] M H Akbari and S J Price. Simulation of dynamic stall for a NACA 0012 airfoil using a vortex method. *Journal of Fluids and Structures*, 17:855–874, 2003.

[70] Karen Mulleners and Markus Raffel. The onset of dynamic stall revisited. *Experiments in Fluids*, 52(3):779–793, 3 2012.

[71] Karen Mulleners and Markus Raffel. Dynamic stall development. *Experiments in Fluids 2013 54:2*, 54(2):1–9, 2 2013.

[72] Rohit Gupta and Phillip J. Ansell. Unsteady flow physics of airfoil dynamic stall. *AIAA Journal*, 57(1):165–175, 2019.

[73] Janik Kiefer, Claudia E. Brunner, Martin O.L. Hansen, and Marcus Hultmark. Dynamic stall at high Reynolds numbers induced by ramp-type pitching motions. *Journal of Fluid Mechanics*, 938, 5 2022.

[74] Anubhav Datta, Hyeonsoo Yeo, and Thomas R. Norman. Experimental investigation and fundamental understanding of a full-scale slowed rotor at high advance ratios. In *Journal of the American Helicopter Society*, volume 58, 4 2013.

[75] Mark Potsdam, Anubhav Datta, and Buvana Jayaraman. Computational investigation and fundamental understanding of a slowed UH-60A rotor at high advance ratios. *Journal of the American Helicopter Society*, 61(2), 4 2016.

[76] N. Guillaud, G. Balarac, and E. Goncalvès. Large Eddy Simulations on a pitching airfoil: Analysis of the reduced frequency influence. *Computers and Fluids*, 161:1–13, 1 2018.

[77] Binbin Wei, Yongwei Gao, and Dong Li. Physics of Dynamic Stall Vortex During Pitching Oscillation of Dynamic Airfoil. *International Journal of Aeronautical and Space Sciences*, 22(6):1263–1277, 12 2021.

[78] Nabil M. Khalifa, Amirsaman Rezaei, and Haithem E. Taha. On computational simulations of dynamic stall and its three-dimensional nature. *Physics of Fluids*, 35(10), 10 2023.

[79] Andrew H. Lind and Anya R. Jones. Unsteady aerodynamics of reverse flow dynamic stall on an oscillating blade section. *Physics of Fluids*, 28(7), 7 2016.

[80] Markus Raffel, Christian E Willert, Fulvio Scarano, Christian J Kähler, Steven T Wereley, and Jürgen Kompenhans. Particle Image Velocimetry A Practical Guide Third Edition. Technical report.

[81] W. A. Timmer. Wind Tunnel Wall Corrections for Two-Dimensional Testing up to Large Angles of Attack. In *Handbook of Wind Energy Aerodynamics*, pages 1–29. Springer, Cham, 2021.

[82] E C Maskell. A theory of the blockage effects on bluff bodies and stalled wings in a closed wind tunnel. Technical report, 11 1963.

[83] Bergh H and Tijdeman H. Theoretical and Experimental Results for the Dynamic Response of Pressure Measuring Systems. Technical report, National Aero- and Astronautical Research Institute, Amsterdam, 1965.

[84] Anindya Chatterjee. An introduction to the proper orthogonal decomposition. *Current science*, 78(7), 2000.

[85] B W Van Oudheusden. PIV-based pressure measurement. *Measurement Science and Technology*, 24:32, 2013.

[86] David E. Rival and Bas van Oudheusden. Load-estimation techniques for unsteady incompressible flows. *Experiments in Fluids*, 58(3), 3 2017.

[87] D. Ragni, B. W. Van Oudheusden, and F. Scarano. Non-intrusive aerodynamic loads analysis of an aircraft propeller blade. *Experiments in Fluids*, 51(2):361–371, 8 2011.

[88] R van de Meerendonk, M Perçin, and B Van Oudheusden. Three-dimensional flow and load characteristics of flexible revolving wings at low Reynolds number. In *18th International Symposium on the Application of Laser and Imaging Techniques to Fluid Mechanics: Lisbon, Portugal*, 7 2016.

[89] Laurent Graftieaux, Marc Michard, and Nathalie Grosjean. Combining PIV, POD and vortex identification algorithms for the study of unsteady turbulent swirling flows. *Measurement Science and Technology*, 12:1422, 2001.

[90] C. E. Morgan, H. Babinsky, and J. K. Harvey. Vortex detection methods for use with PIV and CFD Data. *47th AIAA Aerospace Sciences Meeting including the New Horizons Forum and Aerospace Exposition*, page 74, 2009.

[91] Guanqun Xu, Wei Yu, Andrea Sciacchitano, and Ferreira Simao Carlos. An Experimental Study of the Unsteady Aerodynamics of a Static DU91-W2-150 Airfoil at Large Angles of Attack. *Wind Energy*, 28(3):e2974, 3 2025.

[92] J. Gordon Leishman. Challenges in modelling the unsteady aerodynamics of wind turbines. *Wind Energy*, 5(2-3):85–132, 4 2002.

[93] Hermann Schlichting and Klaus Gersten. *Boundary-Layer Theory*. Springer Berlin Heidelberg, 10 2016.

[94] Alberto Pellegrino and Craig Meskell. Vortex shedding from a wind turbine blade section at high angles of attack. *Journal of Wind Engineering and Industrial Aerodynamics*, 121:131–137, 10 2013.

[95] W A Timmer and R P J O M Van Rooij. Some aspects of high angle-of-attack flow on airfoils for wind turbine application. 2001.

[96] Kai Wang, Vasilis A. Riziotis, and Spyros G. Voutsinas. Aeroelastic stability of idling wind turbines. *Wind Energy Science*, 2(2):415–437, 7 2017.

[97] S M Hasheminasab, S M H Karimian, S Noori, M Saeedi, and C Morton. Experimental investigation of the wake dynamics for a NACA0012 airfoil with a cut-in serrated trailing-edge. *Physics of Fluids*, 33:55122, 2021.

[98] Jerry M. Chen and Yuan-Cheng Fang. Strouhal numbers of inclined flat plates. *Journal of Wind Engineering and Industrial Aerodynamics*, 61(2-3):99–112, 7 1996.

[99] Boorsma K. Comparison of experimental and computational aerodynamic section characteristics of the DU91-W2-250 profile. Technical report, Delft University of Technology, 2003.

[100] Cameron Tropea. Springer Handbook of Experimental Fluid Mechanics. 2007.

[101] Guanqun Xu, Andrea Sciacchitano, Carlos Ferreira, and Wei Yu. On the unsteady aerodynamics of a surging airfoil at 90° incidence. *Experiments in Fluids*, 66(5), 5 2025.

[102] C H K Williamson and A Roshko. Vortex formation in the wake of an oscillating cylinder. *Journal of Fluids and Structures*, 2:355–381, 1988.

[103] R E D Bishop and A Y Hassan. The lift and drag forces on a circular cylinder oscillating in a flowing fluid. *Proceedings of the Royal Society of London. Series A, Mathematical and Physical Sciences*, 277(1368):51–75, 1964.

[104] Deman Tang and Earl H. Dowell. Experimental aerodynamic response for an oscillating airfoil in buffeting flow. *AIAA Journal*, 52(6):1170–1179, 6 2014.

[105] David Holst, Francesco Balduzzi, Alessandro Bianchini, Benjamin Church, Felix Wegner, Georgios Pechlivanoglou, Lorenzo Ferrari, Giovanni Ferrara, Christian Navid Nayeri, and Christian Oliver Paschereit. Static and dynamic analysis of a NACA 0021 airfoil section at low Reynolds numbers based on experiments and computational fluid dynamics. *Journal of Engineering for Gas Turbines and Power*, 141(5):51015–51016, 5 2019.

[106] G. H. Koopmann. The vortex wakes of vibrating cylinders at low Reynolds numbers. *Journal of Fluid Mechanics*, 28(3):501–512, 5 1967.

[107] P Anagnostopoulos. Numerical study of the flow past a cylinder excited transversely to the incident stream. Part 1: Lock-in zone, hydrodynamic forces and wake geometry. *Journal of Fluids and Structures*, 14:819–851, 2000.

[108] Meneghini J.R. and Bearman P.W. Numerical simulation of high amplitude oscillatory flow about a circular cylinder. *Journal of Fluids and Structures*, 9(4):435–455, 1995.

[109] Qingqing Ye, Ferry F.J. Schrijer, and Fulvio Scarano. Boundary layer transition mechanisms behind a micro-ramp. *Journal of Fluid Mechanics*, 793:132–161, 4 2016.

[110] Andrea Sciacchitano and Bernhard Wieneke. PIV uncertainty propagation. *Measurement Science and Technology*, 27(8), 6 2016.

[111] Simon J Corkery, P R R J Stevens, and Holger Babinsky. Low Reynolds number surge response of a flat plate wing at 90 degrees incidence. In *55th AIAA Aerospace Sciences Meeting*, 2017.

[112] Lamb Horace. Hydrodynamics. New York Dover publications, 1945.

[113] Troy R Smith, Jeff Moehlis, and Philip Holmes. Low-dimensional modelling of turbulence using the Proper Orthogonal Decomposition. *Nonlinear Dynamics*, 41:275–307, 2005.

[114] Jeesoon Choi, Tim Colonius, and David R. Williams. Surging and plunging oscillations of an airfoil at low Reynolds number. *Journal of Fluid Mechanics*, 763:237–253, 1 2015.

[115] D. Holst, B. Church, F. Wegner, G. Pechlivanoglou, C. N. Nayeri, and C. O. Paschereit. Experimental Analysis of a NACA 0021 Airfoil under Dynamic Angle of Attack Variation and Low Reynolds Numbers. *Journal of Engineering for Gas Turbines and Power*, 141(3), 3 2019.

[116] Adhyanth Giri Ajay and Carlos Simao Ferreira. A numerical investigation of wake recovery for an H- and X-shaped vertical-axis wind turbine with wake control strategies. *Physics of Fluids*, 36(12), 12 2024.

[117] David Bensason, Jayant Mulay, Andrea Sciacchitano, and Carlos Ferreira. Experimental demonstration of regenerative wind farming using a high-density layout of vertical-axis wind turbines. *Wind Energy Science*, 10(7):1499–1528, 7 2025.

[118] Ching Te Lin, Min Lin Tsai, and Hsieh Chen Tsai. Flow control of a plunging cylinder based on resolvent analysis. *Journal of Fluid Mechanics*, 967, 7 2023.

[119] Renato Miotto, William Wolf, Datta Gaitonde, and Miguel Visbal. Analysis of the onset and evolution of a dynamic stall vortex on a periodic plunging aerofoil. *Journal of Fluid Mechanics*, 938, 5 2022.

[120] Guanqun Xu, Andrea Sciacchitano, Carlos Ferreira, and Wei Yu. Dynamic stall of a pitching airfoil under reverse flow conditions. *Physics of Fluids*, 37(11), 11 2025.

[121] Kiran Ramesh, Ashok Gopalarathnam, Kenneth Granlund, Michael V. Ol, and Jack R. Edwards. Discrete-vortex method with novel shedding criterion for unsteady aerofoil flows with intermittent leading-edge vortex shedding. *Journal of Fluid Mechanics*, 751:500–538, 2014.

[122] Sarasija Sudharsan, B. Ganapathysubramanian, and A. Sharma. A vorticity-based criterion to characterise leading edge dynamic stall onset. *Journal of Fluid Mechanics*, 935, 3 2022.

[123] Xiao Li and Li Hao Feng. Critical indicators of dynamic stall vortex. *Journal of Fluid Mechanics*, 937, 4 2022.

[124] Chengyong Zhu, Hongting Yang, Yingning Qiu, Guanting Zhou, Ling Wang, Yi Feng, Ziyang Shen, Xiang Shen, Xiumei Feng, and Tongguang Wang. Effects of the Reynolds number and reduced frequency on the aerodynamic performance and dynamic stall behaviors of a vertical axis wind turbine. *Energy Conversion and Management*, 293, 10 2023.

[125] Abel John Buchner, Damon Honnery, and Julio Soria. Stability and three-dimensional evolution of a transitional dynamic stall vortex, 7 2017.

[126] John D Anderson. *Fundamentals of Aerodynamics*. McGraw hill, New York, 2011.

[127] Student. The Probable error of a mean. *Biometrika*, 1908.

[128] Andrea Sciacchitano and Fulvio Scarano. Elimination of PIV light reflections via a temporal high pass filter. *Measurement Science and Technology*, 25(8), 8 2014.

[129] Miguel R. Visbal and Stuart I. Benton. Exploration of high-frequency control of dynamic stall using large-eddy simulations. In *AIAA Journal*, volume 56, pages 2974–2991. American Institute of Aeronautics and Astronautics Inc., 2018.

[130] Sarasija Sudharsan, Shreyas Narsipur, and Anupam Sharma. Evaluating dynamic stall-onset criteria for mixed and trailing-edge stall. *AIAA Journal*, 61(3):1181–1196, 3 2023.

[131] Miguel R. Visbal. Numerical exploration of flow control for delay of dynamic stall on a pitching airfoil. In *32nd AIAA Applied Aerodynamics Conference*, Atlanta, GA, 2014. American Institute of Aeronautics and Astronautics Inc.

[132] Joachim Hodara, Andrew H. Lind, Anya R. Jones, and Marilyn J. Smith. Collaborative investigation of the aerodynamic behavior of airfoils in reverse flow. In *Journal of the American Helicopter Society*, volume 61. American Helicopter Society, 7 2016.

[133] Kim SW, Associate K B M Q Zaman, and J Panda. Numerical Investigation of Unsteady Transitional Flow Over Oscillating Airfoil. *J. Fluids Eng.*, 117, 3 1995.

[134] Patrick R. Hammer, Daniel J. Garmann, and Miguel R. Visbal. Effect of Aspect Ratio on Finite-Wing Dynamic Stall. *AIAA Journal*, 60(12):6581–6593, 12 2022.

[135] Gal Berkooz, Philip Holmes, and John L Lumley. The proper orthogonal decomposition in the analysis of turbulent flows. *Annu. Rev. Fluid Mech*, 25:539–75, 1993.

[136] Ricardo Fernandez-Aldama, George Papadakis, Oscar Lopez-Garcia, Sergio Avila-Sanchez, Vasilis A. Riziotis, Alvaro Cuerva-Tejero, and Cristobal Gallego-Castillo. Characterization of vortex-shedding regimes and lock-in response of a wind turbine airfoil with two high-fidelity simulation approaches. *Wind Energy Science*, 10(1):17–39, 1 2025.

[137] Narakorn Srinil, Hossein Zanganeh, and Alexander Day. Two-degree-of-freedom VIV of circular cylinder with variable natural frequency ratio: Experimental and numerical investigations. *Ocean Engineering*, 73:179–194, 2013.

[138] Mohammadreza Rashki, Alireza Mojtahedi, Mohammad Ali Lotfollahi-Yaghin, Vahid Tamimi, Mehran Dadashzadeh, Paulo Rosa Santos, Michael M. Bernitsas, and Narakorn Srinil. A review of two-degree-of-freedom vortex-induced vibrations with hydrokinetic energy harvesting applications, 3 2025.

[139] Carlo L. Bottasso, Filippo Campagnolo, and Vlaho Petrović. Wind tunnel testing of scaled wind turbine models: Beyond aerodynamics. *Journal of Wind Engineering and Industrial Aerodynamics*, 127:11–28, 2014.

[140] Ilmas Bayati, Marco Belloli, Luca Bernini, and Alberto Zasso. Aerodynamic design methodology for wind tunnel tests of wind turbine rotors. *Journal of Wind Engineering and Industrial Aerodynamics*, 167:217–227, 8 2017.

[141] Helena Canet, Pietro Bortolotti, and Carlo L. Bottasso. On the scaling of wind turbine rotors. *Wind Energy Science*, 6(3):601–626, 5 2021.

[142] Wei Yang, Meng Yu, Bowen Yan, Guoqing Huang, Qingshan Yang, Senqin Zhang, Tianhao Hong, Xu Zhou, and Xiaowei Deng. Wind Tunnel Tests of Wake Characteristics for a Scaled Wind Turbine Model Based on Dynamic Similarity. *Energies*, 15(17), 9 2022.

[143] Edgar Buckingham. On physically similar systems; illustrations of the use of dimensional equations. *Physical review*, 4(4), 1914.

[144] Andreas Schröder and Daniel Schanz. 3D Lagrangian Particle Tracking in Fluid Mechanics. *Annual Review of Fluid Mechanics*, 55(1):511–540, 2023.

[145] Patrick O. Bowles, Thomas C. Corke, Dustin G. Coleman, Flint O. Thomas, and Mark Wasikowski. Improved understanding of aerodynamic damping through the Hilbert transform. *AIAA Journal*, 52(11):2384–2394, 11 2014.

[146] Thomas C. Corke and Flint O. Thomas. Dynamic stall in pitching airfoils: Aerodynamic damping and compressibility effects. *Annual Review of Fluid Mechanics*, 47:479–505, 2015.

[147] Leon Li and R. Jason Hearst. Effects of freestream turbulence on the wakes of circular and square cylinders. *Physical Review Fluids*, 10(11), 11 2025.

[148] Daniele Ragni and Carlos Ferreira. Effect of 3D stall-cells on the pressure distribution of a laminar NACA64-418 wing. *Experiments in Fluids*, 57(8), 8 2016.

[149] Elena Llorente and Daniele Ragni. Trailing edge serrations effects on the aerodynamic performance of a NACA 643418. *Wind Energy*, 22(3):392–406, 3 2019.

[150] J Jonkman, S Butterfield, W Musial, and G Scott. Definition of a 5-MW Reference Wind Turbine for Offshore System Development. Technical report, National Renewable Energy Lab.(NREL), Golden, CO (United States), 2 2009.

Acknowledgments

The journey towards the completion of this dissertation has been challenging, yet I feel fortunate to have been supported by so many people, and I would like to thank all of you.

First, I would like to express my deepest gratitude to my supervisory team. **Wei**, thank you so much for your dedicated guidance throughout this period. You supported me from my initial onboarding through every wind tunnel experiment, and you helped with every detail of my stay here at TU Delft. I truly enjoyed our weekly meetings, where our discussions always provided me with valuable ideas for my research. Furthermore, your comments on my paper drafts have directly contributed to the depth and overall quality of my work.

Andrea, I cannot thank you enough for your unwavering support. You generously shared your profound practical and theoretical knowledge of experimental aerodynamics, which was crucial to the success of my wind tunnel campaigns and my growth as a researcher. I also deeply appreciate the significant time you dedicated to our weekly scientific discussions. Your ability to always find a practical way forward whenever I was stuck was invaluable to my progress.

Carlos, my PhD journey would simply not be complete without you. Although you could not participate in the last two years of my PhD, you were always supportive and provided me with many amazing ideas to work on, while also allowing me to explore freely. I am truly grateful!

Additionally, none of my experimental studies could have been conducted without the technical support I received from the wind tunnel labs at TU Delft. Thank you **Stefan Bernardy**, **Frits Donker Duyvis**, **Dennis Bruikman**, and **Peter Duyndam** for your support during my wind tunnel experiments in the LTT and the HSL. Your expertise in all experimental aspects is incredibly valuable.

I am also grateful to the two graduate students I worked with: **Sowmya** and **Pepijn**. You were true comrades during those demanding weeks of wind tunnel testing, and thanks to your talent and tremendous help, our experiments were a great success!

My PhD journey is also supported by my dearest colleagues from the Wind Energy section: **Abhratej, Abhyuday, Ali, Ambar, Anand, André, Anastasia, Andrea Piccolo, Andrea Sanvito, Augustin, Axelle, Bruce, Carlos, Charis, Christina, Christopher, Claudia, Clem, Dachuan, Dani, David, Deepali, Dominic, Donatella, Dylan, Emanuele, Erik, Evert, Federico Di Verniere, Federico Taruffi, Felipe, Fernanda, Flavio, George, Hafiz, Haoyuan, Hasse, Helena, Hendrik, Isaac, Jatinder, Jelle, Jenna, Jiaxin, Jing, Jingna, Kaj, Kiran, Likhitha, Livia, Lucas, Martino, Mathis, Matteo, Mehtab, Mihir, Muhammad, Nikita, Nils, Nirav, Olivier, Oriol, Qingshen, Rention, Ricardo, Rishikesh, Rushikesh, Sebastian, Sen, Shantanu, Shyam, Simone, Sumit, Sylvia, Tercio, Udhaya, Xin, Yan, Yanan, Yannick**. Being a member of this team has been a privilege. Thank you for the generous support of my experiments and the inspiring scientific discussions that constantly pushed my research forward.

Beyond research, I will always cherish the invaluable memories we made from fun trips to conferences to our weekend sports challenges. Most importantly, I appreciate being part of a welcoming environment that so genuinely values diversity and inclusion. These invaluable experiences will stay with me for a very long time.

Meanwhile, I want to thank my colleagues from the Aerodynamics section: **Adrian, Brian, Christoph, Constantin, Edoardo, Gabriel, Ilda, Jane, Kushal**. The discussions with you always lead to positive outcomes for my work.

Additionally, I also met a few other amazing people at (TU) Delft: **Abhishek, Ajay, Anwesha, Arshdeep, Cecilia, Dong, Elian, Gokul, Ilaria, Jiashang, Jinlai, Kaavya, Kaisheng, Li, Mengjie, Ranjan, Reddhi, Renzhi, Taniya, Wencan, Xiang, Xiaodong, and Yifu**. I enjoyed our time together so much through trips, dinners, and paintings!

My close friends before I came to Delft: **晨雨, 林越, 慧倩, 汪林, 嘉诚, 嘉颖, 君妍, 有娜, 晨雪, 君茹, 薇薇, 李儒, 心悦, 芷若**. Although we could not meet as frequently as before due to distance, your support and care have always been constant.

我特别想感谢我的**父母**。你们是我最坚强的后盾，也是我继续探索人生的支柱。谢谢你们的支持与鼓励！

My deepest gratitude goes to my boyfriend **Adhyanth**, whom I feel so lucky to meet during my PhD period! Your unlimited support and companionship provide me with enormous therapeutic energy, which makes me become a better person than I could have ever imagined.

I can not express enough how grateful I am in this short acknowledgment. I hope this dissertation will be a good memory for all of us.

Guanqun
Delft, April 2026

Curriculum Vitæ

Guanqun Xu

1997/10/28	Born in Chuzhou, China
2026 – present	**Postdoc Researcher in Aerodynamics** Delft University of Technology, Delft, The Netherlands
2021 – 2025	**PhD in Wind Energy** Delft University of Technology, Delft, The Netherlands
2019 – 2021	**Master of Science in Wind Energy** Technical University of Denmark, Kongens Lyngby, Denmark
2015 – 2019	**Bachelor of Science in New Energy Science and Engineering** Yangzhou University, Yangzhou, China

List of Publications

JOURNAL AND CONFERENCE PAPERS

7. **G. Xu**, A. Sciacchitano, W. Yu, *Vortex initiation detection and evolution analysis on a pitching airfoil under reverse flow conditions*, Physics of Fluids, *under review.*

6. **G. Xu**, A. Sciacchitano, C. Simão Ferreira, W. Yu, *Unsteady aerodynamics of a plunging airfoil at large angles of attack*, Experiments in Fluids, *accepted.*

5. **G. Xu**, A. Sciacchitano, C. Simão Ferreira, W. Yu, *Dynamic stall of a pitching airfoil under reverse flow conditions*, Physics of Fluids, **37**, (1), 32, 2025.

4. **G. Xu**, A. Sciacchitano, C. Simão Ferreira, W. Yu, *On the unsteady aerodynamics of a surging airfoil at* 90° *incidence*, Experiments in Fluids **66** (5), 85, 2025.

3. **G. Xu**, W. Yu, A. Sciacchitano, C. Simão Ferreira, *An experimental study of the unsteady aerodynamics of a static DU91-W2-150 airfoil at large angles of attack*, Wind Energy **28** (3), 19, 2025.

2. **G. Xu**, W. Yu, C. Simão Ferreira, A. Sciacchitano, S. Iyer, *Experimental comparison of a NACA0021 airfoil in large plunging and surging motions at* 90° *angle of attack*, Journal of Physics: Conference Series **2767** (2), 022047, 2024.

1. **G. Xu**, W. Yu, T. Kim, *Wind turbine load estimation using machine learning and transfer learning*, Journal of Physics: Conference Series **2265** (3), 032108, 2022.

DATASETS

4. **G. Xu**, A. Sciacchitano, C. Simão Ferreira, W. Yu, *Data from the study of PIV measurement flow field of the airfoil NACA0021 under plunging motion*, 4TU.ResearchData, 2026.

3. **G. Xu**, W. Yu, A. Sciacchitano, C. Simão Ferreira, P. Slooter, *Data from the pressure measurement of a pitching airfoil NACA643418*, 4TU.ResearchData, 2024.

2. **G. Xu**, W. Yu, A. Sciacchitano, C. Simão Ferreira, S. Iyer, *Data from the study of PIV measurement flow field of the airfoil NACA0021 under surging motion*, 4TU.ResearchData, 2024.

1. **G. Xu**, W. Yu, A. Sciacchitano, C. Simão Ferreira, *Data underlying the publication: An experimental study of the unsteady aerodynamics of a static DU91-W2-150 airfoil at large angles of attack*, 4TU.ResearchData, 2024.